University of Southern Queensland

Faculty of Health, Engineering and Sciences

DESIGN AND DEVELOPMENT OF AN ELECTRIC MOTOR INVERTER/CONTROLLER FOR A FORMULA SAE ELECTRIC RACE CAR

A dissertation submitted by

Samuel Baker

in fulfillment of the requirements of

ENG4111 and ENG4112 Research Project

towards the degree of

Bachelor of Engineering (Honours) (Power)

Submitted October, 2023

Abstract

Formula SAE (FSAE) is a student-led engineering challenge focussing on designing, engineering and building a formula-style, open-wheeled race car. The developed vehicles are assessed for compliance against the stringent rules and standards set by the Society of Automotive Engineers. Compliant vehicles are then competitively evaluated against competing teams from local and international universities. The University of Southern Queensland (UniSQ) has recently formed the USQ Racing team to compete in the Electrical Vehicle (EV) category, requiring the scratch build of a functional vehicle. This is a significant engineering challenge involving a large team of multidisciplinary students who must coordinate the development of several integrated subsystems to produce a functional, compliant vehicle.

The motivation behind this project is to support the USQ Racing team by developing the powertrain, a key subsystem on the EV. Specifically, this project aims i) to develop and perform the acceptance tests for the previously acquired 55kW 228 EMRAX motor, as well as ii) design and develop a low-cost and customisable electric motor controller and simulation platform for an FSAE application.

A series of tests were performed in the UniSQ Energy Systems Lab to verify the integratory of the motor windings, substantiate the mechanical functionality and confirm the operability of the rotor position sensor. Tests identified the resolver to be faulty. Following rectification, the motor was deemed to be serviceable.

A review was undertaken to inform the selection of components for developing a custom motor controller for an FSAE application and capable of commutating the EMRAX 228 motor. Thermal analysis and modelling were performed to validate the proposed cooling system. Field Oriented Control (FOC) algorithms for motor commutation were adapted from the MathWorks' Simulink environment, compiled and deployed on an STM32 microcontroller. A PCB incorporating power transistors and current feedback was designed and fabricated as a prototype motor controller. Commutation of the EMRAX 228 was successfully demonstrated with this motor controller. The Simulink and microcontroller framework and the developed prototype have produced a sound basis for the ongoing development and optimisation of the FSAE vehicle powertrain and other subsystems.

Future work identified includes i) performance testing of the EMRAX 228 motor under load conditions, ii) improvement of current feedback and rotor position sensing to the motor controller, iii) IGBT thermal monitoring and management, and iv) broader systems integration of the controller and motor in the vehicle.

University of Southern Queensland

Faculty of Health, Engineering and Sciences

ENG4111/ENG4112 Research Project

Limitations of Use

Acknowledgements

I would like to thank my supervisor, Dr Tony Ahfock, for his support, guidance, and wealth of knowledge during this project.

I would also like to thank and acknowledge Dr Craig Lobsey for his support throughout this project and for his substantial contributions to the establishment and development of the USQ Racing team.

S. Baker

Table of Contents

List of Figures

List of Tables

List of Equations

Glossary of Terms

Term	Definition
BLDC	BLDC stands for Brushless Direct Current. This term is specifically in reference to a motor that utilises electronic commutation instead of mechanical brushes. This results in reduced noise and maintenance, while also providing higher efficiency and reliability.
Commutation	Commutation in an electric motor refers to the process of switching the current direction in the motor's windings to generate rotational motion. It is achieved mechanically in brushed motors and electronically in brushless motors.
Inverter	An inverter is an electronic device that converts direct current (DC) to alternating current (AC), allowing devices or systems to utilise AC power from a DC source.
Motor Controller	A motor controller is a device that regulates the performance of an electric motor, controlling aspects such as speed, torque and direction, while also protecting against overloads and faults.
PMSM	PMSM stands for Permanent Magnet Synchronous Motor. Instead of using induction, the magnetic field is created by the permanent magnets attached to the rotor. PMSM motors are known for their high efficiency, high power density, and can deliver a high torque output over a wide speed range. The motor's rotational speed is synchronised with the frequency of the supply current.
PWM	Pulse Width Modulation (PWM) is a technique that controls the average power supplied by an electrical signal. It manages the average voltage (and current) supplied to the load by rapidly alternating the supply between 0 and 100% faster than it takes the load to notably change.

Chapter 1

1. Introduction

Formula SAE (FSAE) is an annual competition series targeting undergraduates and postgraduates to compete in an inter-university, student-led engineering competition (SAE International 2023a). It is a premier automotive racing event requiring teams to design, build, and then race a small-scale, open-wheeled, formula-style race car (SAE International 2023a). Figure 1 below presents UQ Racing's (University of Queensland's FSAE team) 2022 electric vehicle, Capybara (UQ Racing 2023).

Figure 1 - UQ Racing's 2022 "Capybara" car (UQ Racing 2023).

The first student branch of SAE was formed in January 1980 at the University of Texas (UT), with the first competition held by UT in 1981 (Formula SAE 2023). The first competition, attended by four universities, encouraged teams to utilise and modify any 4-stroke engine, including Diesels and Wankels. The competition consisted of four dynamic events: acceleration, manoeuvrability, endurance, and fuel economy, along with two static events: The Appearance Award and the Engineering and Design Creativity Award.

Throughout the 1980s and 1990s, the Formula SAE competition grew steadily, regarding the number of participating teams and the complexity of the engineering challenges involved (Formula SAE 2023).

Universities across the United States and later worldwide started participating, contributing to the competition's reputation as a premier engineering contest (Johnson 2022). By the early 2000s, Formula SAE had become a global competition. Events are now held annually across multiple continents, including North America, Europe, Asia, and Australia. Notable events include Formula Student (Europe), Formula SAE Australasia, Formula SAE Brazil, Formula SAE Japan, and Formula Student India (Formula Student Germany 2023). Table 1 presents the global competitions associated with Formula SAE and their year of inception.

Table 1 - Competitions associated with FSAE, adapted from (Formula Student Germany 2023).

Official Formula SAE and Formula Student Competitions			
Year of Inception	Country	Competition	Website
1981	United States	Formula SAE Michigan	https://www.sae.org/attend/student-events/formula-sae-michigan
1998	United Kingdom	Formula Student United Kingdom	https://www.imeche.org/events/formula-student
2000	Australia	Formula SAE Australasia	https://www.saea.com.au/formula-sae-a
2003	Japan	Formula SAE Japan	https://www.jsae.or.jp/formula/jp
2004	Thailand	TSAE Student Formula	http://www.tsae.or.th/
2005	Italy	Formula SAE Italy	https://www.formula-ata.it/
2005	Brazil	Formula SAE Brasil	https://saebrasil.org.br/programas-estudantis/formula-sae-brasil/
2006	Germany	Formula Student Germany	https://www.formulastudent.de/
2009	Austria	Formula Student Austria	https://fsaustria.at/
2011	China	Formula Student China	http://www.formulastudent.com.cn/
2012	Spain	Formula Student Spain	http://www.formulastudent.es/
2012	South Korea	KSAE Formula	https://www.ksae.org/jajak/competition/
2013	Czech Republic	Formula Student Czech Republic	https://www.fsczech.cz/
2016	Hungary	Formula Student East	https://fseast.eu/
2017	Croatia	Formula Student Alpe Adria	https://fs-alpeadria.com/
2017	India	Formula Bharat - India	https://www.formulabharat.com/
2017	Netherlands	Formula Student Netherlands	https://www.formula-student.nl/
2019	Russia	Formula Student Russia	http://fstudent.ru/
2020	Switzerland	Formula Student Switzerland	https://formulastudent.ch/
2023	Poland	Formula Student Poland	https://fs-poland.pl/
2023	Portugal	Formula Student Portugal	https://www.formulastudent.pt/
2023	Romania	Formula Student Romania	https://formulastudent.ro/

The FSAE rules present teams with the scenario of behaving like they are part of an engineering company tasked with designing, producing, examining, and demonstrating a prototype vehicle (SAE International 2022, p.5). This vehicle should exhibit high performance features and be robust enough to successfully endure all events at the Formula SAE competitions. Other essential design considerations encompass aesthetics, cost, ergonomics, ease of maintenance, and manufacturability (SAE International 2022, p.5). Each prototype will be compared and assessed against others in a range of static and dynamic events to determine the design that most effectively fulfils the design objectives and can be successfully manufactured and marketed. Vehicles participating in Formula SAE competitions should align with sound engineering practices during design and fabrication, while also abiding by the stringent safety requirements and standards mandated by the FSAE rules.

1.1. Formula SAE – Australasian Competition

Formula SAE Australasia (FSAE-A) is the Australasian version of the international Formula SAE competition (Formula SAE-A 2023a). The first FSAE-A event was held in 2000, making it one of the earliest international adaptations of the Formula SAE concept. It has since grown into a significant annual event on the Australasian engineering calendar, drawing student teams from across Australia, New Zealand, the UK, Germany, India, Japan, and the USA (Formula SAE-A 2023a). The competition retains the same core structure as the broader Formula SAE competitions. It comprises of static and dynamic events that test not only the vehicles' design and performance but also the students' understanding of engineering principles, ability to work within a budget, and capability to present their ideas effectively.

Like its international counterparts, FSAE-A has significantly impacted engineering education within the Australasian region. It has provided students with a practical outlet to apply their engineering knowledge and has become a valuable source of real-world experience for undergraduate students (Case 2018).

With prominent event partners and sponsors, including Ford, Toyota, PACCAR Australia, SEA Electric and Red Bull, the FSAE-A competition is considered a valuable pathway for engineering graduates interested in entering the automotive industry. Many participants have gone on to successful careers in the automotive industry and other related fields (Johnson 2022).

1.2. Targeted Engineering Philosophy

The automotive industry is a rapidly evolving environment, driven by the ongoing requirements to enhance sustainability, performance, and efficiency, requiring engineers to be competent in both the theoretical knowledge and practical application of engineering principles.

Formula SAE competitions have become a distinguishing educational platform, blending these attributes together by challenging students to design, engineer, and build a prototype formula-style racing car. It is during this process that the integration of a simulation program and real-world validation becomes a vital skillset. This has resulted in prominence of teams harnessing the capabilities of engineering simulation packages like MathWorks Simulink. It is in these environments that students can model and refine their designs, before safely simulating them for an in-depth analysis prior to the physical build. This valuable stage in the engineering process ensures resource efficiency, effective design development, and, importantly, facilitates a practical application and analysis of real-world engineering principles.

It is acknowledged that with the correct tools available to them, the students will be modelled into the engineering leaders of the future. Therefore, the FSAE-A competition is accepted by the author as an ideal environment to provide students with the opportunity to harness the extensive skillset required to propel their career in the engineering space. As a result, it is accepted that the

establishment and development of simulation framework is a pivotal step in elevating a team from an assembly crew to an engineering powerhouse.

1.3.   Electric Vehicle Category

The Formula SAE competition has significantly impacted the field of automotive engineering education. Over time, the competition's rules and standards have evolved to reflect technological advances and changes in the automotive industry. For example, in 2006, the Formula Hybrid category was founded, utilising gasoline-electric hybrid power plants (SAE International 2023b). Following this, FSAE-A introduced electric vehicles in 2010 (Formula SAE-A 2023b). These expansions in the competition have allowed and encouraged teams to utilise electric powerplants alongside, and instead of, traditional internal combustion vehicles.

1.4.   USQ Racing Team

The University of Southern Queensland's FSAE team, USQ Racing, was formed in September 2021 to provide an avenue for students to engage hands-on within a practical engineering project, thereby bridging the gap between theoretical knowledge and real-world application. Additional motivation was provided by the realisation that all other comparative universities in the South-East Queensland district actively participate in this competition; these include UQ Racing of the University of Queensland, QUT Motorsport of the Queensland University of Technology, and Griffith Racing Team of Griffith University (Society of Automotive Engineers - Australasia 2022).

The University of Southern Queensland previously facilitated an FSAE team known as USQ Motorsport. However, after their final competition, this team appears to have dissolved in late 2008 (FS World 2023). While USQ Motorsport only ever competed in the Internal Combustion category, USQ Racing will be making new ground by becoming the first University of Southern Queensland team to represent the university in the Electric Vehicle category.

To date, USQ Racing has made progress on its first vehicle; however, there is still a considerable way to go. The team have designed their first chassis (Figure 2) and procured a selection of the major components, including the EMRAX 228 HV electric motor. Nevertheless, a lot more work is required, providing the team with numerous opportunities to apply and expand their engineering skills and knowledge in the continuation of this vehicle build. The remaining work is rife with engineering challenges, especially considering the scratch build of the vehicle. Unlike iterations or enhancements of pre-existing models, this undertaking requires the critical application of advanced engineering skills to navigate this project without the predefined parameters or constraints from existing subsystems.

Consequently, the team must embark on an engineering path where every subsystem is yet to be defined and validated, and numerous assumptions must be made. This presents an intricate accumulation of challenges and opportunities from an engineering perspective. The team must conceptualise, design, validate, and integrate various subsystems, each an engineering challenge in its own right, while ensuring cohesive functionality and performance of the final product.
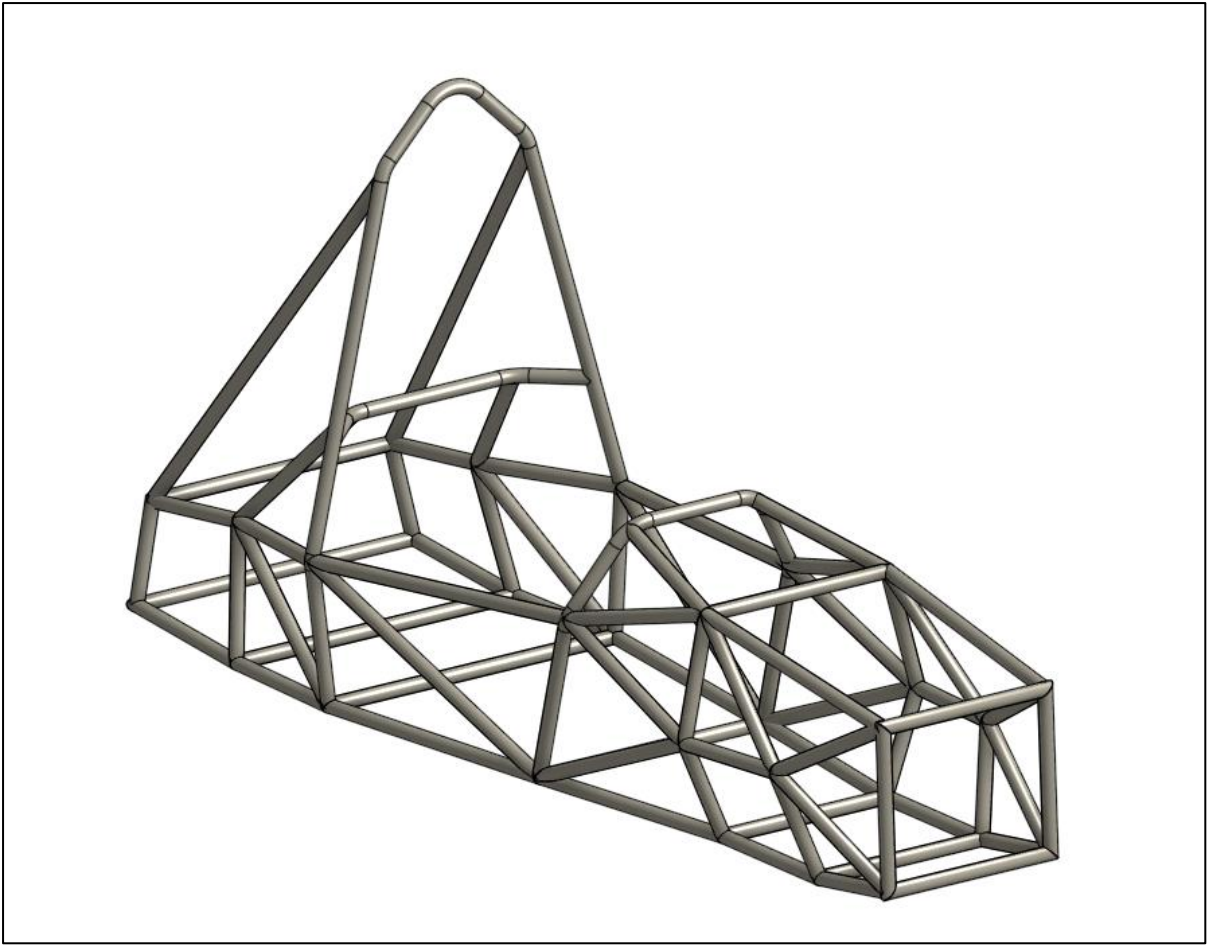
Figure 2 - USQ Racing's first chassis design.

1.5. Project Inspiration

The establishment of USQ Racing, and FSAE-A in the broader context, provides students with an opportunity to gain real-world industry experience in their chosen discipline. Additionally, this environment results in students working together within their team and specialist sub-teams to produce a tangible outcome.

The FSAE-A concept appears simple at first:

- Review competition rules and guidelines
- Assess existing proven examples from previous teams along with the engineering decisions they have made.
- Identify components required for the vehicle build.
- Procure these components.
- Then assemble the vehicle.

All these steps are then documented throughout the vehicle build process to ensure the team meets the stringent requirements of the FSAE-A competition's static events. However, once new teams delve into the design, it becomes progressively apparent that the options are endless, and the examples from previous competitions are distinctively unique and complex, with minimal similarity between each configuration. It is clear that each decision impacts the related and unrelated subsystems within the vehicle. These components and associated subsystem interactions proliferate exponentially as the vehicle design is evaluated at an increasing depth.

My inspiration for this project was to isolate the vehicle's drivetrain and provide a finalised subsystem and development platform for the rest of the vehicle to be built around. The final product from this project serves a dual purpose; it delivers a solid foundation for the current vehicles' powertrain construction and establishes an educational platform for future iterations of the USQ Racing vehicle.

1.6.   Project Aim and Objectives

The aims of this project are twofold:

- Commission the 228 HV EMRAX in support of the first USQ Racing vehicle.
- Support the ongoing development of the USQ Racing team, and FSAE Electric community in general, through the design of a low cost and customisable electric motor controller and simulation platform.

To achieve these aims, the following objectives have been identified:

1. Perform necessary testing and qualification of the second hand 228 HV EMRAX motor purchased from Team Swinburne to confirm its suitability for the USQ Racing team's first vehicle.
2. Review and identify suitable hardware components for the construction of the motor controller, compatible with operation up to the maximum electrical limits of the FSAE rules.
3. Review appropriate control and modulation methods to be utilised by the motor controller.
4. Develop MATLAB scripts and Simulink model to simulate the motor controller and its cooling system during operation.
5. Assemble a prototype motor controller for conducting a performance evaluation of the hardware and control algorithms.
6. Establish the simulation and programming framework for the motor controller's ongoing development.

1.7. Thesis Outline

A summary of the chapters within this dissertation is provided below:

Chapter 2 – Literature Review: This chapter features the research undertaken for the development of the dissertation methodology. The primarily focus is on the design and development of the motor controller, with targeted attention also given to the motor selection and the functional expectations for the resolver. This research refines the design scope to ensure a FSAE-A competition suitable and serviceable motor controller can be developed.

Chapter 3 – Methodology: This chapter outlines the motor commissioning procedure, as well as reviews the relevant technology available for the development of a suitable motor controller. The associated FSAE-A competition rules and prominent proven designs are reviewed to ensure informed decisions are made during the development of the controller design.

Chapter 4 – Results and Discussion: The motor commissioning is documented in this chapter, identifying the issues encountered and the measures taken to resolve them. Justification for the motor selection is presented, as well as the selection criteria used for the major motor controller components. The proposed motor controller's cooling system suitability and thermal response is modelled, resulting in the informed selection of the serviceable cooling system components and their configuration. A motor controller prototype is developed over multiple stages, first through validating the programming method and selected algorithms before a custom model is designed and constructed. The prototype is tested and evaluated, with modifications implemented as issues are identified. The key recommendations of future work are identified for promoting the development of the motor controller in ensuing iterations.

Chapter 5 – Conclusions: Summary of the project aims and objects achieved, as well as recommendations for future work.

Chapter 2

2. Literature Review

This chapter will identify the existing designs in the motor controller space and the control and modulation methods currently used.

The components comprised in electric motor controllers have advanced significantly with the improvements in silicone technology, resulting in reduced die sizes, lower power losses and improved compatibility with modern low-voltage logic devices, such as the latest generation microcontrollers (Toshiba 2019, p.3). These improvements have been a direct result of Moore's Law, which maintains that the number of transistors on a microchip doubles about every two years, enhancing computational and operational capabilities, while reducing costs.

Figure 3 presents a high-level overview of the electrical drivetrain of an FSAE vehicle. While a motor has already been purchased by USQ Racing, a review of the suitability of this selection will be undertaken to ensure its appropriateness during the motor controller design. This motor's selection was based on budgetary constraints, resulting in the procurement of a second-hand unit with cosmetic damage from an undisclosed incident in the past. Prior to this project, no acceptance testing or commissioning of this motor had been completed. The primary focus of this literature review is the selection of principle components required for the motor controller package design, as well as the microcontroller selection and the identification of suitable control methodology and associated algorithms. The driver controls and accumulator identified in this diagram are outside of this project's scope.

The applicable FSAE rules will also be reviewed to ensure that the final design complies with their stringent requirements.
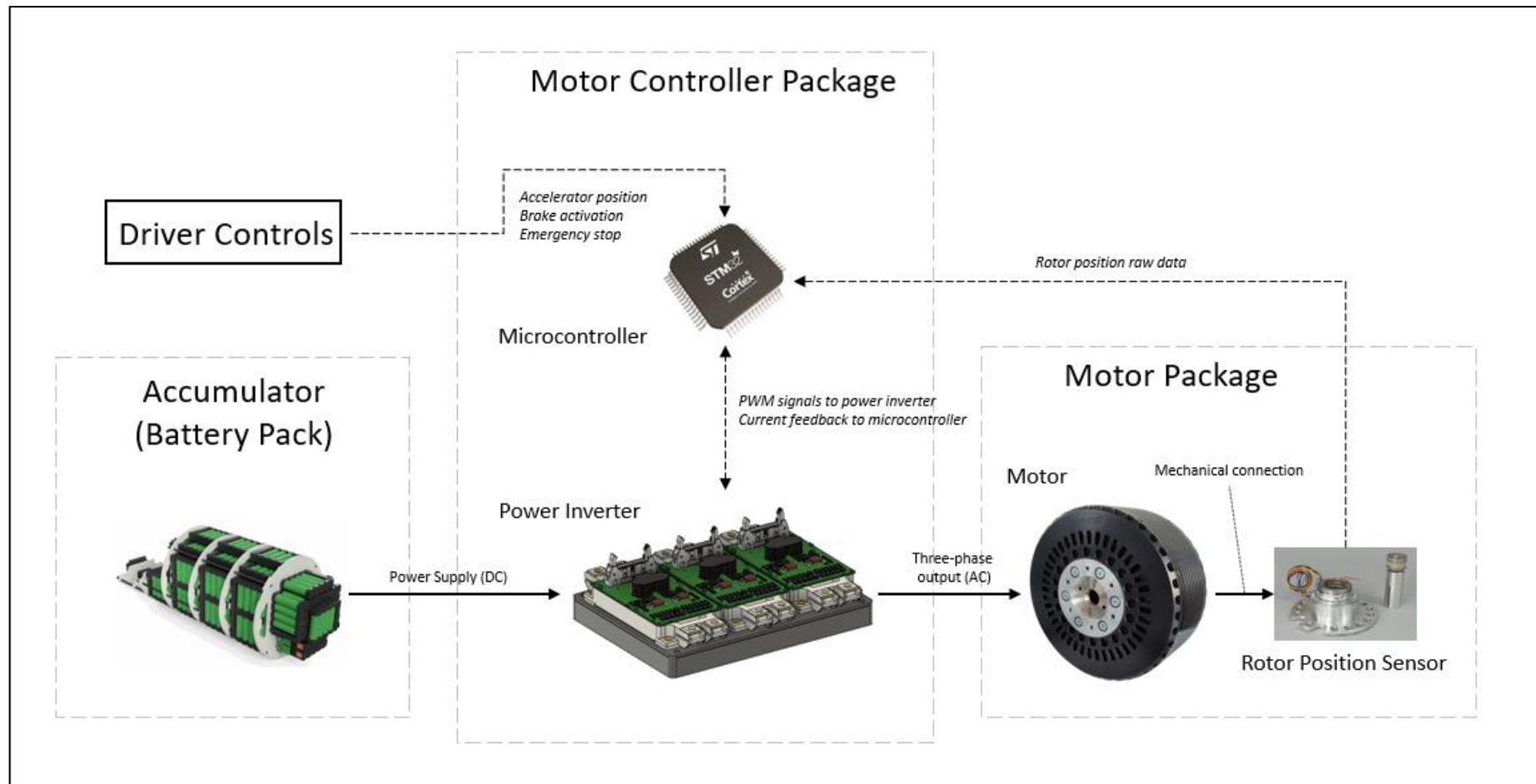
Figure 3 - High-level motor drivetrain electrical block diagram.

Image Sources

Accumulator: (Enepaq n.d.);   Microcontroller: (Element14 n.d.);   Inverter: 3D rendered model of proposed design;

Motor: (EMRAX d.o.o. 2018, p.8);   Resolver: (EMRAX d.o.o. 2018, p.35)

2.1. Motor Types

The motor of an electric vehicle provides the link between transforming electrical energy into mechanical propulsion. With multiple options available for this application, a review of the suitable electric motors for a tractive application was undertaken. While it is acknowledged that the USQ Racing motor had already been purchased before the initiation of this project, a review was still undertaken to ensure this motor was compatible with the controller design and project aims.

Given the wide variety of motor options available, a survey was conducted on the motor designs implemented in a selection of production electric vehicles; the results are presented in Table 2.

Table 2 - Motor types used in production vehicles.

Make	Model	Year	Motor Type	Notes
Tesla	Model S	2012 - 2020	Dual motors - Front is PMSM, Rear is AC Induction	1
		2021+	Dual motors - Front and Rear both PMSM	2
	Model 3 - RWD	2017+	PMSM	3
	Model 3 - AWD	2018+	Dual motors - Front is AC Induction, Rear is PMSM	4
Nissan	Leaf	2010+	Brushless DC	5
BMW	iX M60	2022+	Brushed AC Synchronous	6

Table 3 - Useful links used for the creation of Table 2.

Notes	Useful Links
1	https://www.tesla.com/ownersmanual/2012_2020_models/en_jo/GUID-E414862C-CFA1-4A0B-9548-BE21C32CAA58.html
2	https://www.tesla.com/ownersmanual/models/en_us/GUID-E414862C-CFA1-4A0B-9548-BE21C32CAA58.html
3	https://www.tesla.com/ownersmanual/model3/en_cn/GUID-E414862C-CFA1-4A0B-9548-BE21C32CAA58.html
4	
5	https://researchbank.swinburne.edu.au/file/f63fd114-1fc2-431d-b038-64838f9751be/1/alireza_tashakori_abkenar_thesis.pdf
6	https://www.motortrend.com/news/bmw-ix-m60-brushed-electric-motor-tech-deep-dive/

From the information presented in Table 2, four common motor types have been represented. These motors were investigated further to assist with identifying their practicality for the USQ Racing vehicle and its motor controller design.

2.1.1. AC Induction

An AC induction motor is an electric motor that operates by utilising the principle of electromagnetic induction. It consists of two main parts: the stator, which is stationary and contains electrical windings, and the rotor, which rotates inside the stator. When alternating current is applied to the stator, it creates a rotating magnetic field that induces a current in the rotor, causing it to rotate and perform work. The rotor's speed is slightly less than the speed of the stator's rotating magnetic field, a difference known as 'slip'.

The AC induction motor is widely used in electric vehicle applications because of its ruggedness, dependability, low maintenance requirements and cost-effectiveness (Hanejko 2022).

AC induction motors are typically controlled using either scalar or vector control methods (Marulasiddappa & Pushparajesh 2021).

2.1.2. Brushless DC

A brushless DC motor (BLDC) is an electric motor that employs electronic commutation instead of brushes in a DC motor design, thus improving reliability and efficiency. Powered by direct current and utilising solid-state electronics to operate the motor, a BLDC comprises of a rotor with permanent magnets and a stator with windings. The electronic controller periodically activates the windings, creating a magnetic field that rotates the rotor. Brushless motors avoid issues like brush wear and tear, noise, and sparks while providing superior speed and torque control.

Brushless DC motors can be controlled using either scalar or vector control methods (Renesas n.d.).

2.1.3. Permanent Magnet Synchronous Motor

A Permanent Magnet Synchronous Motor (PMSM) is an electric motor in which the rotor's movement is synchronous with the frequency of the alternating current. Unlike induction motors, the rotor's magnetic field in a PMSM is not induced, but results from the permanent magnets affixed to the rotor. The interaction between the stator windings' rotating magnetic field and the rotor's permanent magnets generates a torque, causing the synchronous rotation of the rotor. While BLDC motors also

have permanent magnets mounted to their rotors, the motors differentiate from each other due to back EMF produced during rotation. BLDC motors produce a trapezoidal waveform, whereas a PMSM produces a sinusoidal waveform.

PMSMs are known for their high power density, high torque at low speed, high efficiency, and low maintenance needs. However, the downside with these motors is the cost (Keating 2022). Due to the cost of the permanent magnets required, these motors are considerably more expensive than AC induction motors (Hanejko 2022).

PMSM can be controlled using either scalar or vector control methods (Biyani et al. 2022).

2.1.4. Brushed AC Synchronous

A brushed AC synchronous motor is similar to an AC induction motor; however, the fundamental difference is in the rotor design. In a brushed AC synchronous motor, the rotor is constructed with windings and uses an external DC supply to produce its electromagnetic field (Daware 2015). These rotor windings are energised through slip-rings and brushes (Daware 2015). The externally supplied electromagnetic field allows the rotor to couple magnetically with the stator's rotating magnetic field, resulting in no 'slip' and allowing the motor to operate at a synchronised speed (Daware 2015).

While the brushed design can lead to higher maintenance requirements due to brush and slip ring wear, they are generally cheaper than a PMSM and far more resistant to high operating temperatures (>80°C) (Jenkins 2022). When compared to a PMSM, the torque and speed of the brushed AC motor is more controllable (Jenkins 2022).

Brushed AC motors are controllable using either scalar or vector control methods.

While all four motors investigated operate uniquely, they can all be controlled using either scalar or vector control methods. Additionally, no concerning attributes were identified for any of these motor types. Therefore, a selection of existing FSAE-A teams were reviewed to identify the motors they use. This data has been compiled in Table 4 below.

Table 4 - Motors used by select FSAE-A teams.

Team	Vehicle	Year	Motor - Make and Model	Motor Type	FSAE-A Placing	Notes
Monash Motorsport [Monash University]	M19-E	2019	EMRAX 228	PMSM	1st [from 16 teams]	1
	M22	2022	4x Fischer Hub Motors	(4x) PMSM	5th [from 20 teams]	2
UQ Racing [University of Queensland]	Chicken	2019	EMRAX 207	PMSM	2nd [from 16 teams]	3
	EV22	2022	AMK Racing Kit [2WD]	(2x) PMSM	9th [from 20 teams]	4
QUT Motorsport [Queensland University of Technology]	QEV-2	2019	4x Plettenburg Nova 15/45	(4x) BLDC - Inrunner	12th [from 16 teams]	5
	Lando	2022			20th [from 20 teams]	6

NOTE: The FSAE-A competitions were not held in 2020 and 2021 due to COVID-19, as noted on their results webpage <https://www.saea.com.au/fsaea-past-results>.

Table 5 - Useful links used for the creation of Table 4.

Notes	Team Link	Motor Link
1	https://www.monashmotorsport.com/m19	https://emrax.com/e-motors/emrax-228/
2	https://www.monashmotorsport.com/m22	https://fischer-elektromotoren.de/en/products/
3	https://www.uqracing.com/past-cars/2019-ev	https://studylib.net/doc/18340117/emrax-207-technical-data-table
4	https://www.uqracing.com/blog/2022-car-launch	https://amk-motion.com/en/content/formula_student_electric
5	https://www.qutmotorsport.com/qev-2-2019	https://plettenbergmotors.com/product/nova-15-en/
6	https://www.qutmotorsport.com/lando-2020-2021	

2.2.   Control Strategies for Electric Motors

Motor control methods generally fall into the two categories of either Scalar Control or Vector Control. Scalar Control regulates the scalar variables individually, disregarding any coupling effect from the motor (Tennessee Technological University n.d., p.81). In comparison, Vector Control manages both the magnitude and direction of the flux for more precise and responsive control of motor speed and torque (Tennessee Technological University n.d., p.85). Vector Control is a superior control method for an EV traction application due to its accurate torque control and rapid dynamic response, although it is significantly more complex to implement (Ibrahim et al. 2022).

2.2.1.   Scalar Control

The quantities typically controlled in Scalar Control are the voltage and frequency supplied to the motor; the most common Scalar Control strategy used is Volts/Hertz (V/f) control (Tennessee Technological University n.d., p.82). This method changes the voltage and frequency proportionally, resulting in the stator's flux remaining constant while the motor's speed is regulated (Tennessee Technological University n.d., p.82).

Scalar control is simple and cost-effective to implement; it is suitable for applications requiring speed control but where precise positioning and torque control are not critical (Tennessee Technological University n.d., p.85).

2.2.2.   Trapezoidal (Six-Step) Control

Trapezoidal Control, also known as Six-Step Commutation, is a Scalar Control method typically used on BLDC motors; however, it can also be applied to PMSMs (MathWorks n.d.a). The name Trapezoidal Control comes from the trapezoidal shape of the back-EMF voltage in the BLDC motor windings during rotation (Akin, Bhardwaj & Warriner 2011, p.2).

This control strategy energizes two of the three phases of the motor at any given time, creating six steps in a complete electrical rotation. This control method results in a BLDC motor generating a predominantly constant output torque; however, some torque ripple is present (Akin, Bhardwaj & Warriner 2011, pp.5).

The trapezoidal control method is simpler and less computationally intensive than methods like Vector Control. It requires relatively simple electronics and does not require current feedback for speed control, resulting in a more straightforward control method that can be implemented using cost-effective microcontrollers (starting from 8-bit) (ST Microelectronics n.d.a).

Trapezoidal Control delivers a reasonable level of speed and torque control; however, it generally produces more torque ripple and is less precise than other control methods (Divakar et al. 2022, pp.2, 6-8).

2.2.3. Vector Control

Vector Control, specifically Field-Oriented Control (FOC), is a technique for controlling three-phase motors, either brushless or induction, providing high performance and smooth operation (Ibrahim et al. 2022).

FOC is a closed-loop system that requires detecting the rotor position at every instant to ensure the correct execution of the control algorithms (Tennessee Technological University n.d., p.89). Rotor position can be established using a position sensor or through sensorless algorithms (Repas 2007).

Figure 4 below represents the time domain motor currents inciting motor rotation. The diagram on the left represents the motor's mechanical rotation. In this diagram, the light blue indicator represents the rotor's relative position, while the red, blue and green vectors represent the three-phase electromagnetic flux traversing their associated magnetic axes. The plot on the right represents the time domain current phasors producing the associated electromagnetic fluxes.
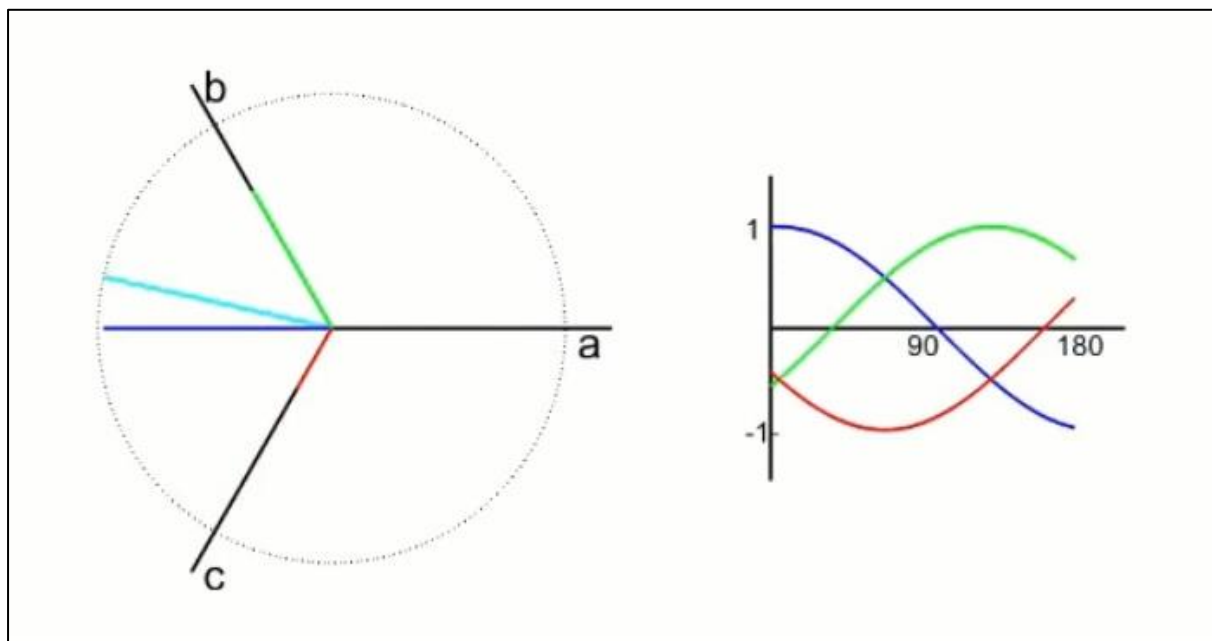
Figure 4 - Time domain components of a three-phase system (MathWorks n.d.b).

FOC calculations start by transforming the motor's three-phase currents (Figure 4) into a two-phase equivalent (Figure 5), using the Clarke transformation to create the I_α and I_β variables, therefore simplifying further analysis (Repas 2007). The resultant output signals, I_α and I_β, of the Clark transform are time-varying quadrature-current values (Repas 2007).
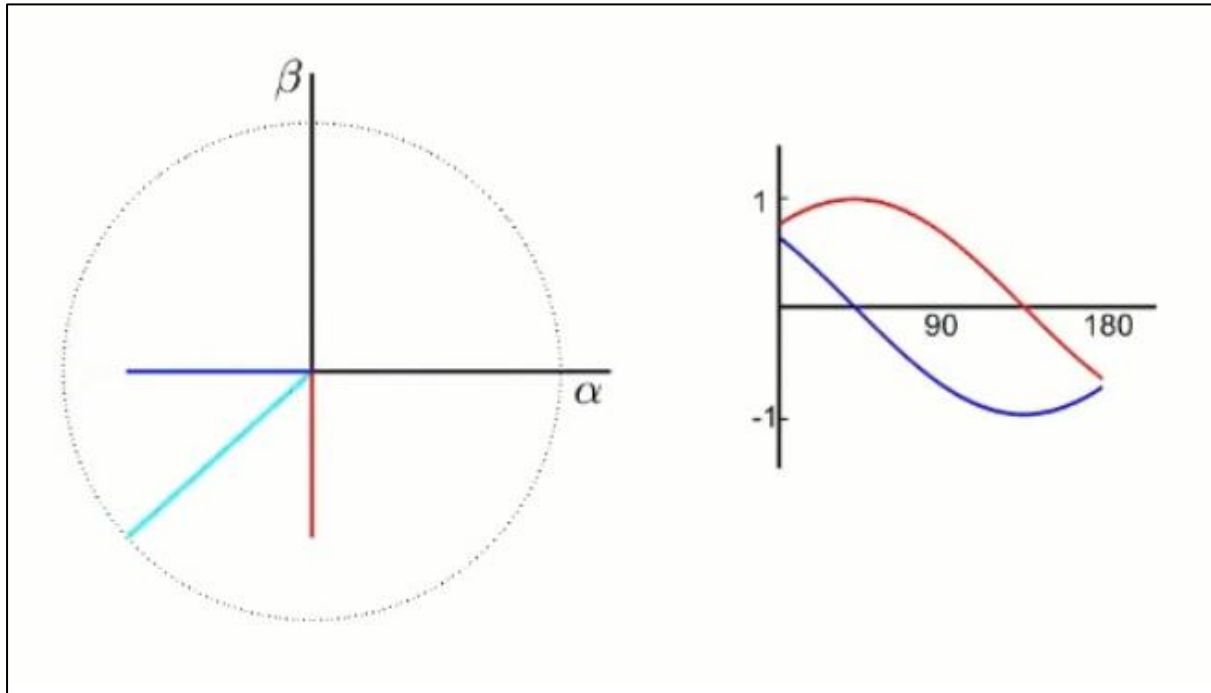
Figure 5 - Resulting signals from the Clark transform $(\alpha\beta)$ (MathWorks n.d.b).

Figure 5 above represents the resultant two components (α and β) of the Clarke transform; these currents are now in the orthogonal stationary frame. Again, the light blue indicator represents the rotor's relative position (MathWorks n.d.b).

From there, the two-axis plot is rotated to align with the rotor's magnetic field using the transformation angle θ (Figure 6); this conversion is performed using a Park transform, which results in the quadrature current variables i_d and i_q (Repas 2007). During steady-state conditions, the i_d and i_q variables remain constant.
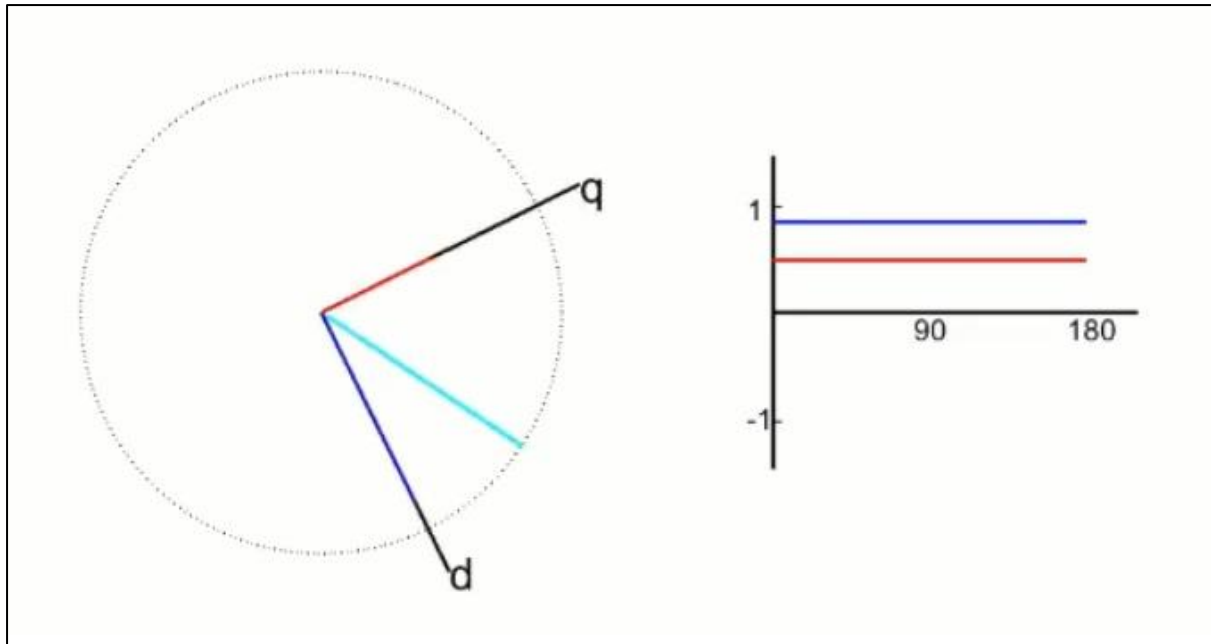
Figure 6 - Resulting signals from the Park transform (dq) (MathWorks n.d.b).

Figure 6 above presents the output provided by the Park transform. This transform has converted the (α and β) components, from the orthogonal stationary frame into the dq components of the rotating reference frame (MathWorks n.d.b). Again, the light blue indicator represents the rotor's relative position.

The motor's torque and magnetic flux can be controlled independently in this new frame. The i_q component controls the motor's torque, while the i_d component controls the magnetising flux.

In the FOC algorithms, PID (Proportional Integral Derivative) controllers play a fundamental role in regulating both the torque and flux of the motor, leading to a high precision and efficient controller. These two controllers work together to ensure that the motor's speed and torque are maintained at their desired values, regardless of any changes in the load or other disturbances. For context, the q reference is set to the required torque, while the d reference is usually set to zero to maximise the efficiency (Frederiksen n.d.).

- **Torque Controller:** This PID controller compares the reference torque (setpoint) with the actual torque of the motor (measured i_q component). The error between these two values is used to generate a corrective action, which adjusts the torque-producing current component with the modification of the $v_q{}^{ref}$ vector.

- **Flux Controller:** Like the torque controller, the flux controller compares the reference flux with the actual flux in the motor (measured i_d component). The error between these two values is used to generate a corrective action, which adjusts the flux-producing current component with the modification of the $v_d{}^{ref}$ vector.

The $v_q{}^{ref}$ and $v_d{}^{ref}$ vectors, along with the rotor position data, are then processed through an inverse Park transform. This transform converts the rotating reference frame quantities (V_q and V_d) to the orthogonal stationary reference frame quantities (V_α and V_β) (Microsemi 2013, p.9). Following this conversion, the reference frame quantities are processed through an inverse Clarke transform, defining the three-phase stationary reference frame quantities V_a, V_b and V_c (Microsemi 2013, p.8). Finally, these three voltage signals are used to generate the PWM duty signals for the power inverter to supply the motor (Repas 2007).

This process is repeated rapidly, often thousands of times per second, allowing precise and dynamic control of the motor's operation throughout the entire rotation period. Figure 8 presents a block diagram of this process.

An important design consideration for FOC techniques is monitoring the current in each phase separately. While FOC algorithms can still be performed using a single leg current measurement and calculating the other two phases, this tends to be less accurate and reduces performance (Infineon Technologies 2019, p.7). The three-leg current measurement requirement is a noticeable variation from six-step commutation where only one leg is needed (Infineon Technologies 2019, p.6).

In a multidrive vehicle, the continuous and precise modulation of torques at each wheel results in vector control strategies being the ideal selection for optimising performance (De Novellis, Sorniotti & Gruber 2014, p.1593).

Figure 7 presents a simplified cornering manoeuvre in an all-wheel drive, vector controlled, electric vehicle. The red arrows represent the torque reference magnitude and direction to maximise the grip and vehicle performance during this turning event (Barham 2017, p.21). The focus of this control strategy is to maximise the cornering effectiveness while minimising the event of any loss of traction.
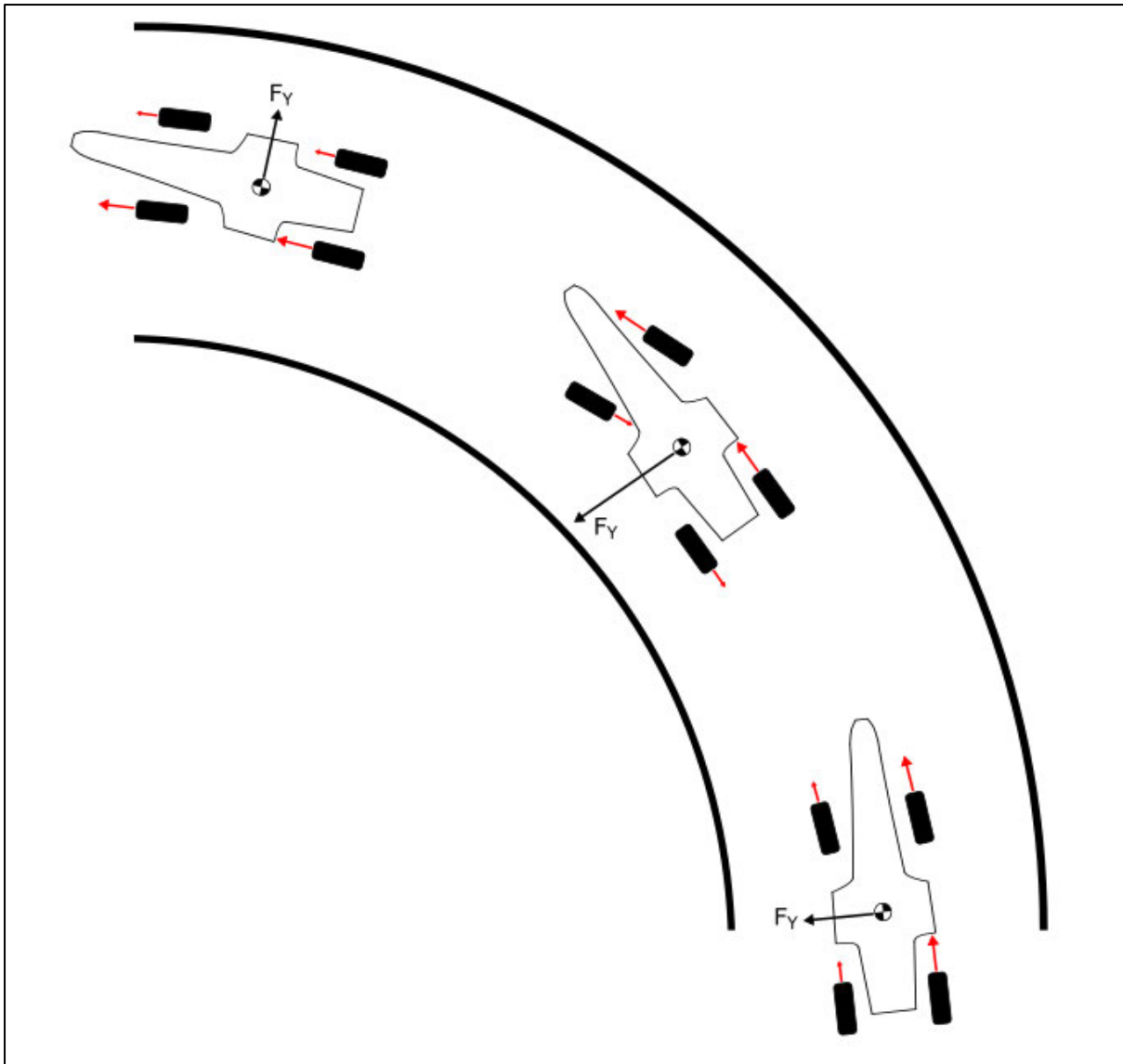
Figure 7 - Simplified representation of the implementation of torque vectoring (Barham 2017, p.21).
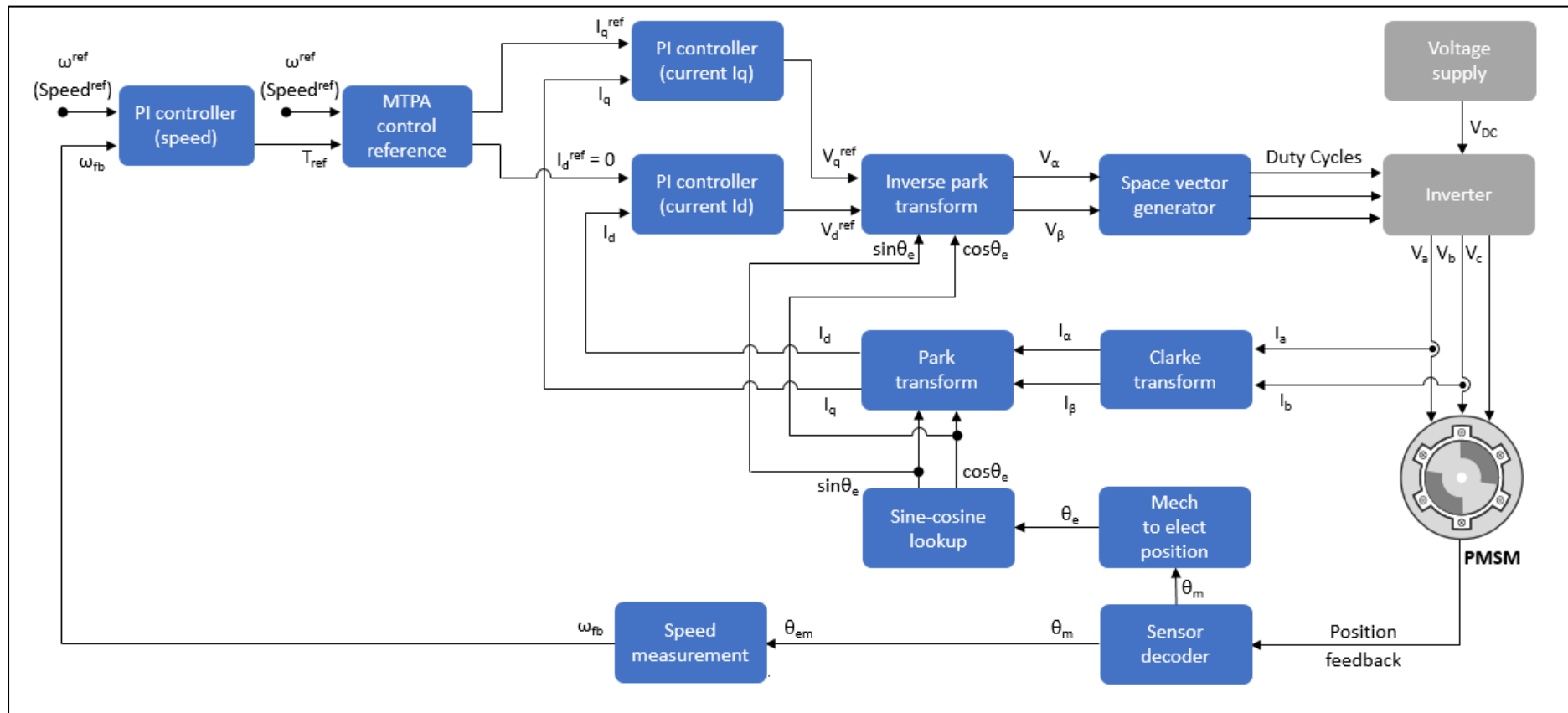
Figure 8 - Motor Control Blockset example of the FOC architecture for a PMSM (MathWorks n.d.c).

NOTE: The Space vector generator block negates the requirement for an Inverse Clarke transform block.

2.2.4. Control Strategy Conclusion

While all three strategies investigated function differently to achieve specific application requirements, they do all share many similarities.

Scalar Control, Trapezoidal Control and Vector control all utilise a three-legged H-Bridge format of power transistors, as represented in Figure 9. Additionally, each strategy is commonly implemented by a microcontroller and a similar selection of power electronic components. Therefore, it is important to recognise that the choice of control strategy primarily depends on factors such as performance requirements, complexity, cost, and the specific type of motor used.
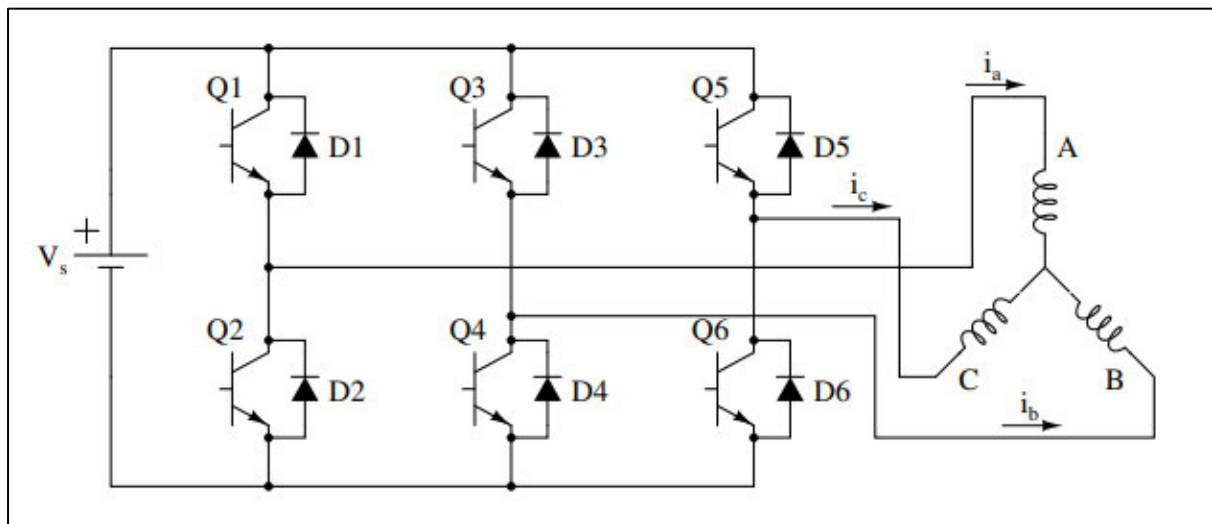
Figure 9 - Three-phase bridge, commonly used to drive three-phase motors (Faiz et al. 2021, p.412).

2.2.5. Motor Position Feedback

Hall Sensors

Hall effect sensors in motors detect the position of the rotor by measuring changes in the magnetic field. They are transducers that vary their output voltage in response to changes in magnetic field. Three Hall sensors are often used in brushless motors, placed 120 degrees apart around the stator. As the rotor's magnetic field rotates, it triggers the sensors individually. This sequence of sensor output can then be used to determine the rotor's exact position and the correct sequence to switch the motor windings, allowing for accurate speed and direction control.

Quadrature Encoder

A quadrature encoder, or incremental rotary encoder, is a sensor that accurately measures a motor's shaft's rotation, position, and direction. It operates based on the principle of optical or magnetic encoding, generating two output signals - often referred to as Channel A and Channel B.

These two channels are out of phase by 90 degrees (a quarter of a cycle, hence the term quadrature), allowing the sensor to not only track incremental changes in position but also to determine the direction of rotation. When Channel A leads Channel B, the motor is moving in one direction, and when Channel B leads Channel A, the motor is moving in the opposite direction.

A controller can, therefore, determine the motor shaft's position, rotation speed, and direction by counting the number of pulses and monitoring the phase relationship between Channels A and B. However, like other incremental encoders, quadrature encoders require a reference or 'home' position for absolute position tracking.

Resolver

A resolver is a rotary electrical transformer used for measuring degrees of rotation, commonly used in electric motors for accurate positioning (Baker 2019).

The typical structure of a resolver includes a rotor and a stator. The stator houses two windings, mechanically offset by 90 degrees. Meanwhile, the rotor is supplied with an AC excitation signal. During operation, the amplitude and phase of the signals induced in the stator windings are continually analysed, collectively determining the rotor's precise angular position (Baker 2019). Figure 10 visually represents the resolver's input signal and two, 90 degree displaced, amplitude modified outputs.

To interface a resolver's analog output with digital control systems they require an analog-to-digital converter, or a resolver-to-digital converter, combined with complex signal processing. Despite their older technology, resolvers are still widely used in applications requiring high reliability, high accuracy, and excellent resistance to harsh environmental conditions (Baker 2019).
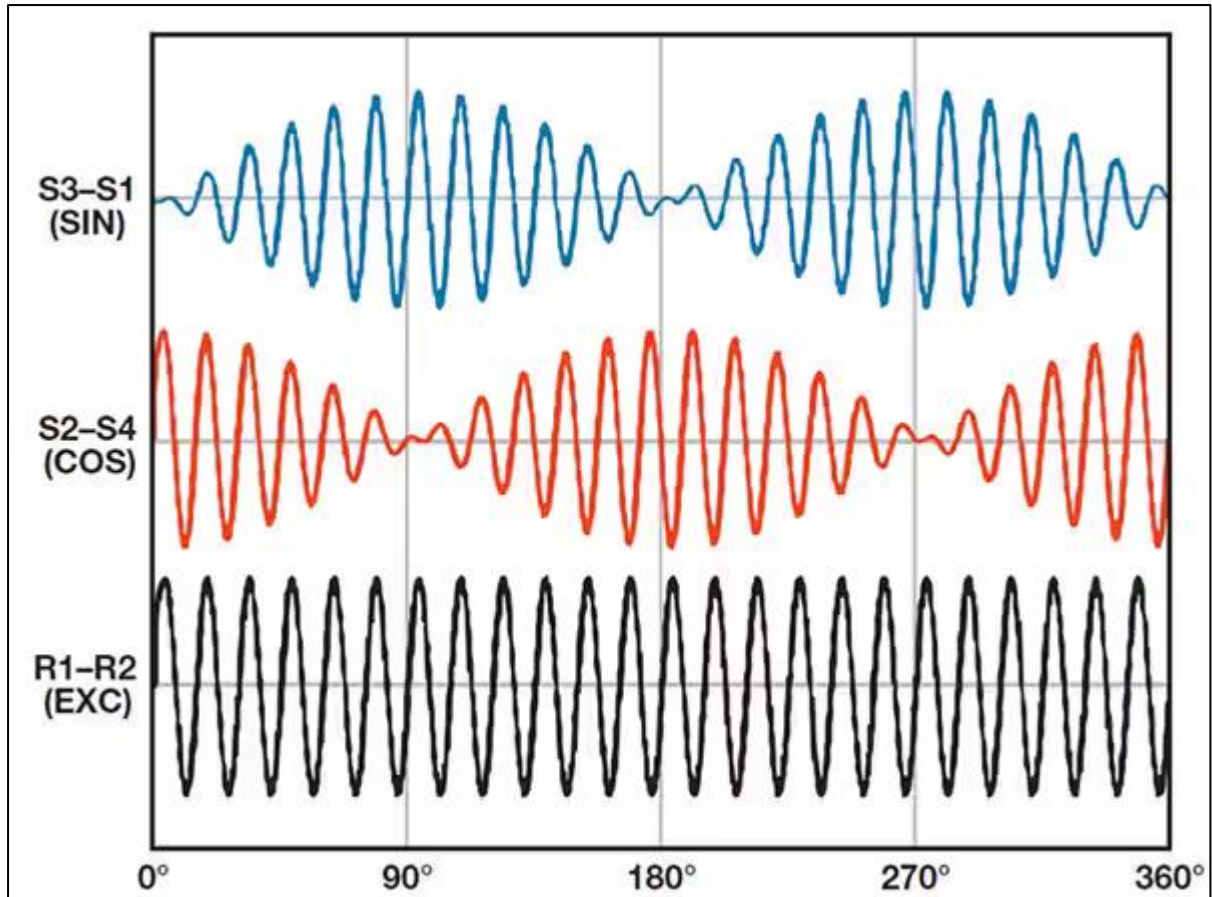
Figure 10 - Resolver output during a full rotation (Baker 2019).

The following formulas represent the outputs relative to the rotors position.

Where:

E_{R1-R2} = Resolver input signal

E_{S1-S3} = Cosine output signal

E_{S2-S4} = Sine output signal

Tr = Transformation ratio (specified by datasheet)

θ = Rotors angular position

Equation 1 - Resolver Cosine Output (Baker 2019).

$$E_{S1-S3} = Tr \cdot E_{R1-R2} \cdot \cos\theta$$

Equation 2 - Resolver Sine Output (Baker 2019).

$$E_{S2-S4} = Tr \cdot E_{R1-R2} \cdot \sin\theta$$

Sensorless

Sensorless refers to a method of controlling a motor without relying on physical sensors for feedback on rotor position. This approach is often used in Brushless DC (BLDC) and Permanent Magnet Synchronous Motors (PMSM).

Sensorless control estimates the rotor position using information derived from the motor's electrical signals, such as back electromotive force (EMF) or current measurements. This data is used to control the switching of power electronic devices (transistors) to energise the motor windings at the precise time required.

Sensorless control simplifies the physical system, eliminating the requirement for position sensors and their associated wiring. This control method enhances the motor's reliability and durability due to a reduced dependency on control components. However, sensorless control can be challenging to implement at low speeds, or during startup, when the back EMF signal is weak.

Sensorless control algorithms require a higher degree of complexity and more computational power than sensor-based control. They are typically implemented using microcontrollers or digital signal processors (DSPs).

2.3.   Controller Options

2.3.1.   Commercial Off-The-Shelf (COTS) Options

COTS products are available from several manufacturers. While COTS solutions provide a ready to go option, they often come at an increased cost and reduced flexibility or customisation.

The table below identifies the suitable controllers for an EMRAX 228 HV. This table is adapted from the table in EMRAX's recommended controller document (EMRAX d.o.o. 2020, List2).

Table 6 - Suitable controllers for an EMRAX 228 HV (EMRAX d.o.o. 2020, List2).

EMRAX MOTOR	SUITABLE CONTROLLERS
228 HV	Drivetrain innovation DTI HV-500 Unitek Bamocar D3-700/200/400, Sevcon Gen4-S10, RMS PM100DZ, RMS PM150DZ

The controllers featured in Table 6 were reviewed to confirm their compatibility as well as retail cost. The results have been consolidated in Table 7. Additionally, the manufacturer's head office locations and controller purchase costs are listed below.

Drivetrain innovation

Head office located in Thököly, Hungary (DriveTrain Innovation 2023).

DTI HV-500 Cost: €3,925.00 (approximately AUD$6,400)

Unitek Bamocar

Head office located in Leutenbach, Germany (Unitek Industrie Elektronik 2023).

D3-700 200/400 Cost: €4,161.00 (approximately AUD$6,800)

Sevcon

This manufacturer's controller was not reviewed.

Cascadia Motion

Formed from the merger of Rinehart Motion Systems (RMS) and AM Racing by BorgWarner in early 2019 (Cascadia Motion 2023a).

Head office located in Wilsonville, USA (Cascadia Motion 2023b).

Please note the Cascadia Motion PM100DZ and PM150DZ controllers have been discontinued, the CM200DZ controller was recommended by the Cascadia Motion sales team as an equivalent replacement.

CM200DZ Cost: USDS6,649.00 (approximately AUD$10,000).

Prohelion

The WaveSculptor200 was originally designed and built by Tritium, however, the design was then purchased in 2021 and is now manufactured and sold by Prohelion (Prohelion 2023a).

Head office located in Brisbane, Australia (Prohelion 2023b).

Cost: AUD$7,000

Table 7 - Specifications and costs of EMRAX recommended controllers, adapted from (EMRAX d.o.o. 2020, List1).

CONTROLLER	PEAK CURRENT [Arms]	CONT. CURRENT [Arms]	PEAK VOLTAGE [Vdc]	PEAK POWER [kW]	SWITCHING FREQUENCY [kHz]	WEIGHT [kg]	BEST SENSOR	OTHER SENSOR OPTIONS	Cost (AUD)
Drivetrain innovation DTI HV-500	350	250	720	250	8–14	6.7	Encoder RM44SI	Hall sensors, encoder, resolver	$6,400
Unitek Bamocar D3 700 200/400	280	200	700	200	8–16	6.8	1-pole pair resolver	sin/cos encoders, hall sensors	$6,800
Cascadia Motion PM100DZ	200	150	800	100	12	7.5	5-pole pair resolver	/	Not available
Cascadia Motion PM150DZ	300	225	800	150	12	10.7			
Cascadia Motion CM200DZ	400	200	840	225	12	6.75	/	sin/cos encoders, resolver	$10,000
Prohelion WaveSculptor200	300	168	450	165		8.5	Encoder	Hall sensors, encoder, resolver	$7,000

2.3.2. Open Source

With the increased global attention given to electric vehicles, an increasing quantity of open-source, high-performance motor controller projects are appearing. A selection of the more prevalent projects were reviewed; the controllers' key features are listed below and summarised in Table 8.

Open source products provide a partially developed platform readily

Odrive Robotics

Founded by Oskar Weigl.

Low cost, low voltage servo motor driver for BLDC and PMSM motors (Weigl 2022).

The latest and most advanced model is the Odrive Pro, with specifications of 58V max with a peak current of 120A and a continuous rating of 70A. All contained within a 51mm x 64mm footprint (Odrive Robotics 2023a).

The microcontroller used is an STM32F4 (Odrive Robotics 2020).

Figure 11 - Odrive Pro (Odrive Robotics 2023a).

Founded by Benjamin Vedder. VESC stands for Vedder Electronic Speed Controllers.

Advanced FOC motor controller (VESC Project 2023).

Multiple options available, the product with largest voltage and current ratings identified is the VESC 100/250 at 100V 250A (Trampa Boards 2023a).

Manufactured in Nottingham, United Kingdom. (Trampa Boards 2023a).

The microcontroller used is an STM32F4 (Vedder 2016).

Figure 12 - VESC 100/250 Controller (Trampa Boards 2023b).

Open-source extension of the VESC products. Uses the VESC firmware but has been designed and assembled to operate at higher voltages and currents than the standard VESC products (Hackaday 2023).

The microcontroller used is a STM32F4 (Endless Sphere 2023).
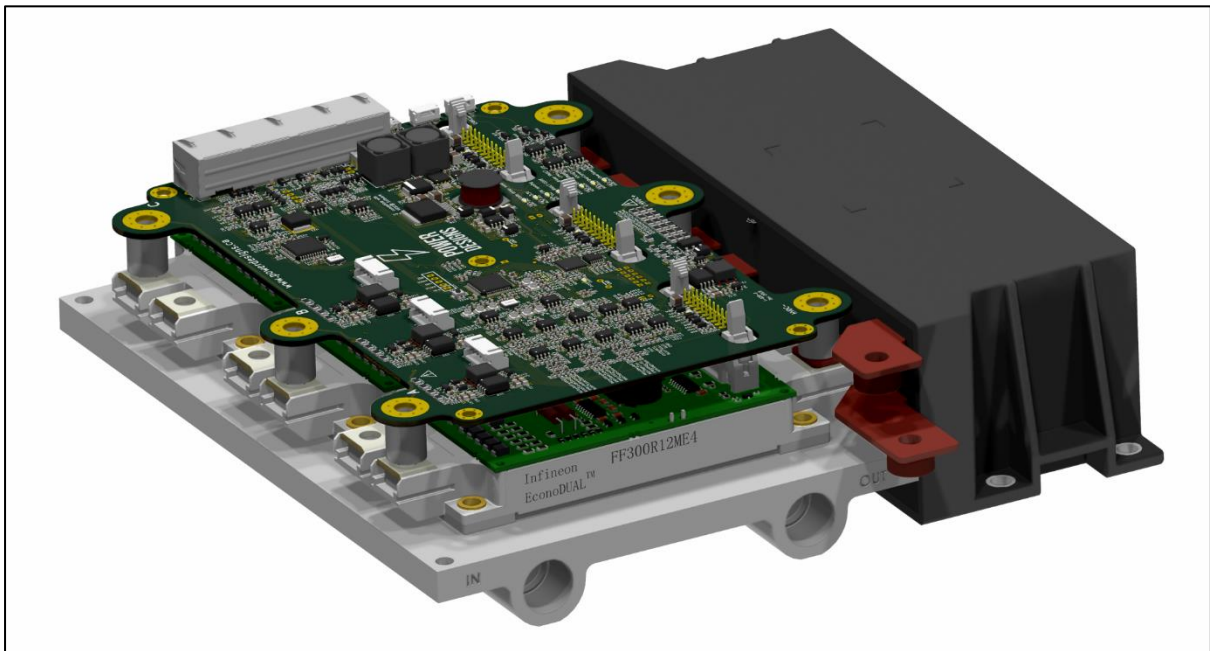
Figure 13 - 3D rendered image of the Axiom Controller (Hackaday n.d.).

Table 8 - Specifications and costs of open-source controllers.

Controller	Peak Current [A]	Cont. Current [A]	Peak Voltage [Vdc]	Dimensions LxWxH [mm]	Sensor Options	Cost (AUD)	Note
Odrive Robotics – Odrive Pro	120	70	58	51x64	Incremental Encoder and Hall Sensor	USD$229 AUD$350	1
VESC – 100/250	400	250	100	141x82x18	Incremental Encoder, Hall Sensor and AS5047 High-Resolution Position Sensor	GBP$400 AUD$750	2
Axiom	-	300	400	193x157x19	Resolver and Absolute Encoder	Not Advertised	3

Table 9 - Useful links used during the creation of Table 8.

Note	Useful Links
1	https://odriverobotics.com/shop/odrive-pro
2	https://trampaboards.com/vesc-100v-250a-in-cnc-t6-silicone-sealed-aluminum-box–p-28113.html
3	https://cdn.hackaday.io/files/1649327056450688/Datasheet-Axiom-control-board.pdf

2.4.   Formula SAE – Australasia Rules

The FSAE-A rules consist of the official FSAE rules with an addendum developed specifically for the Australian competition.

The following rules have been extracted from the official FSAE Rules 2023 [Version 2.0] book (SAE International 2023c). The relevant 2023 Australasian addendum [V1] changes have been applied (Formula SAE-A 2023c).

Only the rules directly impacting the controller and motor package design are listed below:

EV.4   ELECTRICAL LIMITATIONS

EV.4.1   Power and Voltage

- EV.4.1.1 – The maximum power drawn from the Accumulator must not exceed 80 kW.
- EV.4.1.2 – The maximum permitted voltage that may occur between any two points must not exceed 600 V DC.
- EV.4.1.3 – The powertrain must not regenerate energy when vehicle speed is between 0 and 5 km/hr

EV.4.2   Operation

- EV.4.2.1 – Supplying power to the motor to drive the vehicle in reverse is prohibited.
- EV.4.2.2 – Drive by wire control of wheel torque is permitted.
- EV.4.2.3 – Any algorithm or electronic control unit that can adjust the requested wheel torque may only lower the total driver requested torque and must not increase it.

EV.4.4   Violations

- EV.4.4.1 – A Violation occurs when one or two of these exist:
  - a. Use of more than the specified maximum power EV.4.1.1
  - b. Exceed the maximum voltage EV.4.1.2

    for one or both conditions:

    - Continuously for 100 ms or more
    - After a moving average over 500 ms is applied

EV.5   COMPONENTS

EV.5.1   Motors

- EV.5.1.1 – Only electrical motors are allowed. The number of motors is not limited.
  EV.5.5 Accelerator Pedal Position Sensor – APPS
- Refer to T.4.2 for specific requirements of the APPS
  Notable clauses from T.4.2

- o T.4.2.2 – Two or more electrically separate sensors must be used as APPSs. A single OEM type APPS with two completely separate sensors in a single housing is acceptable.
- o T.4.2.3 – The APPS sensors must have different transfer functions which meet one of:
  - ▪ Each sensor has a positive slope sense with different gradients and/or offsets to the other(s).
  - ▪ An OEM pedal sensor with opposite slopes. Non OEM opposite slope sensor configurations require prior approval.
- o T.4.2.4 – Implausibility is defined as a deviation of more than 10% pedal travel between the sensors or other failure as defined in this Section T.4.2. Use of values larger than 10% require justification in the FMEA and may not be approved.
- o T.4.2.5 – If an Implausibility occurs between the values of the APPSs and persists for more than 100msec, the power to the (IC) electronic throttle / (EV) Motor(s) must be immediately stopped completely.
  (EV only) It is not necessary to Open the Shutdown Circuit, the motor controller(s) stopping the power to the Motor(s) is sufficient.
- o T.4.2.8 – The APPS signals must be sent directly to a controller using an analogue signal or via a digital data transmission bus such as CAN or FlexRay.
- o T.4.2.9 – Any failure of the APPS or APPS wiring must be detectable by the controller and must be treated like an Implausibility, see T.4.2.4 above.

EV.5.6 Brake System Encoder – BSE

- Refer to T.4.3 for specific requirements of the BSE
  Notable clauses from T.4.3
- o T.4.3.1 – The vehicle must have a sensor or switch to measure brake pedal position or brake system pressure.
- o T.4.3.3 – The BSE or switch signals must be sent directly to a controller using an analogue signal or via a digital data transmission bus such as CAN or FlexRay.
  Any failure of the BSE or BSE wiring that persists more than 100 msec must be detectable by the controller and treated like an implausibility and power to the (IC) electronic throttle / (EV) Motor(s) must be immediately stopped completely.
  (EV only) It is not necessary to completely deactivate the Tractive System, the motor controller(s) stopping power to the motor(s) is sufficient.
- o T.4.3.5 – When any kind of digital data transmission is used to transmit the BSE signal:
  - ▪ © – In all cases a sensor failure must immediately shutdown power to the motor(s).

EV.5.7 APPS / Brake Pedal Plausibility Check

- • EV.5.7.1 – The power to the Motor(s) must be immediately and completely shut down when the two of these exist at the same time:
  - o The mechanical brakes are engaged EV.5.6, T.3.1.14
  - o The APPS signals more than 25% pedal travel EV.5.5
  This must be demonstrated at Technical Inspection
- • EV.5.7.2 – The Motor shut down must remain active until the APPS signals less than 5% pedal travel, with or without brake operation.

EV.6   ENERGY STORAGE

EV.6.2 Electrical Configuration

- EV.6.2.1 – All Tractive System components must be rated for the maximum Tractive System voltage.
- EV.6.2.4 – Soldering electrical connections in the high current path is prohibited.
  Soldering wires to cells for the voltage monitoring input of the AMS is allowed, these wires are not part of the high current path.

EV.6.6 Precharge and Discharge Circuits

- EV.6.6.1 – The Accumulator must contain a Precharge Circuit. The Precharge Circuit must:
  - Be able to charge the Intermediate Circuit to minimum 90% of the Accumulator voltage before closing the second AIR.
  - Be supplied from the Shutdown Circuit EV.8.1.
    -
  - Not be fused.
- EV.6.6.2 – The Intermediate Circuit must precharge before closing the second AIR. The end of precharge must be controlled by one of the following two options:
  - Feedback by monitoring the voltage in the Intermediate Circuit.
  - A conservative time defined by the longer of:
    - Twice the time to charge to 90%.
    - The time to charge to 90% plus 500ms.
- EV.6.6.3 – The Tractive System must contain a Discharge Circuit. The Discharge Circuit must be:
  - Wired in a way that it is always active when the Shutdown Circuit is open.
  - Able to discharge the Intermediate Circuit capacitors if the HVD has been opened.
  - Not be fused.
  - Designed to handle the maximum discharge current for minimum 15 seconds.
- EV.6.6.4 – Positive Temperature Coefficient (PTC) devices must not be used to limit current for the Precharge Circuit or Discharge Circuit.
- EV.6.6.5 – The precharge relay must be a mechanical type relay.
- EV.6.6.6 – [Added from FSAE-A Addendum] PDOC. The components within the pre-charge and discharge circuits that dissipate heat (power resistors, linear MOSFETs, heatsinks etc.) must be monitored for thermal overload by a Pre-charge/Discharge Overload Circuit. In the case of a thermal overload, the PDOC must open the shutdown circuit before the components exceed their manufacturer's recommended maximum operating temperature. This must be done without the influence of any programmable logic. See also EV.8 Shutdown Circuit regarding shutdown and reactivation of the tractive system after a fault.
  The status of the PDOC must be shown to the driver by a red indicator light in the cockpit that is easily visible even in bright sunlight. This indicator must light up, if the PDOC detects a thermal overload of the pre-charge or discharge circuit. The indicator light must be clearly labelled with "PDOC". The PDOC may be omitted if the pre-charge and discharge circuit is designed for continuous operation in a faulted state and will not adversely affect nearby

devices.

If the PDOC is not fitted, theoretical and experimental evidence must be submitted to demonstrate that the pre-charge and discharge circuit cannot overheat to the point of damage to the vehicle and that the heat generated can be appropriately dissipated when fitted to the vehicle. Any failure modes must be documented in the FMEA with appropriate controls in place as required.

If the PDOC is not fitted, then the rationale/evidence must be submitted concurrent with the FMEA timing.

EV.6.8 Tractive System Measuring Points – TSMP

- EV.6.8.1 – Two Tractive System Measuring Points (TSMP) must be installed in the vehicle which are:
  - Connected to the positive and negative motor controller/inverter supply lines.
- EV.6.8.3 – The TSMPs must be:
  - 4 mm shrouded banana jacks rated to an appropriate voltage level.
  - Color: Red.
  - Marked "HV+" and "HV-".
- EV.6.8.4 – Each TSMP must be secured with a current limiting resistor.
  - The resistor must be sized per the following:

Maximum TS Voltage (Vmax)	Resistor Value
200 V DC < Vmax <= 400 V DC	10 kOhm
400 V DC < Vmax <= 600 V DC	15 kOhm

    Resistor continuous power rating must be greater than the power dissipated across the TSMPs if they are shorted together.
- EV.6.8.5 – Any TSMP must not contain additional Overcurrent Protection.

EV.6.9 Tractive System Active Light – TSAL

- EV.6.9.1 – The vehicle must include a Tractive Systems Active Light (TSAL) that must:
  - Illuminate when the GLV System is energized to indicate the status of the Tractive System.
  - Be directly controlled by the voltage present in the Tractive System using hard wired electronics. Software control is not permitted.
  - Not perform any other functions.
- EV.6.9.2 – The TSAL may be composed of multiple lights inside a single housing.
- EV.6.9.3 – When the voltage outside the Accumulator Container(s) exceeds T.9.1.1, the TSAL must:
  - Be Color: Red.
  - Flash with a frequency between 2 Hz and 5 Hz.
- EV.6.9.4 – When the voltage outside the Accumulator Container(s) is below T.9.1.1, the TSAL must:
  - Be Color: Green.
  - Remain continuously illuminated.
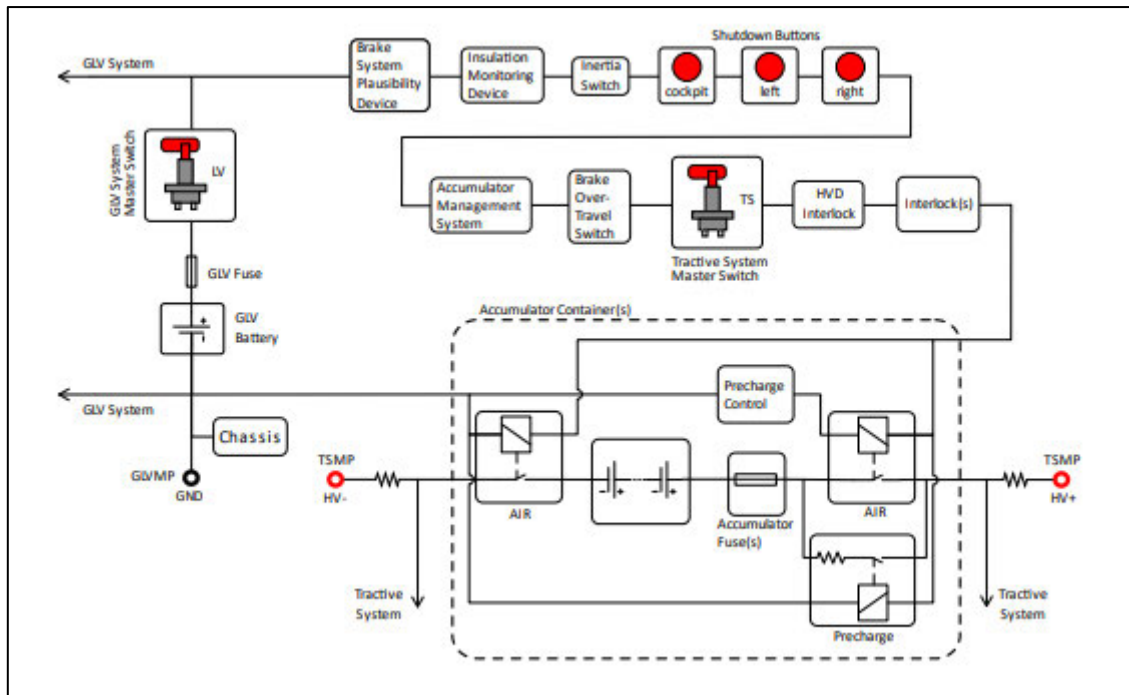
Figure 14 - EV Shutdown Circuit [EV.8.1.6] (SAE International 2023c, p.100).

EV.10   VEHICLE OPERATIONS

EV.10.5 Ready to Drive Sound

- EV.10.5.1 – The vehicle must make a characteristic sound when it is Ready to Drive
- EV.10.5.2 – The Ready to Drive Sound must be:
  - Sounded continuously for minimum 1 second and a maximum of 3 seconds
  - A minimum sound level of 80 dBA, fast weighting IN.4.6
    - **IN.4.6 – Ready to Drive Sound**
      The sound level will be measured with a free field microphone placed free from obstructions in a radius of 2 m around the vehicle against the criteria in EV.10.5.
  - Easily recognizable. No animal voices, song parts or sounds that could be interpreted as offensive will be accepted

2.5. Custom Product Design

The final option is the design and development of a custom solution, while this requires greater expertise, it does provide greater flexibility and the ability to optimise key components for an FSAE application. In developing a custom motor controller, the key factors that require consideration are:

- A microcontroller or computational device for implementing the control algorithms.
- Power transistors to provide high frequency switching at the power level required.
- Adequate cooling must be provided to ensure serviceable operating temperatures are maintained during use.

2.5.1. Microcontroller

FOC-capable microcontrollers were identified and reviewed for the motor controller selection. Multiple options were evaluated, with particular interest given to the STM32F4 due to its popularity in the previously identified open-source controllers. A brief description of three preferred options is provided below. Further data, including suitable evaluation boards and their cost, are compiled in Table 10.

Infineon

The IMC301A chip is the top-of-the-range Infineon PMSM/ BLDC motor controller from the iMOTION IMC300 series (Infineon Technologies 2023). Offering sensorless FOC and the option of using Hall sensor input (Infineon Technologies 2023).

Texas Instruments

The Texas Instruments microcontroller series offers an extensive range of included compatibility options, specifically regarding the ability to interface directly with several rotor position sensors. In particular, the LAUNCHXL-F28379D development boards can directly connect with Hall sensors, resolvers, SinCos transducers and absolute encoders (Texas Instruments 2023). These options and the sensorless algorithms available create the most versatile microcontroller option out of the three reviewed.

A Simulink simulation model with embedded coding capability can be inspected at <https://au.mathworks.com/help/mcb/gs/sensorless-foc-pmsm-smo-fo.html>.

The STM32F4 microcontroller series is already noted as the preferred option for comparable open-source projects currently being developed worldwide. As previously identified in the Open Source section (2.3.2), it is the microcontroller of choice for the Axiom, VESC and Odrive Robotics controllers. While fewer motor position sensor options are available when compared to the Texas Instruments microcontroller, the STM32F401RE chip does provide compatibility for Hall inputs, quadrature (incremental) encoders and sensorless algorithms (ST Microelectronics 2021a, p. 9).

A Simulink simulation model with embedded coding capability can be inspected at <https://au.mathworks.com/help/supportpkg/stmicroelectronicsstm32f4discovery/ug/senorless-stm-example.html>.

ST Microelectronics

Table 10 - Microcontroller options and applicable evaluation boards.

Brand	Chip	Sensor Options Built-in	Three Shunt Evaluation Board	Evaluation Board Cost (exc GST)	Simulink coding compatibility	Note
Infineon	IMC301A	Sensorless, Hall Sensor	EVAL-M1-301FTOBO1	$122.08	NO	1
Texas Instruments	TMS320F28379D-Q1	Sensorless, Hall Sensor, Resolver, Absolute Encoder, SinCos Transducer	LAUNCHXL-F28379D + BOOSTXL-DRV8305EVM	$79.88 + $161.81 = $241.69	YES	2
ST Microelectronics	STM32F401RE	Sensorless, Hall Sensor, Encoder	NUCLEO-F401RE + X-NUCLEO-IHM07M1	$21.31 + $20.48 = $41.79	YES	3

Table 11 - Useful links for information summarised in Table 10.

Note	Useful Links	
1	https://www.infineon.com/cms/en/product/power/motor-control-ics/imotion-integrated/imc301a-f064/	
2	https://www.ti.com/tool/LAUNCHXL-F28379D	https://www.ti.com/tool/BOOSTXL-DRV8305EVM
3	https://www.st.com/en/evaluation-tools/nucleo-f401re.html	https://www.st.com/en/ecosystems/x-nucleo-ihm07m1.html

2.5.2. Power Transistors

Two common preferences for a motor controller application are either MOSFETs (Metal-Oxide-Semiconductor Field-Effect Transistors) or IGBTs (Insulated Gate Bipolar Transistors); these were reviewed in further detail below.

With respect to electric motor controllers, the impact of Moore's Law can be seen in the continuous improvement of microcontrollers and power electronic devices like MOSFETs and IGBTs. These components have become increasingly smaller, more powerful, and more energy-efficient over time (Baliga 2022).

When comparing MOSFETs with IGBTs, the key advantages of MOSFETs are their higher switching speeds (in MHz), greater peak current, and larger safe operating area (SOA). However, their conduction is heavily influenced by the temperature and voltage rating (Schweber, B. n.d.). Additionally, as the voltage rating increases, the performance of their integral diode during reverse recovery deteriorates, leading to a rise in switching losses (Schweber, B. n.d.). On the other hand, IGBTs boast higher current ratings and robustness, but they switch at slower speeds. The absence of an internal reverse-recovery diode means the IGBT must be paired with a diode suitable for the intended application (Schweber, B. n.d.).

For motor drive applications, the basic rule of thumb is that MOSFETs are more suitable at lower voltages (≤ 250V) and currents and at higher switching frequencies. In comparison, IGBTs are the better selection for higher voltages and currents, as well as the lower frequencies (≤ 100 kHz) (Schweber, B. n.d.). It is important to note, however, that these guidelines are not absolute and may not apply to all situations, as the application's specific requirements play a crucial role. Given that most motors only require lower-frequency operation, determined by the number of poles and the maximum rpm, IGBTs are often a suitable choice for these applications (Schweber, B. n.d.).

Power Losses

The power losses of any semiconductor component can be separated into three groups (Gravovac & Purschel 2009, p.3):

- **Conduction Losses** (P_{cond})**:** These losses occur during the on-state conduction period of the switching event.
- **Switching Losses** (P_{sw})**:** These losses are the combination of the energy lost per switching event, occurring at both the switching on and switching off period of the switching event.
- **Blocking (leakage) losses:** These losses are generally considered negligible and are normally neglected in loss calculations.

The design of an Insulated Gate Bipolar Transistor (IGBT) has undergone significant enhancements through the implementation of trench gate field-stop (TGFS) technology. Incorporating a back emitter and field-stop within the IGBT grants superior control over its dynamic behaviour. The trench structure

further refines the trade-off curve between the collector-emitter saturation voltage ($V_{ce,sat}$) and the energy loss during switch-off (E_{off}) (Bourns Inc. 2022, p.7). This technology facilitates a thinner die, leading to higher cell density. The result is superior performance characterised by reduced conduction and switching losses, increased robustness, and substantially lowered thermal resistance (Bourns Inc. 2022, p.7).

For high current applications the noticeable difference in the IGBT and MOSFET losses is in the calculation of their conduction losses. The calculation of MOSFET conduction losses uses the following formula, adapted from (Infineon Technologies 2002, p.14):

Equation 3 - MOSFET conduction losses

$$P_{cond,MOSFET} = \left(\int_{0}^{t_{ON}} R_{ds(ON)} \cdot i_d^2(t) \, dt \right) \cdot f$$

Where:

R_{ds} = On-state drain-source resistance

i_d = Drain current

t_{ON} = On-time period

f = Switching frequency

Whereas, IGBT conduction losses use this formula, adapted from (Gravovac & Purschel 2009, p.3):

Equation 4 - IGBT conduction losses

$$P_{cond,IGBT} = \left(\int_{0}^{t_{ON}} \left(U_{CE0} \cdot i_C(t) + r_C \cdot i_C^2(t) \right) \, dt \right) \cdot f$$

Where:

U_{CE0} = On-state zero-current collector-emitter voltage

i_C = Collector current

r_C = On-state collector-emitter resistance

While both formulas have a squared current value, this has a considerably larger impact on the MOSFET in the higher current operation range.

For reference, the values from a 225A 1200V MOSFET and IGBT datasheet were compared. The following values have been selected with a thermal junction temperature (T_{vj}) of 25°C and a turn on voltage (V_{GS} for the MOSFET and V_{GE} for the IGBT) of 15V.

The r_C of the IGBT is 5.88 mΩ, this has been derived from the IGBT typical output characteristic of the IGBTs datasheet (Infineon Technologies 2017, p.5). The derivation has been accomplished as per the prompts shown in Figure 15.

Whereas the MOSFET's R_{ds} is 8.9 mΩ (Infineon Technologies 2022, p.4). The MOSFETs resistance is approximately 1.5 times larger. When these values are multiplied by the current squared, it results in a significantly larger power loss for the MOSFET.
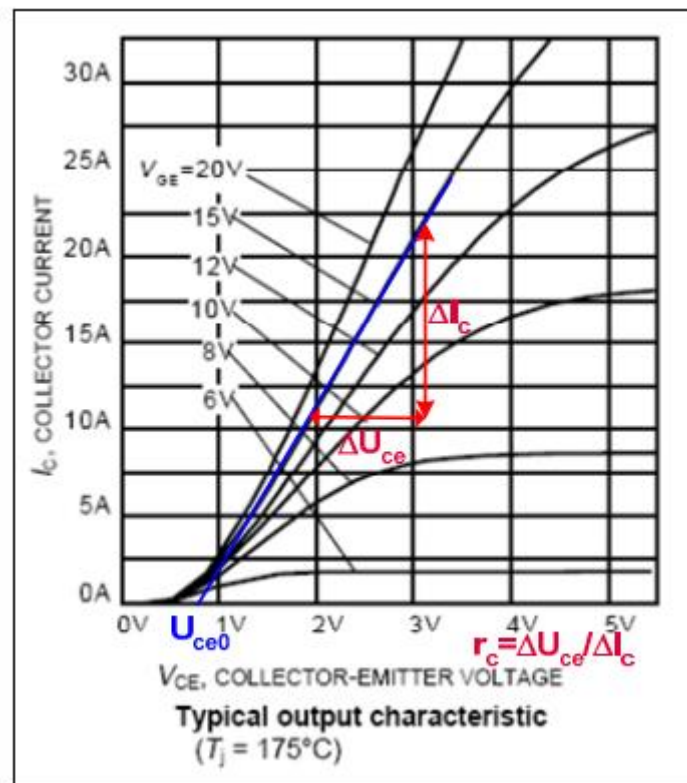
Figure 15 - Example of reading the U_{CE0} and r_C from a datasheet diagram (Gravovac & Purschel 2009, p.4).

2.5.3. Cooling

High-power transistors will generate significant heat during operation; this must be managed to ensure optimal performance and longevity (Varma 2018).

Thermal management has always been a crucial aspect of electronic design. This holds especially true in today's era, as power densities intensify while component form factors continue to shrink. While these reduced sizes assist with packaging demands, they have reduced the component's thermal mass, requiring improved cooling systems to ensure junction temperatures are not exceeded (Varma 2018).

Forced-air and liquid cooling are the two options for power transistor cooling (Mikros Technologies n.d.).

Galvanic Corrosion

Galvanic corrosion is a phenomenon that arises when two dissimilar metals are in electrical contact in an electrolyte environment, causing the more active metal to corrode (TWI Global n.d.). In liquid cooling systems, such as those used in high-performance electronics, the coolant can act as the electrolyte (SSINA n.d.).

Aluminium is relatively low on the galvanic scale, meaning it is more susceptible to corrosion when in contact with more noble metals like brass or copper in the presence of an electrolyte (SSINA n.d.). Therefore, if the cooling system incorporates elements such as brass fittings or copper heat exchangers, there exists a potential risk of galvanic corrosion to the aluminium constituents within the cooling loop.

2.5.4. Regenerative Braking

Regenerative braking was considered unnecessary for this project. While it is permissible to be incorporated into the motor controller design, it would add complexity to both the control algorithms and hardware assembly. Therefore, no further consideration or research was undertaken on this topic.

2.6.   Summary of Component Selections for Controller Design

This literature review was utilised to identify suitable hardware components for the motor controller build and review the previously completed procurement of the USQ Racing's EMRAX motor. From the literature review, the informed selection of suitable motor controller system components was undertaken.

The primary focus of the hardware selection was to ensure the components selected do not hinder the ongoing development of the USQ Racing team while also providing a low-cost and customisable electric motor controller. To accommodate this project aim, the components must be capable of the project objective of operating up to the maximum electrical limits of the FSAE rules.

Preference was given to components that could be readily acquired and assembled while also allowing a reasonably user-friendly interface to be produced, promoting future improvements.

Suitable component selection was critical to the project's aim of producing a low-cost and customisable electric motor controller and simulation platform to support the ongoing development of the USQ Racing team and the FSAE Electric community in general.

2.6.1.   Motor Selection Assessment

The research conducted and summarised in Table 2 highlights the ability of several prominent motor designs to be utilised in an electric vehicle application. While notable production vehicles include PMSM, AC Induction, BLDC and brushed AC motors, the PMSM stands out as the preferred choice for an FSAE application. This decision is based on their high power density, high torque at low speed, high efficiency, and low maintenance requirements.

A selection preference for the PMSM is further supported by Table 4. The data compiled in Table 4 identifies a preference by prominent teams in the FSAE-A competition, specifically Monash Motorsport and UQ Racing, who placed first and second, respectively, in 2019 FSAE-A, before both teams transitioned to new drivetrain formats in 2022.

Additionally, following a review of the suitable electric motor control strategies available, a PMSM is compatible with all strategies identified. Therefore, a single PMSM motor would be suitable for the USQ Racing team's first vehicle.

2.6.2. Power Transistor Selection

The power transistor selection is critical to the longevity and overall performance of the motor controller. While an extensive range of options was available, confidence from proven designs currently operating at or able to scale up to comparable electrical requirements was leveraged to assist with selection. The competition's maximum electrical limits allow the vehicle to operate at a supply of 600VDC, with a maximum of 80kW of power to be drawn from the accumulator. As identified in the literature review, the preferred option was an IGBT to reduce the power losses in the motor controller design.

After reviewing the existing motor controller designs, the Axiom was selected as the primary inspiration for the hardware design. The Axiom already operates at voltages and currents comparable to the proposed targets for this design while also being assembled from readily available modular components and conforming to a compressed package size. The reduced package size is achieved by integrating Infineon dual IGBT modules, featuring two IGBTs per unit, as shown in Figure 16, and Power Integrations dual driver boards that mount directly on top of the IGBT, as shown in Figure 17.

T To allow for transient overvoltages caused by the high-speed switching of an inductive load, the maximum voltage of the IGBT was selected at double the nominal service voltage, resulting in the selection of 1200V IGBTs.
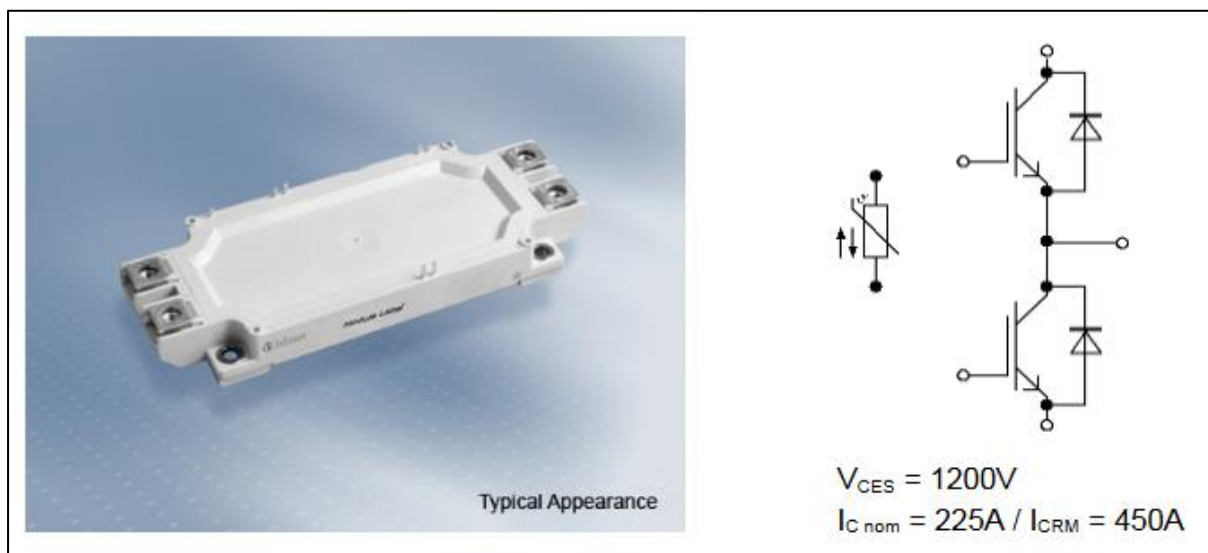
Figure 16 - Infineon EconoDUAL™3 module [FF225R12ME4P] (Infineon Technologies 2017, p.1).
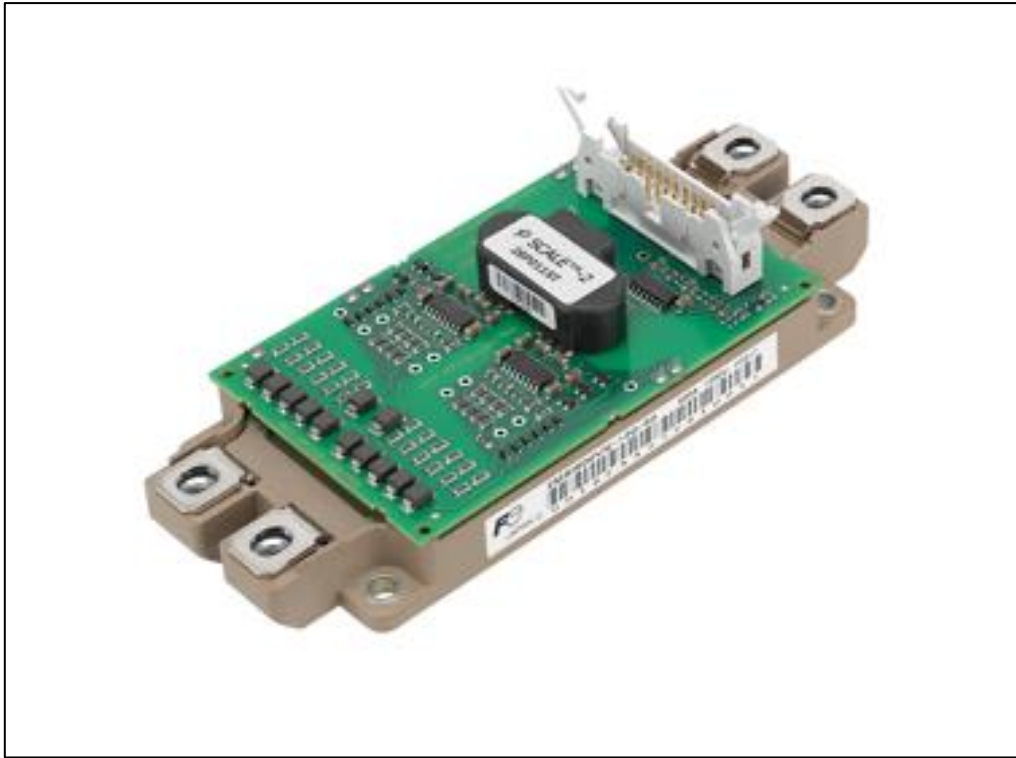
Figure 17 - Power Integrations 2SP0115T driver board mounted to an Infineon EconoDUAL™3 module (Power Integrations n.d.).

Multiple maximum current options were available in the Infineon 1200V EconoDUAL module range. The selection criteria used to assist with the final selection was the realisation that the EMRAX 228 motor has a continuous motor current of 115A RMS and a maximum current draw of 240A RMS (EMRAX d.o.o. 2018, p.15).

The three models closest to these current thresholds were analysed and summarised in Table 12 and Table 13. These modules are:

- FF150R12ME3G with a maximum collector current of 150A.
- FF225R12ME4P with a maximum collector current of 225A.
- FF300R12ME4P with a maximum collector current of 300A.

While it is acknowledged that the maximum current draw can peak at 240A RMS (2-minute maximum with sufficient cooling), the continuous motor current of 115A RMS is equivalent to a peak DC current of $\sqrt{2}\cdot115 = 162.6$ A (EMRAX d.o.o. 2018, p.15). In addition to these values, the FSAE-A competition limit of 80kW drawn from the accumulator limits the likelihood of the peak current of $\sqrt{2}\cdot240 = 339.4$ A ever being approached. At a 600V service voltage, the accumulator current draw is limited to $80kW/600V = 133.33A$. While the current value of 133.33A is less than the 150A limit of the FF150R12ME3G, consideration of the project's second aim of supporting the ongoing development of the electric motor controller encouraged the decision to select the 225A module (FF225R12ME4P). This selection allows the IGBT to have additional redundancy when operating at the

80kW limit while also allowing the service voltage to be reduced, consequentially resulting in the possibility of the continuous running current exceeding the FF150R12ME3G module's limit of 150A.

While this selection decision was made based primarily on the continuous current loading the IGBT will experience, consideration was also given to the second part of the second aim, which is to design a low-cost motor controller, therefore eliminating the desire to select the more expensive 300A, FF300R12ME4P module unnecessarily.

Based on the analysis in this this section, the final selected power transistor components consist of:

- 3x Infineon FF225R12ME4P
- 3x Power Integrations 2SP0115T2A0-12

The Infineon FF225R12ME4P is a 1200V, 225A, dual IGBT module.

The Power Integrations 2SP0115T2A0-12 is the driver board suitable for the Infineon 1200V IGBT series.

Table 12 - Infineon IGBT specification comparison for motor controller selection.

IGBT MODULE							
Make	Model	IGBT Voltage Class	IGBT Rated Current (Ic Max)	Max Switching Frequency	Power - Output/ channel (Max)	Gate Peak Current (Max)	Logic Input Voltage
Infineon	FF150R12ME3G	1200 V	150 A	40.0 kHz	1.2 W	15 A	5
	FF225R12ME4P	1200 V	225 A	36.0 kHz	1.2 W	15 A	5
	FF300R12ME4P	1200 V	300 A	26.0 kHz	1.2 W	15 A	5

Table 13 - Infineon IGBT cost comparison for motor controller selection.

IGBT MODULE		27-March-2023	
Make	Model	Mouser	
		Stock Level	COST
Infineon	FF150R12ME3G	0	$230.72
	FF225R12ME4P	4	$272.73
	FF300R12ME4P	6	$338.37

2.6.3. Microcontroller Selection

The microcontroller for this design is a critical component; the motor controller's operating functionality and overall reliability primarily depend on the selected microcontroller's capability.

Based on the precedence set by the Axiom, VESC and Odrive Robotics controllers; the presence of an ST Microelectronics endorsed MathWorks Simulink model; and the reduced cost of the ST Microelectronics development boards (identified in Table 10), the STM32F401RE was selected as the ideal option for the development of this motor controller.

The final selected microcontroller components consist of:

- 1x NUCLEO-F401RE
- 1x X-NUCLEO-IHM07M1

The NUCLEO-F401RE is an STM32 Nucleo development board with an STM32F401RET6 MCU.

The X-NUCLEO-IHM07M1 is a three-phase brushless DC motor driver expansion board based on an L6230 chip; this board is an add-on component in the STM32 Nucleo series.

2.6.4. Motor Controller Control Strategy

The crucial design decision regarding control strategy selection is multifaceted, precisely due to the varying range of implementation complexity and performance metrics. However, the project's second aim of supporting the ongoing development results in vector control becoming the premier selection.

Vector control optimises the motor's torque output and is the choice strategy for multiple-motor vehicles. By supporting the ongoing development of a vector-control based motor controller, the USQ Racing team will be able to regulate and optimise the torque output of their vehicle. A vector-controlled motor controller also allows the USQ Racing team to transition to a multiple-motor configuration in future vehicle iterations rapidly.

This control strategy selection also aligns with the existing Simulink sensorless simulation model with embedded coding capability for the STM NUCLEO-F401RE. This Simulink model has been produced to provide sensorless field-oriented control of PMSM using stm32 processor based boards; therefore, selecting a vector-controlled motor controller allows this Simulink model to assist with the prototype coding and simulation immediately.

2.6.5. Motor Position Sensor Selection

The suitable motor position sensors identified in the literature review were assessed to identify the configuration most compatible with the second project's aim of supporting the ongoing development of this motor controller.

The metrics reviewed were the sensor's performance, microcontroller compatibility, initial purchase cost and installation complexity.

After reviewing the position sensors investigated, the first motor controller design was determined to use the proprietary sensorless algorithms available from ST Microelectronics.

This decision allows the rapid prototyping of a motor controller design due to eliminating the complexity of instigating either of the two following situations:

- Developing a suitable signal processing component to utilise the existing resolver within the motor controller's programming. The requirement of a digital signal processing component is due to the STM microcontroller not readily accepting input directly from a resolver.

- Custom installing an incremental encoder or Hall sensor arrangement onto the EMRAX 288. While the STM microcontroller could accept input from either of these position sensors, developing and installing a custom mounting system would likely prolong the motor controller's design and prototyping unnecessarily.

The existence of a Simulink sensorless simulation model with embedded coding capability for the STM NUCLEO-F401RE is expected to assist with accelerating the prototyping process. This existing sensorless Simulink model is anticipated to reduce the initial prototype's development time due to the design providing a proven baseline program explicitly based on the STM sensorless algorithms. This Simulink model provides confidence that the sensorless design is readily achievable, promoting the decision to proceed with this design proposal.

2.6.6. Project Component Selection Summary

Following the informed selection of the principal motor controller components, in-depth engineering analysis and justification will be undertaken to determine the appropriate complementary design decisions. While it is acknowledged that commercial off-the-shelf options are available for motor controllers that can be adopted for an FSAE application, the second aim of this project is to support the ongoing development of the USQ Racing team, and FSAE Electric community in general, through the design of a low cost and customisable electric motor controller and simulation platform. Therefore, the investigations and analysis performed throughout this project are working towards producing an FSAE-specific motor controller design, one that can be customised to suit the nuances of any team's vehicle design, rather than selecting a generic off-the-shelf option and adjusting the vehicle design to suit the controller.

Components Selected:

- 1x NUCLEO-F401RE
- 1x X-NUCLEO-IHM07M1
- 3x Infineon FF225R12ME4P
- 3x Power Integrations 2SP0115T2A0-12

Decisions around the cooling system requirements and overall packaging will be investigated later in this project.

Chapter 3

3. Methodology

3.1. Commission the EMRAX 228

*Figure 18 - EMRAX 228 Motor (**EMRAX d.o.o. 2018, p.8**).*

The motor purchased by USQ Racing is a 2018 model Combined Cooled (CC), High Voltage (HV) EMRAX 228. The USQ Racing team were assured that the motor was still completely functional at the time of sale. Figure 18 exhibits an EMRAX 228 secured to the OEM X-bracket.

The following proposal was developed for the acceptance testing and commissioning of this electric motor:

1. Confirm winding resistance is acceptable and identical for all three windings.
2. Ensure insulation resistance has not been compromised.
3. Perform a mechanical rotation test to confirm the bearings' condition is acceptable.
4. Execute a generated waveform test to confirm the back EMF waveform is characteristically satisfactory for this motor.
5. Test and analyse the resolver output to ensure it is operational.
6. Confirm the operation of the motor using the USQ Racing's Prohelion WaveSculptor200 motor controller.

Stage 1 – Winding Resistance

The EMRAX motor is a three-phase motor with three electrically identical windings in the stator. Testing will be performed using a digital multimeter, validating the results against the manufacturer's datasheet. Figure 19 below provides a visual representation of the testing process. Results will be recorded for three tests; the three tests will be:

1. Winding resistance from terminal "U" to terminal "V".
2. Winding resistance from terminal "U" to terminal "W".
3. Winding resistance from terminal "V" to terminal "W".

Once these results are recorded, the next step is to confirm that they are all equal and within an acceptable tolerance to the datasheet values.
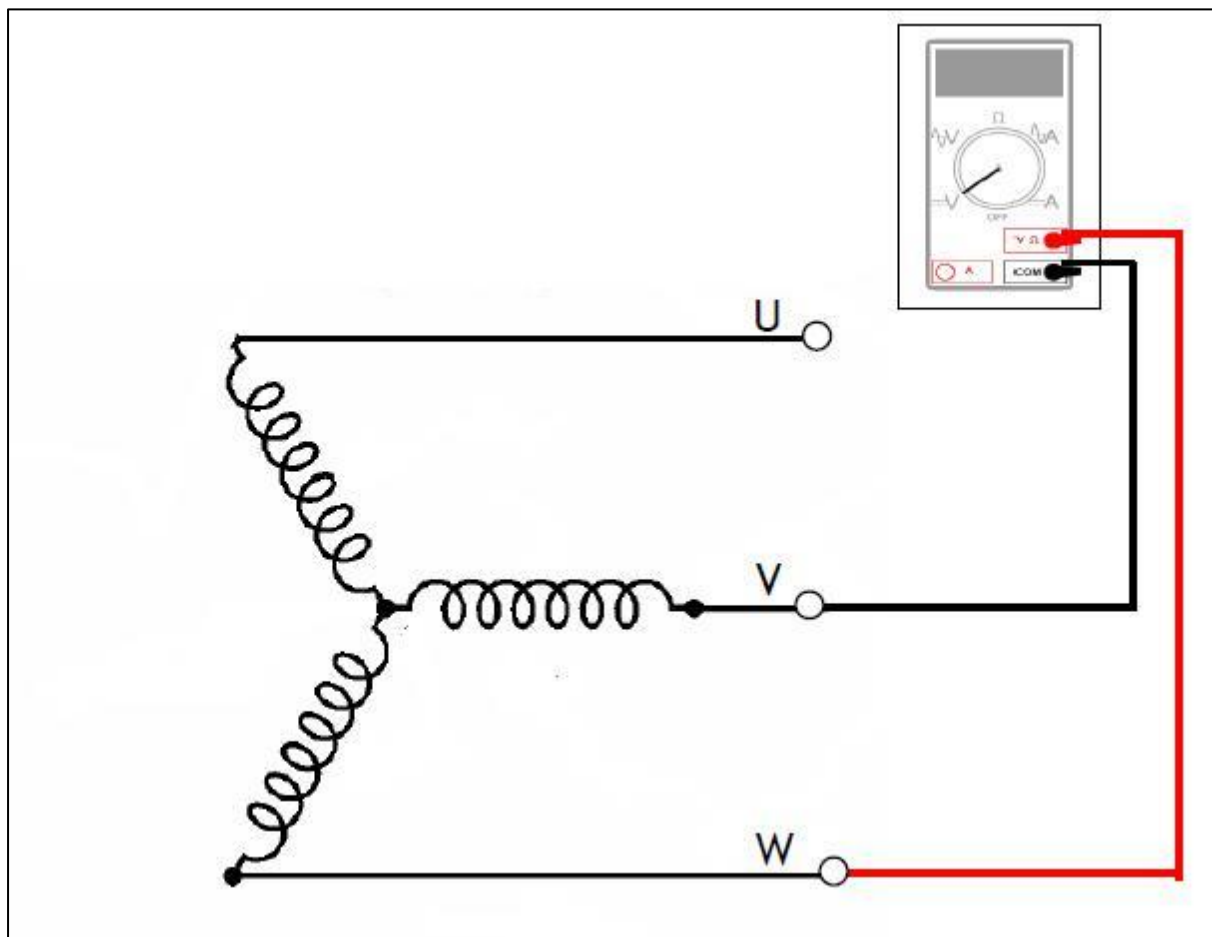
Figure 19 - Winding resistance testing of a three-phase motor (Electrical Engineering Toolbox 2015).

Stage 2 – Insulation Resistance

An insulation resistance test is required to ensure the motor windings insulation has not been compromised. This test ensures the windings have not become shorted to the frame of the motor. If a short has occurred, the motor would be deemed unserviceable.

The insulation resistance test voltage used will be 1000VDC. This test voltage was selected because it is the closest standard Insulation Resistance (IR) test voltage exceeding the intended service voltage of 600VDC. The test will be performed between each winding and the stator case.

To eliminate any risk of damage to the motor bearings, insulation resistance testing will not be performed between the rotor frame/ casing and any other test point. This eliminates the possibility of current travelling through and damaging the motor's bearings.

Figure 20 below displays the testing arrangement between one of the motor windings and the stator's case.
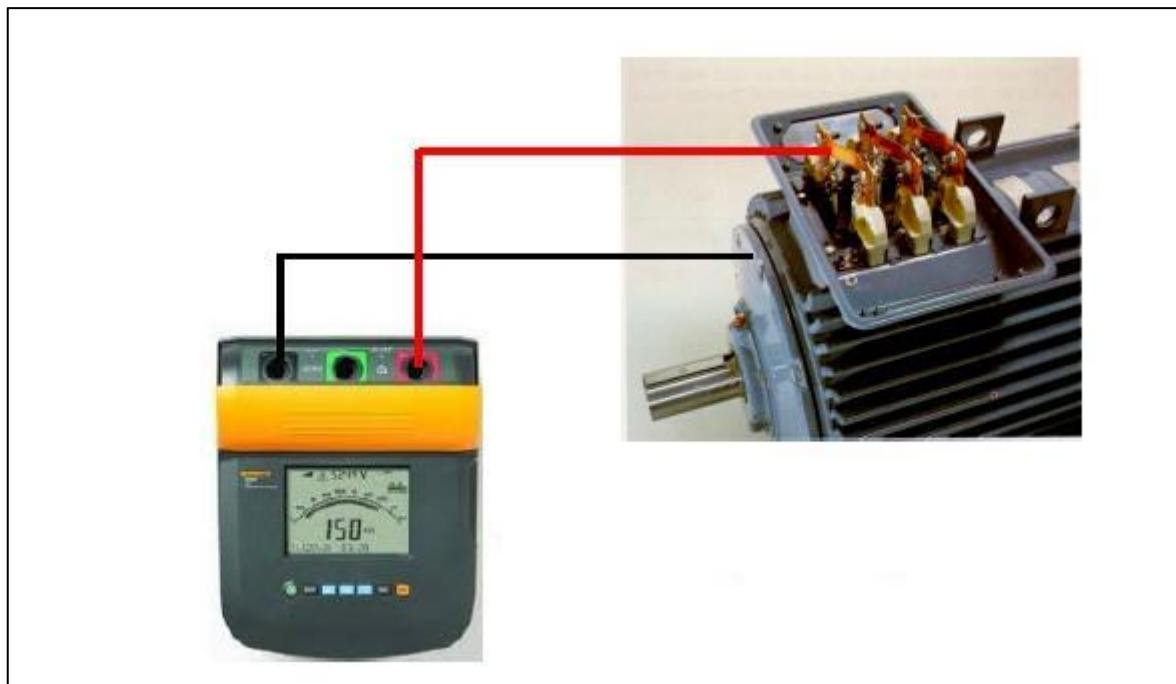
Figure 20 - Insulation resistance testing of a three-phase motor (Electrical Engineering Toolbox 2016).

Stage 3 – Mechanical Rotation

The EMRAX 228 motor is constructed as an outrunner, indicating that the rotating section, the rotor, is the outer section of the motor (EMRAX d.o.o. 2018, p.4). This design requires an external mounting frame to secure the motor for rotational tests. The proprietary mounting bracket design suitable for the 228 motor, as featured in Figure 18, will be acquired from EMRAX and fabricated through the University of Southern Queensland Workshop (Toowoomba Campus).

Stage 4 – Back EMF Waveform Generation

Following the successful completion of the preceding tests, the EMRAX motor will be operated as a waveform generator. This test will allow the EMRAX to produce waveforms for inspection from an oscilloscope. This test will confirm that the three waveform phases are equal in amplitude and sinusoidal shape, featuring 120-degree separation without any unexpected distortions.

The 5kW, 230VDC machine in the University of Southern Queensland's Energy Systems Lab will spin the EMRAX at a controlled speed. This DC machine will be configured as a motor with a variable DC supply to provide speed control capability. Prior to energisation, an oscilloscope will be connected to the three phases of the EMRAX motor to monitor the waveforms generated. The motor terminal voltages and waveforms will be monitored throughout the process to ensure they are presented as expected while ensuring the voltages generated do not create a safety concern for personnel.

The DC motor and EMRAX will be coupled together using a separable connection. This two-piece connection will allow the DC motor to drive the EMRAX while also providing the ability to separate and run the DC motor unloaded. The pre-existing lever system, which will traverse the EMRAX 228 mounting base horizontally, will readily engage and disengage the DC motor and EMRAX 228.

Before engaging the EMRAX 228 for the waveform generation testing, the EMRAX and DC motor will be separated, allowing for preliminary speed control checks. These checks verify that the DC motor can be readily controlled, confirming that the likelihood of an uncontrolled event occurring is as low as reasonably practicable.

Once all preliminary checks have been performed, the following will occur:

1. The three-probed oscilloscope will be secured to the EMRAX 228 windings.
2. The DC motor and EMRAX will be coupled together; a custom-fabricated output shaft is required for the coupler to be fitted to the EMRAX 228.
3. The DC motor will be slowly accelerated to a speed that allows the generated waveforms to be evaluated.
4. The DC motor speed will remain constant to confirm that the waveforms are uniform, sinusoidal and present with a consistent 120-degree separation.
5. Following these tests, the motor will be de-energised and the testing configuration disassembled.

Stage 5 – Resolver Testing

The resolver will be tested by applying a generated signal to the excitation coil and monitoring the sine and cosine outputs. As mentioned in the resolver component of section 2.2.5 - Motor Position Feedback, the resolver outputs should present as an amplitude-modulated signal at the same frequency as the excitation signal, with the sine and cosine outputs 90-degree phase shifted from each other, as shown in Figure 10.

The resolver installed on the 228 EMRAX is an LTN Servotechnik GmbH - RE-15-1-A14 unit. As per the datasheet in Appendix B, this resolver specifies a 10kHz 7 V_{rms} input signal. This input signal will be applied to the excitation coil using a waveform generator, and both output signals will be monitored. Both the sine and cosine should produce a waveform with a peak output dependent on the rotor position and transformation ratio, as shown by Equation 1 and Equation 2.

The output waveforms will be inspected through the full rotation of the motor shaft to ensure they are consistent with the expected output across all rotor positions.

Stage 6 – Confirm Motor Function

The function of the motor will be confirmed by utilising the USQ Racing team's WaveSculptor200. This controller will require the assembly and commissioning of the required electrical and cooling systems. The controller will be operated in the Energy Systems Lab to utilise the DC supply available there.

The following items will need addressing for this test:

- Prohelion (2021a, p.20) recommends a minimum supply of 24VDC for the controller to test motor function. However, during the initial configuration, Prohelion (2021b, p.18) recommends a 60VDC supply for the parameter extraction algorithms. Both specified voltage selections require investigation to confirm their availability in the Energy Systems Lab.

- A capacitor precharge circuit will be required to limit the inrush current at the initial energisation (Prohelion 2021a, p.19).

- The motor controller is controlled and programmed over CANBUS; therefore, the CAN circuit must be established from the motor controller to the driver control unit and CAN-ethernet bridge (Prohelion 2021a, pp.11-15).

- Following the commissioning of the electrical and water-cooling circuits, the motor controller will be configured by engaging the PhasorSense and ParamExtract algorithms, as specified in the WaveSculptor Config Software User's Manual (Prohelion 2021b, pp.15-19).

  PhasorSense provides the controller with the phase sequence and determines the rotor position sensor offset count.

  ParamExtract determines the motor's electrical parameters: the stator winding resistance and inductance.

  With all these points addressed, the motor will be subjected to an initial bench test; detailed steps are identified in section 13.4 of the WaveSculptor User's Manual (Prohelion 2021a, p.21).

The precharge circuit provides a controlled charging of the internal capacitor of the motor controller.

In the schematic shown in Figure 21, K1 and K3 will be closed for initial energisation. The precharge resistor R1 will limit the charge current. The internal capacitor will be confirmed as wholly charged once the voltage at voltmeter Vc displays the full supply voltage. When the internal capacitor is confirmed as fully charged, K2 will be closed. The controller (system Load in Figure 21) can then be operated.
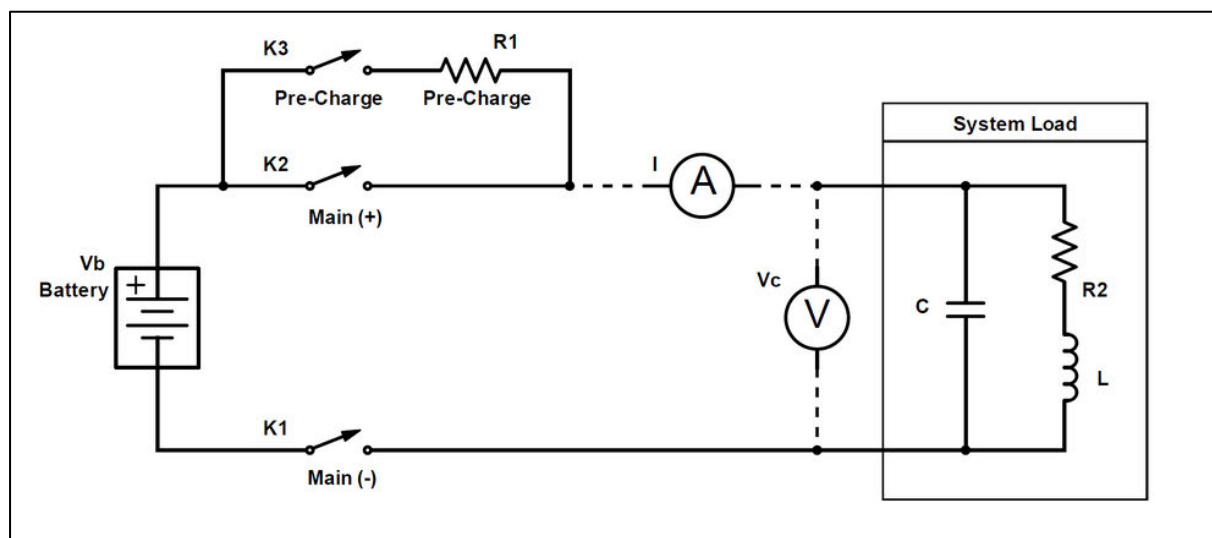

Figure 21 - Schematic of capacitor precharge circuit (Sensata 2023).

3.2. Packaging and Cooling

The finalised product packaging size is primarily dictated by the IGBT mounting configuration, coupled with the overall size of the cooling plate required. While a minimal package size is desirable, engineering analysis is required to ensure the cooling circuit equipment selected can adequately cater to the operational heat loads anticipated.

Cooling System Component Selection

With specific consideration given to galvanic corrosion, the EMRAX 228 motor datasheet was reviewed to identify the materials used to construct the motor. This review confirmed that the motor is constructed from aluminium (EMRAX d.o.o. 2018, p.43).

To ensure the longevity of the cooling circuit elements, all subsequent selected components will be constructed of either aluminium or non-conductive materials. This selection criteria significantly reduced the range of suitable cooling plates and heat exchanges. However, a suitable collection of cooling plates was identified during the associated research. Advanced Thermal Solutions manufactures these cooling plates. Following consultation with their product engineering department, they confirmed that a suitable product had been designed to apply three Infineon EconoDUAL modules. This cooling plate is their ATS-CP-1001 model; the specific datasheet for this cooling plate has been included in Appendix B.

While many aluminium radiators/ heat exchangers were identified during the cooling system research, suitable options with associated cooling analysis and coolant flow characteristic curves (flow rate versus pressure drop) could not be identified. To assist with the calculations, data for the Advanced Thermal Solutions HE-23 was used; these heat exchangers do feature copper tubing, which is outside of the design specifications. However, it is assumed that this data, for selection analysis, is comparable to similar aluminium units available.

Regarding the cooling pump selection, the recommendations of both Prohelion and UQ Racing identified Koolance pumps as the preferred pump manufacturer for the motor controller cooling system. Prohelion recommended a Koolance PMP-400 for their WaveSculptor200 cooling circuit (Prohelion 2021a, p.10). In contrast, discussions with UQ Racing identified that the cooling circuit for their WaveSculptor200 and EMRAX 207 motor combination utilised two Koolance PMP-500 pumps in series.

In order to analyse the performance of the identified cooling pump selections, the coolant flow characteristic curve (flow rate versus pressure drop) was obtained for all cooling system components. These included:

- Advanced Thermal Solutions – ATS-CP-1001 Cooling Plate
- EMRAX 228 Motor
- Advanced Thermal Solutions – ATS-HE23 Heat exchanger

The factory-supplied data for the EMRAX 228 motor is shown in Figure 22. This data was acquired directly from the EMRAX sales and technical support team.
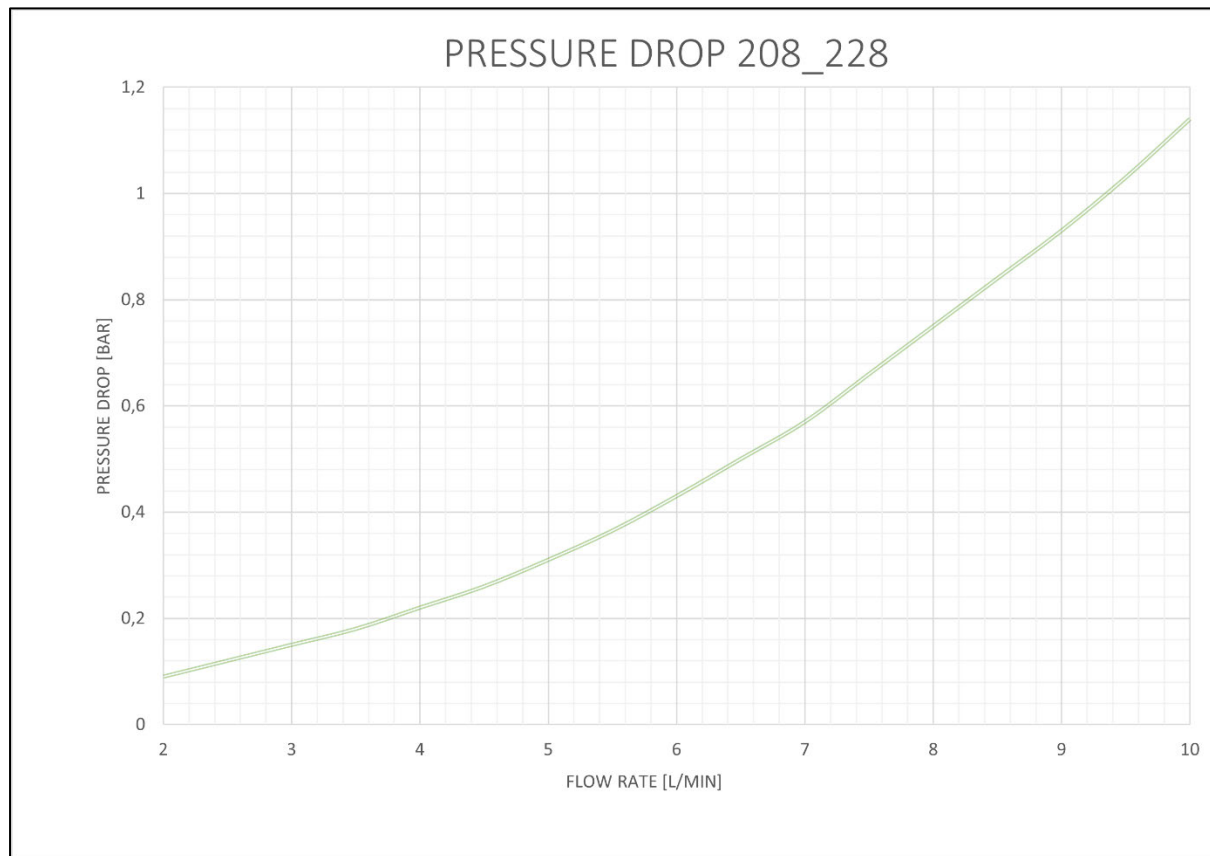
Figure 22 - EMRAX 228 motor coolant flow characteristic curve (Flow Rate vs Pressure Drop) (source: EMRAX).

3.2.1. Cooling System Thermal Model Construction

To produce an applicable cooling system thermal model, the coolant flow characteristic curves of the cooling plate, heat exchanger and EMRAX 228 motor will be interpolated and extrapolated for a flow range of 0 to 10 litres per minute. Following this, they will be bit-wise summed together and cross-referenced to the output response of single and dual Koolance PMP-400 and PMP-500 configurations. Regarding the pump configuration, "dual" refers to two pumps in series with each other to increase output pressure. All values will be standardised during these calculations to litres per minute for flow and kPa for pressure.

The resultant coolant flow rates calculated from this procedure will be utilised to determine the ideal water pump selection from the options investigated. The primary selection criteria will focus on the

cooling flow requirements required by the EMRAX 228 motor. Page 42 of the EMRAX user manual identifies that the motor requires a flow rate of 6 to 8 litres per minute during operation to achieve and maintain the continuous motor power and torque values specified in the associated datasheet (EMRAX d.o.o. 2018).

The selected cooling pump configuration will then dictate the coolant flow rate and, subsequently, the cooling plate (Figure 23) and heat exchanger (Figure 24) thermal resistances.
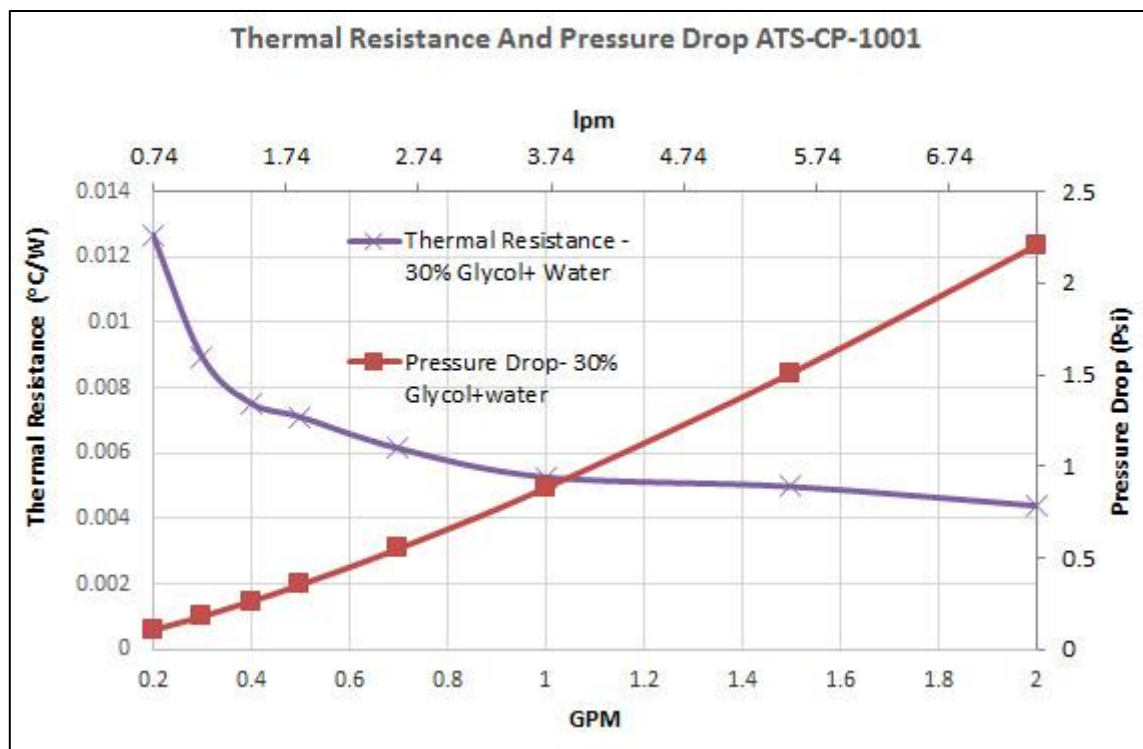
Figure 23 - ATS-CP-1001 cooling plate performance (Flow Rate vs Thermal Resistance and Pressure Drop) (Advanced Thermal Solutions n.d.a, p.2).
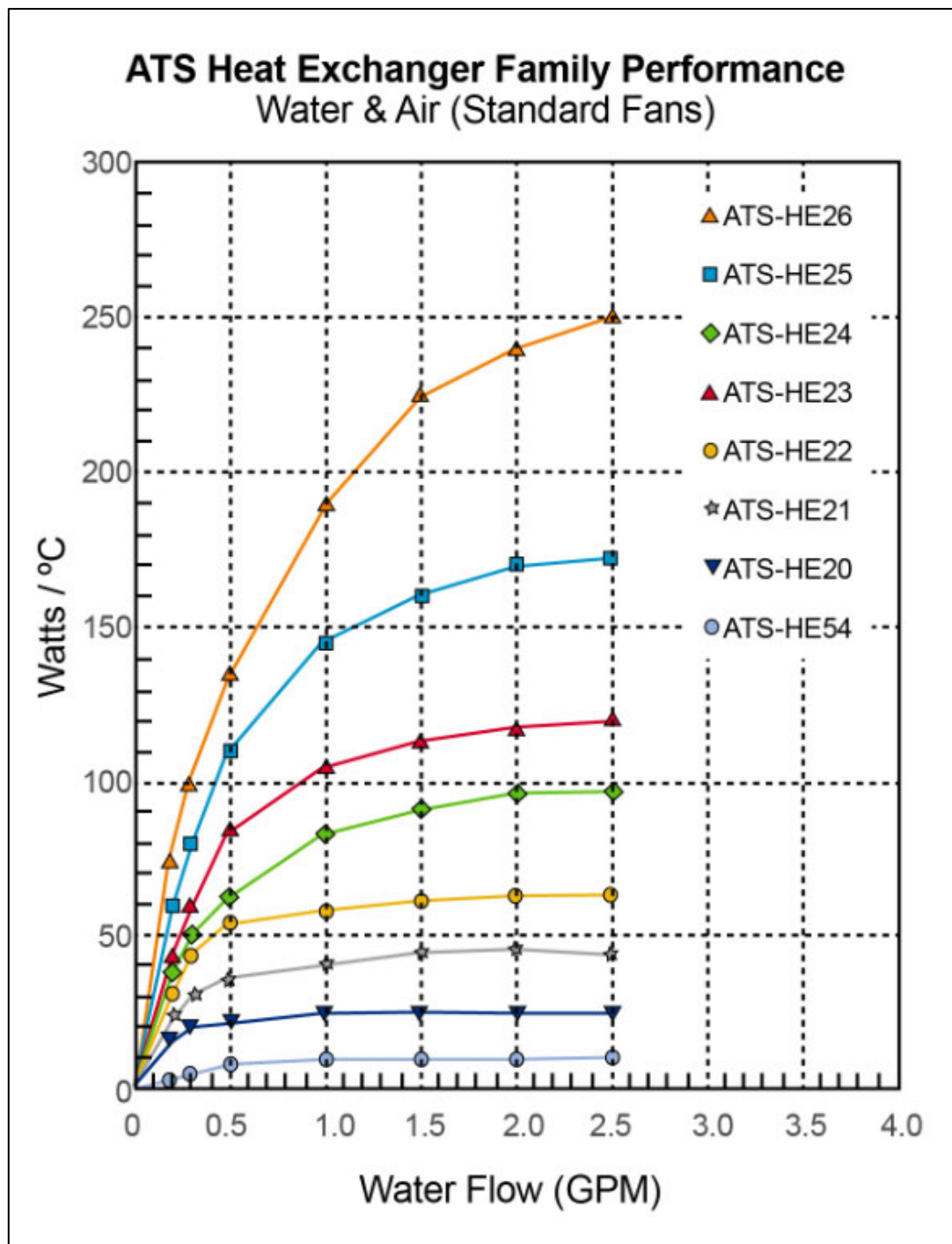
Figure 24 - Advanced Thermal Solutions - Heat exchange thermal conductance (Advanced Thermal Solutions n.d.b).

Once the cooling system is defined, the known system data will be entered into the Infineon Power Simulation program – IPOSIM (https://iposim.infineon.com/application/en/). This simulation program will provide the IGBT modules' expected operational losses and junction temperature rise during operation.

The motor controller's steady-state temperatures will be calculated using the IPOSIM simulated power losses and the simplified thermal schematic featured in Figure 25 . The IGBT datasheet will define the IGBT and embedded diode thermal resistances referenced in the simplified thermal schematic of Figure 25. In contrast, the thermal resistances for the cooling plate and heat exchanger will have been calculated from the coolant flow rate and interpolation of Figure 23 and Figure 24, respectively.
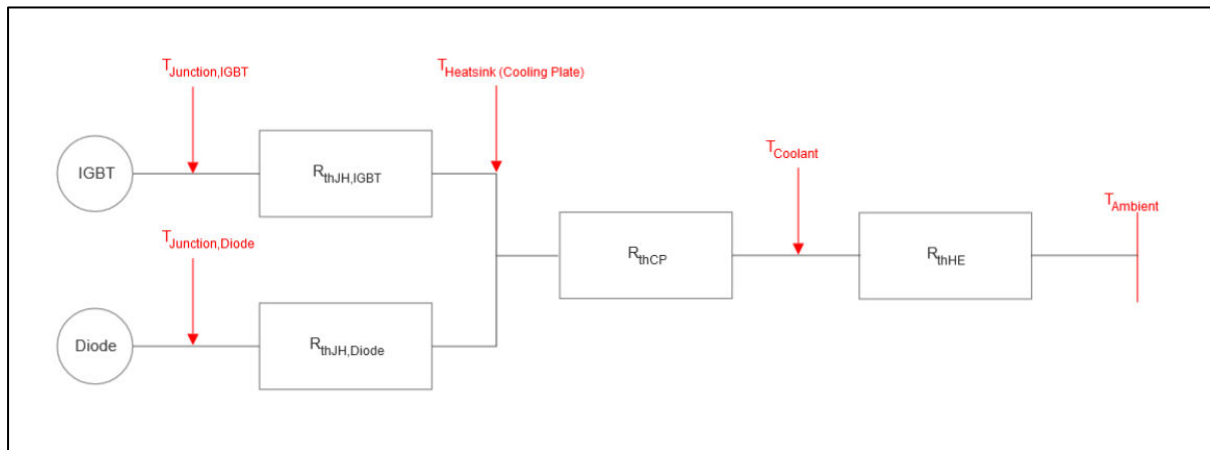
Figure 25 - Simplified thermal schematic for motor controller system.

An ambient temperature of 50°C has been selected for the steady-state temperature calculations. This selection reflects the maximum temperature expected during operation in Toowoomba, QLD or Winton, VIC. Toowoomba is the location of the USQ Racing team's vehicle build and performance testing, while Winton is acknowledged as the location of the FSAE-A competition. The ambient temperature of 50°C exceeds the maximum ambient temperatures ever recorded for both Queensland and Victory, as supported by the information acquired from the Australian Bureau of Meteorology, displayed in Figure 26.

▶ Highest temperature

State	Temperature (°C)	Date	Place name	Station no.	Latitude	Longitude
WA	50.7	13 January 2022	Onslow Airport	5017	−21.67	115.11
SA	50.7	2 January 1960	Oodnadatta Airport	17043	−27.56	135.45
NSW	50.1	11 January 1939	Wilcannia Post Office	46043	−31.56	143.37
Qld.	49.5	24 December 1972	Birdsville Police Station	38002	−25.90	139.35
Vic.	48.8	7 February 2009	Hopetoun Airport	77010	−35.72	142.36
NT	48.3	2 January 1960	Finke Post Office	15526	−25.58	134.57
	48.3	1 January 1960	Finke Post Office	15526	−25.58	134.57
Tas.	42.2	30 January 2009	Scamander	92094	−41.46	148.26

Figure 26 - Bureau of Meteorology - Australia's maximum recorded temperature by state (BOM 2023).

With all operational data defined, the steady state temperatures will be calculated to determine whether the selected cooling system can cater to the expected power losses, ensuring the IGBT junction temperatures do not exceed their maximum permissible limits.

3.3.   Motor Controller Prototype Development

The prototype development will be completed in stages, allowing the ability to modify the approach if the expected results are not achievable at each stage.

The initial focus will be validating the microcontroller algorithms to ensure they can rotate the EMRAX 228 motor before developing a more extensive scale model. The programming and simulation framework will be developed during these stages.

3.3.1.   Validation of Microcontroller Algorithms

With the major components selected, the subsequent essential step is confirming that the microcontroller algorithms can operate the EMRAX 228 motor. The applicable development boards for the microcontroller and motor driver will be acquired and configured for the initial validation.

The selected ST Microelectronics STM32F401RE microcontroller has specific development boards already identified in the literature review that are suitable for validating the motor control algorithms; these boards are shown in Table 14 below.

Table 14 - ST Microelectronics selected development boards for initial development.

Model	Description	Cost	Link
NUCLEO-F401RE	STM32 Nucleo-64 development board with STM32F401RE MCU, supports Arduino and ST morpho connectivity.	$20.02 + GST	https://www.st.com/en/evaluation-tools/nucleo-f401re.html
X-NUCLEO-IHM07M1	Three-phase brushless DC motor driver expansion board based on the L6230 for STM32 Nucleo.	$19.25 + GST	https://www.st.com/en/ecosystems/x-nucleo-ihm07m1.html

These development boards can operate a motor between 8VDC and 48VDC, up to a peak output current of 2.8 A (ST Microelectronics 2021a, p. 2).

The two development boards are part of the STM Nucleo series; they are specifically designed to merge via the ST Morpho connectors, with the boards forming a development platform for the functional evaluation, as demonstrated in Figure 27.
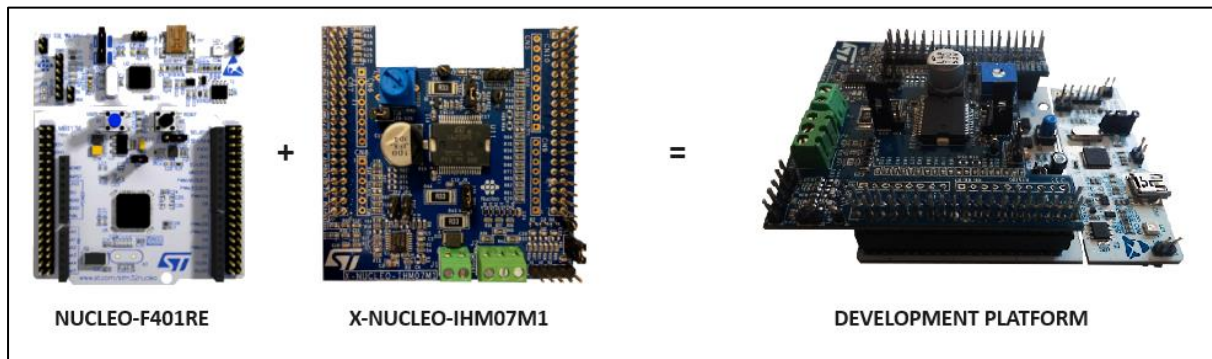
Figure 27 - STM Nucleo development board combination, figures compiled from X-NUCLEO-IHM07M1 User Manual (ST Microelectronics 2021a, p. 3).

To operate, the development platform requires a primary DC supply, a three-phase connection to the EMRAX 228 motor and an auxiliary USB-based power supply for the microcontroller. The programming will be achieved directly from the Simulink sensorless PMSM FOC model designed explicitly for the STM32 processor based boards (ST Microelectronics n.d.b). Modifications will be made to the associated MATLAB script to update the motor details, specifically the motor's electrical parameters, which have been informed by the datasheet (EMRAX d.o.o. 2018, p.15).

Table 15 - ST Microelectronics Simulink updated motor parameters.

Parameter	Description	Data
emrax_228_HV_CC.p	% Number of motor pole pairs	10
emrax_228_HV_CC.Rs	% Motor stator winding resistance (Ohms)	19 mΩ
emrax_228_HV_CC.Ld	% Motor winding inductance in Direct axis (Henries)	177 µH
emrax_228_HV_CC.Lq	% Motor winding inductance in Quadrature axis (Henries)	183 µH
emrax_228_HV_CC.J	% Rotor inertia (kg*m^2 or N*m*s^2)	0.0383 kg·m^2
emrax_228_HV_CC.B	% Viscous damping (Nm/rad/s)	1 µNm·rad^{-1}·s^{-1}
emrax_228_HV_CC.Ke	% Back emf Voltage (Vrms/kRPM)	73 Vrms·kRPM^{-1}
emrax_228_HV_CC.Kt	% Torque constant (Nm/A)	1.1 Nm·A^{-1}
emrax_228_HV_CC.I_rated	% Rated current (A)	115 A
emrax_228_HV_CC.N_max	% Motor maximum application speed (rpm)	5500 RPM
emrax_228_HV_CC.FluxPM	% Permanent flux linkage constant (Wb (or V*s))	0.0542 V·s
emrax_228_HV_CC.T_rated	% Rated torque (Nm)	120 Nm

The initial Simulink model will be downloaded from MathWorks; it is preconfigured with the FOC motor algorithms actioned by the STM32 peripheral blocks in the model, allowing the rapid functional testing of the ST Microelectronics components. Programming directly from the Simulink environment will be enabled through the Embedded Coder Support Package for STMicroelectronics STM32 Processors. This Simulink model provides both simulation and programming capability as well as the ability to perform hardware-in-the-loop analysis, all in one location; it is noted that this method provides consistency between the physical programming used in the field and the parameters actioned in the simulated environment (ST Microelectronics n.d.b).

After updating the motor's characteristics and system voltage, the development platform will be electrically connected to the EMRAX 228 for functional evaluation. The primary power source for the motor will be supplied through three 12.8V LiFePO4 7Ah batteries in series, supplying a nominal 38.4VDC power supply. A USB powerpack will provide the auxiliary USB power supply, allowing the laptop utilised for programming to be separated from the system during operation.

3.3.2. Prototype Component Selection

Following the successful operation of the EMRAX 228 motor with the development boards, the motor controller prototype development will commence. An interfacing PCB will be produced to establish the required circuitry between the microcontroller and power transistor driver circuits. The required system feedback and control inputs need to be identified so that the complementary circuitry can be adequately designed. The design and analysis of this circuitry are critical to ensuring that a suitable motor controller will be successfully produced.

The primary focus will be ensuring the motor and controller can be operated safely without creating hazardous conditions for personnel and associated property, particularly regarding overcurrent or short-circuit events.

Controller Firmware Alterations

The initial prototype will be constructed to replace the X-NUCLEO-IHM07M1 motor driver development board. The X-NUCLEO-IHM07M1 board provided the desired function in the development platform; however, it is constrained by the electrical limits of the L6230 chip.

The ST Microelectronics L6230 Electronic Limits (ST Microelectronics n.d.c):

- Operating supply of 8VDC to 52VDC
- Peak output current of 2.8 A

During the design of the motor controller prototype, the decision to build a small-scale version was made. This decision was made to limit the first design's financial outlay while reducing the potential failure's financial liability. This decision, therefore, required the identification and selection of an equivalent IGBT module that would still facilitate the second project aim of supporting the ongoing development of the USQ Racing team by producing a suitable motor controller.

To ensure the selected component are as close to the previously proposed motor controller IGBTs, the selection criteria was limited to the same manufacturer, Infineon. The initial prototype will be constructed from components capable of functioning at the Energy Systems Lab power supply rating of 300VDC. Additionally, functional testing is only planned to be performed with the motor unloaded; therefore, to limit the complexity and cost, the prototype will not be designed for the maximum power limits permissible in the FSAE-A competition, negating the need for a high-power system.

The Infineon IM535-U6D, with a purchase price of under AUD$40, was the resultant module selected. This chip operates at electrical limits of 600 VDC and 30 A, enabling suitable functional tests to be performed.

The initial design requires the identification of the required subcircuits utilised within the X-NUCLEO-IHM07M1 board. Consequently, Table 16 has been produced using data from the ST Microelectronics X-NUCLEO-IHM07M1 user manual and the STM32CubeMX configuration file (2021a, pp. 4-6). The STM32CubeMX provides a visual pinout of all inputs and outputs utilised in the microcontroller file; the pinout for the development platform microcontroller file is shown in Figure 28.
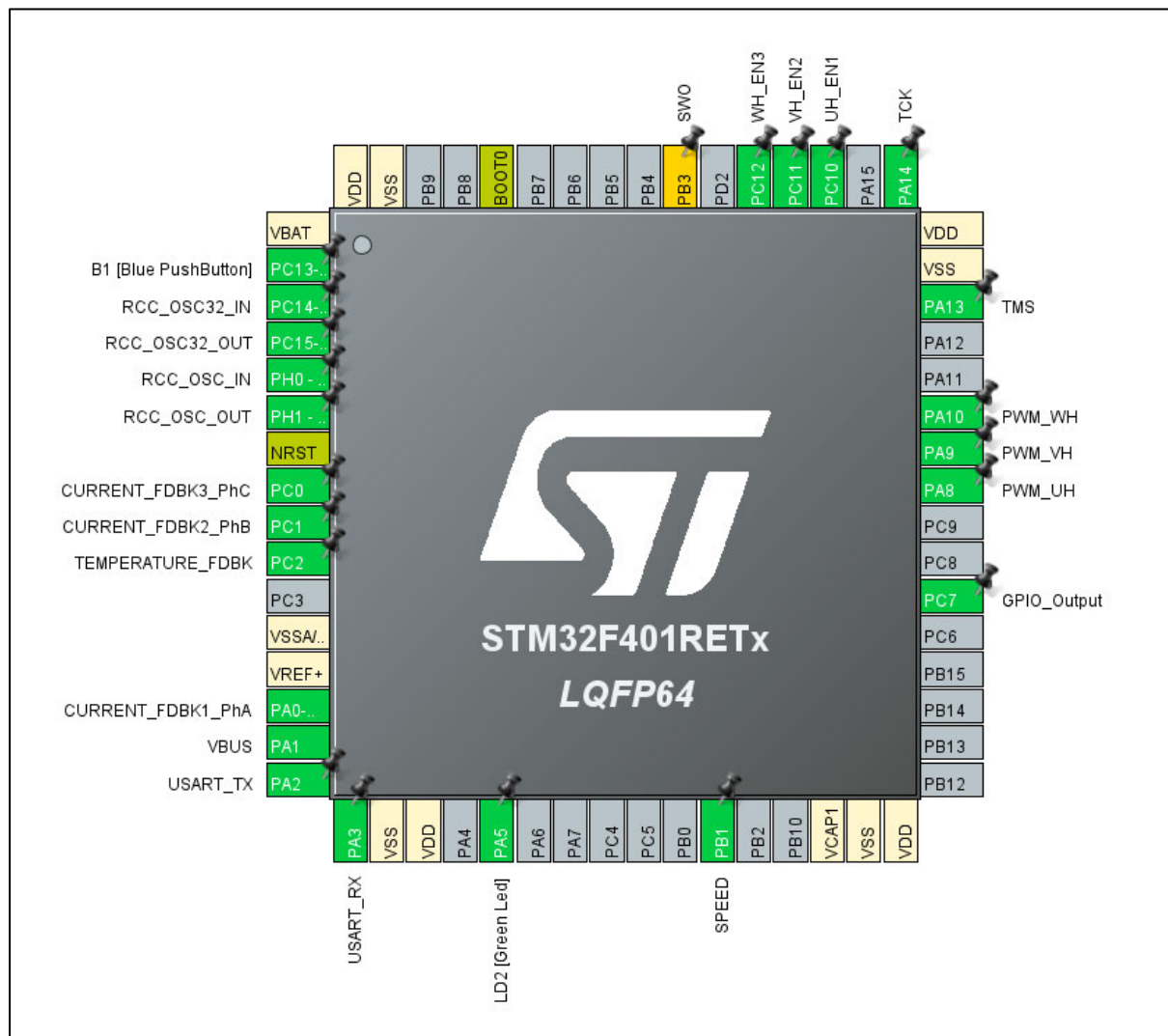

Figure 28 - Initial development controller STM32CubeMX pinout.

The notable pin changes identified from the review of the pinout in Figure 28, the L6230 chip, and the design required for the prototype motor controller, were the following:

- **PC10, PC11 and PC12**
  These pins operate as "enable" inputs for the PWM circuit in the L6230 and work in conjunction with three PWM outputs from the microcontroller. However, the IGBTs intended for the prototype motor controller do not require these "enable" inputs; instead, they require six PWM outputs. The three additional PWM signals are the inverse of the already established PWM signals.

- **PB3**
  This pin is unused.

Additionally, it was identified that pins PB13, PB14 and PB15 would be required to generate the complementary PWM signals.

During the review of the ST Microelectronics PWM configuration, it was identified that a PWM break function was available to be programmed into the ST Microelectronics microcontroller. This pin would be an emergency input to stop the PWM output (ST Microelectronics 2023a, pp.6-7). This input (PA6) is noted in Table 16 ; however, it was not incorporated in the prototype design.

The addition of the three PWM signals required a deadtime to be hard-coded into the microcontroller; this ensured a shoot-through event could not occur. A shoot-through event is when a high-side and complimentary low-side power transistor trigger at the same time. The IM535 requires a minimum external deadtime of $2\mu s$ (Infineon Technologies 2021, p.10).

The complementary PWM signals and required deadtime will be programmed through the STM32CubeMX, as identified in Figure 29 ; the STM32CubeMX handles the microcontroller's firmware configuration. Motor and inverter parameters are handled in the associated MATLAB script, whereas all other programming is implemented in the Simulink environment.

Table 16 - Pins utilised by NUCLEO-F401RE for motor controller.

|						
NUCLEO-F401RE - Required Pin Configuration						
Connector	Pin	Default	Signal	Solder Bridge	Utilised	Description	Components Required
CN7	1	PC10	Enable_CH1-L6230	R58	N	Enable L6230 gate driver 1	Will not be required
	2	PC11	Enable_CH2-L6230	R67	N	Enable L6230 gate driver 2	
	3	PC12	Enable_CH3-L6230	R72	N	Enable L6230 gate driver 3	
	23	PC13	Blue Button		Y	Initiate button located on STM32F401RE board	None
	28	PA0	Curr_fdbk_PhA	R47	Y	Current feedback for phase A	External op-amp circuitry
	30	PA1	VBUS_sensing	R51	Y	Bus Voltage	Voltage divider circuit
	35	PC2	Temperature feedback	R54	Y	IGBT Temperature feedback	Voltage divider circuit
	36	PC1	Curr_fdbk_PhB	R48	Y	Current feedback for phase B	External op-amp circuitry
	38	PC0	Curr_fdbk_PhC	R50	Y	Current feedback for phase C	External op-amp circuitry
CN10	11	PA5	GPIO_Output	R80	Y	Green LED located on STM32F401RE board	None
	13	PA6	TIM1_BKIN	R53		PWM shutdown input, not used currently.	PWM break input - not used on rev.0, recommended for future iterations
	21	PA9	VH_PWM	R64	Y	High side IGBT PWM 2	Connect to IGBT driver board
	23	PA8	UH_PWM	R56	Y	High side IGBT PWM 1	Connect to IGBT driver board
	24	PB1	POTENTIOMETER	R78	Y	Maximum speed set point	10kΩ Potentiometer
	26	PB15	WL_PWM	R66	Y	Low side IGBT PWM 3	Activate channels and establish deadtime setting in controller
	28	PB14	VL_PWM	R49	Y	Low side IGBT PWM 2	
	30	PB13	UL_PWM	R82	Y	Low side IGBT PWM 1	
	33	PA10	WH_PWM	R70	Y	High side IGBT PWM 3	Connect to IGBT driver board
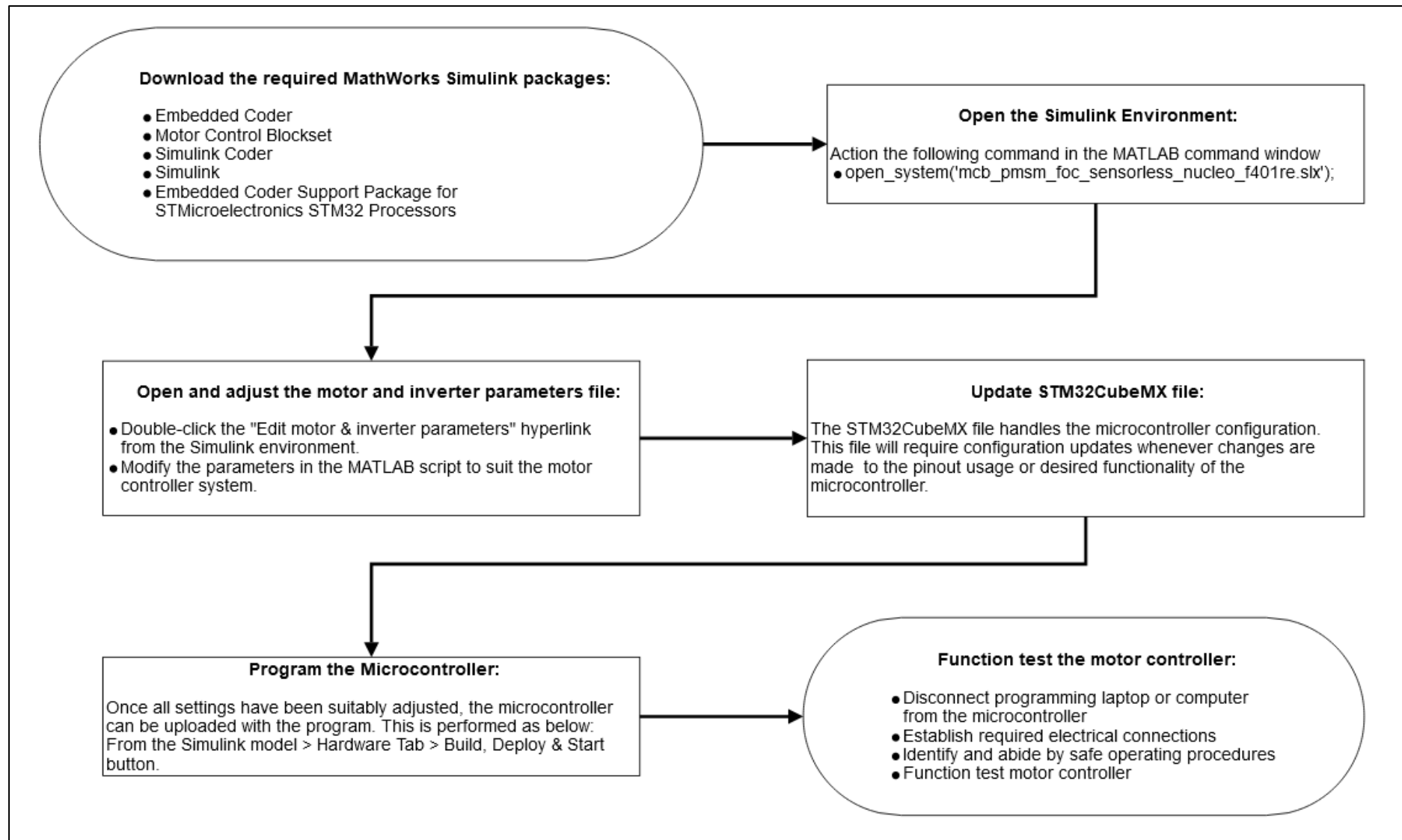
Figure 29 - High level flow chart of Simulink embedded programming process.

Table 16 identifies the following segments of the PCB development that require the associated design to be examined. These are summarised below:

1. **Operational amplifier circuit design required for the current feedback circuits.**
   - Pins PA0 (A Phase), PC1 (B Phase) and PC0 (C Phase).

2. **Voltage divider circuit for monitoring the service voltage.**
   - Pin PA1

3. **Voltage divider circuit for the temperature monitoring.**
   - Pin PC2

4. **Integration of 10kΩ potentiometer for the speed reference.**
   - Pin PB1

Each of the segments identified has been investigated to ensure that informed design decisions are made.

i. Operational amplifier circuit design required for the current feedback circuits.

The operational amplifier circuit for the current feedback requires two stages of development:

- The first stage will focus on monitoring the output current and providing an over-current shutdown input (ITRIP) to the IM535 module (Infineon Technologies 2021, p.5).

- While the second stage will monitor, amplify, and centre bias the current sense signal to provide feedback to the microcontroller. The op-amp output will utilise the entire 3.3 V ADC range. It will be designed to ensure it can operate at the maximum expected output current without subsequent saturation of the ADC input.

The output current is monitored by the volt drop over a sense resistor connected to the open emitter connections of the IM535 chip. An example of this for one phase is shown in Figure 30. The sense resistors' resistance must be large enough to produce a quantifiable voltage signal while being as practically small as possible to reduce power losses.
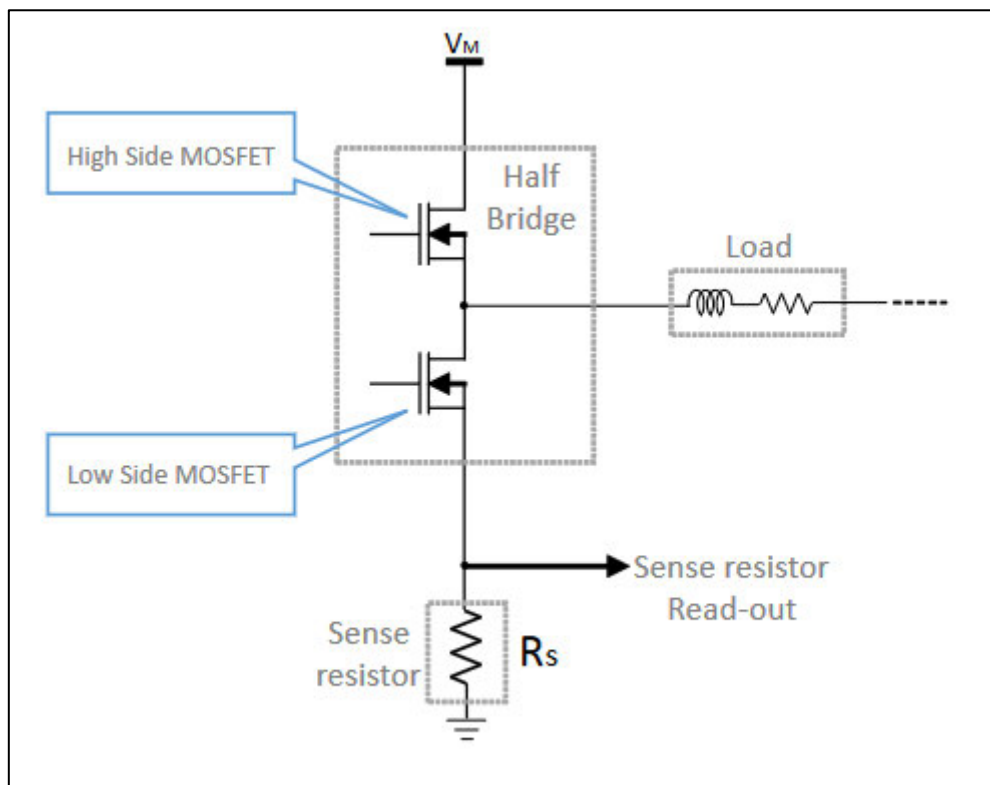

Figure 30 - Example of current sense resistor in a half bridge configuration (ST Microelectronics 2019, p. 3).

The IM535 chip datasheet nominates the continuous collector current as ±30 A and the maximum peak (less than 1ms) at ±60 A (Infineon Technologies 2021, p.8).

Considering the ±30 A continuous rating, the current sense resistor was selected as a 3 mΩ, 3 W, 1% unit. This selection allowed continuous operation, producing a readily detectable 9 mV signal and dissipating only 2.7 W during the maximum continuous operation.

For the following component selection, calculations were performed for a maximum current of ±50 A; this value was selected instead of ±60 A to allow a greater portion of the ADC range to be utilised under normal operation while allowing some redundancy in the ADC range for transient currents.

The 50 A maximum current value results in a current sense voltage of 0.15 V; this value will be referenced for the following op-amp circuit designs.

ITRIP signal

The ITRIP positive threshold is a typical 525 mV for an overcurrent event to initiate a module shutdown (Infineon Technologies 2021, p.11). However, this input is combined with the other two phases via individual diodes; refer to the red circled section of Figure 65. These circuits utilise a 3kΩ pull-down resistor, therefore resulting in a circuit current of 175µA (Equation 5) and, subsequently, a forward voltage drop of 530 mV through the 1N4148 diodes (interpolated from the forward voltage vs. forward voltage chart of the datasheet) (Vishay 2017, p.2).

Equation 5 - ITRIP diode current.

$$I_{diode} = I_F = \frac{V_{ITRIP}}{R16} = \frac{0.525}{3 \cdot 10^3} = 175 \; \mu A$$

The gain required for the ITRIP input is therefore calculated to appease the summation of ITRIP (525 mV) and anticipated forward voltage of the 1N4148 diode (530 mV), resulting in a gain requirement of 7.03, as per Equation 6.

Equation 6 - ITRIP required gain calculation.

$$G_{ITRIP,min} = \frac{\left(V_{ITRIP} + V_{F,1N4148}\right)}{V_{sense}} = \frac{0.525 + 0.530}{0.15} = 7.03$$

A non-inverting op-amp will be constructed to achieve this gain. While the minimum gain calculated was 7.03, the gain selected for this op-amp design will be 8.5. This increased gain value allows the trip current to be closer to the maximum continuous operating current, reducing the likelihood of the motor operating in an overcurrent condition.

Microcontroller Current Feedback

The IGBT emitter current feedback is required for the microcontroller to execute the motor control algorithms effectively. This current is an alternating signal requiring detection over the selected ±50 A range. To ensure accurate monitoring, the ADC requires a centre-biased signal operating on an ADC range of 0 V - 3.3 V. Subsequently, a current of 0 A will produce a 1.65 V output, whereas the ±50 A range will produce outputs of 0 V and 3.3 V respectively. The ST Microelectronics AN5397 Application Note assisted with these op-amp circuit designs (2019, pp. 5-9).
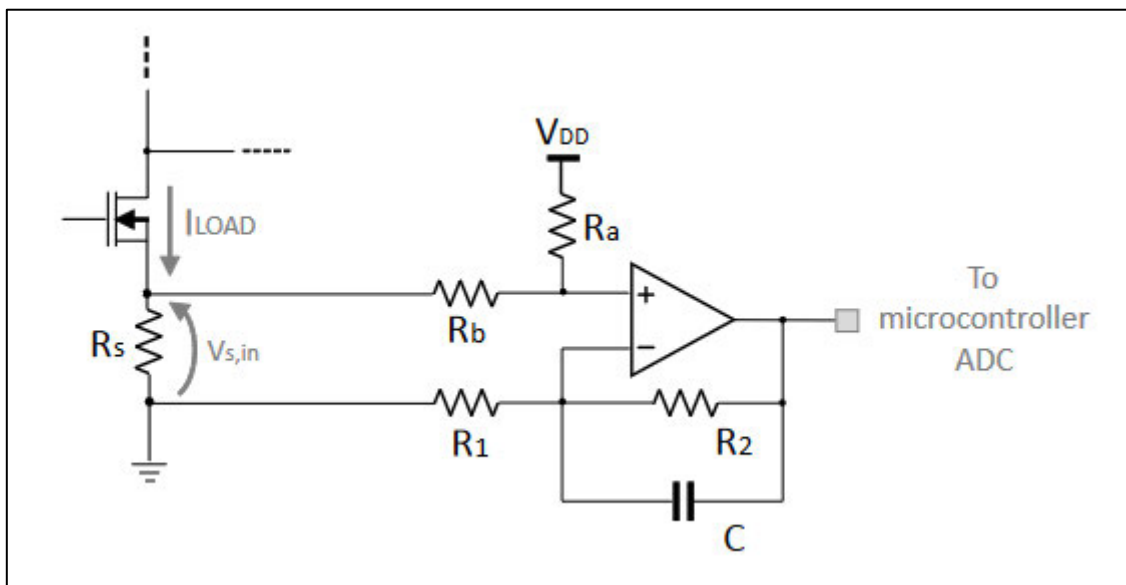

Figure 31 - Schematic of the amplification circuit (ST Microelectronics 2019, p.6).

The following equations will be utilised for the op-amp resistor selection in reference to the Figure 31 circuit design. Equation 7 identifies the maximum gain value permitted, while Equation 8 is utilised to determine suitable resistors for the op-amp circuit.

Equation 7 - Current sense op-amp gain selection (ST Microelectronics 2019, p.7).

$$G_{curr.sense,max} = \frac{V_{ADC}}{2 \cdot I_{max} \cdot R_s} = \frac{3.3}{2 \cdot 50.0 \cdot 0.003} = 11$$

While a maximum gain of 11 was calculated, a smaller gain was selected so the ADC would not saturate if the 50.0 A limit was reached; the selected gain will be 10.5.

$$(a) \ \frac{R_a}{R_b} = 2G, \qquad (b) \ \frac{R_2}{R_1} = G - 0.5, \qquad (c) \ \frac{R_b}{R_1} = 1 - \frac{0.5}{G}$$

The ST Microelectronics AN5397 Application Note recommended the selection of the TSV99x family of op-amps due to their low bias current inputs mitigating the impacts of slight resistor mismatches for Equation 8(c) (ST Microelectronics 2019, p. 9).

ii. Voltage divider circuit for monitoring the service voltage.

The prototype controller will be developed for the maximum service voltage of 300VDC available in the University of Southern Queensland's Energy Systems Lab. Therefore, the selection of resistors for this voltage divider circuit shall not supply an ADC voltage exceeding the input maximum of 3.3V when the 300V service voltage is applied.

For simplicity and to allow for some transient voltage during operation, an ADC maximum of 3V was utilised for this selection process. This resulted in a 600 kΩ voltage divider circuit being selected, with the ADC input coming from this circuit's first 6 kΩ resistor. Therefore, at 300V, a 3V ADC input is achieved.

iii. Voltage divider circuit for the temperature monitoring.

The V_{FO} pin on the IM535 module indicates a module fault in case of undervoltage at the V_{DD} pin or an ITRIP input has been received. The V_{FO} pin can also be monitored to determine the module's internal temperature via the embedded thermistor (ST Microelectronics 2019, p. 6, 13). Figure 32 features a circuit schematic of the V_{FO} pin and its associated internal circuits. While Figure 33 provides the embedded thermistor's thermal response curve. The controller programming will be explored to ensure suitable temperature monitoring and fault detection for the IM535 module is provided.
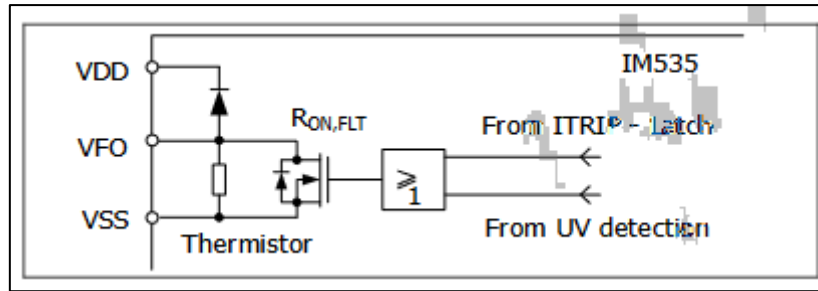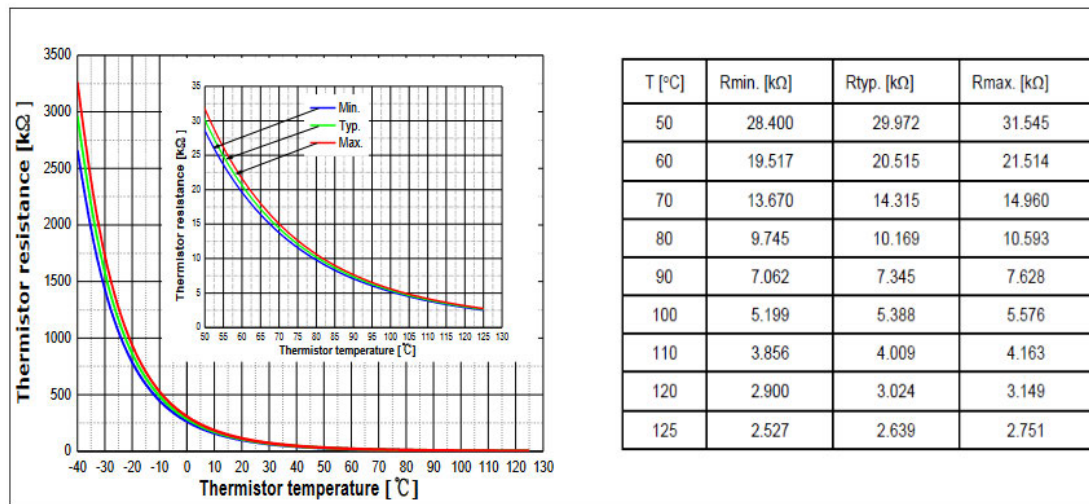
Figure 32 - IM535 internal circuit at pin VFO (ST Microelectronics 2019, p. 6).

Figure 33 - IM535 embedded thermistor resistance - temperature curve and table (ST Microelectronics 2019, p. 13).

iv. Integration of 10kΩ potentiometer for the speed reference.

The speed reference circuit supplies a microcontroller ADC input with the speed regulation reference value. This circuit will comprise of the controller 3.3 V power supply connected across a 10 kΩ potentiometer, with the wiper terminal of this potentiometer connected to the ADC.

Complementary Passive Components

All other supporting passive components were selected under the advisement of Infineon Application Note – AN2016-12 (Infineon Technologies 2016, p.3,11).

The PWM signals, characterised by square waves, inherently produce harmonics at every other frequency, namely the 3rd, 5th, 7th, 9th, and so on. Consequently, to mitigate any interference in the current monitoring, a low-pass filter is required to reduce the harmonic noise on the current sense signals. A first-order low-pass filter circuit will be implemented across the current sense resistors to attenuate the harmonic noise originating from the PWM output.

3.3.3. Produce PCB Design

A suitable PCB will be designed following the identification of all passive electronic components required. Through investigation on the internet and consultation with academic staff at the university, it was determined that the most suitable software to develop the PCB design would be KiCad EDA. Additionally, the PCB manufacturer JLCPCB.com was highly recommended; therefore, the PCB design will be manufactured through them once the design has been completed.

To assist with manual assembly, the component packages selected will primarily be a through-hole design for the passive components and a larger SMD or DIP package for the IC components.

3.3.4. Assemble Prototype PCB

Following the manufacturing of the PCB and the procurement of the electronic components, the manual assembly will be completed. Relevant safe operating practices and procedures will be followed during the PCB assembly. Testing and investigation will be undertaken to ensure no solder bridging or unsatisfactory soldering has occurred prior to the first operation.

3.4. Evaluate Performance

The prototype motor controller will be electrically connected to the EMRAX 228 for functional evaluation. The modified programming will be deployed from the Simulink model to the microcontroller. Power will be supplied to the motor controller through a 40V, current limited power supply. A 15V current limited power supply will be provided to the motor controller circuitry. The current limitation ability will be engaged to reduce the possibility of an overcurrent or short-circuit event causing significant damage to the equipment or motor controller. The microcontroller will be powered from a USB power pack to eliminate the connection to the programming laptop. Once motor function has commenced, the motor reference speed will be slowly increased to monitor and evaluate the motor and control algorithm response.

Chapter 4

4. Results and Discussion

4.1. Commission the EMRAX 228

Stage 1 – Winding Continuity

Consulting the 2018 EMRAX 228 technical data table (shown in Appendix B), the winding resistance is specified at 19 mΩ. All three winding resistances were measured using a FLUKE 115 multimeter during testing. The results are shown in Table 17 below:

Table 17 - EMRAX 228 winding resistance test results.

Test	Result
U phase to V phase	0.13Ω
U phase to W phase	0.13Ω
V phase to W phase	0.13Ω

While it would appear there is a discrepancy between the expected winding resistance of 19 mΩ and the measured values of 0.13Ω, such a discrepancy is expected and is acceptable in the context of a continuity test. The expected result was achieved; all measured values were a low value and presented as identical across all three tests.

During simulation and programming in the later stages of this project, the datasheet values were utilised for the winding resistance parameters required in the motor controller algorithms.

Stage 2 – Insulation Resistance

Insulation resistance testing was performed with a Kyoritsu 3132A Insulation Tester at a nominal test voltage of 1000VDC. The satisfactory test results are shown in Table 18 below.

Table 18 - EMRAX 228 insulation resistance test results at 1000VDC.

Test	Result
U phase to stator frame	>400 MΩ
V phase to stator frame	>400 MΩ
W phase to stator frame	>400 MΩ

Stage 3 – Mechanical Rotation

Modifications were made to the proprietary mounting bracket design prior to fabrication; these changes were necessary to suit the custom installation for this project. The final designs for the custom mounting bracket, the custom stand and the custom shaft were then supplied to the University of Southern Queensland Workshop (Toowoomba Campus) for fabrication. These components were all used to mount and then couple the EMRAX to the motor/ generator in the University of Southern Queensland's Energy Systems Lab. These designs are located in Appendix C. The mounting bracket and custom-fabricated output shaft (fitted with the required coupling) are shown in Figure 34.

With the motor adequately secured, the rotor section was spun manually to ensure no concerning noises or vibrations were experienced. This manual test produced acceptable results; the motor made some audible noise while rotating; however, no concerning vibrations or sounds were produced.
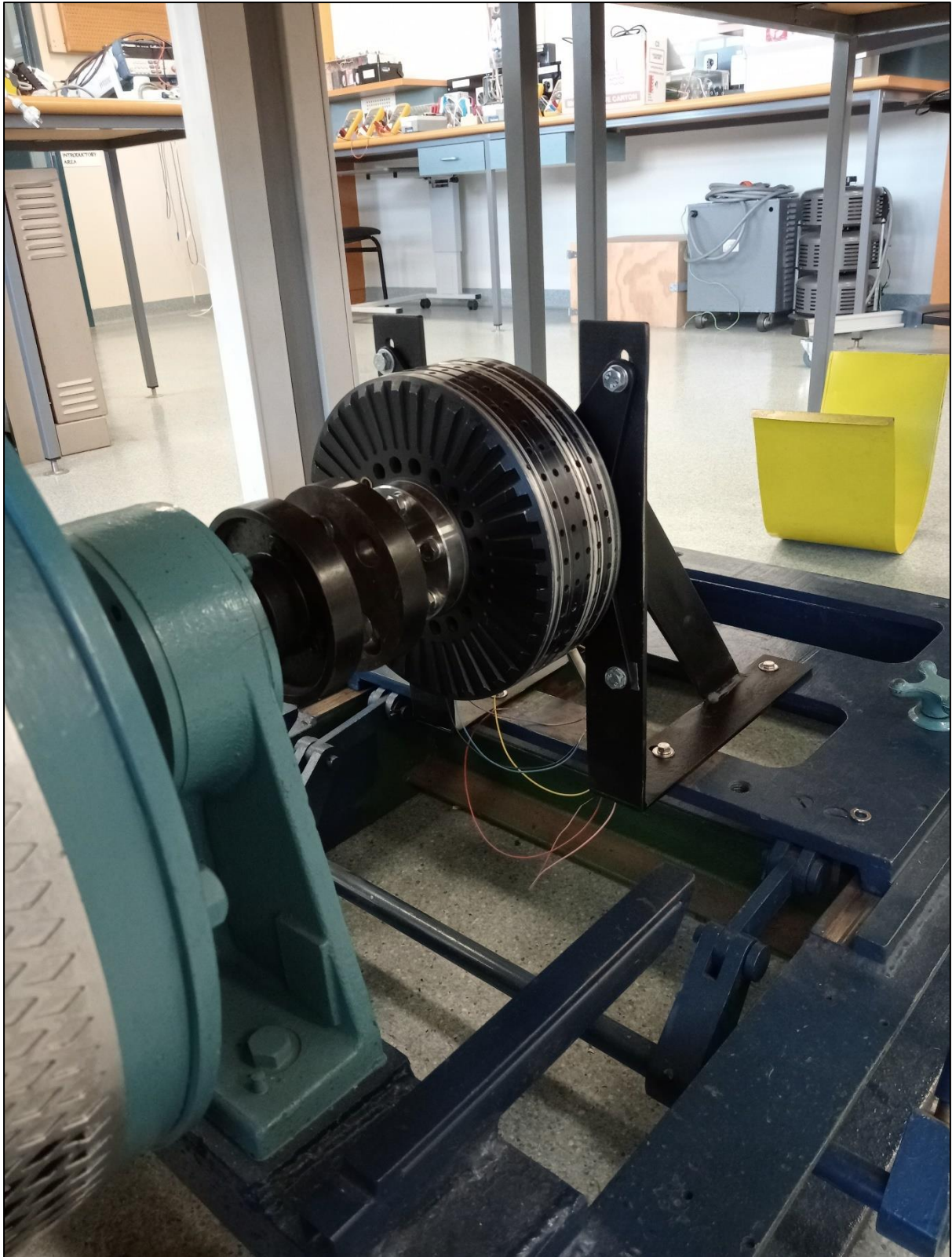
Figure 34 - Custom mounting frame securing the EMRAX motor in the Energy Systems Lab during testing.

Stage 4 – Back EMF Waveform Generation

The preliminary tests on the EMRAX 228 motor provided satisfactory results, so the motor was deemed suitable for the back EMF waveform generation examination.

The Energy Systems Lab 300VDC variable power supply and 230VDC machine were utilised for this stage; this machine can be configured to operate as either a generator or a motor. The DC machine was configured as a compound-wound DC motor for this testing. The shunt field winding was configured with the full rated voltage of 230VDC, while the armature and series field windings were connected in series with a variable supply to provide suitable speed control. The variable supply was achieved through the inclusion of a 50Ω potentiometer. The wiring connections employed are shown in Figure 35 and Figure 36.
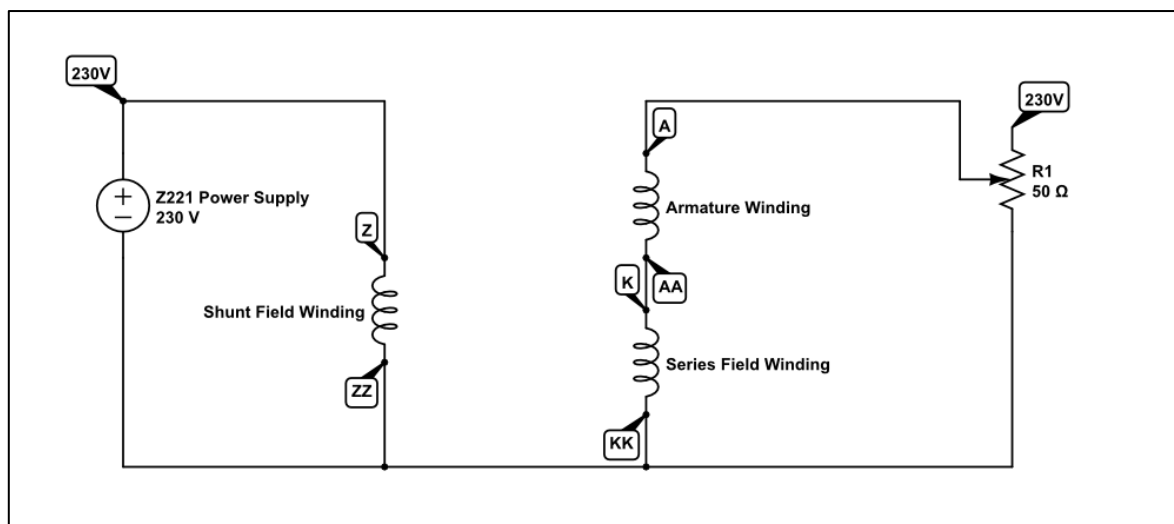

Figure 35 - The Energy Systems Lab DC motor schematic.

Figure 36 - The Energy Systems Lab DC motor connections.

The initial test resulted in a motor speed of 416 rpm and a peak-to-peak output from the EMRAX 228 of approximately 6V. The waveform generated is shown in Figure 37 ; the visible cogging is due to the interaction between the rotor's permanent magnets and the stator's slots. While the distortion from the cogging is visible in the generated waveforms, its appearance is consistently replicated across all three phases. Satisfactory results in waveform peaks, phase offsets, and shapes accompany it.

The EMRAX 228 was then driven at an increased speed to reduce the impact of the cogging and ensure no concerning factors could be identified at an increased rotational speed. This second test was performed at a rotational speed of 1224 rpm; the generated waveform is presented in Figure 38, showing a smoother waveform with the cogging content being a reduced percentage of the overall waveform. The waveforms generated have maintained an equal base shape, with equivalent phase offset and peaks, supporting the original findings that this motor's generated waveforms are satisfactory.

The satisfactory results from these waveform generation tests have confirmed that the EMRAX motor is serviceable.
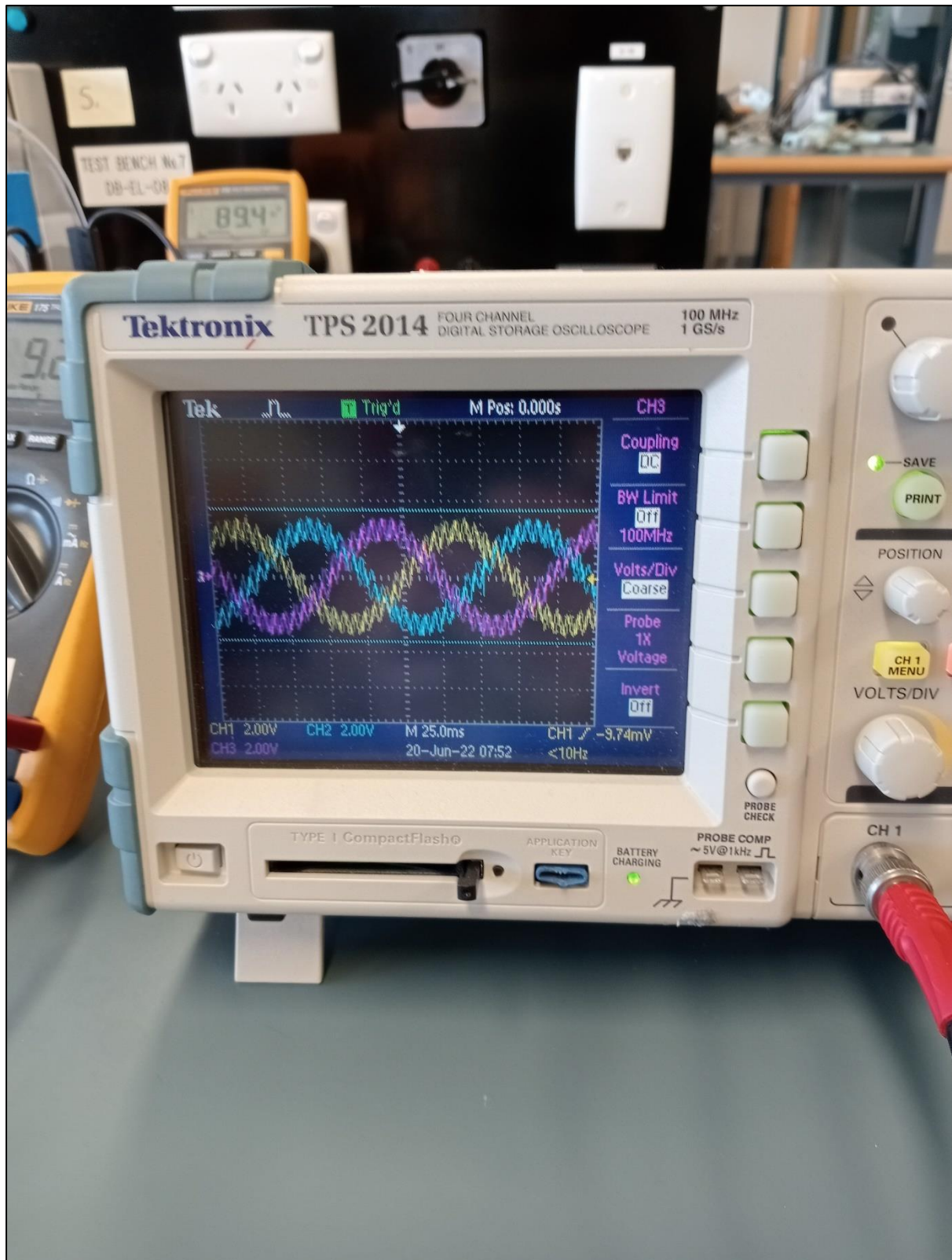
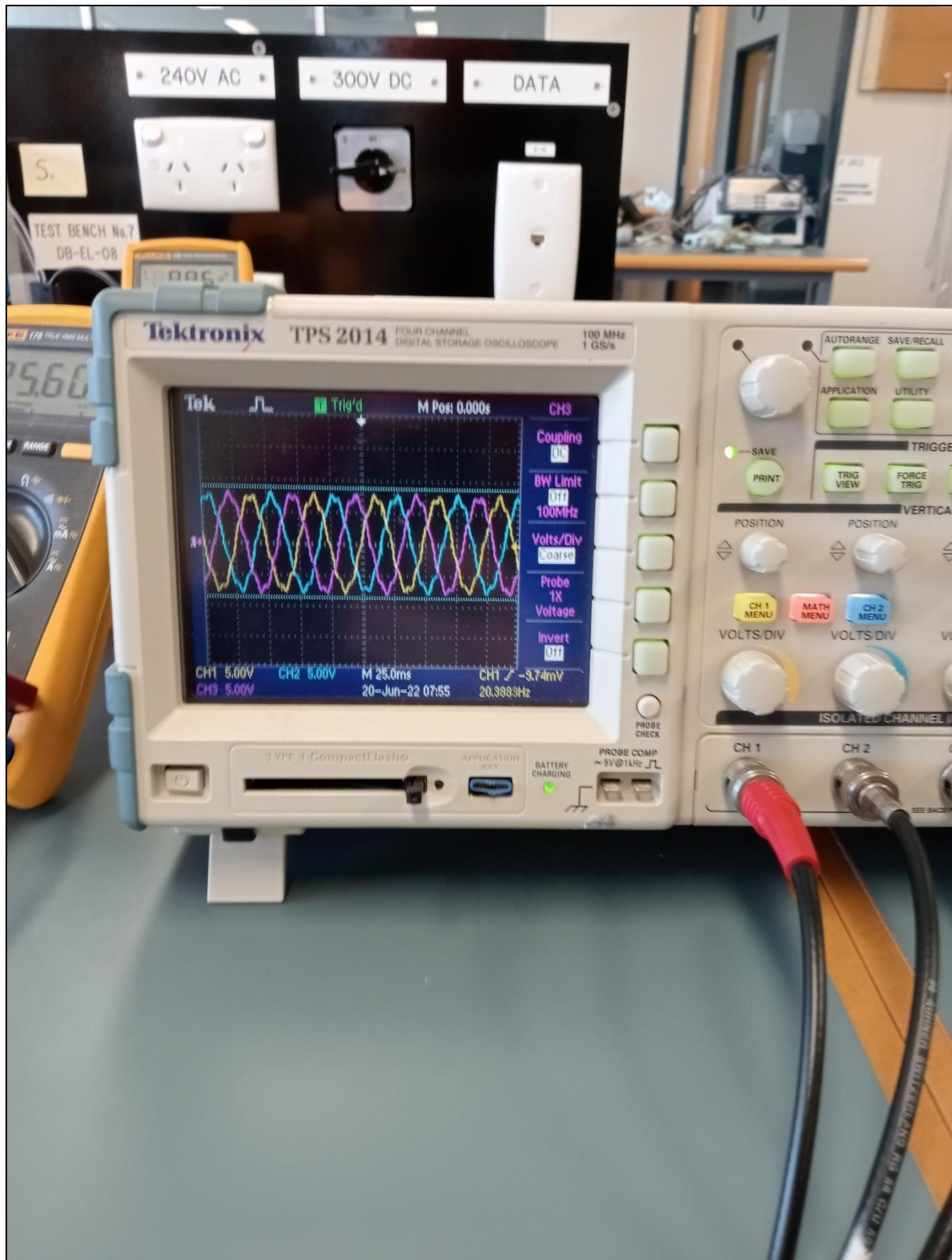*Figure 37 - Initial waveform generation of EMRAX 228 (416 rpm).*

Figure 38 - Second waveform generation of EMRAX 228 (1224 rpm).

Stage 5 – Resolver Testing

The resolver function was investigated next. Initial testing could not produce the expected functional results; following thorough investigation and fault finding, it was determined that the resolver rotor (centre section) was incompatible with the resolver stator. Figure 39 shows the mismatched resolver rotor and stator components. It was initially assumed that these pieces were merely offset from each other, resulting in a misalignment; however, further investigation proved they were, in fact, from two separate models and not compatible.
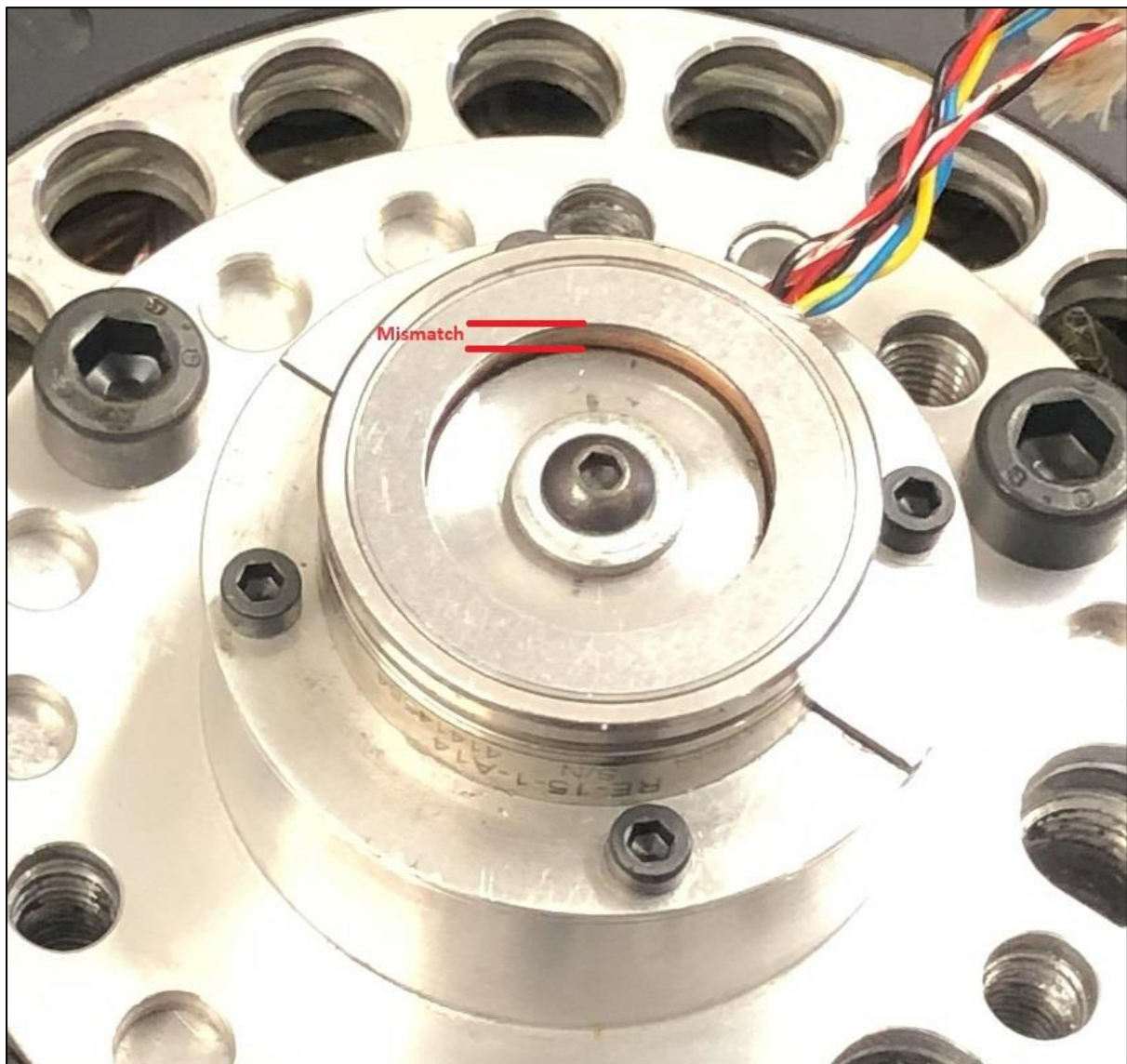
Figure 39 - Picture showing the mismatched resolver rotor and stator.

An equivalent model resolver to the original specified unit was identified and procured to replace them. This replacement model was a TE Connectivity 1-1414631-0; its datasheet is provided in Appendix B. This replacement resolver had comparable specifications to the original model, summarised in Table 19.

Table 19 - Comparison of Replacement Resolver.

Make	LTN Servotechnik GmbH	TE Connectivity
Model	RE-15-1-A14	1-1414631-0
Input Voltage (RMS)	7 V	7 V
Input Current	58 mA	40 mA
Input Frequency	10 kHz	10 kHz
Transformation Ratio	0.5 ± 10%	0.5 ± 5%
Maximum Rotational Speed	20,000 rpm	20,000 rpm
Phase Shift	-6° ± 3°	3° ± 5°

During the installation of the new resolver, misalignment issues were again encountered. With the assistance of a custom-designed 8.2mm 3D printed spacer, Figure 40, the resolver was successfully installed.
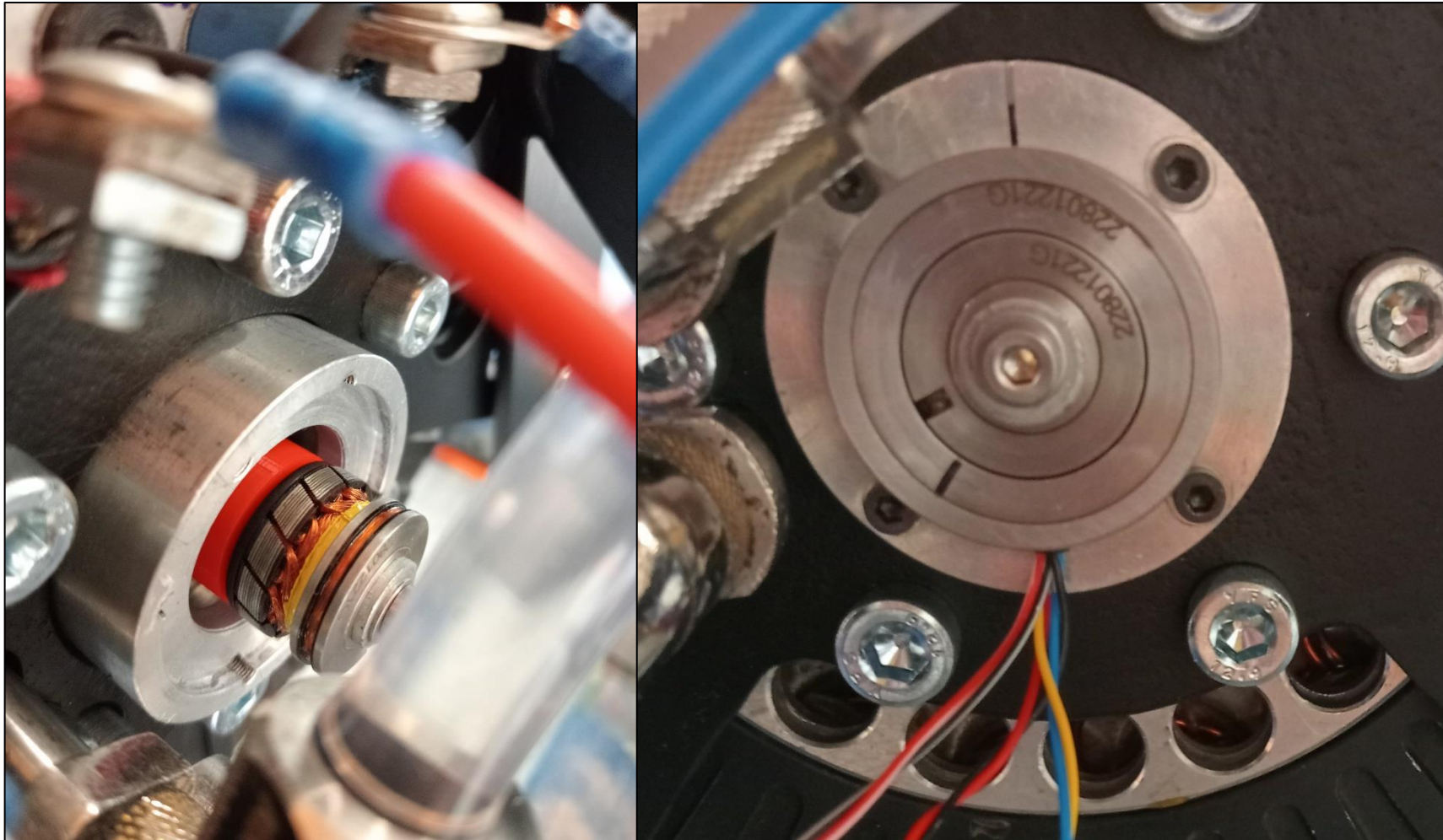
Figure 40 - New resolver fitted, sitting flush with assistance from the internal spacer.

Following the satisfactory fitment, performance testing was conducted on the resolver with a function generator and a two-channel oscilloscope. The resolver functioned as expected, producing two waveforms 90 degrees phase shifted from each other and alternating proportionally to the rotor's position.

Figure 42 shows the resolver's output waveforms with the rotor at a position of $\theta = 30°$. These waveforms are both presenting as expected; the red signal is the Cosine output (E_{S1-S3}), while the blue signal is the Sine output (E_{S2-S4}). To numerically confirm that these outputs are correct, Equation 1 and Equation 2 will be employed.

Equation 9 - Resolver signal ratio. Equation 1/Equation 2

$$\frac{E_{S1-S3}}{E_{S2-S4}} = \frac{\cos\theta}{\sin\theta}$$

Where:

E_{S1-S3} = 4.0 V_{peak}

$$E_{S2-S4} = E_{S1-S3} \cdot \frac{\sin\theta}{\cos\theta} = 4.0 \cdot \frac{\sin(30)}{\cos(30)}$$

$$\therefore E_{S2-S4} = 2.31 \text{ V}_{peak}$$

The calculated result of 2.31 V for the Sine output is consistent with the peak values displayed in Figure 41. Figure 41 is a cropped section of Figure 42, highlighting the peak amplitudes of both the Sine and Cosine resolver outputs.
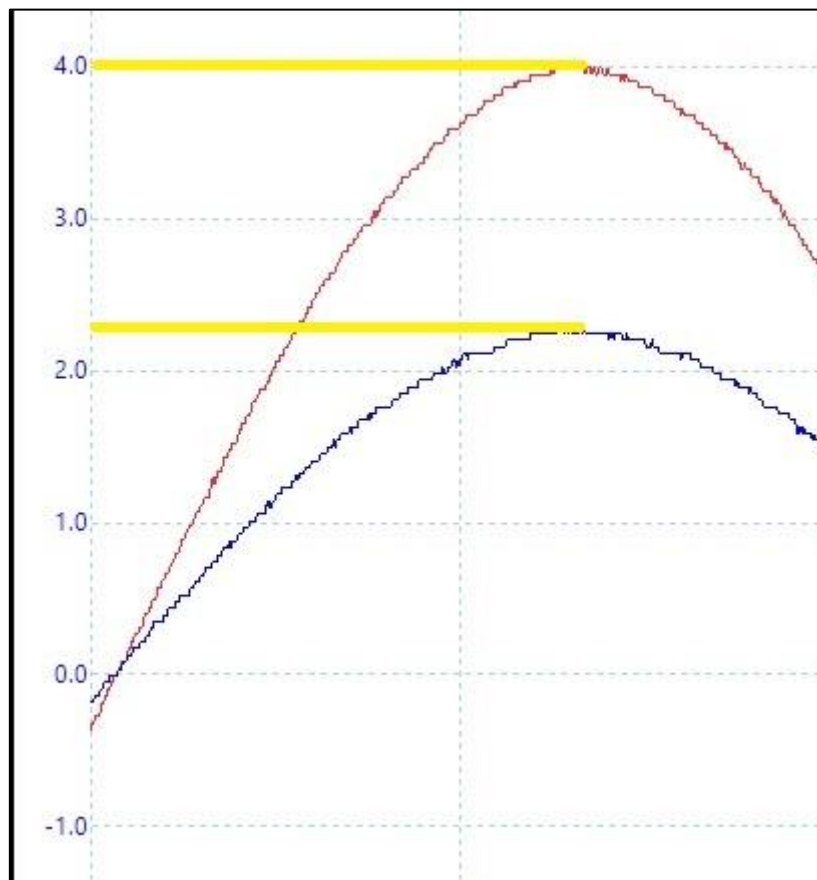
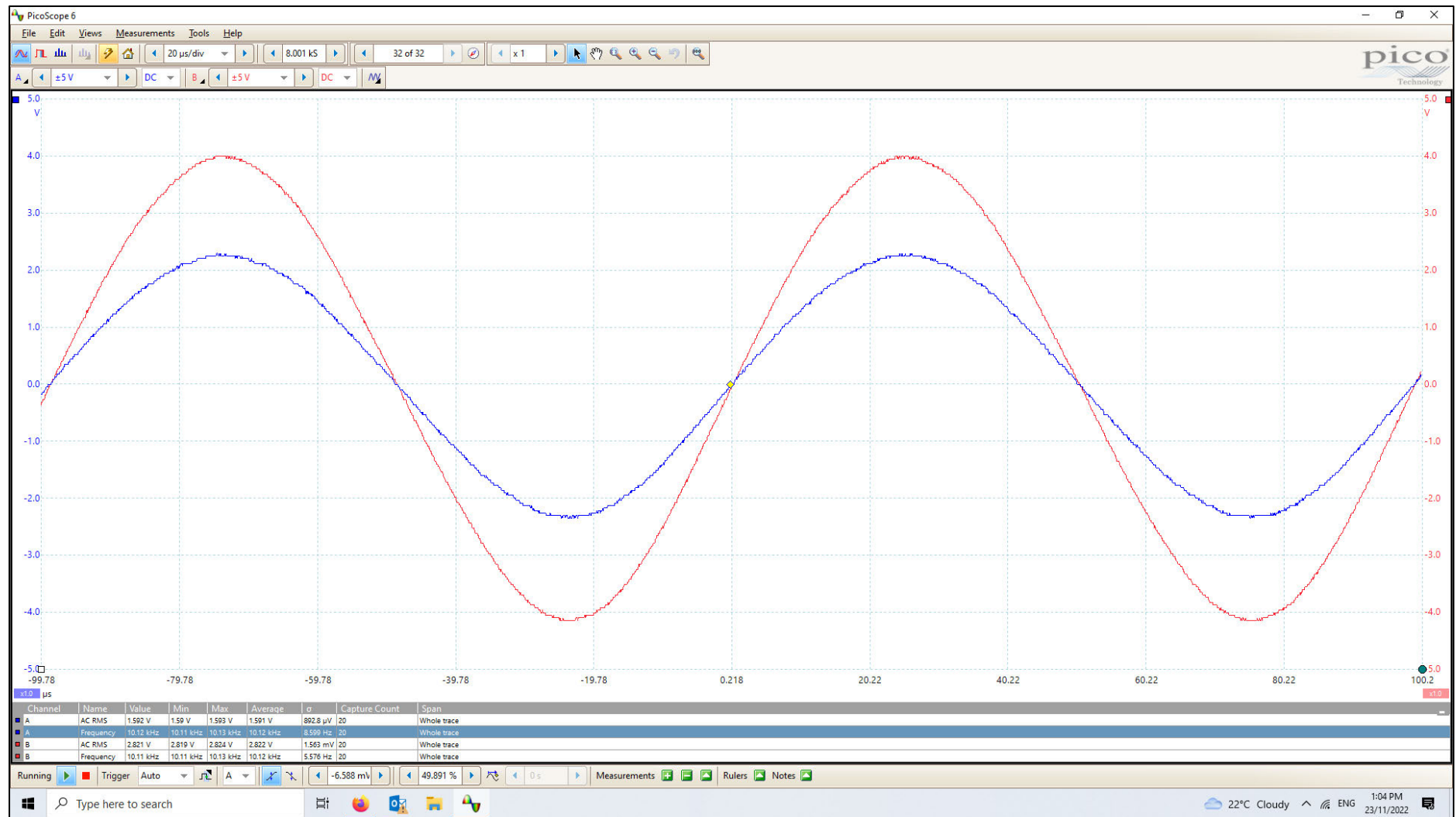*Figure 41 - Cropped section of Sine and Cosine output of Resolver at a 30° rotor position.*

Figure 42 - Sine and Cosine outputs from the EMRAX resolver at a 30° rotor position.

Stage 6.1 – Confirm Motor Function: Prohelion WaveSculptor200

The motor was now ready for function testing. The USQ Racing team's WaveSculptor200 was engaged for this test.

Following a review of the Prohelion user manuals for the WaveSculptor200, the block diagram featured in Figure 43 was developed. The specific Prohelion manuals reviewed were:

- WaveSculptor200 User Manual (Prohelion 2021a)
- WaveSculptor200 Configuration Software User Manual (Prohelion 2021b)
- EV Driver Controls User Manual (Prohelion 2021c)
- CAN-Ethernet Bridge User Manual (Prohelion 2021d)
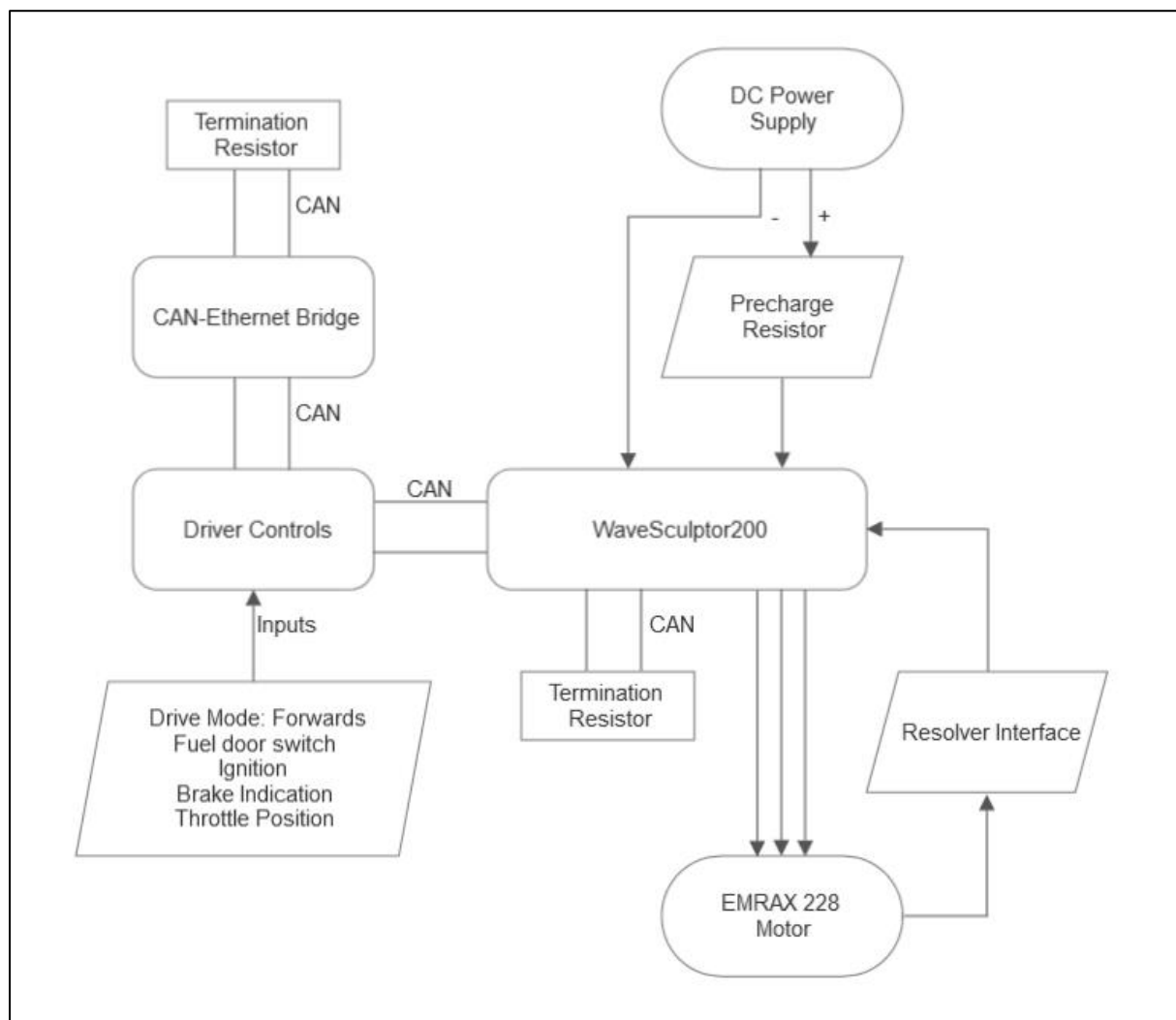- WaveSculptor Motor Interface – Type 3 (Prohelion 2021e)

Figure 43 - Block Diagram of WaveSculptor200 electrical connections.

The materials used for the construction, as advised by the previously mentioned user's manuals are summarised in the table below.

Table 20 - Materials used during EMRAX 228 function test with WaveSculptor200.

| Item	Design
DC Power Supply	60V, to satisfy parameter extraction algorithm recommendations.
Precharge Resistor	50Ω, 4.5A Resistor. Supply is 60V, therefore this arrangement reduced the maximum inrush current to 1.2A.
Termination Resistor	1/8W 120Ω Resistors.
CAN Cable	LAPP KABEL – DeviceNet [2170345], screened two pair.
Driver control inputs	10kΩ potentiometer for throttle; hardwired drive mode, fuel door switch, ignition ON and no brake indication present.
Resolver interface	Type 3 to match resolver used, as recommended by Prohelion.
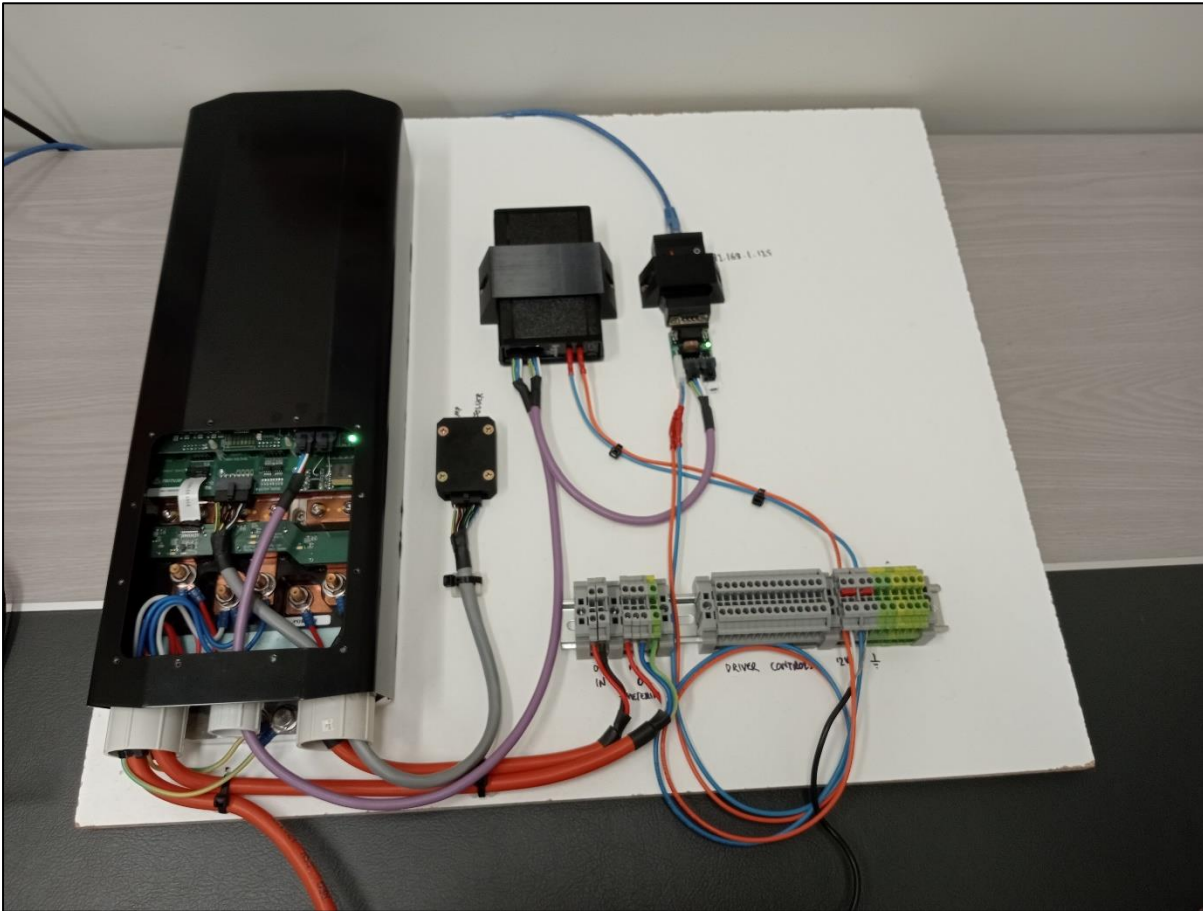
Figure 44 - WaveSculptor200 physical connections.

With the electrical design established, the water-cooling circuit was constructed (Figure 45). As recommended in the WaveScupltor200 User Manual (Prohelion 2021a, p.25), the cooling circuit was constructed using Koolance equipment, and the following equipment presented in Table 21 was utilised.

Table 21 - Cooling Circuit - Koolance Equipment List.

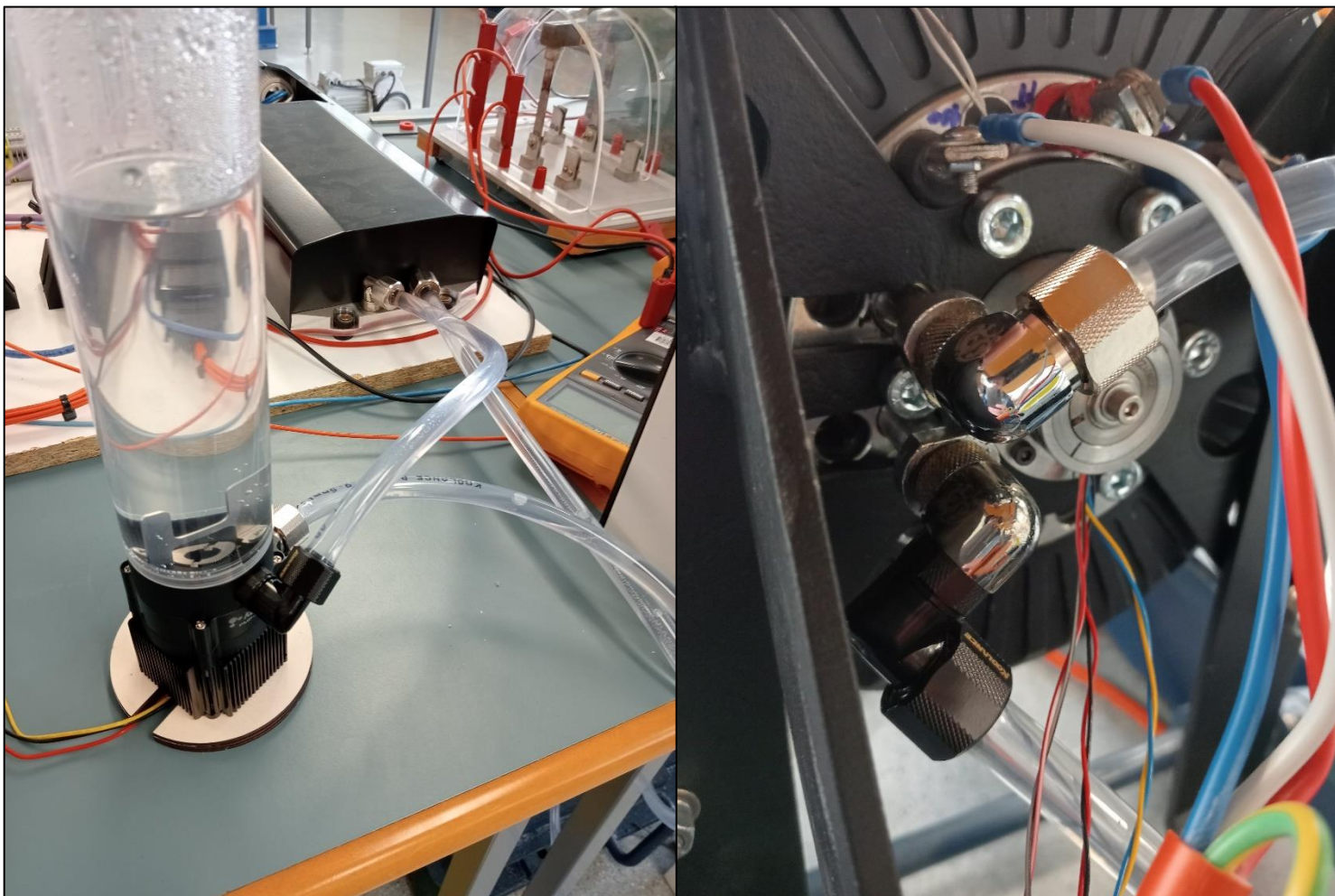| Item	Part Number
Pump	PMP-500
Pump Reservoir Base	CNT-PMP500T
Reservoir Body	BDY-TK200
Reservoir Top	COV-TKTOP
Tubing – 10mm x 13mm	HOS-10CL-15M
Straight Compression Fittings	FIT-V10X13-BK
Elbow Compression Fittings	FIT-L10X13-BK

Figure 45 - WaveSculptor/EMRAX cooling circuit.

With the physical system built, extensive work was undertaken to commission the controller and operate the motor. Communications were established over the CANBUS network; initial programming was performed through Prohelion's proprietary Profinity software. Following this, the WaveSculptor Config software was engaged. It was during the process of using the PhasorSense configuration tool that difficulties were encountered.

Figure 46 displays the failed result during the Phase Acquire process of the PhasorSense configuration tool. The fault indication is shown by the two circle components in Figure 46 ;* 1 – highlights the "Failed" banner, whereas *2 – identifies the section where the third Hall input should be displayed. During the debugging of this fault, it was identified that the Type 3 Resolver Interface was unserviceable; Prohelion later confirmed this, and the interface component was replaced.
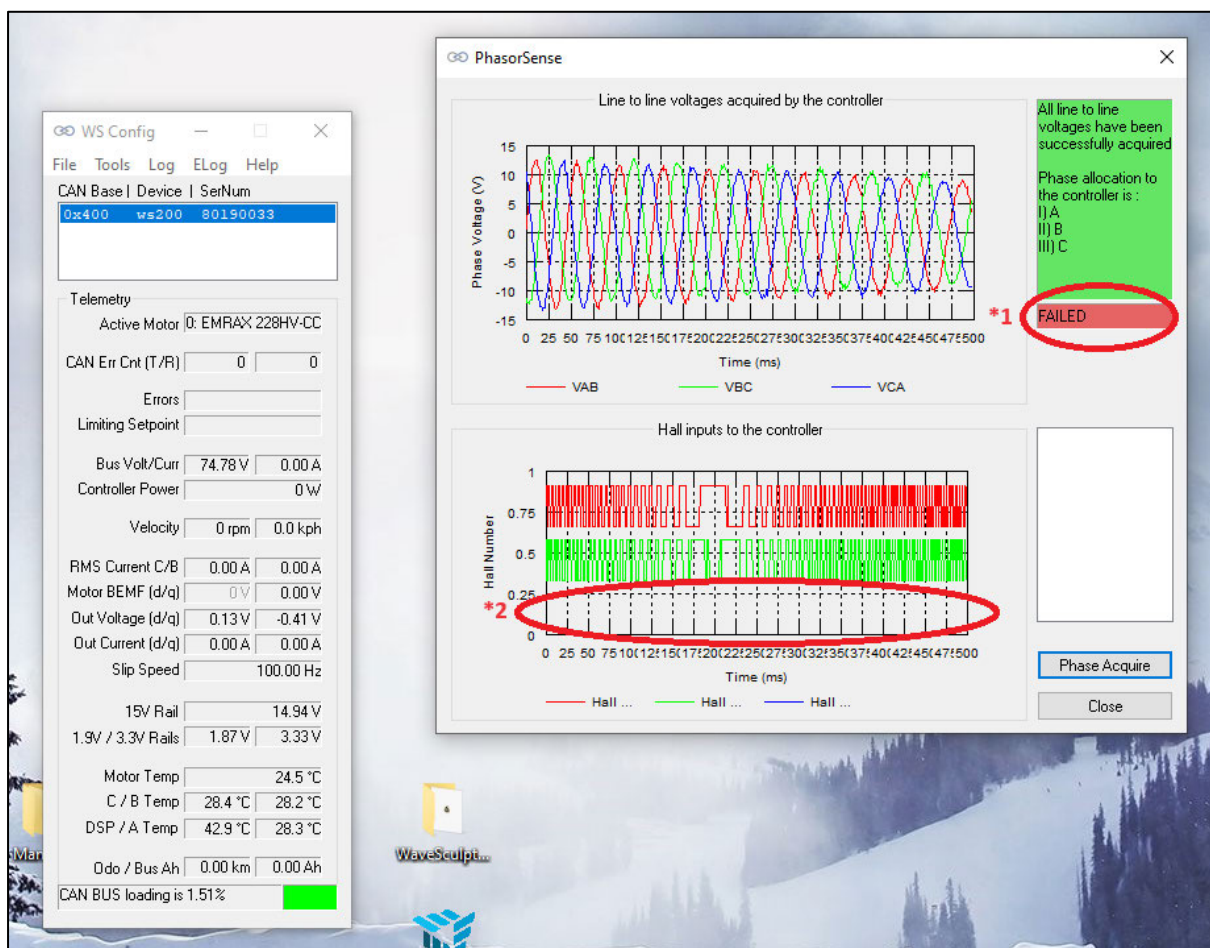

Figure 46 - Screenshot following unsuccessful Phase Acquire.

With the WaveSculptor200 unable to immediately operate the motor, alternate options were investigated. During this process, it was identified that an Odrive Robotics controller was readily available. The utilisation of this controller is discussed in the following section.

Stage 6.2 – Confirm Motor Function: Odrive v3.6 Controller

The Odrive Robotics controller provided by Dr Craig Lobsey was an Odrive v3.6. This controller (Figure 47) was a 56V version that could be readily programmed with Python 3. The additional appeal of this controller was its ability to operate a motor without a physical position feedback sensor, operating entirely with sensorless algorithms and not requiring any resolver interface hardware.
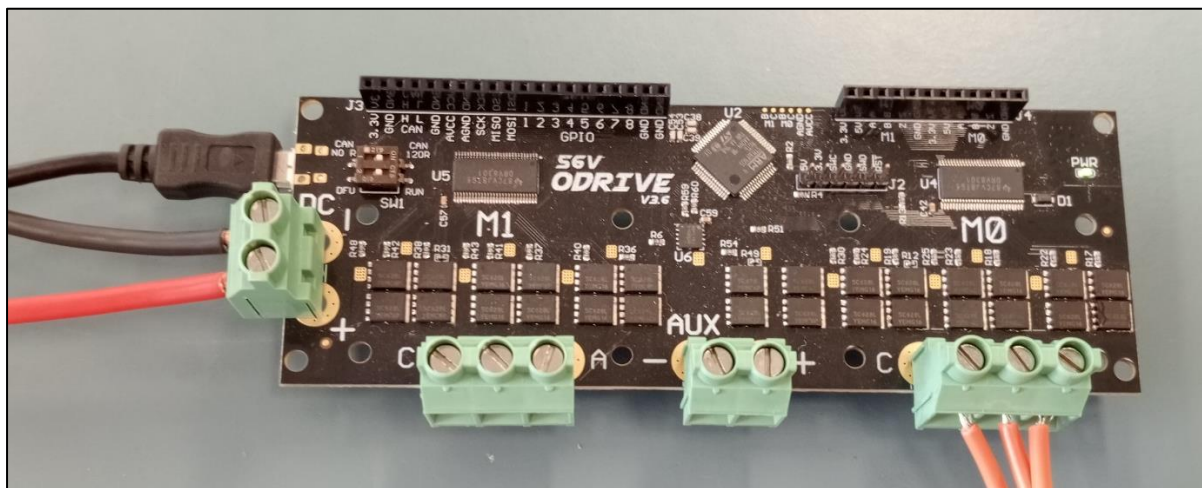

Figure 47 - Odrive v3.6 controller used to operate EMRAX 228 Motor.

This controller was provided with a 36V supply and programmed as per the Odrive documentation provided online (Odrive Robotics 2023b). The block diagram of Figure 48 highlights the simplicity of this controller setup, allowing for rapid functional testing.
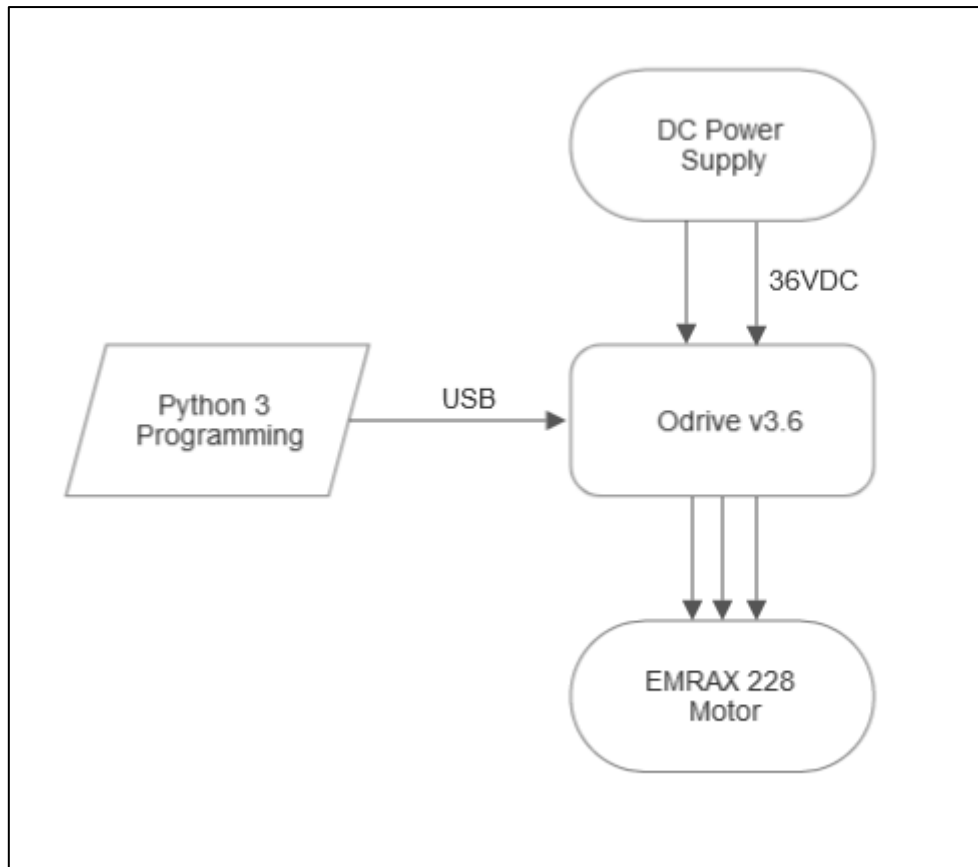
Figure 48 - Block Diagram of Odrive v3.6 electrical connections.

The programming used for this functional testing is provided in Appendix D. Let it be noted that the programming of this controller was not optimised and that during operation, the controller would fault partway through the acceleration of the motor. While this programming issue would need further investigation if the Odrive controller were to be used as the primary controller for this motor, the fault was deemed negligible as the principal focus was to confirm the motor's function and ability to be controlled by the electrical source.

The successful operation of the USQ Racing team's EMRAX 228 with the Odrive v3.6 controller, as evident in Figure 49 , resulted in the achievement of the first project aim. Additionally, the simplicity of the Odrive controller highlighted the appeal of maintaining a user-friendly interface to improve the likelihood of successful functionality for end users.
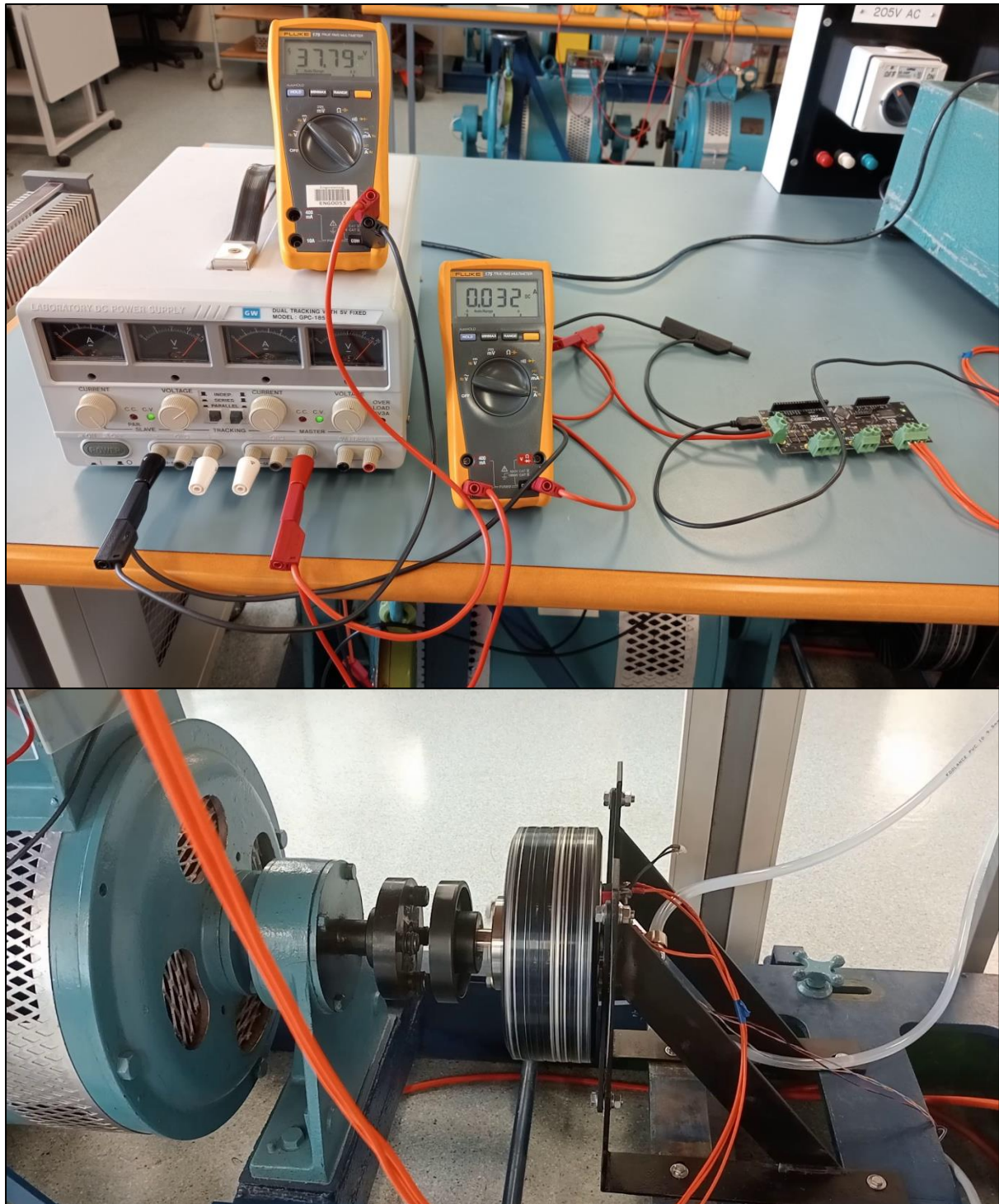
Figure 49 - EMRAX 228 motor under operation from Odrive v3.6 controller.

4.2. Motor Controller Packaging and Cooling

4.2.1. Cooling System Thermal Model

This analysis produced the Figure 50 plot and predicted the cooling system performance (coolant flow rate, pressure drop and cooling plate thermal resistance) displayed in Table 22. The manufacturer's specified cooling plate thermal resistance response is shown in Figure 23.

The MATLAB script used to produce Figure 50 and the results in Table 22 is located in Appendix E.
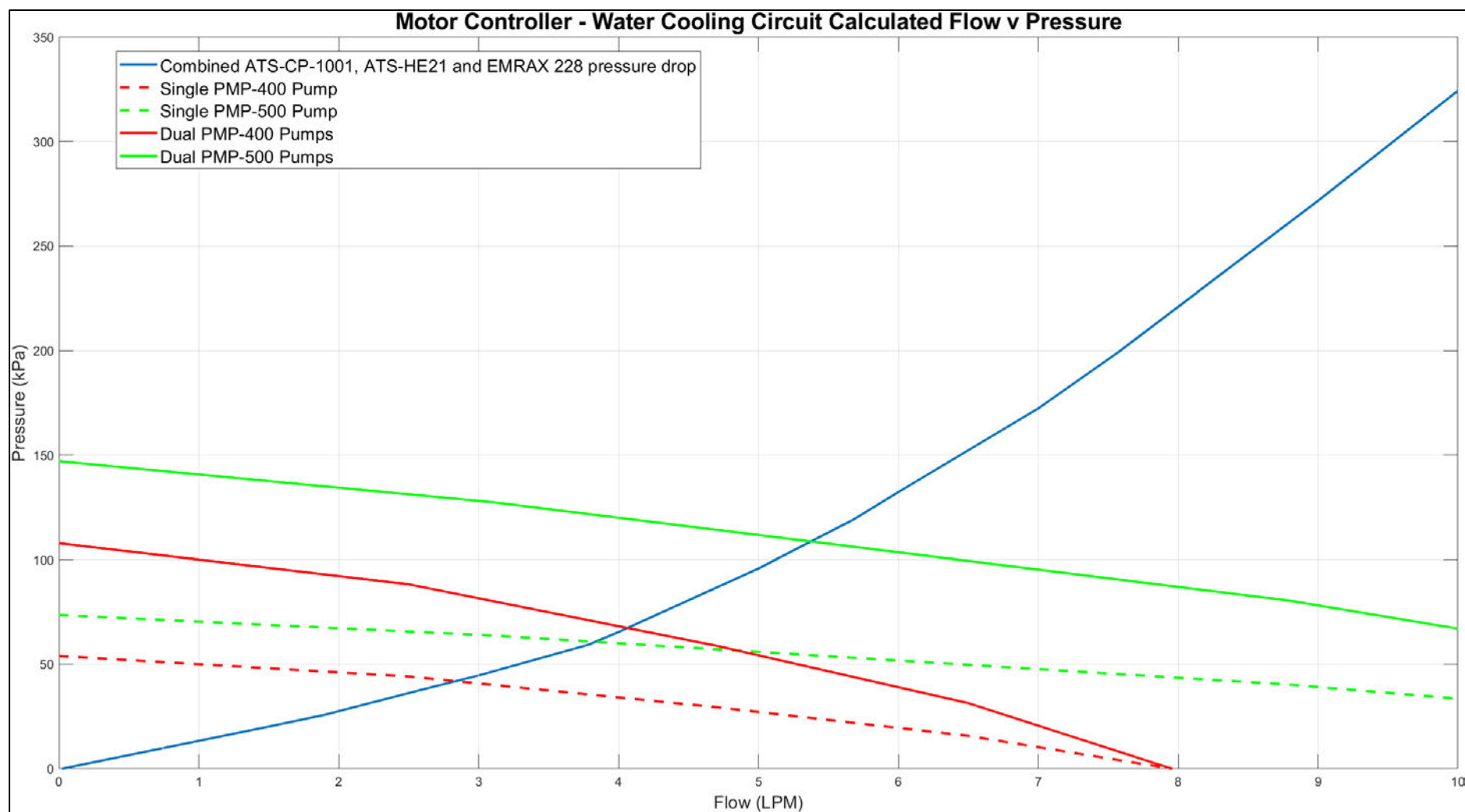
Figure 50 - Motor controller - water cooling circuit calculated performance (flow rate vs pressure drop).

Table 22 - Cooling system calculated performance (flow rate, pressure drop and cooling plate thermal resistance) results.

Pump Configuration	System Flow Rate (lpm)	System Pressure Drop (kPa)	Cooling Plate Thermal Resistance (°C/W)
Single Koolance PMP-400	2.84 lpm (0.75 GPM)	41.88 kPa (6.07 PSI)	0.0061 (°C/W)
Single Koolance PMP-500	3.83 lpm (1.01 GPM)	60.71 kPa (8.81 PSI)	0.0053 (°C/W)
Dual Koolance PMP-400	4.06 lpm (1.07 GPM)	67.35 kPa (9.77 PSI)	0.0053 (°C/W)
Dual Koolance PMP-500	5.38 lpm (1.42 GPM)	108.70 kPa (15.77 PSI)	0.0050 (°C/W)

Table 22 displays the system flow rates, pressure drop and correlated cooling plate thermal resistances for the four pump configurations investigated. While the changes in thermal resistance are negligible, specifically between the single PMP-400, dual PMP-400 and dual PMP-500 results, significant variations are identified in the cooling system flow rates. These differences in flow rate are particularly relevant to the cooling of the EMRAX 228, specifically the requirement of a flow rate of 6 to 8 litres per minute during operation (EMRAX d.o.o. 2018, p.42).

From a review of the results in Table 22, it is proposed to engage a dual Koolance PMP-500 water pump configuration in the motor controller cooling circuit. It is acknowledged that the calculated flow does not meet the specified 6 to 8 litre per-minute requirements of the datasheet for the EMRAX 228. However, it is anticipated that the motor will not be uninterruptedly functioning at the full continuous power rating and is therefore assumed to operate within its safe thermal limits with the dual PMP-500 configuration. Further research and testing would be required to confirm these assumptions. Characterising an aluminium radiator would also assist with the final selection of a heat exchanger. A review of the Koolance PMP-500 specifications also identified that the wet-end components for this pump are non-conductive, therefore assisting with the design specifications of eliminating the potential of galvanic corrosion (Koolance 2023).

The MATLAB script in Appendix E was configured to interpolate the ATS-HE23 heat exchange's thermal resistance at the calculated flow rate of 1.42 GPM. This interpolation resulted in an anticipated thermal resistance of 0.0090 °C/W (a thermal conductance of 111.1 W/°C), verified against the Advanced Thermal Solutions - Heat exchange thermal conductance chart in Figure 24.

With the cooling system defined, the known system data was entered into the Infineon Power Simulation program – IPOSIM (https://iposim.infineon.com/application/en/). This simulation program provided the IGBT modules' expected operational losses and junction temperature rise during operation.

Table 23 identifies all data provided to the simulation program.

Table 23 - Infineon Power Simulation program (IPOSIM) input data.

Parameter	Data	Justification
Topology	DC/AC Applications - Three Phase - 2 Level (Module)	Three-legged H-Bridge configuration for three phase motor application.
Device	FF225R12ME4P_B11	As selected
Modulation Algorithm	SVPWM	Space Vector PWM, as utilised by STM microcontroller algorithms.
DC Link Voltage (Vdc)	600 V	The maximum service voltage the motor controller is designed for.
Output Current (Iout)	115 A RMS	The continuous operating current of the EMRAX 228 (EMRAX d.o.o. 2018, p.15).
Output Frequency	460 Hz	The EMRAX 228 motor's maximum rotational speed is 5500 rpm and the motor contains 10 pole pairs (P). Therefore: $$f = \frac{RPM \cdot P}{120} = \frac{5500 \cdot 10}{120}$$ $$\therefore f = 458.33 \approx 460 \text{ Hz}$$
Switching Frequency	20 000 Hz	Switching frequency of 20 000 Hz, as utilised by STM microcontroller algorithms.
Modulation Index	1	Modulation index of 1, as utilised by system design.
Power Factor cos(φ)	0.95	Assumed power factor for EMRAX 228.
Load Type	Inductive Load (Lagging)	A motor is an inductive load.
Cooling Method	Liquid Cooling	Intended cooling system is liquid.
Heatsink	Good	It is assumed due to using quality components that the heatsink would be deemed "Good" for the purpose of this simulation.
T_{in}	50°C	Maximum ambient temperature expected to be experienced on a summer day.
$R_{th,h}$	0.0050 K/W	As identified in the calculated system values, Table 22 (dual PMP-500 configuration).
$\tau_{th,h}$	30s	This was a prefilled variable that is assumed to be appropriate.
Switch Q1: R_{Gon}	1.6 Ω	Recommended values for the FF225R12ME4P IGBTs, as per the Power Integrations 2SP0115T2A0-12 datasheet (Power Integrations 2019, p.6).
Switch Q1: R_{Goff}	2.4 Ω	

The IPOSIM simulation for the selected IGBTs resulted in the steady state power losses of the three-legged H-bridge and individual junction temperatures of each IGBT module, as displayed in Figure 51.

Maximum Junction Temperature	
Switch	97.05 °C
Diode	75.61 °C
Switching Losses	
Switch	170.61 W
Diode	103.48 W
Conduction Losses	
Switch	69.24 W
Diode	7.72 W
Total Losses	
Switch	239.85 W
Diode	111.19 W

Figure 51 - Results produced from Infineon Power Simulation [IPOSIM] program.

The thermal resistances referenced in the simplified thermal schematic of Figure 25 are defined in Table 24.

Table 24 - Simplified schematic thermal resistance values.

Thermal Resistance	Description	Value (K/W)	Source
$R_{thJH,IGBT}$	IGBT junction to heatsink	0.175	(Infineon Technologies 2017, p.2)
$R_{thJH,Diode}$	Diode junction to heatsink	0.197	(Infineon Technologies 2017, p.3)
R_{thCP}	Cooling plate	0.005	Table 22 – Dual PMP-500 pumps
R_{thHE}	Heat exchanger	0.0090	Interpolation of Figure 24

The MATLAB script created for calculating the steady-state temperatures is featured in Appendix F ; it has been developed to estimate the steady-state temperatures at all reference points in the cooling system during the EMRAX 228 motor's maximum continuous operation of 115A RMS. The FF225R12ME4P module has a maximum junction point temperature limit of 150°C for both the IGBT and embedded diode; therefore, these calculations will assist with confirming that these temperatures will not be exceeded during operation (Infineon Technologies 2017, pp.1-3).

The losses calculated by the Infineon IPOSIM simulation have been propagated through the simplified thermal system for the motor controller; the results are displayed in Figure 52. These results support the IPOSIM simulated maximum junction temperatures and confirm that the system is not expected to exceed the IGBT modules' maximum junction temperatures, confirming the feasibility of all selected components.

However, these calculations have not allowed for the additional heat losses from the EMRAX 228. Further investigation is required to quantify the impact this would have on the cooling system's steady-state temperatures.
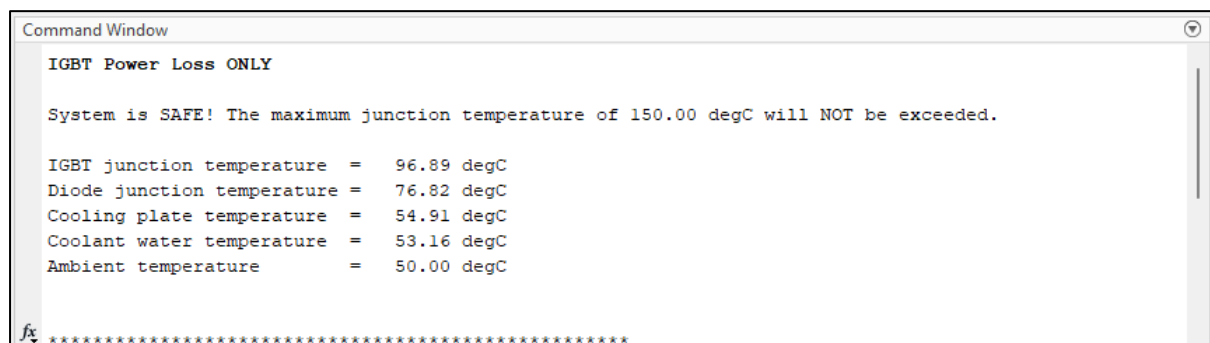

Figure 52 - Steady state temperatures calculated from IGBT losses in MATLAB script.

The results shown in Figure 52 identify some thermal redundancy in the system. Based purely on the simulated IGBT losses, the IGBT junction temperature has a redundancy of 53.11°C before the critical junction temperature of 150°C is reached. While this value does not directly translate to the allowable losses by the EMRAX 228, it does provide confidence that the system would accommodate the additional heat losses.

To quantify the expected losses from the EMRAX 228, contact was made with the EMRAX sales and technical support team in regard to obtaining thermal response data. It had been previously identified that this information was not readily available on the EMARX website or user manual. The response from the EMRAX team is in the email snippet of Figure 53 ; while defined values were not provided, an estimate of heat dissipation to the liquid cooling system was supplied. This data was utilised to assess the effect of this additional heat on the steady-state temperatures.

Cooling explained:
Liquid cooled motor
Stator of the motor is cooled with liquid. Around 2/3 of heat dissipates through liquid. Rotor with the magnets also generates some heat therefore about 1/3 of the heat should be dissipated through rotor to achieve required performance. Rotor and Stator are sealed and achieve IP66.
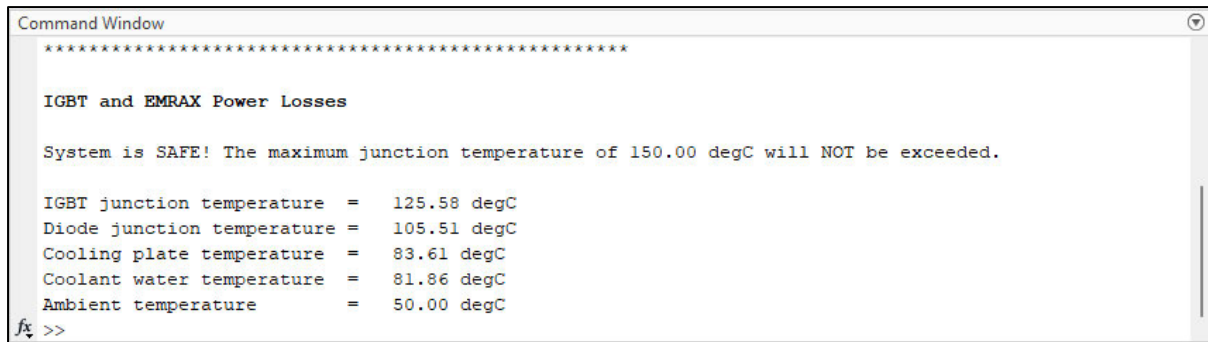**Air cooled motor**
Air coled motor is only appropriate for vehicles where cold ambient air (<20°C) with high air speed (>20 m/s) can be induced to cool the stator and the rotor. There are holes made through the rotor and stator through which air circulates and cools down the motor. Consecuently motor achieves IP21.
Combined cooled motor
Is a combination of both motors. Where stator is liquid cooled but in this case rotor is not sealed and alows ambient air to aditionaly cool down the stator and rotor hence the beter continuous performance. But if you are not able to induce high speed cold air cooling than diference between CC and LC would be minimal.

Figure 53 - Snippet of cooling information received from EMRAX via email (source: EMRAX).

Calculations were performed assuming the EMRAX 228 was operating at the maximum continuous motor power of 55kW while operating at the lowest recorded efficiency of 92%, as specified in the EMRAX 228 Technical Data Table (EMRAX d.o.o. 2018, p.15). Figure 54 features the results of this analysis. The associated MATLAB script is located in Appendix F.

Figure 54 - Steady state temperatures calculated from IGBT and EMRAX losses in MATLAB script.

The results presented in Figure 54 provide further confidence that the selected cooling system components are suitable for supporting the motor controller development. Both the IGBT and diode junction temperatures are noted as remaining below the 150°C maximum. While the investigation only identified thermal resistance values and the resultant steady-state temperatures, the thermal capacitance and thermal time constants were not analysed. The thermal capacitance data was not readily available and was not deemed critical at this stage of investigation.

It is expected that the EMRAX 228 motor, at a nominal 12.3kg, possesses a reasonable thermal capacitance, thereby mitigating the impacts of short-term transient thermal loads, specifically, those expected during rapid acceleration periods (EMRAX d.o.o. 2018, p.15). However, due to the constraints identified in the thermal analysis, the omissions of the pressure losses in the tubing and the exclusion of a cooling fan, further research and investigation would be required to characterise the complete cooling system more accurately.

4.2.2. The Cooling System Package Components Selected

The cooling plate size primarily dictates the anticipated package size. As shown in Figure 55, the controller footprint will be a compact 198mm x 147mm. With the addition of the IGBTs and driver boards, the controller is anticipated to be 65.1mm high; this measurement was determined with the assistance of the 3D model produced for Figure 57.
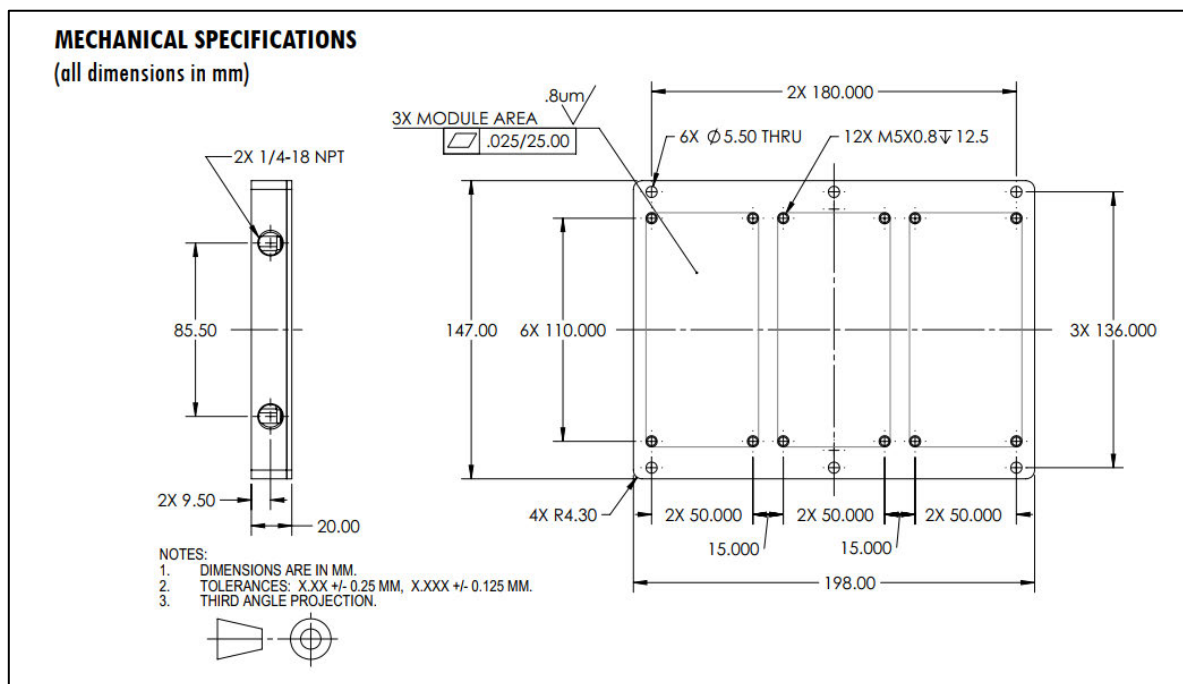

Figure 55 - Advanced Thermal Solutions cooling plate [ATS-CP-1001] dimensions (Advanced Thermal Solutions n.d.a).

The final motor controller package is proposed to comprise the following:

- 3x Infineon FF225R12ME4P IGBT modules.
- 3x Power Integrations 2SP0115T2A0-12 driver boards.
- 1x Advanced Thermal Solutions Cooling Plate ATS-CP-1001.
- 2x Koolance PMP-500 Water Pumps.
- 1x Heat Exchanger. The Advanced Thermal Solutions ATS-HE23 was utilised for simulation; however, an entire aluminium design with comparable thermal and hydraulic performance is recommended to eliminate the possibility of galvanic corrosion.

A simplified system flow chart is featured in Figure 56, while a rendered model of the controller is shown in Figure 57.
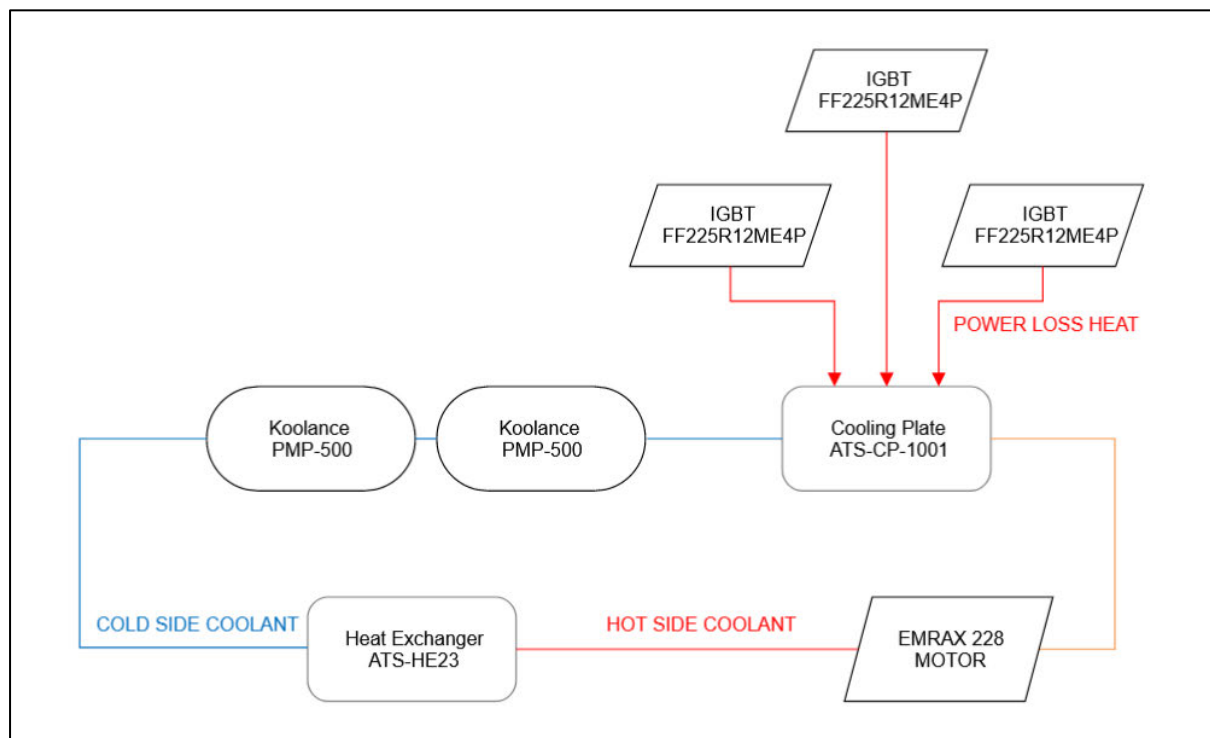

Figure 56 - Flow chart of proposed motor controller cooling system.
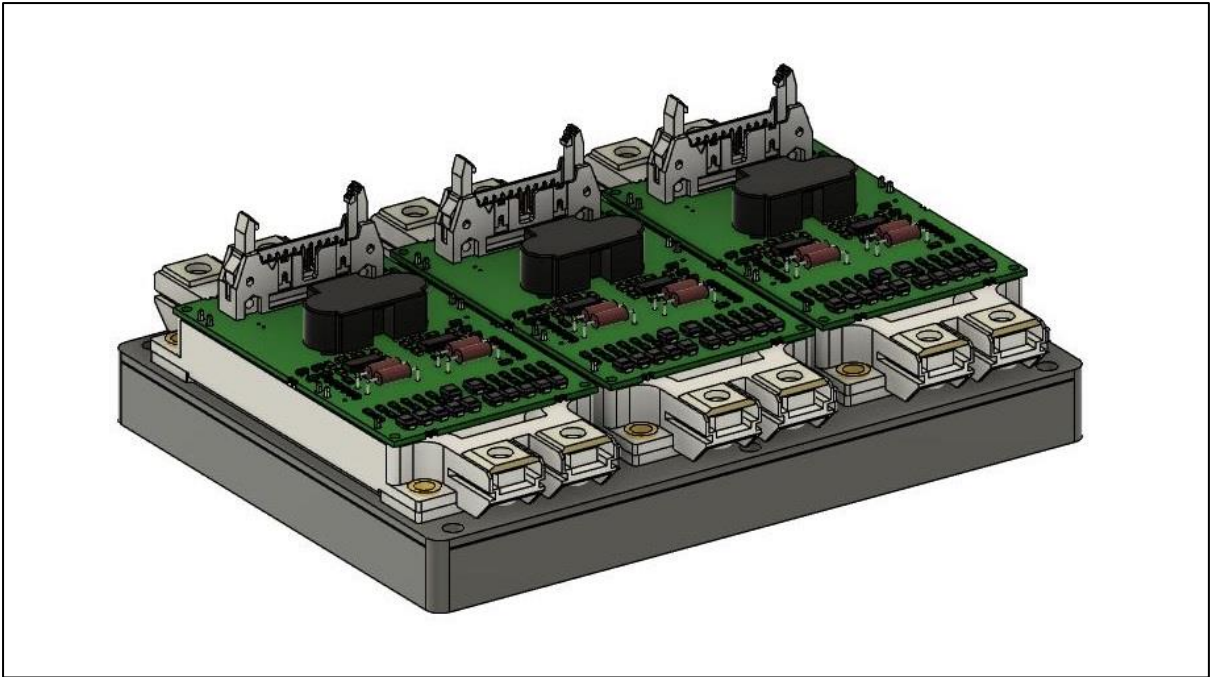
Figure 57 - Rendered 3D model of proposed motor controller.

4.3. Prototype Development

4.3.1. Validate Microcontroller Algorithms

The procedure outlined in the methodology was successfully followed, producing the system configuration shown in Figure 59 The procedure outlined in the methodology was successfully followed, producing the system configuration shown in Figure 58 provides a close-up view of the development platform, capturing the multimeter as it indicates the current at that specific moment of operation.

The successful programming from the Simulink model and deployment onto the microcontroller enabled the successful operation of this initial development platform. The ST Microelectronics FOC motor control algorithms, were validated, resulting in the controlled commutation of the EMRAX motor. This has provided confidence to progress with developing the prototype motor controller.
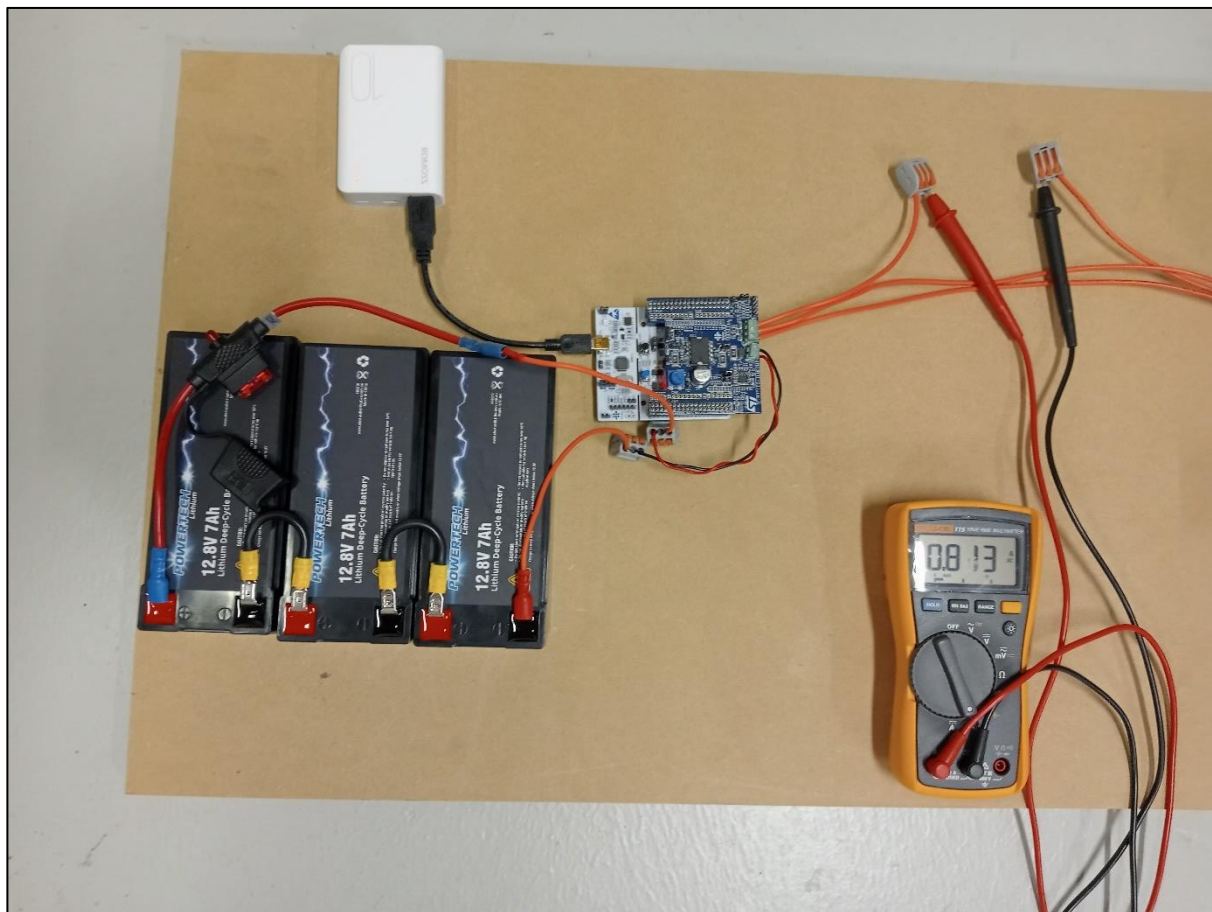

Figure 58 - Initial development platform, batteries, and multimeter during EMRAX 228 motor function.
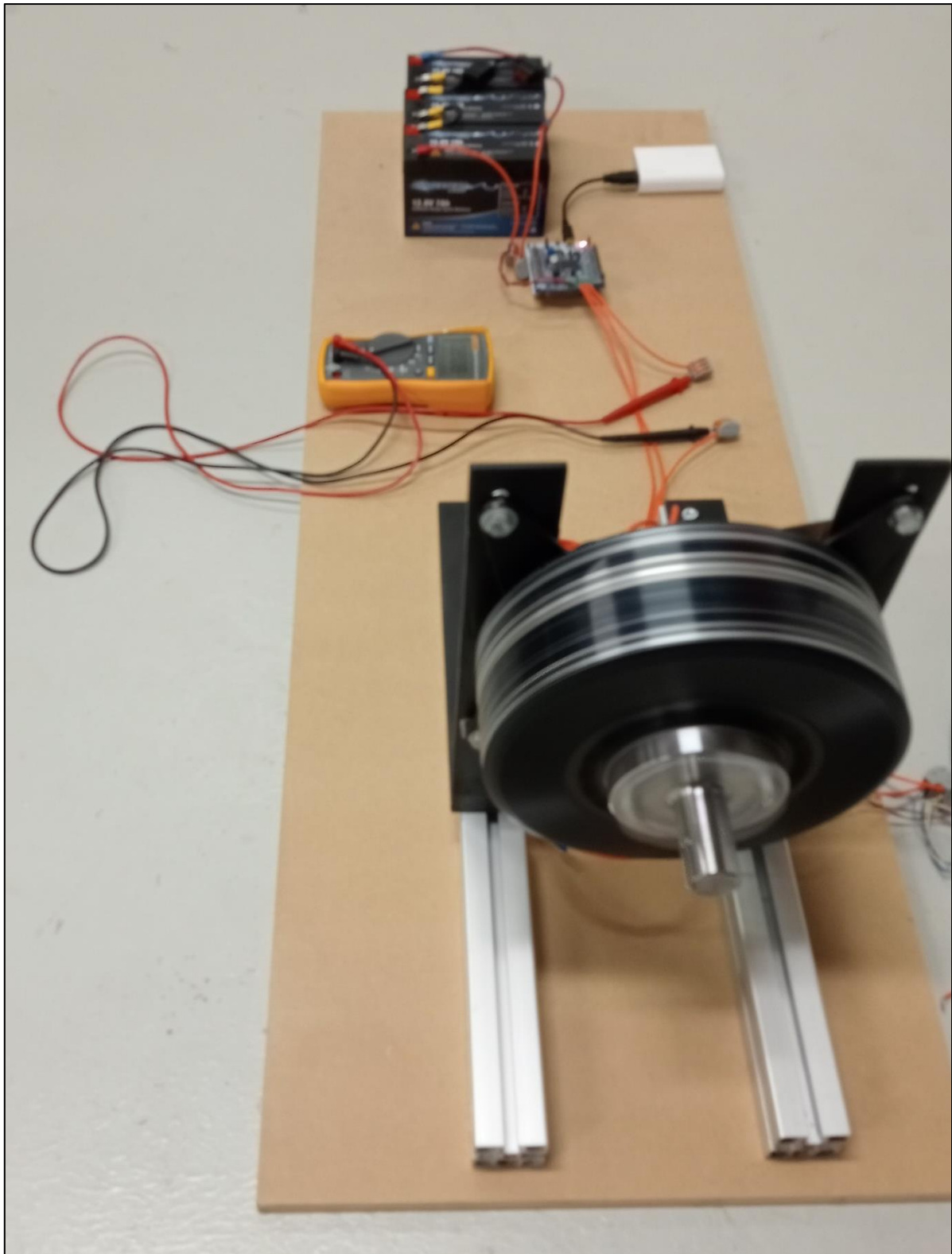
Figure 59 - EMRAX 228 operating using the initial development platform.

4.3.2. Prototype Motor Controller Development

Microcontroller Firmware Alterations

The complementary PWM channel generation was achieved by modifying the PWM configuration of the microcontroller. Figure 60 shows the selection change from "PWM Generation CH1" to "PWM Generation CH1 CH1N" in the STM32CubeMX programming application, informing the microcontroller to generate complementary PWM signals. Pins PB13, PB14 and PB15 were assigned to the complementary signals, while the original "enable" pins PC10, PC11 and PC12 were deactivated. The required deadtime between each original signal and its complement was necessary to program.
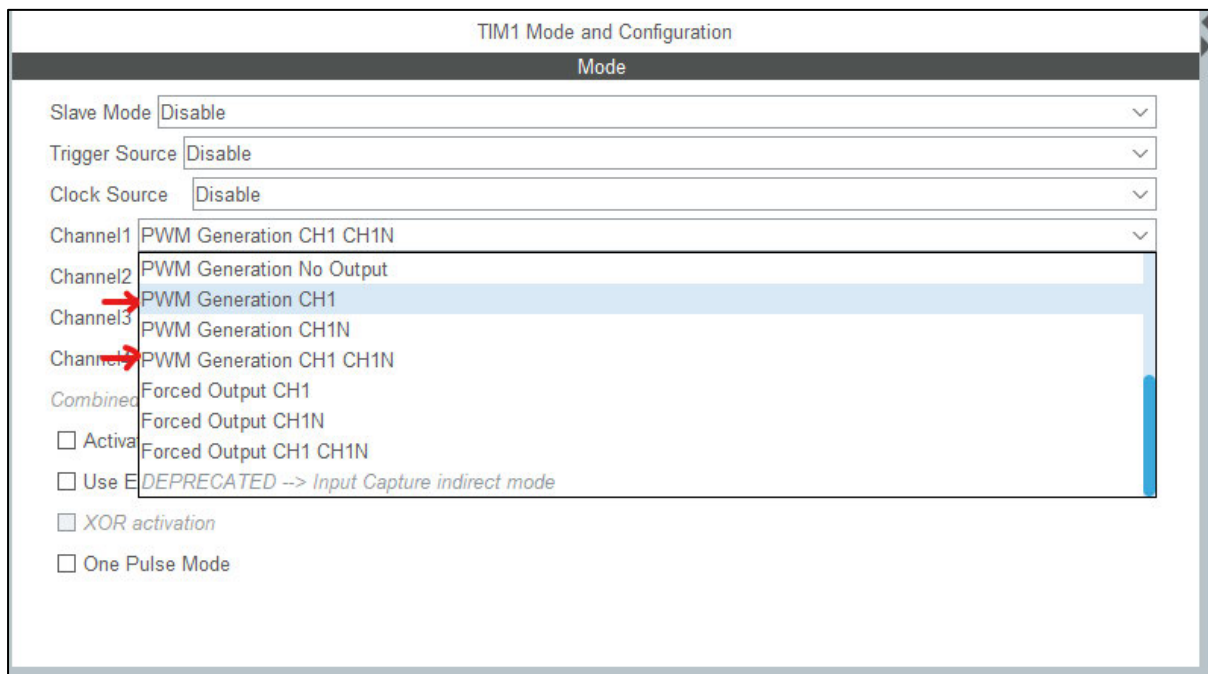

Figure 60 - STM32CubeMX PWM Generation selection.

The deadtime programming is established as an 8-bit value; determining this setting was deemed non-intuitive, so a MATLAB script was developed to assist with this process. This MATLAB script is provided in Appendix G ; it is based on the process documented in the ST Microelectronics Application Note 4013 (2023b, pp.30-31).

The realisation of this complicated deadtime calculation process was highlighted during the prototype testing and evaluation. The first IM535 module was deemed to have suffered an overcurrent event through one of the IGBTs, identified due to the resultant short circuit condition. On the succeeding examination, the PWM signals were identified to exhibit an extremely short deadtime period well

under the specified 2µs. The cause was realised to be the incorrect deadtime setting of "16", which resulted in a deadtime of 0.19µs. Following a revision of this process, the deadtime was correctly set to "148" (Figure 61), resulting in the correct deadtime of exactly 2µs.

∨ Break And Dead Time management - Output Configuration	
Automatic Output State	Disable
Off State Selection for Run Mode (OSSR)	Disable
Off State Selection for Idle Mode (OSSI)	Disable
Lock Configuration	Off
Dead Time	148

Figure 61 - Deadtime setting in STM32CubeMX for 2µs.

An ensuing examination of the PWM-generated signals was undertaken; however, the resultant signals were a considerably larger duty period than anticipated. Further investigation identified an unexpected multiplier block and summation block applied to the PWM signal processing in the Simulink environment (Figure 62). These blocks first scaled the PWM signals by a factor of 0.5 and then applied an offset of 0.5. This process was needed to meet the requirements of the original L6230 chip to operate from one set of three PWM signals; however, it was now redundant, with the IM535 module requiring the full complement of six PWM signals. Therefore, these multiplier and summation blocks were removed from the program (Figure 63). Suitable PWM generation was achieved following these program modifications.

With all firmware configuration modifications implemented in the STM32CubeMX program, the pinout featured in Figure 64 was produced. All pin changes identified in Table 16 have now been incorporated.
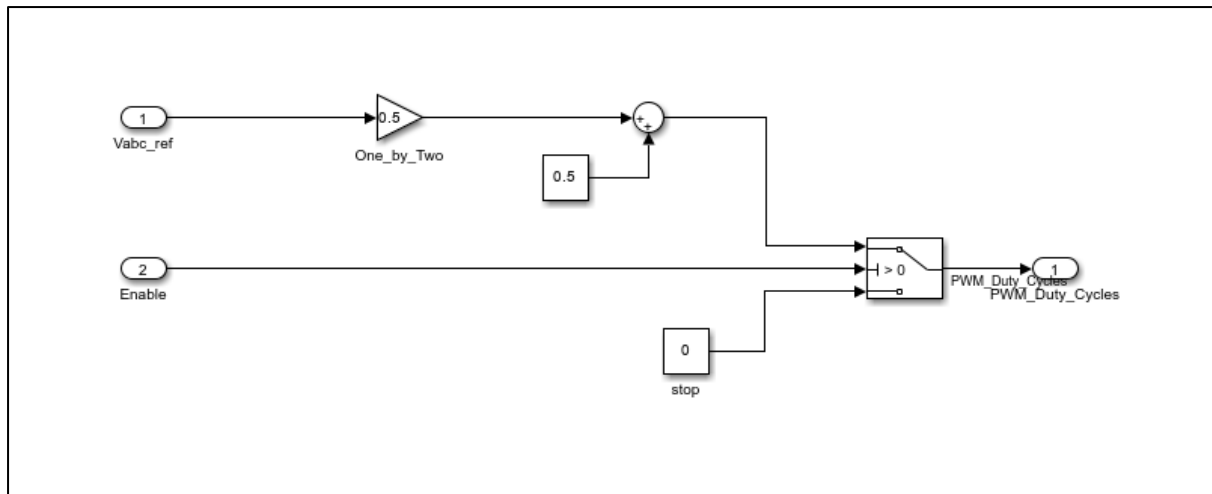
Figure 62 - Simulink programming featuring a 0.5x gain and 0.5 offset for L6230 PWM signal generation.
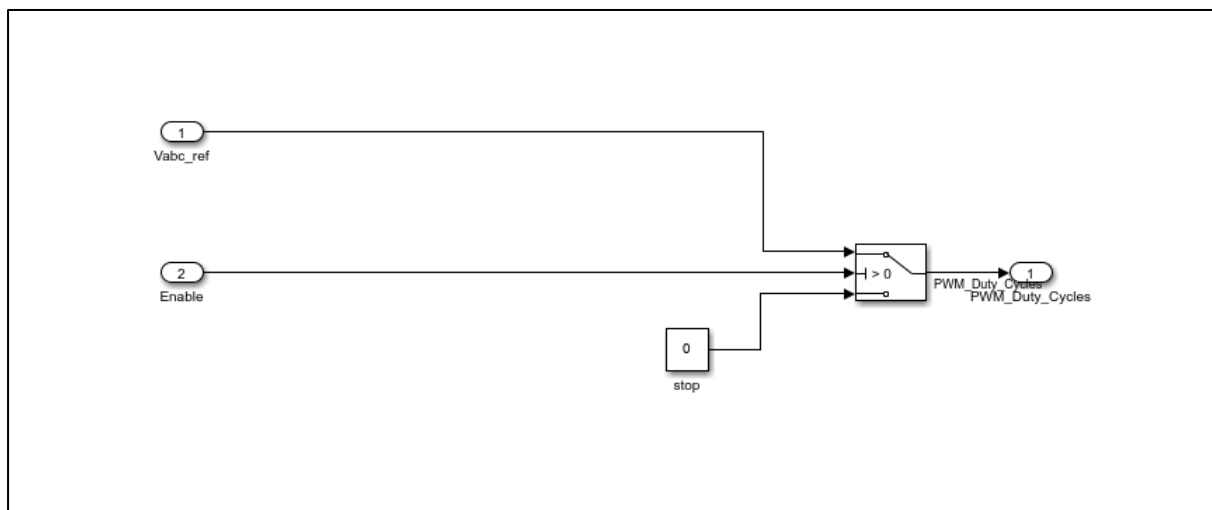

Figure 63 - Simulink programming with 0.5x multiplier and 0.5 offset removed for the IM535 PWM signal generation.
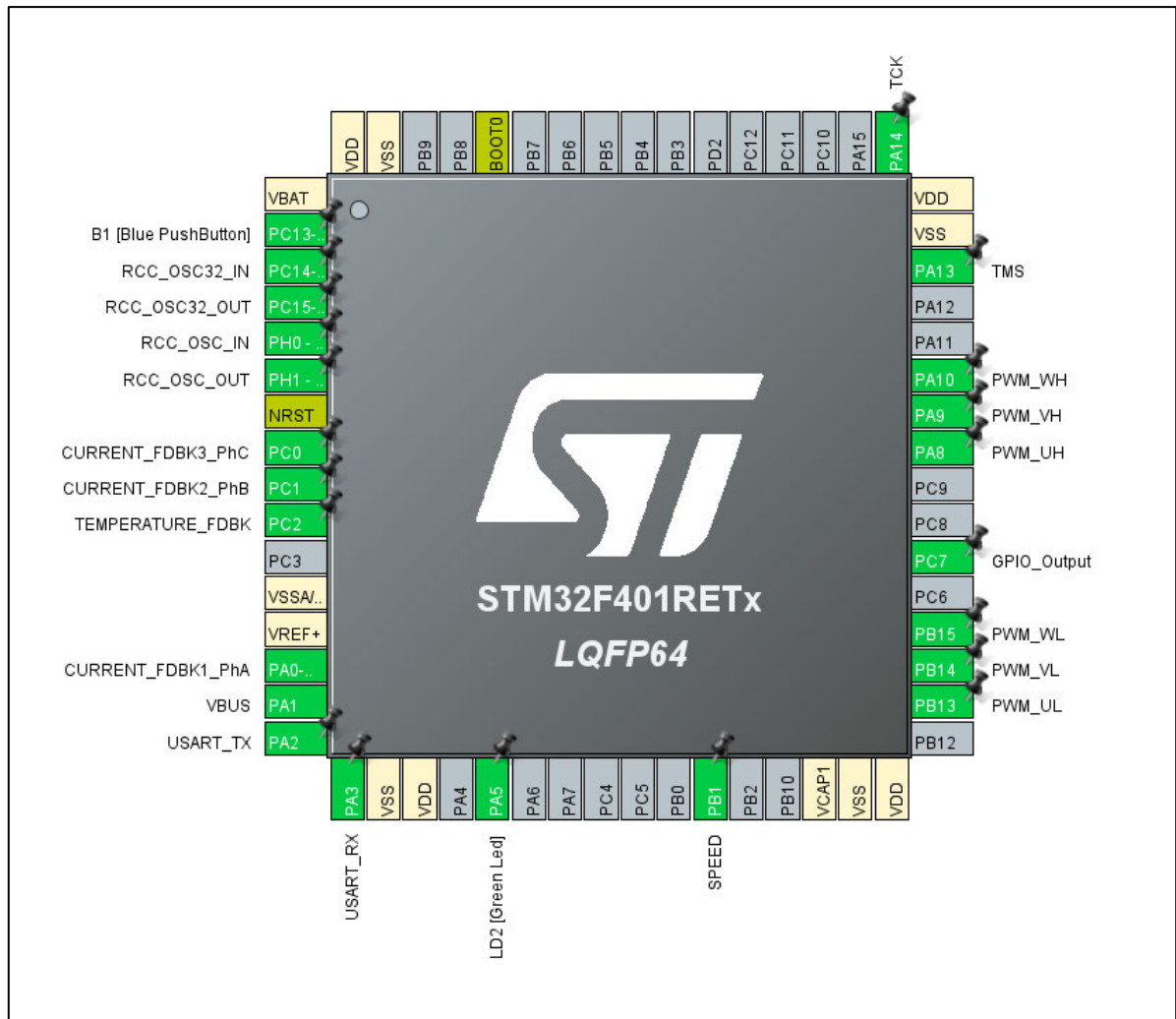
Figure 64 - Modified STM32CubeMX pinout for prototype motor controller.

The processes outlined in the methodology section regarding the passive component selection are detailed in the following pages. Table 25 at the end of this section presents all component selections utilised in the PCB prototype.

ITRIP signal

The resistors selected for producing the specified gain of 8.5 were $R_1 = 21 \text{ k}\Omega$ and $R_2 = 2.8 \text{ k}\Omega$ (Equation 10).

Equation 10 - ITRIP op-amp actual gain.

$$G_{ITRIP,actual} = 1 + \frac{R_1}{R_2} = 1 + \frac{21 \cdot 10^3}{2.8 \cdot 10^3} = 8.5$$

The finalised ITRIP circuitry is presented in Figure 65. The red circled section of Figure 65 is referenced in the methodology section, where this circuit design was examined and subsequently established.

Microcontroller Current Feedback

The current sense amplification circuits were designed to meet the selected gain of 10.5. During the resistor selection process, it was identified to be onerous due to the three components of Equation 8 required to be satisfied. To accelerate this process, a specific MATLAB script was produced; this script is presented in Appendix H.

The finalised motor current sense amplification circuits are presented in Figure 66. To ensure the circuits operate as anticipated, a simulation was executed through circuitlab.com. The circuit layout is shown in Figure 67, with the successful simulation results presented in Figure 68. Over the designed current range of ±50 A, the op-amp circuit provided an output between 75 mV and 3.225 V, 0 A producing an output of 1.65 V. These results delivered the designed centre-biased output between 0 V and 3.3 V as expected.
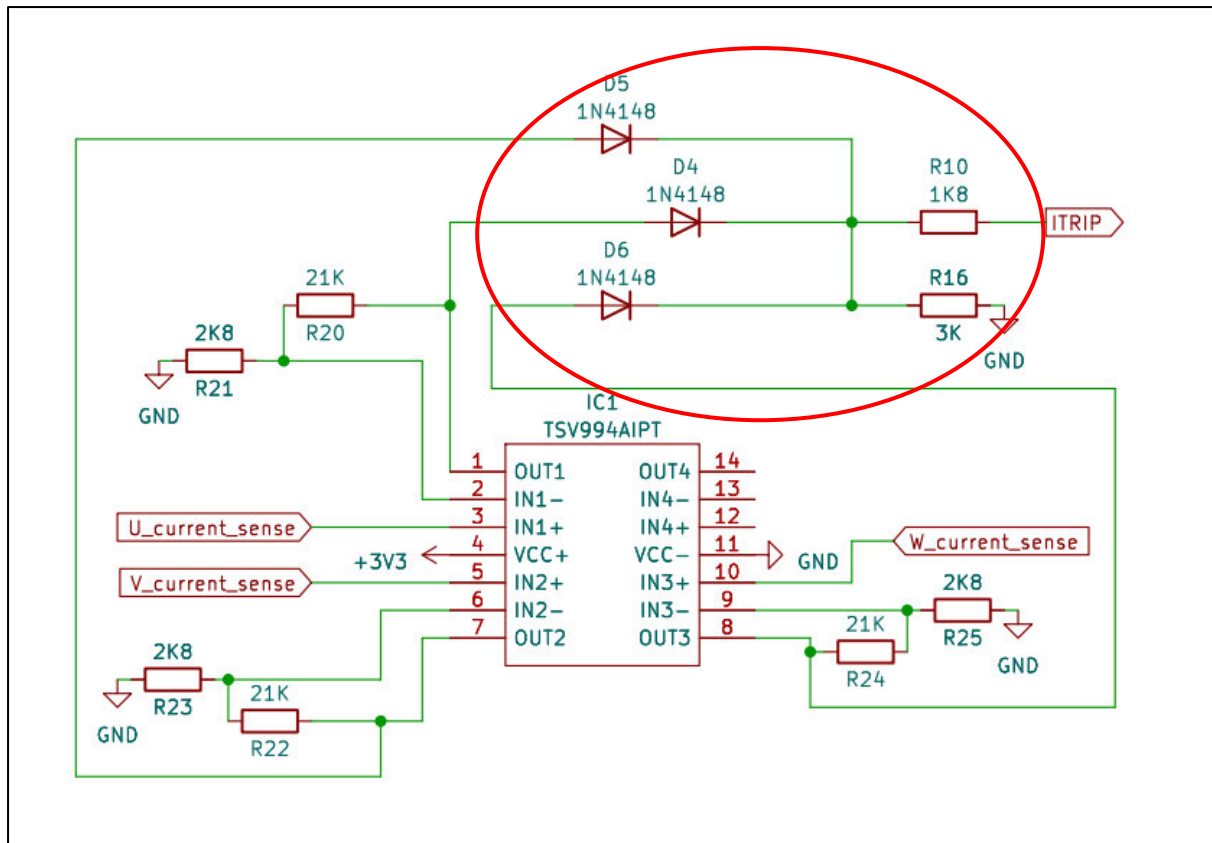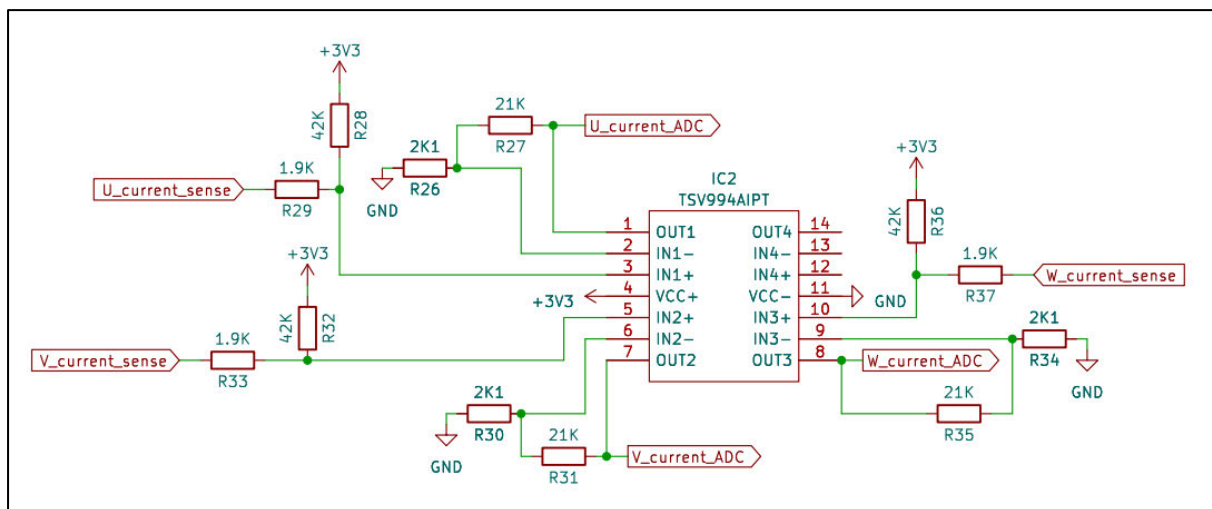
Figure 65 - IM535 ITRIP circuit design.

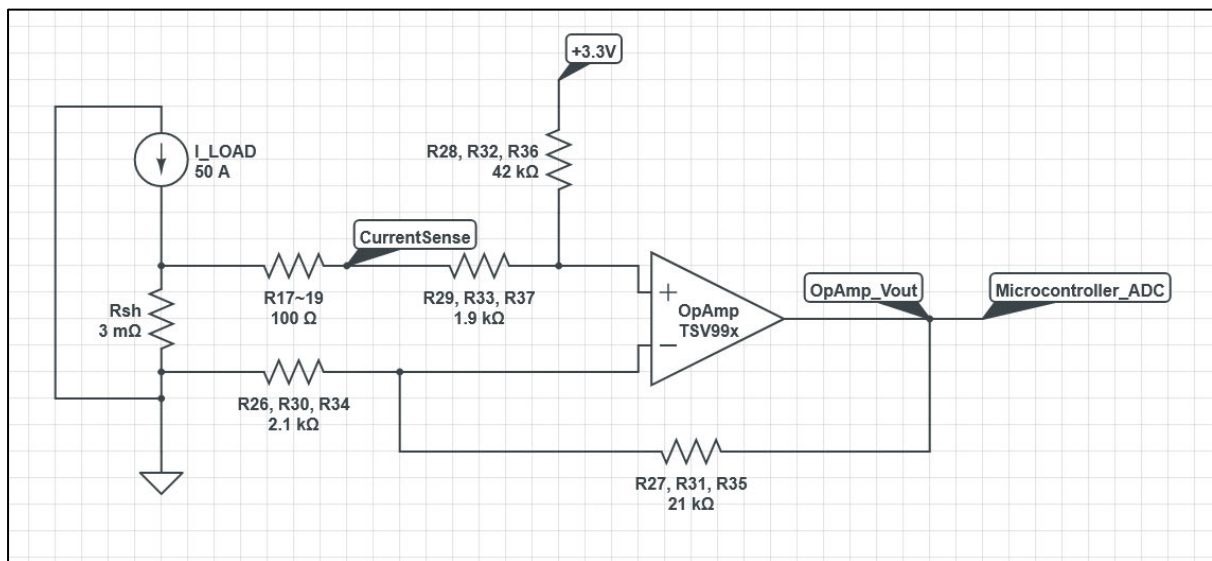*Figure 66 - Microcontroller current feedback op-amp design.*

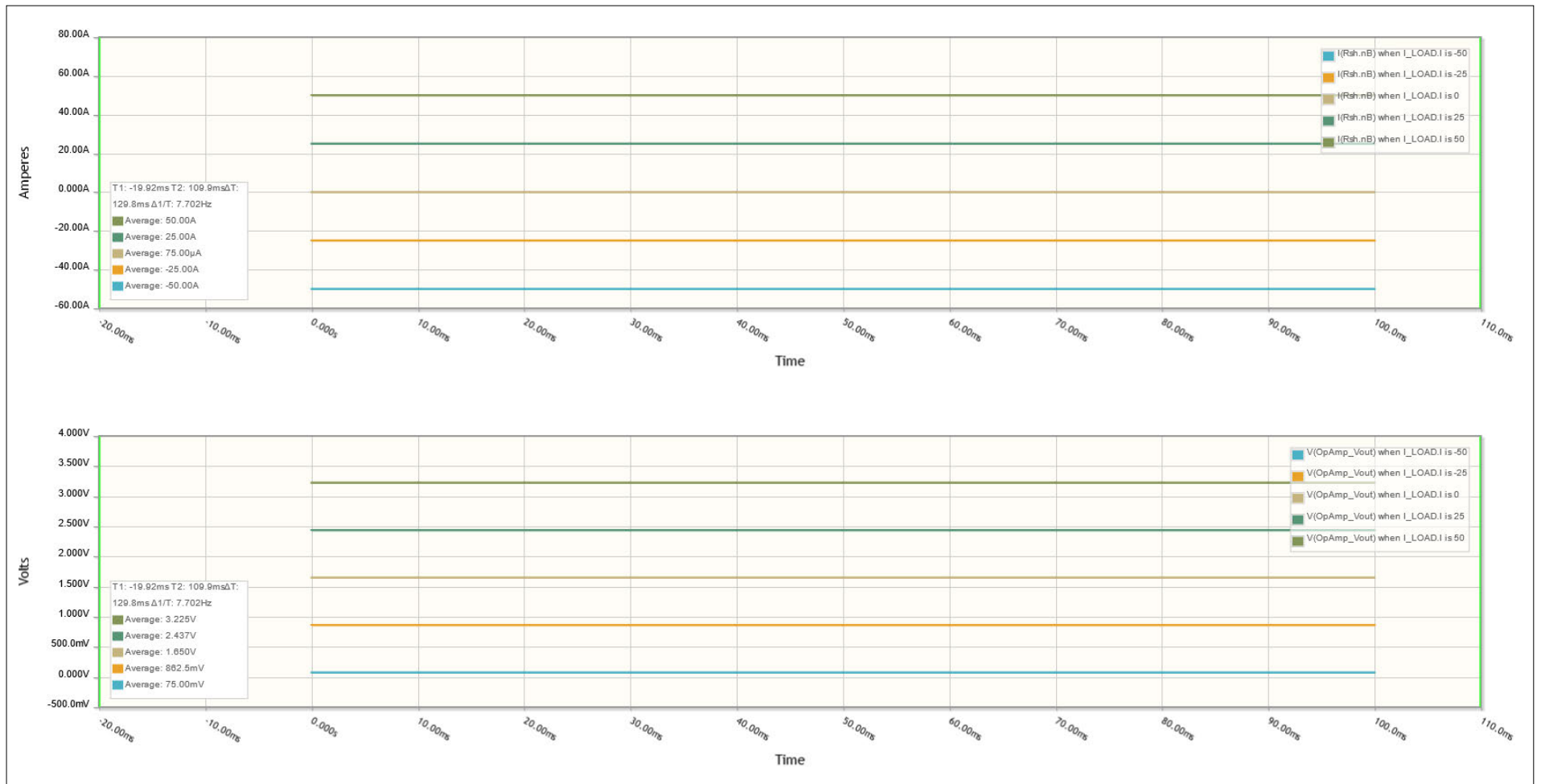*Figure 67 - Microcontroller current feedback op-amp simulation schematic.*

Figure 68 - Simulation results for microcontroller current feedback op-amp.

Voltage Divider Circuit for Service Voltage Monitoring

The selected component resistances are as shown in Figure 69. As specified in the methodology section, the total voltage divider resistance is 600 kΩ, with the monitored value taken from the volt drop over 6 kΩ of that circuit. Resulting in a 100:1 ratio achieved. The Energy System Lab's 300V supply will be measured as 3 V at the microcontroller ADC, sufficiently not exceeding the ADC maximum of 3.3 V.
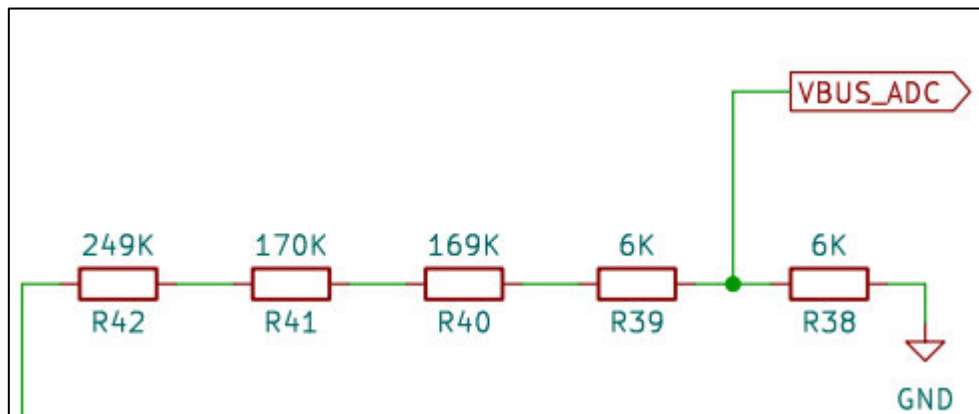

Figure 69 - Motor controller service voltage monitoring circuit.

Voltage Divider Circuit for IM535 Temperature Monitoring

Due to the low load operating condition and short run time, the temperature monitoring for this prototype was deemed unnecessary. It is recommended that this monitoring be implemented in future iterations of the motor controller; however, for this prototype, it was excluded from the design. A heatsink for the IM535 was selected as a precautionary measure, and a cooling fan to force air toward the heatsink and PCB in general. The heatsink and cooling fan arrangement can be seen in Figure 72.

Final Component Selection

The finalised electronic schematic is featured in Appendix I and a Bill of Materials is provided in Table 25.

Table 25 - Prototype electronic component BOM.

Component	Value	Qty	Rating	Tol.	Cost	Total
C1, C2, C3, C4, C5, C6, C17, C18, C19	1nF	9	25 V		$0.168	$1.512
C7, C8, C9, C14, C16	0.1uF	5	25 V		$0.139	$0.695
C10, C11, C12	22uF	3	35 V		$0.601	$1.803
C13	100uF	1	35 V		$0.231	$0.231
C15	220uF	1	35 V		$0.462	$0.462
C20, C21, C22	1.33uF (1uF + 330nF)	3	25 V		$1.956	$5.868
C23	0.1uF	1	630 V		$0.662	$0.662
Cooling Fan	12VDC, 28mm	1	24.38 CFM		$25.130	$25.130
D1, D2, D3	1N4947-B	3			$0.567	$1.701
D4, D5, D6	1N4148	3			$0.119	$0.357
Heat Sink	35mm x 35mm x 25mm	1	Veritcal fins		$3.170	$3.170
IC1, IC2	TSV994AIPT	2	Quad op-amp		$3.300	$6.600
J1	2 pin terminal block	1			$1.460	$1.460
J2	3 pin terminal block	1			$1.820	$1.820
J3	16 pin header strip	1			$1.450	$1.450
J4	2 pin header strip	1				
R1, R2, R3, R4, R5, R6	100R	6	1/8 W	5%	$0.048	$0.288
R7, R8, R9	39R	3	7 W	5%	$2.170	$6.510
R10	1K8	1	1/8 W	1%	$0.154	$0.154
R11	3K6	1	1/8 W	1%	$0.154	$0.154
R12	1K	1	1/8 W	5%	$0.154	$0.154
R13, R14, R15	3m	3	3 W	1%	$1.860	$5.580
R16	3K	1	1/8 W	5%	$0.154	$0.154
R17, R18, R19	100R	3	1/8 W	1%	$0.154	$0.462
R20, R22, R24, R27, R31, R35	21K	6	1/8 W	1%	$0.117	$0.702
R21, R23, R25	2K8	3	1/8 W	1%	$0.154	$0.462
R26, R30, R34	2K1	3	1/8 W	1%	$0.154	$0.462
R28, R32, R36	42K	3	1/8 W	1%	$0.116	$0.348
R29, R33, R37	1K9	3	1/8 W	1%	$0.154	$0.462
R38, R39	6K	2	1/2 W	1%	$1.360	$2.720
R40	169K	1	1/2 W	1%	$0.246	$0.246
R41	170K	1	1/2 W	1%	$0.246	$0.246
R42	249K	1	1/2 W	1%	$0.246	$0.246
U1	IM535U6DXKMA1	1			$39.270	$39.270
VR1	10k Potentiometer	1			$1.450	$1.450
					Total	$112.991

4.3.3. PCB Design

The PCB design was undertaken in the KiCad EDA software. The design was performed on only two layers to minimise complexity. The top view of the finalised PCB design is presented in Figure 70; a 3D render of this design is displayed in Figure 71.
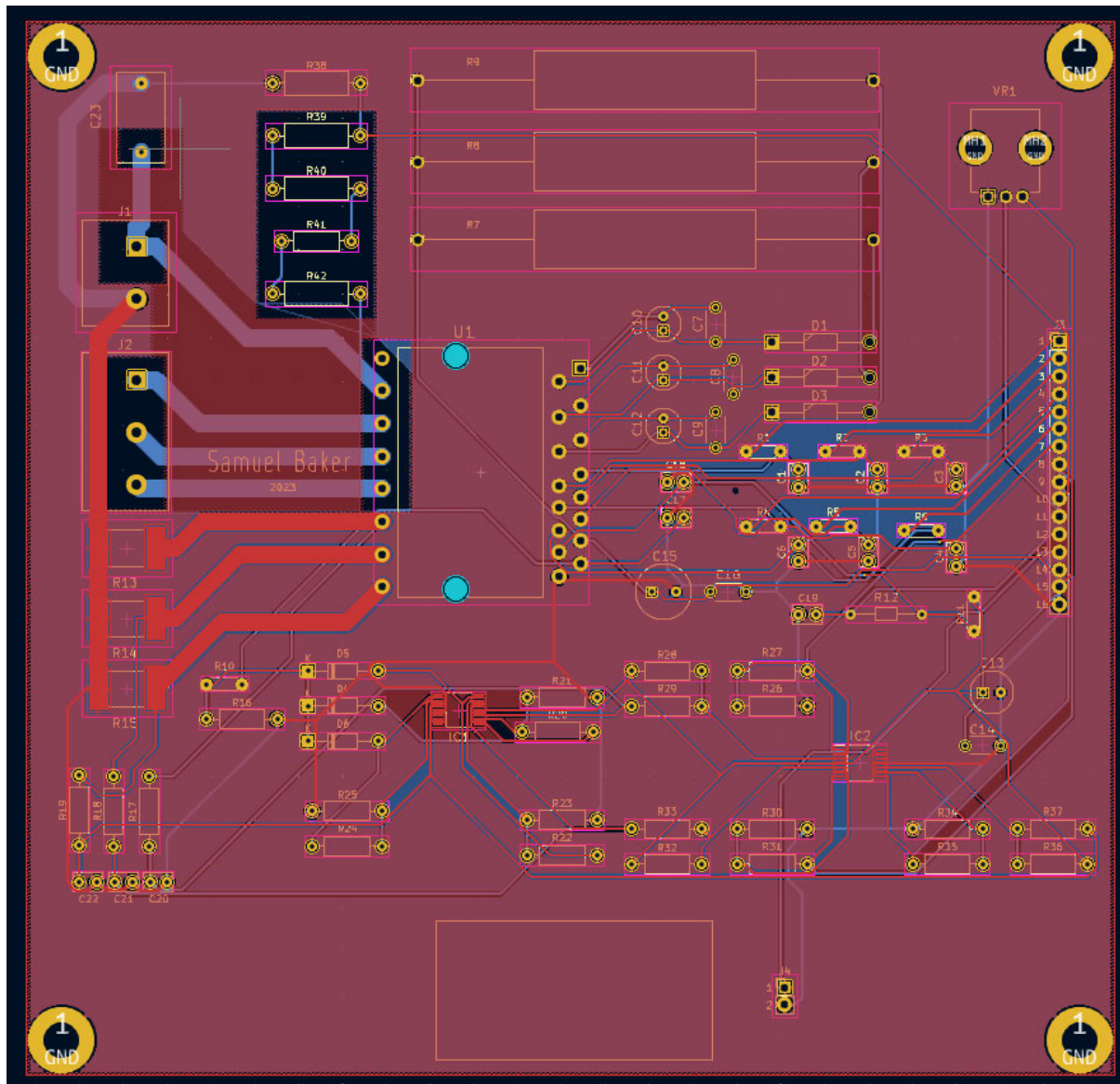

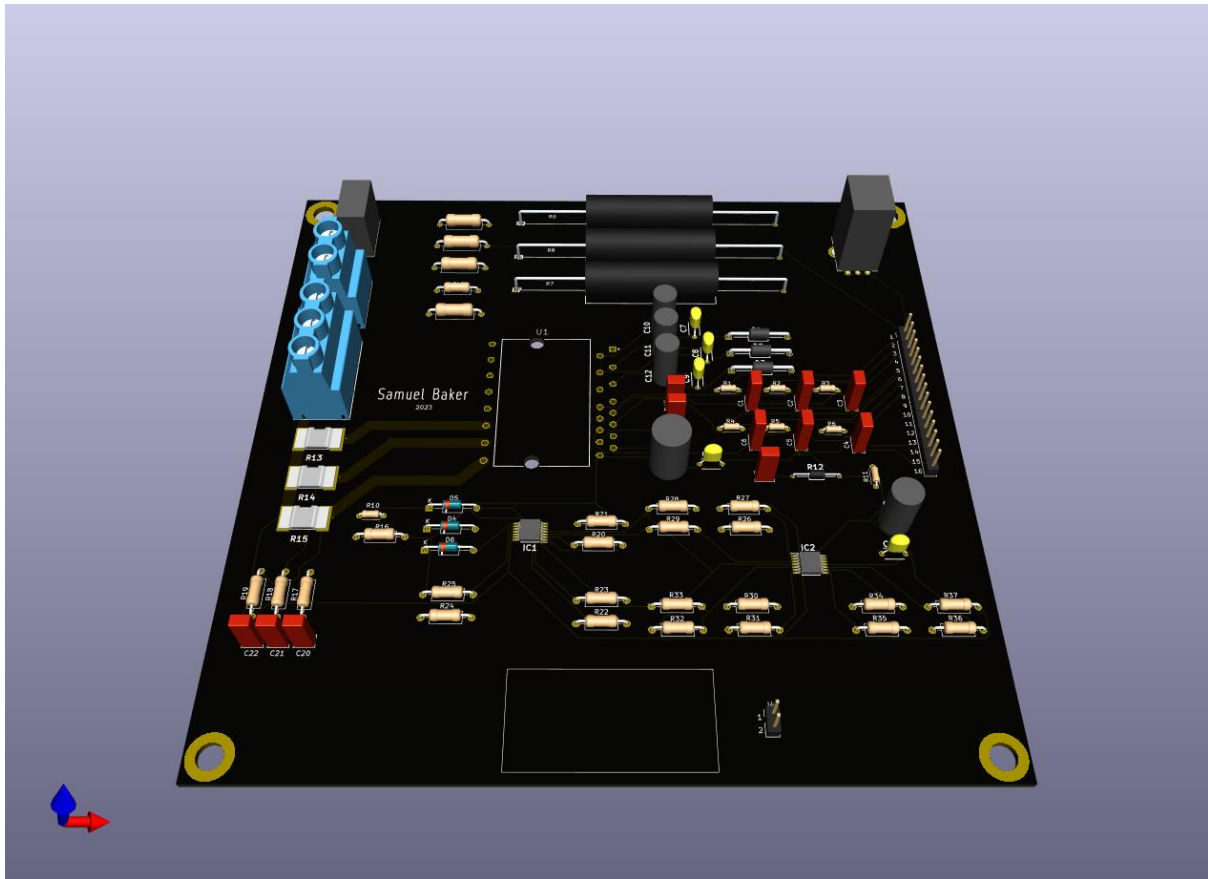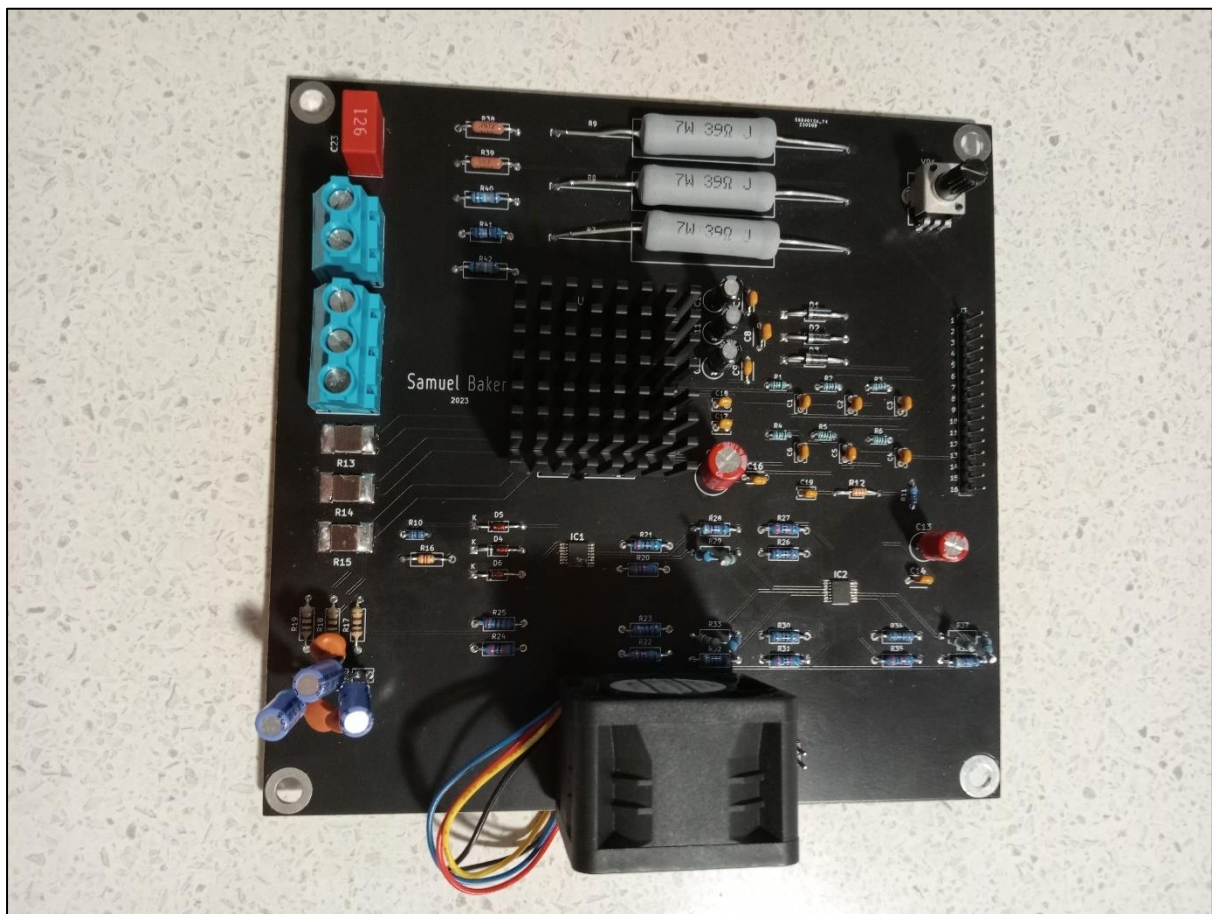*Figure 70 - Prototype motor controller PCB design.*

Figure 71 - 3D render of motor controller PCB.

4.3.4. PCB Assembly

Following the satisfactory PCB design, JLCPCB.com was engaged to manufacture the board. The PCB was promptly manufactured in their China-based manufacturing plant and then delivered to Toowoomba, Australia. Upon arrival, manual assembly was undertaken without incidence; the finished product is featured in Figure 72.

Figure 72 - Assembled microcontroller PCB.

4.4. Functional Testing of Prototype Motor Controller

Prior to functional testing, the MATLAB motor and inverter parameters script was updated for the modified components. The changes implemented to suit this prototype PCB design are summarised in Table 26. The current sense voltage per ampere value was calculated as per Equation 11.

Equation 11 - Current sense voltage per ampere calculation.

$$\text{V per A} = (I \cdot R_{SH}) \cdot G = (1 \cdot 0.003) \cdot 10.5$$

$$\therefore I_{Sense} = 31.5\text{mV per A}$$

Table 26 - Updated programming parameters for prototype motor controller.

Parameter	Description	Data
inverter.V_dc	DC Link Voltage of the Inverter	40 V
inverter.I_trip	Max current for trip	5.0 A
inverter.Rshunt	Rshunt = 3mOhm, 3W, 1%	3 mΩ
inverter.ISenseVoltPerAmp	Current sense voltage output per 1 A current (Rshunt * iSense op-amp gain)	31.5 mV

4.4.1. Test Results

Testing and evaluation proceeded over several iterations, where different issues were identified and corrected. These iterations are described below.

Attempt 1

With all programming changes implemented and the hardware constructed and connected, power was applied to the microcontroller, IM535 module and cooling fan. The initial result was that no control power was present for the microcontroller, and the 3.3 V control supply was absent. It was identified that the source-stabilising capacitor C13 (100µF) was too large for the default power supply on the microcontroller development board to charge. This capacitor was removed, the system was repowered, and the microcontroller control power supply was now present.

Attempt 2

The following functional test resulted in the failure of the first IM535 module due to the incorrect PWM parameters. As described earlier in this section, the PWM deadtime and generation were incorrectly established for this module. This incorrect deadtime is accepted as resulting in a shoot-through event that damaged this IGBT. The IM535 module was replaced, and the firmware code was updated to the correct configuration. The power supply's current limitation was reduced to assist with preventing this damage from occurring to a subsequent IGBT.

Attempt 3

Motor function was achieved; however, issues were encountered. The motor would rotate while in the open-loop section of the sensorless code; yet, once the speed reference potentiometer (VR1) was positioned greater than 10%, the program would transition into closed-loop control, and the PWM output would hold in one state, no longer creating a rotating field in the motor's stator. As a result, the motor would instantly cease motion and remain in a locked rotor condition. During the fault finding of this situation, a second IM535 module failed and required replacing. This damage was accepted as resulting from the immediate halting of the EMRAX motor, producing a transient voltage spike across the motor windings; this event is believed to have compromised the IGBT.

Attempt 4

The circuit and programming were reviewed to identify the condition creating the locked rotor state during closed-loop control. Oscilloscope monitoring identified a significant noise level across the current feedback to the microcontroller, with no definable component pertaining to the current sense voltage feedback. This noise was attributed to the insufficient filtering circuit, particularly because it is only a first-order system. On review, it was identified that comparable systems on the open-source Axiom controller (the overcurrent protection monitoring) all engage second-order filtering (Hackaday 2019, p.3). The resultant signals displayed an extremely high signal-to-noise ratio; this was attributed to the volt drop across the 3 mΩ current sense resistors producing an extremely low value during unloaded operation, resulting in the noise completely enveloping and distorting the signal, therefore resulting in a practically undefinable signal.

It is noted that in the X-NUCLEO-IHM07M1 development board, the current sense resistors are 330 mΩ, a factor of 110 times larger and therefore producing a volt drop 110 times more significant during the same operating currents (ST Microelectronics 2021a, p.8). This resistor size reduction was one of the significant changes made during the prototype development; however, it was an essential alteration required to reduce the motor controller power losses during high current operation. A review of the Axiom controller schematic identifies the use of Haff Effect current sensors for the current sense circuit instead of current sense resistors (Hackaday 2019, p.1). This current monitoring method is expected to reduce harmonic noise's impact on the current sense circuit.

The sensorless FOC algorithms utilised by the microcontroller require a detectable current sense value to estimate the rotor position. Due to previously noted unserviceable current sense signals, it is accepted that the microcontroller cannot determine the rotor position and, therefore, cannot execute the FOC algorithms in the closed-loop section of the program. This interpretation of the system error is accepted to align with the motor, assuming a locked rotor condition once closed-loop control is initiated. This is mainly due to the previously proven functional algorithms on the development platform utilising the X-NUCLEO-IHM07M1 development board.

4.5.   Future Work

The EMRAX 228 motor testing and commissioning were completed; the commissioning tests suitably confirmed the motor functions as intended, confirming the motor's suitability for the USQ Racing vehicle's development. The future testing recommended for the motor is for it to be operated under load, therefore validating its satisfactory evaluation and characterising the thermal response of the motor. The operation of the EMRAX 228 under load may identify defects within the windings or internal connections that are not yet apparent under low-load conditions, while the thermal response data obtained would be critical to optimising the cooling system further. This testing would be best performed in a controlled dynamometer arrangement or fitted to a car for real-world performance results.

4.5.1. Key Recommendations

The following recommendations should be addressed before developing the next motor controller prototype.

Current Sense Monitoring

The implementation of the microcontroller current sense monitoring for the ITRIP fault detection and microcontroller current feedback was identified as inadequate in the prototype motor controller. These systems may be improved by implementing second-order filtering and Hall Effect current sensors. By separating the ITRIP overcurrent trip circuit from the microcontroller current feedback, the ITRIP circuit could have second-order filtering implemented. This approach would allow the ITRIP circuit to provide the fault input when an overcurrent event is detected; however, the impact from harmonic distortion should be reduced. Introducing Hall Effect current sensors for the microcontroller current feedback will provide galvanic isolation between the PWM current waveforms and the ADC input. These techniques are used by comparable motor controllers like the open-source Axiom (Hackaday 2019, p.1, 3).

Rotor Position Sensor

The failure of this motor controller to not operate in closed-loop control is likely due to the microcontroller's sensorless algorithms not being able to identify the rotor position. The implementation of an encoder, or the integration of the resolver, would enable the rotor position to be accurately measured. The microcontroller FOC algorithms could then use this position data in place of the existing sensorless determinations, allowing full FOC implementation.

IGBT Temperature Feedback

The IGBT module in the prototype motor controller and the IGBTs selected for the proposed final motor controller both have an NTC temperature monitoring circuit embedded in their design. Future iterations of the motor controller should incorporate this temperature monitoring for the thermal management of these power transistors.

4.5.2. Other Recommendations

The following areas of future work have been identified to assist with the ongoing development of the motor powertrain.

Validate Cooling System Data

The modelled cooling system provides an initial design but requires further validation to identify the system flow characteristics and thermal response. The particular areas to be addressed are the characterisation of a suitable aluminium radiator/ heat exchanger and the pressure drop over the complete system during operation. The thermal losses of the IGBTs and EMRAX 228 are based respectively on proprietary simulation and published data; this should be experimentally validated in future work.

Hardware-in-the-Loop (HIL) Simulation

This project demonstrated the compilation of Simulink models and deployment to real microcontroller hardware. This now opens the avenue for Hardware-in-the-Loop (HIL) simulation.

Hardware-in-the-loop (HIL) simulation is a critical technique for validating control algorithms by mimicking the physical system in a virtual real-time environment (MathWorks n.d.d). This method allows for thoroughly testing control algorithms without necessitating physical prototypes, thereby reducing costs and potential iterations in hardware fabrication. The HIL simulation process involves the creation of a real-time virtual model of physical components (such as plants, sensors, and actuators), which is then run on a target computer. Subsequently, the control algorithm is executed on an embedded controller, interacting with the simulated environment through various input/output channels, offering an avenue to refine software representations and gradually integrate actual hardware components. HIL simulation is notably employed in aerospace, automotive, and industrial automation, where testing control algorithms on real systems can be dangerous, resource-intensive, or financially prohibitive (MathWorks n.d.d).
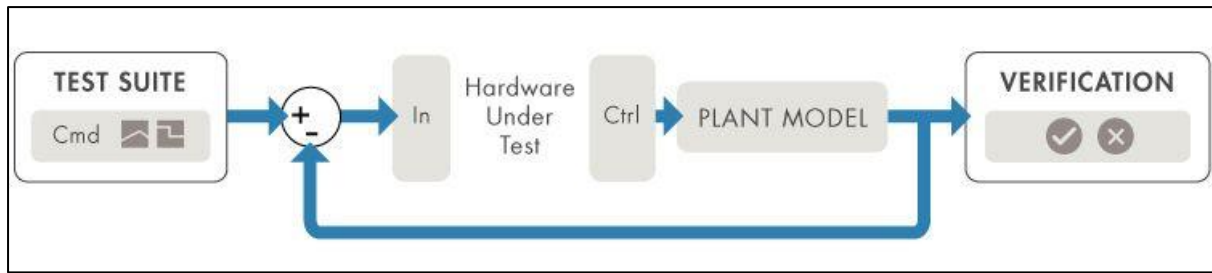
Figure 73 - Hardware-in-the-loop (HIL) simulation setup (MathWorks n.d.d).

For USQ Racing, HIL simulation (Figure 73) offers the ability to test real hardware and control algorithms under simulated scenarios that may be impractical to test in the real world, e.g. due to safety considerations or in the absence of a physical vehicle/ test platform. While HIL testing is not specific to the motor controller developed, with the inclusion of a high-speed data acquisition system, HIL could be engaged from the framework demonstrated in this project.

Chapter 5

5. Conclusions

This project aimed to i) commission the previously procured USQ Racing EMRAX 228 motor and ii) support the ongoing development of the USQ Racing team and FSAE Electric community in general through the design of a low-cost and customisable electric motor controller and simulation platform.

From the commissioning tests performed and the results obtained, it can be concluded that the motor is functional and suitable for use by the USQ Racing team. However, further testing under load conditions should be performed to rule out defects within the windings or internal connections.

As presented in Table 27, several tests were performed to verify the serviceability of the EMRAX 228 motor. The tests performed were effective, and of particular note, they identified defects in the resolver that may otherwise have been difficult to isolate once in use. The tests were relatively easy to perform and utilised hardware that would be readily available in an energy systems laboratory. It is an effective procedure that could be followed when other motors are procured.

The future load testing of the EMRAX 228 motor could be performed with a dynamometer (If available); alternatively, the motor could be evaluated in a vehicle under load conditions with suitable data collection methods implemented.

The custom motor controller designed and constructed in this project successfully commutes the EMRAX 228. In addition, a development framework based on Simulink combined with real-time microcontroller hardware provides a sound platform for ongoing powertrain development and optimisation.

The approach to the design and prototype of this motor controller was sound; in hindsight, additional focus on current sense feedback and rotor position sensing would have been beneficial.

The utilisation of the MathWorks' Simulink model and the STM32 microcontroller was an effective way to develop a custom motor controller and implement FOC algorithms in real hardware. This approach provides flexibility in future development and optimisation, through close integration of simulation and hardware validation. This project's combined Simulink and hardware framework will support future development using HIL simulation.

In addition to the current and rotor position feedback improvements, future work should also address IGBT thermal monitoring and management, and broader systems integration of the controller and motor in the vehicle.

A summary of the project outcomes is presented in Table 27, with the end column identifying the project objectives satisfied by these outcomes.

The outcomes of this project provide tangible progress on the USQ Racing powertrain. This is a crucial vehicle subsystem that will provide a sound foundation for developing other vehicle subsystems and producing a fully functional FSAE-suitable motor controller.

Table 27 - Project Outcomes.

Objective	Activities Conducted	Results Obtained	Objectives Achieved
Commission the EMRAX 228	**Static Tests** • Winding Resistance. • Insulation Resistance. **Dynamis Tests** • Mechanical Rotation. • Back-EMF Waveform Generation. **Functional Tests** • Resolver Testing. • Confirm Motor Function.	The commissioning of the EMRAX 228 produced successful results for all static, dynamic and motor function tests. However, the original resolver fitted to the motor was determined to be unserviceable. A suitable replacement was identified and installed; this resolver was then function-tested and confirmed to perform satisfactorily. The motor commissioning was successfully completed.	[1];
Controller Packaging and Cooling Design	• Selection of suitable cooling plate and heat exchanger. • Identification of a suitable cooling pump configuration. • Development and analysis of a thermal system model	Through multifaceted investigation and research, suitable cooling system components were identified; this included the cooling plate, a provisional heat exchanger and the identification of functional cooling pump configurations utilised in comparable scenarios. The engineering analysis of the selected cooling system components informed the selection of the cooling pump configuration most capable of satisfying the minimum flow requirements. With the cooling system flow quantified and the thermal losses produced by the Infineon IPOSIM program, the cooling system's thermal performance was modelled with MATLAB scripts. The anticipated thermal losses from the EMRAX 228 were later included in this thermal analysis, confirming a serviceable cooling system for the operation of the motor controller and EMRAX 228 up to the motor's continuous power rating.	[2]; [4];

| Motor Controller Prototype | Passive electronic component selection. Program modifications for the generation of complementary PWM signals with sufficient deadtime. PCB development and construction. Programming achieved direct from the Simulink model. Successful operation of the EMRAX 228. | The validation of the proprietary FOC algorithms through the initial development platform encouraged the construction of a prototype motor controller. This prototype required identifying and procuring suitable passive components, assisted by creating multiple MATLAB scripts to inform component selections. Modifications to the initial programming were made to facilitate the change of power transistors used. The motor controller programming was then finalised and uploaded directly from the Simulink platform. A custom PCB was designed, manufactured, and assembled. Motor controller commissioning was undertaken with minor fault finding and modifications required; however, these improvements led to the successful commutation of the EMRAX 228 motor. Future development work has been identified, yet the aims of producing and programming a motor controller and evaluating the performance of its selected control algorithm was achieved. | [3]; [4]; [5]; |
| Simulink Model Framework | Ongoing modification and development during the motor controller design stages. | The successful implementation of programming directly from the Simulink model was achieved, validating the ability to utilise the Simulink environment as the platform for future development and simulation of the motor controller system. | [4]; [5]; [6]; |

References

Advanced Thermal Solutions n.d.a, *IGBT Cold Plates*, Data Sheet No. R3_0419, viewed 27 May 2023.

Advanced Thermal Solutions n.d.b, *Heat Exchangers*, Data Sheet No. R14_0222, viewed 27 May 2023.

Akin, B, Bhardwaj, M & Warriner, J 2011, *Trapezoidal Control of BLDC Motors Using Hall Effect Sensors*, Application Report, Texas Instruments, Dallas, TX, United States, viewed 27 May 2023, <https://www.ti.com/lit/an/sprabz4/sprabz4.pdf>.

Baker, B 2019, *How to Precisely Determine Motor Angular Position and Velocity with a Resolver*, Digi-Key Electronics, Thief River Falls, Minnesota, USA, viewed 27 May 2023, <https://www.digikey.com.au/en/articles/how-to-precisely-determine-motor-angular-position-and-velocity-with-a-resolver>.

Baliga, B 2022, *History and Emerging Designs of Power Transistors*, Vol. 29 No. 3, IEEE, Online, viewed 27 May 2023, <https://www.ieee.org/ns/periodicals/EDS/EDS-JULY-2022-HTML/index.html>.

Barham, M 2017, *DESIGN AND DEVELOPMENT OF THE ELECTRICAL SYSTEMS IN AN ELECTRIC FORMULA SAE RACE CAR*, Masters Thesis, University of Canterbury, Christchurch, New Zealand.

Biyani, V, R, J, Eswar, T, Sourya, S, & K, P 2022, 'Comparative Study of Different Control Strategies in Permanent Magnet Synchronous Motor Drives', 2021 IEEE 5th International Conference on Condition Assessment Techniques in Electrical Systems (CATCON), IEEE, viewed 27 May 2023, <https://ieeexplore.ieee.org/document/9670516>.

Bourns Inc. 2022, *IGBT vs. MOSFET: Determining the Most Efficient Power Switching Solution*, white paper, Bourns, United States, viewed 27 May 2023, <https://www.bourns.com/docs/technical-documents/technical-library/igbt/bourns_igbt_vs_mosfet_determining_efficient_power_switching_solution_white_paper.pdf>.

BOM 2023, *Rainfall and temperature records*, Bureau of Meteorology, Australia, viewed 1 October 2023, <http://www.bom.gov.au/climate/extreme/records.shtml>.

Cascadia Motion 2023a, *About*, Cascadia Motion, Wilsonville, Oregon, USA, viewed 27 May 2023, <https://www.cascadiamotion.com/about>.

Cascadia Motion 2023b, *Contact*, Cascadia Motion, Wilsonville, Oregon, USA, viewed 27 May 2023, <https://www.cascadiamotion.com/contact>.

Case, D 2018, 'How to get into racing: Formula SAE opens doors on the tech side', *Autoweek*, 26 September, viewed 27 May 2023, <https://www.autoweek.com/racing/a1708031/how-break-racing-formula-sae-opens-doors-tech-side/>.

Daware, K 2015, *Difference between Synchronous Motor and Induction Motor*, Electrical Easy, viewed 27 May 2023, <https://www.electricaleasy.com/2015/06/difference-between-synchronous-and-induction-motor.html>.

De Novellis, L, Sorniotti, A & Gruber, P 2014, 'Wheel Torque Distribution Criteria for Electric Vehicles with Torque-Vectoring Differentials', *IEEE Transactions on Vehicular Technology*, Vol. 63, No. 4, viewed 24 August 2023, <https://ieeexplore-ieee-org.ezproxy.usq.edu.au/document/6656947>.

Divakar, B, Naidu, RSRK, Divya, G, Yugandhar, S, Deepak, GM & Sindhusha, D 2022, 'A Review On Brushless DC Motor Control Techniques ', *Journal of Pharmaceutical Negative Results*, Vol. 13, No. 7, viewed 27 May 2023, <https://www.pnrjournal.com/index.php/home/article/download/5930/7406/7168>.

DriveTrain Innovation 2023, *Contact*, DriveTrain Innovation, Thököly, Hungary, viewed 27 May 2023, <https://drivetraininnovation.com/contact>.

Electrical Engineering Toolbox 2015, *How to Test Three-Phase AC Motors*, Electrical Engineering Toolbox, viewed 27 May 2023, <https://www.electricalengineeringtoolbox.com/2015/12/how-to-test-three-phase-ac-motors.html>.

Electrical Engineering Toolbox 2016, *How to Measure Electric Motor Insulation Resistance*, Electrical Engineering Toolbox, viewed 27 May 2023, <https://www.electricalengineeringtoolbox.com/2016/02/how-to-measure-electric-motor.html>.

Element14 n.d., *STMICROELECTRONICS STM32F401RET6*, Element14, viewed 11 October 2023, < https://au.element14.com/productimages/standard/en_GB/GE64LQFP_STM32-40.jpg>.

EMRAX d.o.o. 2018, *Technical Data and Manual for EMRAX Motors / Generators*, Version No. 5.1, User Manual, EMRAX d.o.o., Kamnik, Slovenia, viewed 27 May 2023, <https://emrax.com/wp-content/uploads/2017/10/user_manual_for_emrax_motors.pdf>.

EMRAX d.o.o. 2020, *Recommended Controllers for EMRAX Motors*, Excel Spreadsheet, Version No. 5.3, EMRAX d.o.o., Kamnik, Slovenia, viewed 27 May 2023, <https://emrax.com/wp-content/uploads/2020/03/recommended_controllers_for_emrax_motors_5.3.xlsx>.

EMRAX d.o.o. 2022, *Motor Installation and Maintenance Manual*, Manual, Version No. 1.4, EMRAX d.o.o., Kamnik, Slovenia, viewed 27 May 2023, <https://emrax.com/wp-content/uploads/2022/11/Manual_1.4.pdf>.

Enepaq n.d., *Custom Battery Pack Design Services*, Enepaq, Lithuania, viewed 11 October 2023, <https://enepaq.com/wp-content/uploads/2023/02/Custom-Battery-Module-Design-Services-Battery-Management-System-BMS-And-Battery-Module-For-Prototype-And-Industrial-Application-1024x640.jpg>.

Endless Sphere 2023, *AXIOM: A 100kW Motor Controller*, Endless Sphere, viewed 27 May 2023, <https://endless-sphere.com/sphere/threads/axiom-a-100kw-motor-controller.89056/#p1458465>.

Faiz, A, Azam, N, Jidin, A, Ngatiman, N.A, Jopri, M.H, Manap, M, Herlino, A & Alias, F 2021, 'Current Control of BLDC Drives for EV Application', *IEEE 7th International Power Engineering and Optimization Conference*, 3-4 June 2013, Langkawi, Malaysia, pp.411-416.

Formula SAE 2023, *History of Formula SAE*, SAE International, Warrendale, PA, USA, viewed 09 April 2023, <https://fsaeonline.com/page.aspx?pageid=c4c5195a-60c0-46aa-acbf-2958ef545b72>.

References

Formula SAE-A 2023a, *Formula SAE-A*, SAE Australasia, Werribee, Victoria, Australia, viewed 10 April 2023, <https://www.saea.com.au/formula-sae-a>.

Formula SAE-A 2023b, *Formula SAE-A Participation History 2000 - 2022*, SAE Australasia, Werribee, Victoria, Australia, viewed 28 May 2023, <https://www.saea.com.au/fsae-history>.

Formula SAE-A 2023c, *LOCAL ADDENDUM TO FORMULA SAE 2023 RULES*, Version No. 1, Addendum, SAE Australasia, Werribee, Victoria, Australia, viewed 28 May 2023, <https://www.saea.com.au/content.cfm?page_id=1887467&current_category_code=21462 >.

Formula Student Germany 2023, *Competitions*, Formula Student Germany, Germany, viewed 27 May 2023, <https://www.formulastudent.de/world/competitions/>.

Frederiksen, A n.d., *Sensorless Vector Control Techniques* for Efficient Motor Control Continues, Analog Devices, Norwood, Massachusetts, United States, viewed 27 May 2023, <https://www.analog.com/en/technical-articles/sensorless-vector-control-techniques.html>.

FS World 2023, *Formula Student past achievements for University of Southern Queensland*, Formula Student Germany, Germany, viewed 27 May 2023, <https://fs-world.org/p2.php?u=493&c=1>.

Gravovac, D & Purschel, M 2009, *IGBT Power Losses Calculation Using the Data-Sheet Parameters*, Version No. 1.1, Application Note, Infineon Technologies, Munich, Germany, viewed 27 May 2023, <https://community.infineon.com/gfawx74859/attachments/gfawx74859/IGBT/1341/1/IGBT%20Power%20Losses%20Calculation%20using%20the%20Data%20Sheet%20Parameters.pdf>.

Hackaday 2019, *Axiom_Rev1_schematic*, Hackaday, viewed 27 May 2023, <https://cdn.hackaday.io/files/1649327056450688/Axiom_Rev1_schematic.pdf >.

Hackaday 2023, *AXIOM 100kW+ Motor Controller*, Hackaday, viewed 27 May 2023, <https://hackaday.io/project/164932-axiom-100kw-motor-controller>.

Hackaday n.d., *Image [Axiom Controller]*, Hackaday, viewed 27 May 2023, <https://cdn.hackaday.io/images/5871221560546934778.png>.

Hanejko, F 2022, 'Induction vs Permanent Magnet Motor Efficiency for Auto Electrification', Blog Post, Horizon Technology, viewed 27 May 2023, <https://www.horizontechnology.biz/blog/induction-vs-permanent-magnet-motor-efficiency-auto-electrification>.

Ibrahim, N, Abdelaziz, M, Ghoneima, M & Hammad, S 2020, 'Implementation of vector control on electric vehicle traction system', *Bulletin of the National Research Centre*, Vol. 44, No. 22, Springer Open, viewed 27 May 2023, <https://bnrc.springeropen.com/articles/10.1186/s42269-019-0258-8>.

Infineon Technologies 2002, *How to Select the Right CoolMOS™*, Version No. 1.2, Application Note, Infineon Technologies, Munich, Germany, viewed 27 May 2023, <https://www.infineon.com/dgdl/Infineon-ApplicationNote_MOSFET_CoolMOS_How_to_select_the_right_CoolMOS-AN-v01_00-EN.pdf?fileId=db3a304412b407950112b40acf580693>

Infineon Technologies 2016, CIPOS Inverter IPM Reference Board Type 3 for 3 -Shunt Resistor – AN2016-12, Application Note, Version No. 1.11, Infineon Technologies, Munich, Germany, viewed 27 May 2023, <https://www.infineon.com/dgdl/Infineon-

References

CIPOS_Mini_Inverter_module_reference_board_type3_for_3-shunt_resistor-ApplicationNotes-v01_11-EN.pdf?fileId=5546d462566bd0c7015674af23662589>.

Infineon Technologies 2017, FF225R12ME4P datasheet, Product Datasheet, Version No. 3.0, Infineon Technologies, Munich, Germany, viewed 27 May 2023, <https://www.infineon.com/dgdl/Infineon-FF225R12ME4P-DS-v03_00-EN.pdf?fileId=5546d4625b3ca4ec015b3e4257d506a6>.

Infineon Technologies 2019, *Block Commutation vs. FOC in power tool motor control*, Application Note, Version No. 1.0, Infineon Technologies, Munich, Germany, viewed 27 May 2023, <https://www.infineon.com/dgdl/Infineon-Motor_power_tool_Block_Commutation_vs_FOC-ApplicationNotes-v01_00-EN.pdf?fileId=5546d4626eab8fbf016ed37fee474a65>.

Infineon Technologies 2021, *IM535-U6D/IM535-U6DS Datasheet*, Infineon Technologies, Munich, Germany, viewed 27 May 2023, <https://www.infineon.com/dgdl/Infineon-IM535-U6D-DataSheet-v02_01-EN.pdf?fileId=5546d4627506bb3201754a6d015075fd>.

Infineon Technologies 2022, *IMW120R007M1H Datasheet*, Product Datasheet, Version 01.10, Infineon Technologies, Munich, Germany, viewed 27 May 2023, <https://www.infineon.com/dgdl/Infineon-IMW120R007M1H-DataSheet-v01_10-EN.pdf?fileId=8ac78c8c7f2a768a017f8783822631b2>.

Infineon Technologies 2023, *IMC301A-F064*, Infineon Technologies, Munich, Germany, viewed 27 May 2023, <https://www.infineon.com/cms/en/product/power/motor-control-ics/imotion-integrated/imc301a-f064/>.

Intel n.d., *Moore's Law*, Intel, Santa Clara, California, USA, viewed 27 May 2023, <https://www.intel.com/content/www/us/en/history/virtual-vault/articles/moores-law.html>.

Jenkins, J 2022, 'A closer look at Brushed AC motors in EVs', *Charged EVs*, 7 August, viewed 27 May 2023, <https://chargedevs.com/features/a-closer-look-at-brushed-ac-motors-in-evs/>.

Johnson, S 2022, 'THE RIGHT STUFF', *The Red Bulletin*, 26 April, viewed 27 May 2023, <https://www.redbull.com/us-en/theredbulletin/global-formula-racing-formula-sae>.

Keating, R 2022, 'Why use Permanent Magnet Motors?', Fisher & Paykel Technologies, viewed 27 May 2023, <https://www.fisherpaykeltechnologies.com/knowledge-hub/why-use-permanent-magnet-motors>.

Koolance 2023, *PMP-500 Pump, G 1/4 BSP*, Koolance, Auburn, WA, USA, viewed 2 October 2023, <https://koolance.com/pmp-500-pump-g-1-4-bsp>.

MathWorks n.d.a, *Six-Step Commutation*, MathWorks, Natick, Massachusetts, United States, viewed 27 May 2023, <https://au.mathworks.com/help/mcb/gs/six-step-commutation.html>.

MathWorks n.d.b, *Clarke and Park Transforms*, MathWorks, Natick, Massachusetts, United States, viewed 27 May 2023, <https://au.mathworks.com/solutions/electrification/clarke-and-park-transforms.html>.

MathWorks n.d.c, *Field Oriented Control (FOC)*, MathWorks, Natick, Massachusetts, United States, viewed 27 May 2023, <https://au.mathworks.com/help/mcb/gs/implement-motor-speed-control-by-

References

using-field-oriented-control-foc.html?searchHighlight=field%20oriented&s_tid=srchtitle_field%20oriented_2>.

MathWorks n.d.d, *Hardware-in-the-Loop (HIL)*, MathWorks, Natick, Massachusetts, United States, viewed 12 August 2023, <https://au.mathworks.com/discovery/hardware-in-the-loop-hil.html>.

Marulasiddappa, HB & Pushparajesh, V 2021, 'Review on different control techniques for induction motor drive in electric vehicle', *IOP Conference Series: Materials Science and Engineering*, Vol. 1055, viewed 27 May 2023, <https://iopscience.iop.org/article/10.1088/1757-899X/1055/1/012142/pdf>.

Microsemi 2013, *Park, Inverse Park, Clarke, Inverse Clarke Transformations MSS Software Implementation User Guide*, User Guide, Microchip Technology, Chandler, Arizona, United States, viewed 27 May 2023, <https://www.microsemi.com/document-portal/doc_view/132799-park-inverse-park-and-clarke-inverse-clarke-transformations-mss-software-implementation-user-guide>.

Mikros Technologies n.d., *IGBT Liquid Cooling*, Mikros Technologies, Claremont, NH, United States, viewed 27 May 2023, <https://www.mikrostechnologies.com/home/applications/renewable-energy/>.

Nanda, G & Kar, N.C 2006, 'A SURVEY AND COMPARISON OF CHARACTERISTICS OF MOTOR DRIVES USED IN ELECTRIC VEHICLES', *2006 Canadian Conference on Electrical and Computer Engineering*, Ottawa, May 2006, pp.811-814

ODrive Robotics 2020, *Motor Controller Design Question*, ODrive Robotics, United States, viewed 27 May 2023, <https://discourse.odriverobotics.com/t/motor-controller-design-question/5980>.

ODrive Robotics 2023a, *ODrive Pro*, ODrive Robotics, United States, viewed 27 May 2023, <https://odriverobotics.com/shop/odrive-pro>.

ODrive Robotics 2023b, *V 0.5.6 – Getting Started*, ODrive Robotics, United States, viewed 27 May 2023, <https://docs.odriverobotics.com/v/0.5.6/getting-started.html>.

Power Integrations n.d., *2SP0115T*, Power Integrations, UK, viewed 27 September 2023, <https://www.power.com/products/scale-2-plug-and-play-drivers/2sp0115t>.

Power Integrations 2019, *2SP0115T2A0-12 Data Sheet*, Version 2.0, Datasheet, Power Integrations, UK, viewed 27 September 2023, <https://www.power.com/downloads/documents/2SP0115T2A0-12.pdf>.

Prohelion 2021a, *WaveSculptor 200 Motor Drive User's Manual*, Prohelion, Brisbane, Australia, Version 1, viewed 27 May 2023, <https://www.prohelion.com/wp-content/uploads/2021/11/PHLN74.021v1-Users-Manual.pdf>.

Prohelion 2021b, *WaveSculptor Config Software User's Manual*, Prohelion, Brisbane, Australia, Version 1, viewed 27 May 2023, <https://www.prohelion.com/wp-content/uploads/2021/08/PHLN4.040v1-Wavesculptor-Config-software-users-manual.pdf>.

Prohelion 2021c, *EV Drivers Control User's Manual*, Prohelion, Brisbane, Australia, Version 1, viewed 27 May 2023, <https://www.prohelion.com/wp-content/uploads/2021/08/PHLN86.002v4-EV-Driver-Controls-Users-Manual.pdf>.

References

Prohelion 2021d, *CAN-Ethernet Bridge User's Manual*, Prohelion, Brisbane, Australia, Version 1, viewed 27 May 2023, <https://www.prohelion.com/wp-content/uploads/2021/10/PHLN82.002v1-CAN-Ethernet-Bridge-Users-Manual.pdf>.

Prohelion 2021e, - *WaveSculptor Motor Interface: Type 3 – Resolver & PT100*, Prohelion, Brisbane, Australia, Version 1, viewed 27 May 2023, <https://www.prohelion.com/wp-content/uploads/2022/03/PHLN74.032v1-Motor-Interface-Datasheet-Type-3.pdf>.

Prohelion 2023a, *Tritium WaveSculptor*, Prohelion, Brisbane, Australia, viewed 27 May 2023, <https://docs.prohelion.com/Profinity/Tritium_WaveSculptor.html>.

Prohelion 2023b, *Home Page*, Prohelion, Brisbane, Australia, viewed 27 May 2023, < https://www.prohelion.com/>.

Renesas n.d., 'BLDC Motor Control Algorithms', Renesas, viewed 27 May 2023, <https://www.renesas.com/us/en/application/key-technology/motor-control-robotics/bldc-motor-control-algorithms>.

Repas, R 2007, 'Field-oriented control for motors', *Machine Design*, 8 November, viewed 27 May 2023, <https://www.machinedesign.com/news/article/21816702/fieldoriented-control-for-motors>.

SAE International 2022, *Formula SAE Rules 2023*, Version No. 2.0, Competition Rules, SAE International, Warrendale, PA, USA, viewed 10 April 2023 <https://www.fsaeonline.com/cdsweb/gen/DownloadDocument.aspx?DocumentID=96d652ca-a506-444e-917a-dbf695321ab3>.

SAE International 2023a, *University Programs*, SAE International, Warrendale, PA, USA, viewed 09 April 2023, <https://www.sae.org/attend/student-events>.

SAE International 2023b, *About Formula SAE Electric*, SAE International, Warrendale, PA, USA, viewed 27 May 2023, <https://www.sae.org/attend/student-events/formula-sae-electric/about>.

SAE International 2023c, *Formula SAE Rules*, Version No. 2.0, SAE International, Warrendale, PA, USA, viewed 27 May 2023, < https://www.fsaeonline.com/cdsweb/gen/DownloadDocument.aspx?DocumentID=96d652ca-a506-444e-917a-dbf695321ab3>.

Schweber, B. n.d., *Industrial Motor Control: Using MOSFETs to Drive Motor Performance*, web page, Mouser Electronics, Mansfield, TX, viewed 27 May 2023, <https://au.mouser.com/applications/industrial-motor-control-mosfets/>

Sensata 2023, *Precharge Calculator*, Sensata Technologies, viewed 27 May 2023, <https://www.sensata.com/calculator/precharge>.

Society of Automotive Engineers - Australasia 2022, *Formula SAE-A 2022 Final Results – EV Class*, Results Table, Formula SAE – Australasia, Victoria, Australia, viewed 9 October 2023, <https://www.saea.com.au/client_images/2458436.pdf>.

Specialty Steel Industry of North America (SSINA) n.d., 'Galvanic Corrosion', SSINA, viewed 27 May 2023, <https://www.ssina.com/education/corrosion/galvanic-corrosion/>.

References

ST Microelectronics 2019, *AN5397 – Current Sensing in motion control applications*, Rev 1, Application Note, STMicroelectronics International N.V., Geneva, Switzerland, viewed 19 April 2023, <https://www.st.com/resource/en/application_note/an5397-current-sensing-in-motion-control-applications-stmicroelectronics.pdf>.

ST Microelectronics 2021a, *UM1943 – Getting started with the X-NUCLEO-IHM07M1 motor driver expansion board based on the L6230 for STM32 Nucleo*, Rev 2, User Manual, STMicroelectronics International N.V., Geneva, Switzerland, viewed 19 April 2023, <https://www.st.com/resource/en/user_manual/um1943-getting-started-with-the-xnucleoihm07m1-motor-driver-expansion-board-based-on-the-l6230-for-stm32-nucleo-stmicroelectronics.pdf>.

ST Microelectronics 2021b, *DB2665 – Three-phase brushless DC motor driver expansion board based on L6230 for STM32 Nucleo*, Rev 2, Data Brief, STMicroelectronics International N.V., Geneva, Switzerland, viewed 19 April 2023, <https://www.st.com/resource/en/data_brief/x-nucleo-ihm07m1.pdf>.

ST Microelectronics 2023a, *AN4277 - Using STM32 device PWM shut-down features for motor control and digital power conversion*, STMicroelectronics, Geneva, Switzerland, viewed 27 May 2023, <https://www.st.com/resource/en/application_note/an4277-using-stm32-device-pwm-shutdown-features-for-motor-control-and-digital-power-conversion-stmicroelectronics.pdf>.

ST Microelectronics 2023b, *AN 4013 - STM32 cross-series timer overview*, STMicroelectronics, Geneva, Switzerland, viewed 27 May 2023, <https://www.st.com/resource/en/application_note/an4013-stm32-crossseries-timer-overview-stmicroelectronics.pdf>.

ST Microelectronics n.d.a, *3-Phase 6-Step Control*, STMicroelectronics, Geneva, Switzerland, viewed 27 May 2023, <https://www.st.com/en/applications/industrial-motor-control/3-phase-6-step-control.html>.

ST Microelectronics n.d.b, *Sensorless Field-Oriented Control of PMSM Using STM32 Processor Based Boards*, Geneva, Switzerland, viewed 27 May 2023, <https://au.mathworks.com/help/ecoder/stmicroelectronicsstm32f4discovery/ug/senorless-stm-example.html>.

ST Microelectronics n.d.c, *L6230 - DMOS driver for three-phase brushless DC motor*, Geneva, Switzerland, viewed 27 May 2023, <https://www.st.com/en/motor-drivers/l6230.html?rt=um&id=UM1943>.

Tennessee Technological University n.d., *Chapter 5: Control Scheme and Controller Design for Induction Motor Drives*, Tennessee Technological University, Cookeville, TN, United States, viewed 27 May 2023, <https://www.tntech.edu/engineering/pdf/cesr/ojo/asuri/Chapter5.pdf>.

Texas Instruments 2023, *LAUNCHXL-F28379D*, Texas Instruments, Dallas, Texas, United States, viewed 27 May 2023, <https://www.ti.com/tool/LAUNCHXL-F28379D>.

Toshiba 2019, *Smooth, quiet and efficient motion*, White Paper, TOSHIBA ELECTRONICS EUROPE GMBH, Dusseldorf, Germany, viewed 27 May 2023, <https://toshiba.semicon-storage.com/content/dam/toshiba-ss-v3/master/en/semiconductor/design-development/innovationcentre/whitepapers/TCM0200A_ENG.pdf>.

References

Trampa Boards 2023a, *VESC*, Trampa Boards, Nottingham, UK, viewed 27 May 2023, <https://trampaboards.com/vesc--c-1434.html>.

Trampa Boards 2023b, *VESC 100V 250A in CNC T6 Silicone Sealed Aluminium Box*, Trampa Boards, Nottingham, UK, viewed 27 May 2023, <https://trampaboards.com/vesc-100v-250a-in-cnc-t6-silicone-sealed-aluminum-box--p-28113.html>.

TWI Global n.d., *What is galvanic corrosion and how can it be Prevented?*, TWI Global, Cambridge, United Kingdom, viewed 27 May 2023, <https://www.twi-global.com/technical-knowledge/faqs/faq-what-is-galvanic-corrosion-and-how-can-it-be-avoided>.

Unitek Industrie Elektronik 2023, *Contacts*, Unitek Industrie Elektronik, Leutenbach, Germany, viewed 27 May 2023, <https://www.unitek-industrie-elektronik.de/contacts>.

UQ Racing 2023, *Past Cars: 2022 EV - Capybara*, Photograph, UQ Racing, Brisbane, Australia, viewed 27 May 2023, <https://www.uqracing.com/past-cars/2022-ev>.

Varma, SS 2018, 'Thermal Management Techniques for Optimal Design', *Electronics For You*, 19 October, viewed 27 May 2023, <https://www.electronicsforu.com/technology-trends/tech-focus/thermal-management-techniques-optimal-design>.

Vedder, B 2016, *VESC – Open Source ESC*, Blog Post, viewed 27 May 2023, <http://vedder.se/2015/01/vesc-open-source-esc/>.

VESC Project 2023, *VESC Project*, VESC Project, viewed 27 May 2023, <https://vesc-project.com/>.

Vishay 2017, *1N4148 - Small Signal Fast Switching Diodes*, Data Sheet No. 91000, viewed 27 May 2023, , <https://www.vishay.com/docs/81857/1n4148.pdf>.

Weigl, O 2022, *ODrive High Performance Motor Control*, Hackaday, viewed 27 May 2023, <https://hackaday.io/project/11583-odrive-high-performance-motor-control>.

References

Project Specification

ENG4111/4112 Research Project

Project Specification

For: Samuel Baker

Title: Motor Commissioning Tests for FSAE Application

Major: Power Engineering

Supervisor: Tony Ahfock

Enrollment: ENG4111 – EXT S1, 2022

                ENG4112 – EXT S2, 2023

Project Aim:

• Commission the 228 HV EMRAX in support of the first USQ Racing vehicle.

• Support the ongoing development of the USQ Racing team, and FSAE Electric community in general, through the design of a low cost and customisable electric motor controller and simulation platform.

Programme: Version 2, 16th March 2023

1. Conduct initial background research on the motor and the verification tests required for the commissioning. Obtain the manufacturers manual for the motor and Prohelion controller, as well as any additional information regarding specific testing requirements. Research applicable standards and competition rules that the motor and installation must comply with for its intended use.
2. Identify suitable components for the development of a motor controller, as well as review commercial off-the-shelf and open-source motor controllers to identify proven design configurations.
3. Design and organise the fabrication of brackets for mounting the motor to the Energy Systems Laboratory DC Machine.
4. Identify and document the testing procedures required for the commissioning of the EMRAX 228 motor.
5. Select and procure the materials and components required for the construction of the motor controller.
6. Design and organise the manufacture of a PCB for the motor controller construction.
7. Organise the power supply and additional equipment for the functional testing of the motor controller.
8. Analyse controller test results and confirm its suitability for further development of the USQ FSAE vehicle.

If time and resource permit:

Appendix A

9. Initiate loaded testing in the USQ Racing Formula SAE vehicle.
10. Experiment with output gearing to optimise the powertrain performance.

Appendix A

Appendix B

Datasheets

CONTENTS

EMRAX 228 Technical Data Table (dynamometer test data)

Type / Technical data	EMRAX 228 High Voltage			EMRAX 228 Medium Voltage			EMRAX 228 Low Voltage		
Air cooled = AC Liquid cooled = LC Combined cooled = Air + Liquid cooled = CC	AC	LC	CC	AC	LC	CC	AC	LC	CC
Ingress protection	IP21	IP65	IP21	IP21	IP65	IP21	IP21	IP65	IP21
Cooling medium specification (Air Flow = AF; Inlet Water/glycol Flow = WF; Ambient Air = AA) If inlet WF temperature and/or AA temperature are lower, then continuous power is higher.	AF=20m/s AA=25°C	WF=8l/min at 50°C; AA=25°C	WF=8l/min at 50°C; AA=25°C	AF=20m/s AA=25°C	WF=8l/min at 50°C; AA=25°C	WF=8l/min at 50°C; AA=25°C	AF=20m/s AA=25°C	WF=8l/min at 50°C; AA=25°C	WF=8l/min at 50°C; AA=25°C
Weight [kg]	12,0	12,4	12,3	12,0	12,4	12,3	12,0	12,4	12,3
Diameter ø / width [mm]	228/86								
Maximal battery voltage [Vdc] and full load/no load RPM	670 Vdc (5300/6500 RPM)			470 Vdc (5170/6500 RPM)			130 Vdc (4400/5200 RPM)		
Peak motor power at max RPM (few min at cold start / few seconds at hot start) [kW]	100								
Continuous motor power (at 3000-5000 RPM) depends on the motor RPM [kW]	28 - 42	28 - 42	35 - 55	28 - 42	28 - 42	35 - 55	28 - 42	28 - 42	35 - 55
Maximal rotation speed [RPM]	5500 (6500 RPM peak for a few seconds) (with maximal battery voltage or magnetic field weakening)								
Maximal motor current (for 2 min if cooled as described in Manual) [Arms]	240			340			900		
Continuous motor current [Arms]	115			160			450		
Maximal motor torque (for a few seconds) [Nm]	230								
Continuous motor torque [Nm]	120								
Torque / motor current [Nm/1Aph rms]	1,1			0,75			0,27		
Maximal temperature of the copper windings in the stator and max. temperature of the magnets [°C]	120								
Motor efficiency [%]	92 – 97								
Internal phase resistance at 25 °C [mΩ]	19			8,0			1,2		
Input phase wire cross-section [mm²]	10,2			15,2			38		
Wire connection	star								
Induction in Ld/Lq [µH] of 1 phase	177/183			76/79			10,3/10,6		
Controller / motor signal	sine wave								
AC voltage between two phases [Vrms/1RPM]	0,0730			0,0478			0,0176		
Specific idle speed (no load RPM) [RPM/1Vdc]	9,8			14			40		
Specific load speed (depends on the controller settings) [RPM/1Vdc]	8 – 9,8			11 – 14			34 – 40		
Magnetic field weakening (for higher RPM at the same power and lower torque) [%]	up to 100								
Magnetic flux – axial [Vs]	0,0542			0,0355			0,0131		
Temperature sensor on the stator windings	kty 81/210								
Number of pole pairs	10								
Rotor inertia LC motor [kg*m²]	0,0383								
Bearings (front:back) - SKF/FAG	6206:6206 (for radial forces) or 6206:7206 (for axial-radial forces; for pull mode; focusing on very high axial load, e.g. air propeller) or 6206:3206 (for axial-radial forces; for pull-push mode, α=25°); other bearings are possible (exceptionally)								

LTN

LTN Servotechnik GmbH

Resolver

RE-15

- Hollow shaft Ø: 12 mm max.
- Outer Ø: 36.8 mm
- Length: 16 mm

RE-21

- Hollow shaft Ø: 17 mm max.
- Outer Ø: 52.4 mm
- Length: 26 mm
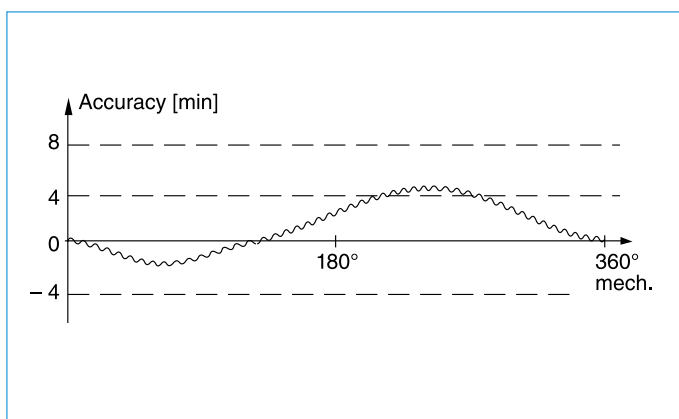
Main features

- Operating temperature: –55°C ... +155°C
- Permissible speed: 20,000 rpm max.

- Accuracy absolute: ±4'/±6'/±10'
- Accuracy ripple: 1' max.

- Rotor and stator completely impregnated

- 1/2/3/4 pole pairs

LTN Servotechnik GmbH

Operating Principle

A resolver is a rotary transformer that provides information on the rotor position angle θ.

The stator bobbin winding is energized with an AC voltage E_{R1-R2}. This AC voltage is transferred to the rotor winding with transformation ratio **Tr**.

The AC voltage then induces the voltages E_{S1-S3} and E_{S2-S4} into the two output windings of the stator.

The magnitude of the output voltages vary with the sine and the cosine of the rotor position angle θ, because the two secondary windings are shifted by 90°.

Input: E_{R1-R2}

Output: E_{S1-S3}
E_{S2-S4}
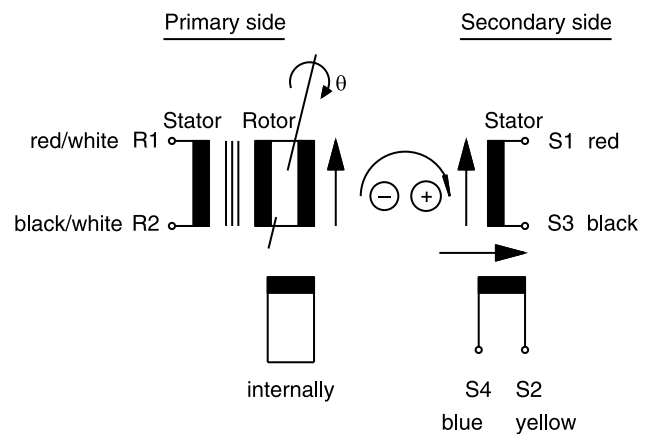
Input Signal:

$$E_{R1-R2} = E_0 \sin(\omega t)$$
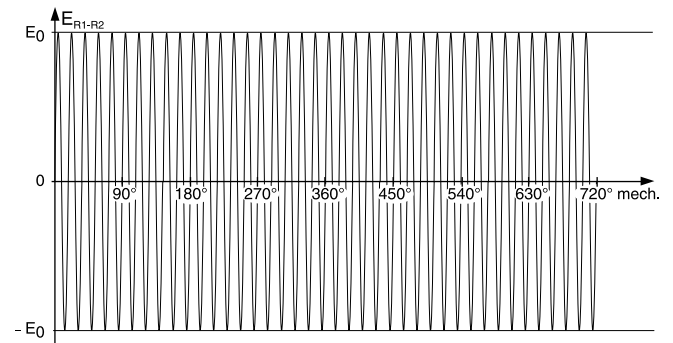
Output Signal:

$$E_{S1-S3} = Tr \cdot E_{R1-R2} \cdot \cos\theta$$
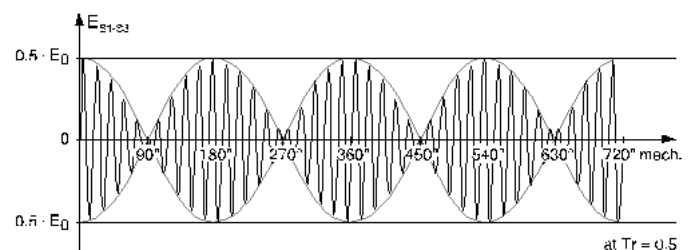
Output Signal:

$$E_{S2-S4} = Tr \cdot E_{R1-R2} \cdot \sin\theta$$

LTN Servotechnik GmbH
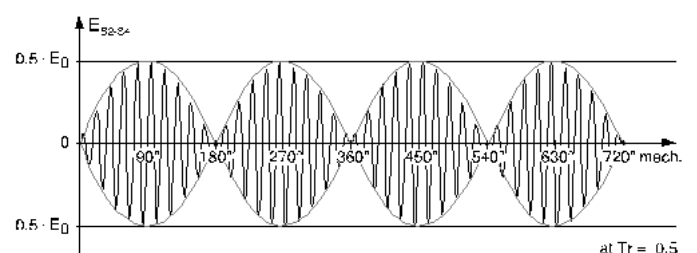
Accuracy

The accuracy ε is defined as the difference between the electrical angle θ_{el}, indicated by the output voltages of the secondary windings, and the mechanical angle or rotor position angle θ_{mech}:

accuracy (ε) = electrical angle (θ_{el}) – mechanical angle (θ_{mech})

For each LTN resolver the accuracy is indicated in the data sheet by the terms 'accuracy absolute', 'accuracy spread' and 'accuracy ripple'.

The **'accuracy absolute'** or the **'accuracy spread'** is caused by the internal error of the resolver and the mounting error resulting in 1st and 2nd order harmonics of the sinusoidal signal.

At low speeds the **'accuracy ripple'** effects the speed stability of a drive. This ripple is caused by 3rd and higher order harmonics. To ensure smooth drive performance even at low speeds LTN resolvers have an accuracy ripple of <u>less than 1'</u>. It is achieved by a patented procedure of stepping two lamination assemblies in the rotor.
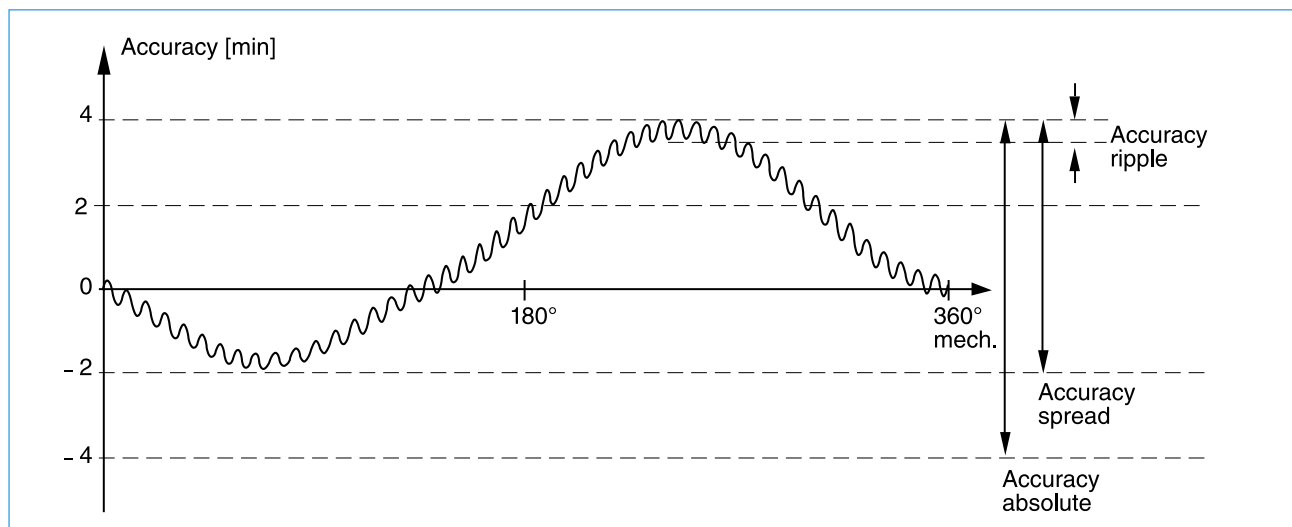
Straight lamination assembly:
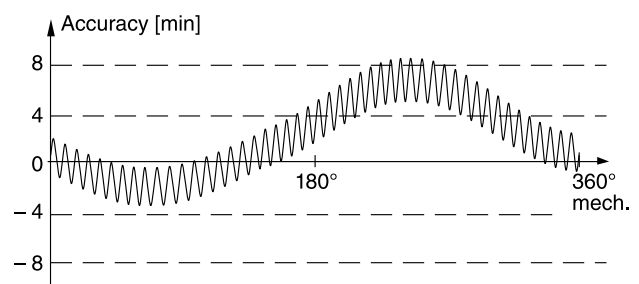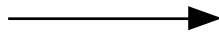
Stepped lamination assembly:
(LTN patent)

LTN

LTN Servotechnik GmbH
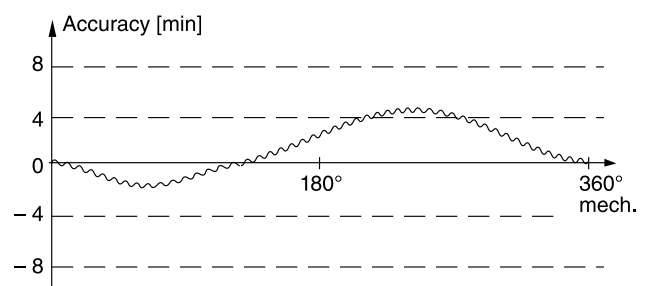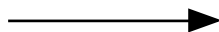
Resolver RE-15: Selection Guide for Electrical Data

Various mechanical versions available

| Basic Model	RE-15-1-A14		RE-15-1-K01		RE-15-1-V07		RE-15-3-D04		RE-15-4-D04	
Primary Side	R1 – R2									
Pole Pairs	1						3		4	
Transformation Ratio	0.5 ± 0.05									
Input Voltage	7 V$_{rms}$	7 V$_{rms}$	5 V$_{rms}$	5 V$_{rms}$	7 V$_{rms}$	7 V$_{rms}$	7 V$_{rms}$	7 V$_{rms}$	7 V$_{rms}$	7 V$_{rms}$
Input Current	58 mA	36 mA	48 mA	17 mA	58 mA	36 mA	50 mA	24 mA	16 mA	10 mA
Input Frequency	5 kHz	10 kHz	1 kHz	4.5 kHz	5 kHz	10 kHz	4 kHz	10 kHz	5 kHz	10 kHz
Phase Shift (± 3°)	8°	–6°	26°	0°	8°	–6°	15°	0°	15°	1°
Null Voltage	30 mV max.									
Impedance Z_{ro} in Ω Z_{rs} in Ω Z_{so} in Ω Z_{ss} in Ω	75 j 98 70 j 85 180 j 230 170 j 200	110 j 159 96 j 150 245 j 400 216 j 370	55 j 87 62 j 81 248 j 105 256 j 88	164 j 255 145 j 210 315 j 340 278 j 280	75 j 98 70 j 85 180 j 230 170 j 200	110 j 159 96 j 150 245 j 400 216 j 370	74 j 120 78 j 110 430 j 450 435 j 410	145 j 250 135 j 240 570 j 1030 535 j 970	208 j 393 207 j 375 831 j 2496 840 j 2396	319 j 657 306 j 636 939 j 4272 899 j 4145
D.C. Resistance (± 10%) Rotor Stator	40 Ω 102 Ω		17.5 Ω 200 Ω		40 Ω 102 Ω		34 Ω 380 Ω		58 Ω 659 Ω	
Accuracy	±10', ±6' on request				± 4'		± 5'		± 6'	
Accuracy Ripple	1' max.						3' max.		3' max.	
Operating Temperature	–55°C ... +155°C									
Max. Permissible Speed	20,000 rpm									
Shock (11 ms)	≤ 1000 m/s^2									
Vibration (10 to 500 Hz)	≤ 500 m/s^2									
Weight Rotor/Stator	25 g / 60 g		25 g / 70 g		25 g / 60 g		25 g / 60 g		25 g / 60 g	
Rotor Moment of Inertia	0.02 × 10^{-4} kgm^2									
Hi-pot Housing/Winding	500 V min.									
Hi-pot Winding/Winding	250 V min.									
Rotor	Completely impregnated									
Stator	Completely impregnated									
Length of stator	16.1 mm		21.3 mm		20.0 mm		16.1 mm		16.1 mm	

The selection guide and the mounting dimensions contain a sample of resolvers designed and manufactured by LTN. The performance parameters and mechanical dimensions can also be used as a guideline for new mechanical or electrical designs to satisfy your future requirements with an innovative, cost effective solution.

Housed bearing-type resolvers are also designed and manufactured by LTN, but not subject to this data sheet. Please contact us for further information.

LTN Servotechnik GmbH

Resolver RE-15: Mounting Dimensions

RE-15-1: Version A/B
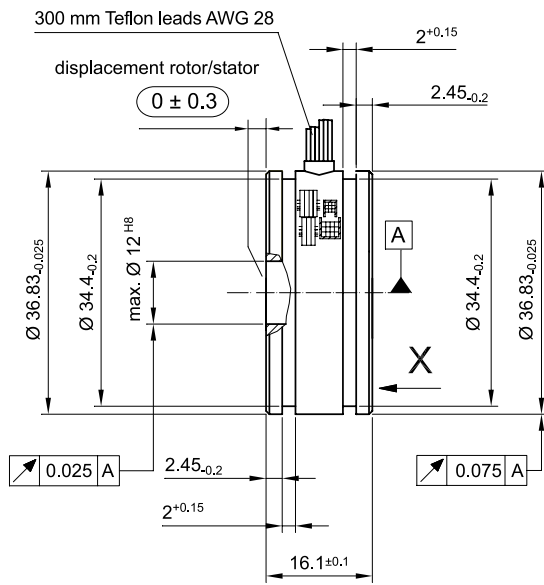
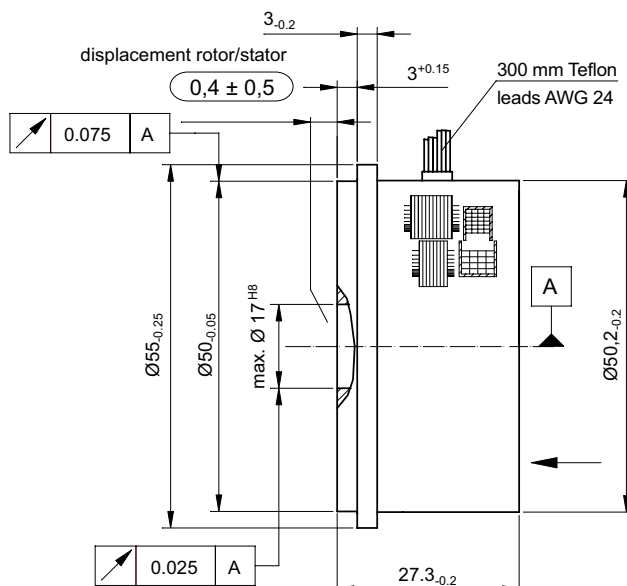Inner diameter stator = 22.800 min.
Outer diameter rotor = 22.325 max.

Positive counting direction:
Rotor cw as viewed from bobbin end (X ←)

Dimensions in mm

RE-15-1: Version C/D
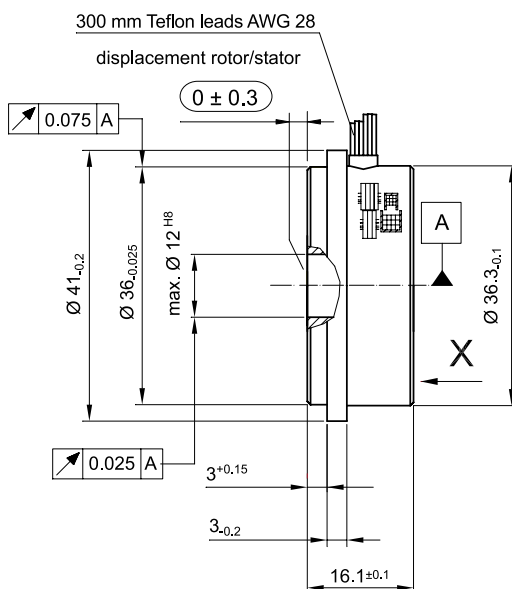
Inner diameter stator = 22.800 min.
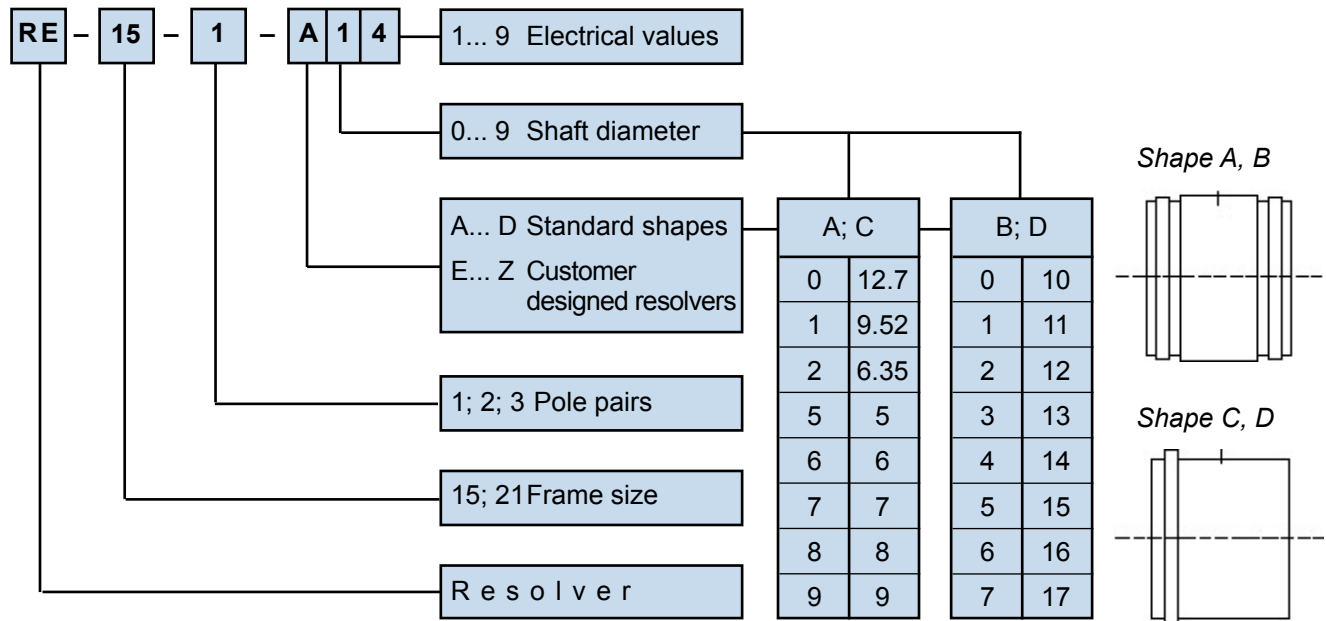Outer diameter rotor = 22.325 max.

Positive counting direction:
Rotor cw as viewed from bobbin end (X ←)

Dimensions in mm

LTN

LTN Servotechnik GmbH

Resolver RE-21: Selection Guide for Electrical Data

Various mechanical versions available

Basic Model	RE-21-1-A01		RE-21-1-A06		RE-21-1-A05		RE-21-1-K05		RE-21-3-A03	
Primary Side	R1 – R2									
Pole Pairs	1								3	
Transformation Ratio	1.0 ± 0.1		0.5 ± 0.05							
Input Voltage	7 V$_{rms}$	7 V$_{rms}$	7 V$_{rms}$	7 V$_{rms}$	7 V$_{rms}$	7 V$_{rms}$	5 V$_{rms}$	5 V$_{rms}$	7 V$_{rms}$	7 V$_{rms}$
Input Current	40 mA	30 mA	47 mA	30 mA	70 mA	56 mA	32 mA	17 mA	70 mA	40 mA
Input Frequency	5 kHz	10 kHz	5 kHz	10 kHz	5 kHz	7 kHz	1 kHz	4,5 kHz	5 kHz	10 kHz
Phase Shift (± 3°)	11°	−7.5°	8°	−8°	6°	−3°	26°	−6°	12°	1°
Null Voltage	30 mV max.									
Impedance Z$_{ro}$ in Ω Z$_{rs}$ in Ω Z$_{so}$ in Ω Z$_{ss}$ in Ω	133 j 115 122 j 105 800 j 1454 740 j 1230	170 j 200 149 j 190 1310 j 2400 1150 j 2270	92 j 120 82 j 100 154 j 275 140 j 240	122 j 203 103 j 185 245 j 454 202 j 415	78 j 84 70 j 75 114 j 205 101 j 184	88 j 108 76 j 100 138 j 263 117 j 243	86 j 108 92 j 95 195 j 210 205 j 178	180 j 375 150 j 330 390 j 695 325 j 615	55 j 85 53 j 80 105 j 335 104 j 312	77 j 154 71 j 145 175 j 624 160 j 590
D. C. Resistance (± 10°) Rotor Stator	90 Ω 260 Ω		56 Ω 53 Ω		48 Ω 31 Ω		47 Ω 143 Ω		34 Ω 58 Ω	
Accuracy	±6', ±4' on request									
Accuracy Ripple	1' max.									
Operating Temperature	−55°C ... +155°C									
Max. Permissible Speed	20,000 rpm									
Shock (11 ms)	≤ 1000 m/s^2									
Vibration (10 to 500 Hz)	≤ 500 m/s^2									
Weight Rotor/Stator	90 g / 200 g									
Rotor Moment of Inertia	0.14 × 10^{-4} kgm^2									
Hi-pot Housing/Winding	500 V min.									
Hi-pot Winding/Winding	250 V min.									
Rotor	Completely impregnated									
Stator	Completely impregnated									
Length of stator	25.6 mm									

The selection guide and the mounting dimensions contain a sample of resolvers designed and manufactured by LTN. The performance parameters and mechanical dimensions can also be used as a guideline for new mechanical or electrical designs to satisfy your future requirements with an innovative, cost effective solution.

Housed bearing-type resolvers are also designed and manufactured by LTN, but not subject to this data sheet. Please contact us for further information.

LTN Servotechnik GmbH

Resolver RE-21: Mounting Dimensions

RE-21-1: Version A/B
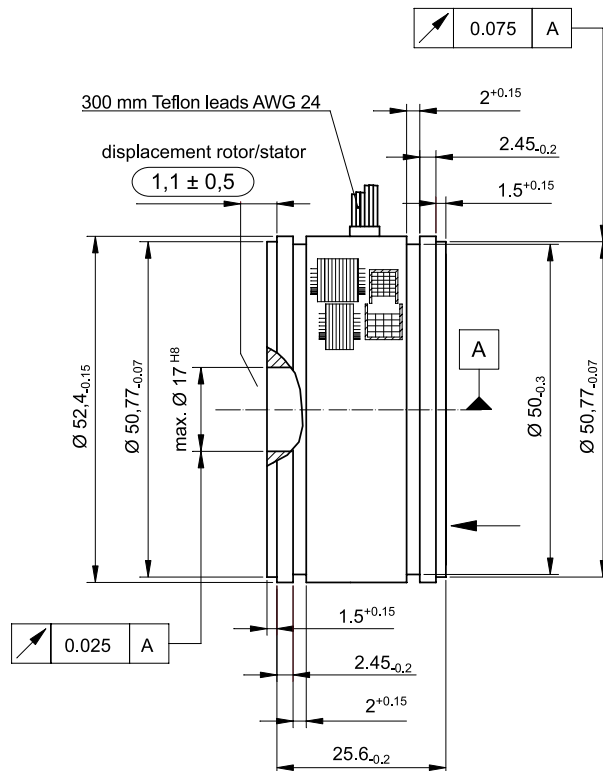
Inner diameter stator = 33.470 min.
Outer diameter rotor = 32.735 max.

Positive counting direction:
Rotor cw as viewed from bobbin end (X ←)

Dimensions in mm

RE-21-1: Version C/D

Inner diameter stator = 33.470 min.
Outer diameter rotor = 32.735 max.

Positive counting direction:
Rotor cw as viewed from bobbin end (X ←)

Dimensions in mm

LTN Servotechnik GmbH

Ordering Information

| RE | – | 15 | – | 1 | – | A | 1 | 4 |

	A; C		B; D	
0	12.7	0	10
1	9.52	1	11
2	6.35	2	12
5	5	3	13
6	6	4	14
7	7	5	15
8	8	6	16
9	9	7	17

1... 9 Electrical values

0... 9 Shaft diameter

A... D Standard shapes
E... Z Customer designed resolvers

1; 2; 3 Pole pairs

15; 21 Frame size

R e s o l v e r

Shape A, B

Shape C, D

Printed in Germany · Subject to change without prior notice · Issued 09/2005

DATA SHEET - HOLLOW SHAFT RESOLVER

PN	1-1414631-0			
Description:	V23401-		S1001-B101	
Size	15			
Shaft	B1			
Speed (pair of poles) [p]	1			
Number of poles	2			
Application Spec				
Test protocol	Results saved to manufacturing site archives. Available by request			
Electrical parameters:				
Input voltage [V]	7.0		Input resistance R1R2 [Ω]	82
Frequency Typical [kHz]	10.0		R1R2 tolerance [%]	± 10
Input current max [mA]	40		Input resistance S1S3 or S2S4 [Ω]	68
Transformation ratio (rT)	0.50		S1S3 or S2S4 tolerance [%]	± 10
Transf. ratio tolerance [%]	± 5	Based on specified Input voltage and Frequency		
Phase shift min [º]	-2			
Phase shift max [º]	8			
Electrical Angular Error max [']	20			
Residual voltage max [mV]	25			
High Voltage test	Voltage: $500V_{AC}$ (A)		Measured between:	
	$250V_{AC}$ (B)		A: Winding R1-R2 and housing	
	Time: 1s		Winding S1-S3 and housing Winding S2-S4 and housing	
Isolation test	Voltage: $500V_{DC}$ (A, B)		B: Windings S1-S3 and S2-S4	
	Criterium: $R_{isol.} > 50M\Omega$			
"Zero" setting:	Electrical "0" is when Coils $V_{S2\text{-}S4} = 0$ and $V_{S1\text{-}S3}$ are in phase with $V_{R1\text{-}R2}$			
Transfer function	Looking at Transformation part and turning Rotor clockwise			
	$V_{S1\text{-}S3} = +rT * V_{R1\text{-}R2} * \cos(p*\alpha)$			
	$V_{S2\text{-}S4} = +rT * V_{R1\text{-}R2} * \sin(p*\alpha)$			
Rotor Inertia	approx. 20g.cm^2			
Max. Rotational Speed	20,000 rpm			
Shock resistance (11ms sine)	1000 m/s^2			
Vibration	200 m/s^2			
Operating temp.	-55°C…+150°C			

1-1414631-0

A–A

Ø36.83 1)

Ø9.52 H8

16.1 1)

Ø34.4 1)

2 1)

2.45 1)

16.1 1)

DATE	PN. REV.	DWN	APP	DS. REV.
05/06/2018	D	H.Bernardo	D.Ondrej	A

![ATS Advanced Thermal Solutions, Inc. logo — Innovations in Thermal Management®]

IGBT Cold Plates
High Performance

ATS-CP-1001

ATS IGBT cold plates have unmatched thermal performance because of their mini-channel fin design. The ATS-CP-1001 cold plate, at a flow rate of 4 L/min, can transfer 1kW of heat at 5°C temperature difference between the cold plate base and inlet fluid temperature. If the coolant has particles, a #60 filter or finer is recommended to remove possible particles in the liquid.

Image for illustration purposes only

FEATURES AND BENEFITS

» More than 30% improvement in thermal performance compared to commercially available cold plates

» Compatible with industry accepted coolants

» 1/4 NPT threaded input and output

» Low pressure drop

» Lightweight for ease of transportation

» Provides uniform cold plate surface temperature when IGBTs are installed

» Maximum pressure: 60 psi

» **Applications:** Automotive Industry, Uninterruptible Power Supplies, Wind Turbines, Photovoltaic Inverters, Power Electronics, Induction Heaters, Motor Devices, Utility Vehicles, Anywhere power devices are used

DIMENSIONS (L X W X H)
198 X 147 X 20 mm
(7.8 X 5.8 X 0.8")

INLET/OUTPUT PORTS
1/4 – 18 NPT

MATERIAL
ALUMINUM, UNFINISHED

WEIGHT
1,340g

ATS COLD PLATES

» **Innovative Technology**
Superior heat transfer, flexible design platform

» **Compact Design**
Designed to fit standard IGBT and other power electronics applications

» **Easy Connections**
Industry standard threaded hole sizes allows for hassel-free connection options

» **Safe & Reliable**
Leak Free (100% tested:100 psi)

» **Custom Options**
Choose from various options, i.e; fitting types, material types, device mounting and more. Contact ATS for additional information

» **Customization Available!**
ATS will customize any of the cold plates to fit into your application

IGBT COMPATIBILITY

» Semikron SemiX® 3
» Infineon EconoDUAL™3
» Fuji Semiconductor Spring Contact Module
» Powerex NX™ Series
» Other IGBTs or high power devices

ADDITIONAL COMPONENTS DEPLOYED IN LIQUID COOLING LOOPS

Flow Meter
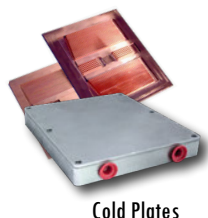
Cold Plates

Chillers
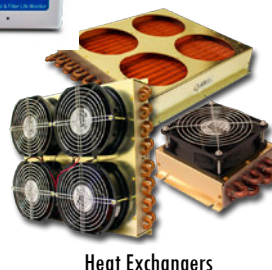
Heat Exchangers

ATS has the products needed to design a complete liquid cooling loop: **Cold Plates** to transfer and remove the heat from the source, **Heat Exchangers** to transfer heat from the liquid to the air with or without a fan, and **Chillers** to circulate and condition the fluid in the system. In addition, ATS offers **Flow Meters** to instantaneously measure the volumetric flow rate of the fluid in the system and **Leak Detectors** to notify users of any leaks in the system.

RoHS COMPLIANT

PERFORMANCE CURVES

Thermal Resistance And Pressure Drop ATS-CP-1001
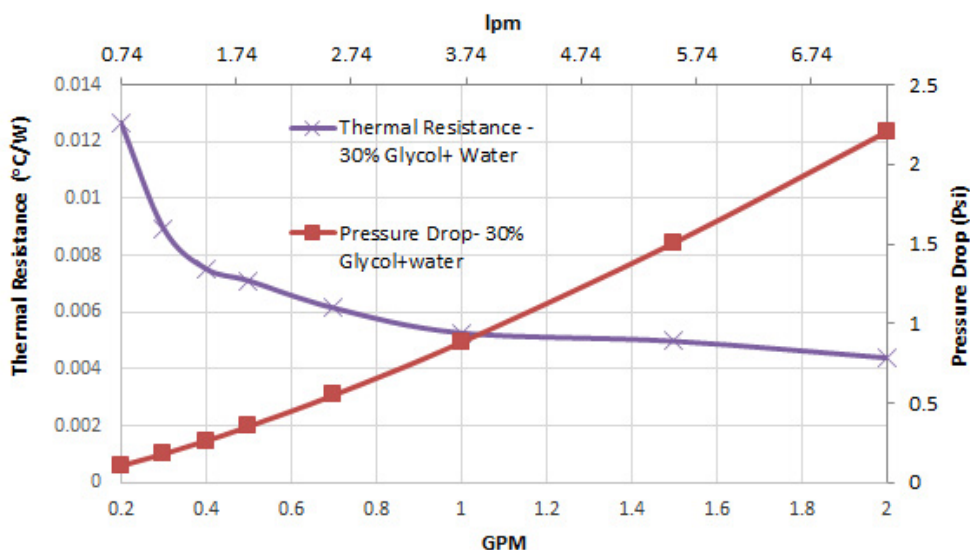
ATS Cold Plate Family			
Part Number	Dimensions* (L x W x H)	Flow Rate (L/min)	ΔT @ 1kW
ATS-CP-1000	202 x 130 x 20	4 L/min	5.50°C
ATS-CP-1001	198 x 147 x 20	4 L/min	5.00°C
ATS-CP-1002	162 x 136 x20	4 L/min	7.00°C
ATS-CP-1003	162 x 147 x 20	4 L/min	6.80°C
ATS-CP-1004	162 x 172 x 20	4 L/min	5.90°C

Flow rate (gallon/min)**	R (°C/W)	DeltaP (psi)
2	0.0044	2.2
1	0.0053	0.88
0.5	0.007	0.35
0.2	0.013	0.1

* All Dimensions in mm
** Note: To convert to l/min, multiply by 3.7

MECHANICAL SPECIFICATIONS

(all dimensions in mm)

NOTES:
1. DIMENSIONS ARE IN MM.
2. TOLERANCES: X.XX +/- 0.25 MM, X.XXX +/- 0.125 MM.
3. THIRD ANGLE PROJECTION.
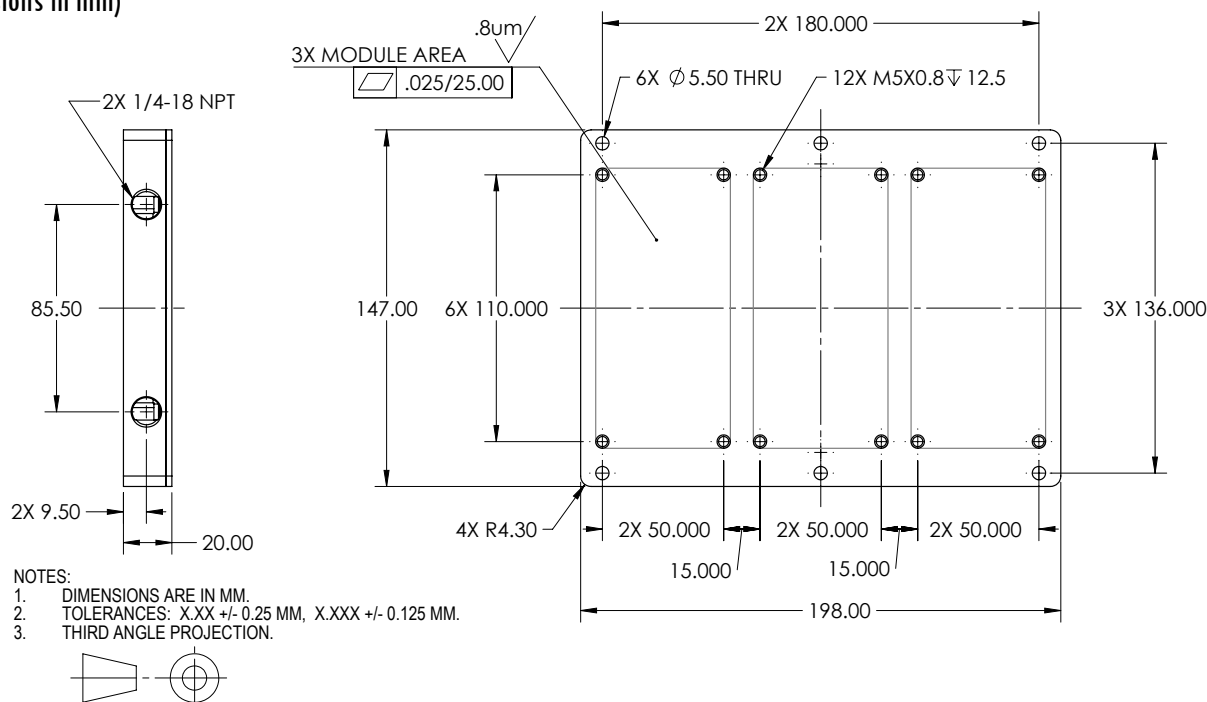
For further technical information, please contact Advanced Thermal Solutions, Inc.
by phone: **1-781-769-2800**, email **ats-hq@qats.com** or visit **www.qats.com**

FF225R12ME4P

EconoDUAL™3 Modul mit Trench/Feldstopp IGBT4 und Emitter Controlled HE Diode und NTC / bereits aufgetragenem Thermal Interface Material

EconoDUAL™3 module with Trench/Fieldstop IGBT4 and Emitter Controlled HE diode and NTC / pre-applied Thermal Interface Material

Typical Appearance
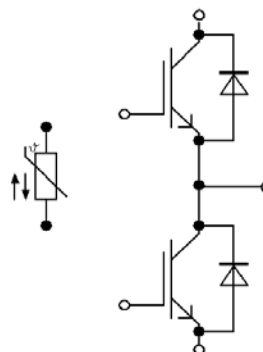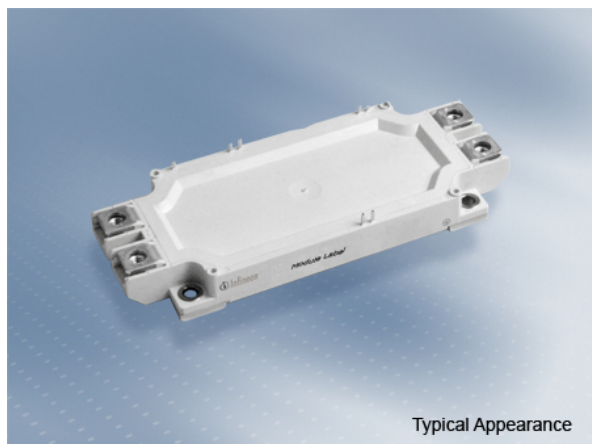
V_{CES} = 1200V
$I_{C\,nom}$ = 225A / I_{CRM} = 450A

Typische Anwendungen
- Motorantriebe
- Servoumrichter
- USV-Systeme
- Windgeneratoren

Typical Applications
- Motor drives
- Servo drives
- UPS systems
- Wind turbines

Elektrische Eigenschaften
- Niedriges V_{CEsat}
- $T_{vj\,op}$ = 150°C

Electrical Features
- Low V_{CEsat}
- $T_{vj\,op}$ = 150°C

Mechanische Eigenschaften
- Standardgehäuse
- Thermisches Interface Material bereits aufgetragen

Mechanical Features
- Standard housing
- Pre-applied Thermal Interface Material

Module Label Code

Barcode Code 128

Sample
000001234560000000000000

DMX - Code

Content of the Code	Digit
Module Serial Number	1 - 5
Module Material Number	6 - 11
Production Order Number	12 - 19
Datecode (Production Year)	20 - 21
Datecode (Production Week)	22 - 23

IGBT,Wechselrichter / IGBT,Inverter
Höchstzulässige Werte / Maximum Rated Values

Kollektor-Emitter-Sperrspannung Collector-emitter voltage	T_{vj} = 25°C	V_{CES}		1200	V
Kollektor-Dauergleichstrom Continuous DC collector current	T_H = 70°C, $T_{vj\ max}$ = 175°C	$I_{C\ nom}$		225	A
Periodischer Kollektor-Spitzenstrom Repetitive peak collector current	t_P = 1 ms	I_{CRM}		450	A
Gate-Emitter-Spitzenspannung Gate-emitter peak voltage		V_{GES}		+/-20	V

Charakteristische Werte / Characteristic Values

			min.	typ.	max.	
Kollektor-Emitter-Sättigungsspannung Collector-emitter saturation voltage	I_C = 225 A, V_{GE} = 15 V T_{vj} = 25°C I_C = 225 A, V_{GE} = 15 V T_{vj} = 125°C I_C = 225 A, V_{GE} = 15 V T_{vj} = 150°C	$V_{CE\ sat}$		1,85 2,10 2,15	2,15	V V V
Gate-Schwellenspannung Gate threshold voltage	I_C = 7,80 mA, V_{CE} = V_{GE}, T_{vj} = 25°C	V_{GEth}	5,20	5,80	6,40	V
Gateladung Gate charge	V_{GE} = -15 V ... +15 V	Q_G		1,55		µC
Interner Gatewiderstand Internal gate resistor	T_{vj} = 25°C	R_{Gint}		3,3		Ω
Eingangskapazität Input capacitance	f = 1 MHz, T_{vj} = 25°C, V_{CE} = 25 V, V_{GE} = 0 V	C_{ies}		13,0		nF
Rückwirkungskapazität Reverse transfer capacitance	f = 1 MHz, T_{vj} = 25°C, V_{CE} = 25 V, V_{GE} = 0 V	C_{res}		0,705		nF
Kollektor-Emitter-Reststrom Collector-emitter cut-off current	V_{CE} = 1200 V, V_{GE} = 0 V, T_{vj} = 25°C	I_{CES}			3,0	mA
Gate-Emitter-Reststrom Gate-emitter leakage current	V_{CE} = 0 V, V_{GE} = 20 V, T_{vj} = 25°C	I_{GES}			400	nA
Einschaltverzögerungszeit, induktive Last Turn-on delay time, inductive load	I_C = 225 A, V_{CE} = 600 V T_{vj} = 25°C V_{GE} = ±15 V T_{vj} = 125°C R_{Gon} = 1,6 Ω T_{vj} = 150°C	$t_{d\ on}$		0,16 0,17 0,18		µs µs µs
Anstiegszeit, induktive Last Rise time, inductive load	I_C = 225 A, V_{CE} = 600 V T_{vj} = 25°C V_{GE} = ±15 V T_{vj} = 125°C R_{Gon} = 1,6 Ω T_{vj} = 150°C	t_r		0,04 0,04 0,04		µs µs µs
Abschaltverzögerungszeit, induktive Last Turn-off delay time, inductive load	I_C = 225 A, V_{CE} = 600 V T_{vj} = 25°C V_{GE} = ±15 V T_{vj} = 125°C R_{Goff} = 1,6 Ω T_{vj} = 150°C	$t_{d\ off}$		0,38 0,47 0,50		µs µs µs
Fallzeit, induktive Last Fall time, inductive load	I_C = 225 A, V_{CE} = 600 V T_{vj} = 25°C V_{GE} = ±15 V T_{vj} = 125°C R_{Goff} = 1,6 Ω T_{vj} = 150°C	t_f		0,07 0,09 0,10		µs µs µs
Einschaltverlustenergie pro Puls Turn-on energy loss per pulse	I_C = 225 A, V_{CE} = 600 V, L_S = 80 nH T_{vj} = 25°C V_{GE} = ±15 V, di/dt = 5750 A/µs (T_{vj} = 150°C) T_{vj} = 125°C R_{Gon} = 1,6 Ω T_{vj} = 150°C	E_{on}		6,80 12,5 15,0		mJ mJ mJ
Abschaltverlustenergie pro Puls Turn-off energy loss per pulse	I_C = 225 A, V_{CE} = 600 V, L_S = 80 nH T_{vj} = 25°C V_{GE} = ±15 V, du/dt = 3400 V/µs (T_{vj} = 150°C) T_{vj} = 125°C R_{Goff} = 1,6 Ω T_{vj} = 150°C	E_{off}		17,0 26,5 29,5		mJ mJ mJ
Kurzschlußverhalten SC data	V_{GE} ≤ 15 V, V_{CC} = 800 V V_{CEmax} = V_{CES} -L_{sCE} ·di/dt t_P ≤ 10 µs, T_{vj} = 150°C	I_{SC}		900		A
Wärmewiderstand, Chip bis Kühlkörper Thermal resistance, junction to heatsink	pro IGBT / per IGBT valid with IFX pre-applied thermal interface material	R_{thJH}			0,175	K/W
Temperatur im Schaltbetrieb Temperature under switching conditions		$T_{vj\ op}$	-40		150	°C

Diode, Wechselrichter / Diode, Inverter
Höchstzulässige Werte / Maximum Rated Values

Periodische Spitzensperrspannung Repetitive peak reverse voltage	T_{vj} = 25°C		V_{RRM}	1200	V
Dauergleichstrom Continuous DC forward current			I_F	225	A
Periodischer Spitzenstrom Repetitive peak forward current	t_P = 1 ms		I_{FRM}	450	A
Grenzlastintegral I²t - value	V_R = 0 V, t_P = 10 ms, T_{vj} = 125°C V_R = 0 V, t_P = 10 ms, T_{vj} = 150°C		I²t	10000 8100	A²s A²s

Charakteristische Werte / Characteristic Values

				min.	typ.	max.	
Durchlassspannung Forward voltage	I_F = 225 A, V_{GE} = 0 V I_F = 225 A, V_{GE} = 0 V I_F = 225 A, V_{GE} = 0 V	T_{vj} = 25°C T_{vj} = 125°C T_{vj} = 150°C	V_F		1,65 1,65 1,65	2,10	V V V
Rückstromspitze Peak reverse recovery current	I_F = 225 A, - di_F/dt = 5750 A/µs (T_{vj}=150°C) V_R = 600 V V_{GE} = -15 V	T_{vj} = 25°C T_{vj} = 125°C T_{vj} = 150°C	I_{RM}		300 320 340		A A A
Sperrverzögerungsladung Recovered charge	I_F = 225 A, - di_F/dt = 5750 A/µs (T_{vj}=150°C) V_R = 600 V V_{GE} = -15 V	T_{vj} = 25°C T_{vj} = 125°C T_{vj} = 150°C	Q_r		22,5 43,0 49,5		µC µC µC
Abschaltenergie pro Puls Reverse recovery energy	I_F = 225 A, - di_F/dt = 5750 A/µs (T_{vj}=150°C) V_R = 600 V V_{GE} = -15 V	T_{vj} = 25°C T_{vj} = 125°C T_{vj} = 150°C	E_{rec}		12,0 22,0 25,0		mJ mJ mJ
Wärmewiderstand, Chip bis Kühlkörper Thermal resistance, junction to heatsink	pro Diode / per diode valid with IFX pre-applied thermal interface material		R_{thJH}			0,197	K/W
Temperatur im Schaltbetrieb Temperature under switching conditions			$T_{vj\ op}$	-40		150	°C

NTC-Widerstand / NTC-Thermistor
Charakteristische Werte / Characteristic Values

			min.	typ.	max.	
Nennwiderstand Rated resistance	T_{NTC} = 25°C	R_{25}		5,00		kΩ
Abweichung von R100 Deviation of R100	T_{NTC} = 100°C, R_{100} = 493 Ω	ΔR/R	-5		5	%
Verlustleistung Power dissipation	T_{NTC} = 25°C	P_{25}			20,0	mW
B-Wert B-value	R_2 = R_{25} exp [$B_{25/50}$(1/T_2 - 1/(298,15 K))]	$B_{25/50}$		3375		K
B-Wert B-value	R_2 = R_{25} exp [$B_{25/80}$(1/T_2 - 1/(298,15 K))]	$B_{25/80}$		3411		K
B-Wert B-value	R_2 = R_{25} exp [$B_{25/100}$(1/T_2 - 1/(298,15 K))]	$B_{25/100}$		3433		K

Angaben gemäß gültiger Application Note.
Specification according to the valid application note.

FF225R12ME4P

Modul / Module

			min.	typ.	max.	
Isolations-Prüfspannung Isolation test voltage	RMS, f = 50 Hz, t = 1 min	V_{ISOL}		2,5		kV
Material Modulgrundplatte Material of module baseplate				Cu		
Innere Isolation Internal isolation	Basisisolierung (Schutzklasse 1, EN61140) basic insulation (class 1, IEC 61140)			Al_2O_3		
Kriechstrecke Creepage distance	Kontakt - Kühlkörper / terminal to heatsink Kontakt - Kontakt / terminal to terminal			14,5 13,0		mm
Luftstrecke Clearance	Kontakt - Kühlkörper / terminal to heatsink Kontakt - Kontakt / terminal to terminal			12,5 10,0		mm
Vergleichszahl der Kriechwegbildung Comperative tracking index		CTI		> 200		
Modulstreuinduktivität Stray inductance module		L_{sCE}		20		nH
Modulleitungswiderstand, Anschlüsse - Chip Module lead resistance, terminals - chip	T_H = 25°C, pro Schalter / per switch	$R_{CC'+EE'}$		1,30		mΩ
Lagertemperatur Storage temperature		T_{stg}	-40		125	°C
Höchstzulässige Bodenplattenbetriebstemperatur Maximum baseplate operation temperature		T_{BPmax}			125	°C
Anzugsdrehmoment f. Modulmontage Mounting torque for modul mounting	Schraube M5 - Montage gem. gültiger Applikationsschrift Screw M5 - Mounting according to valid application note	M	3,00		6,00	Nm
Anzugsdrehmoment f. elektr. Anschlüsse Terminal connection torque	Schraube M6 - Montage gem. gültiger Applikationsschrift Screw M6 - Mounting according to valid application note	M	3,0	-	6,0	Nm
Gewicht Weight		G		345		g

Lagerung und Transport von Modulen mit TIM => siehe AN2012-07
Storage and shipment of modules with TIM => see AN2012-07

FF225R12ME4P

Ausgangskennlinie IGBT,Wechselrichter (typisch)
output characteristic IGBT,Inverter (typical)
$I_C = f(V_{CE})$
$V_{GE} = 15\ V$
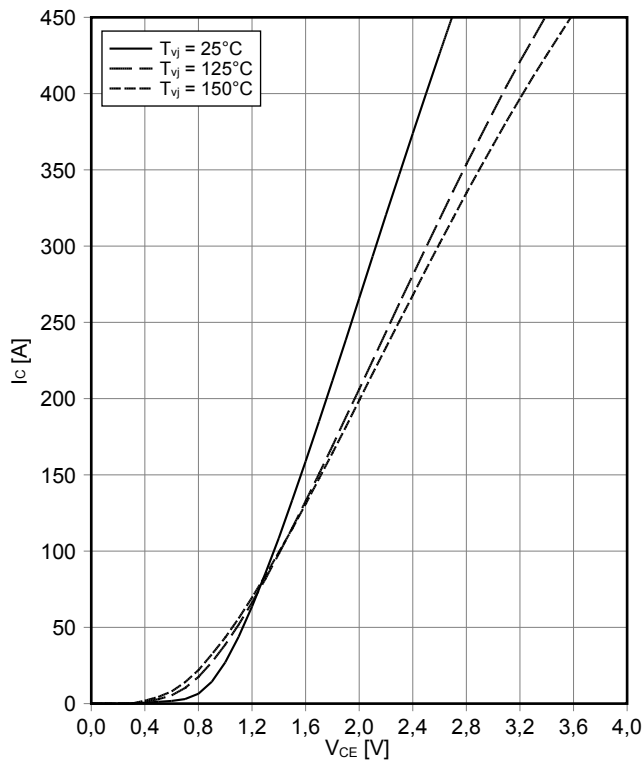
Ausgangskennlinienfeld IGBT,Wechselrichter (typisch)
output characteristic IGBT,Inverter (typical)
$I_C = f(V_{CE})$
$T_{vj} = 150°C$
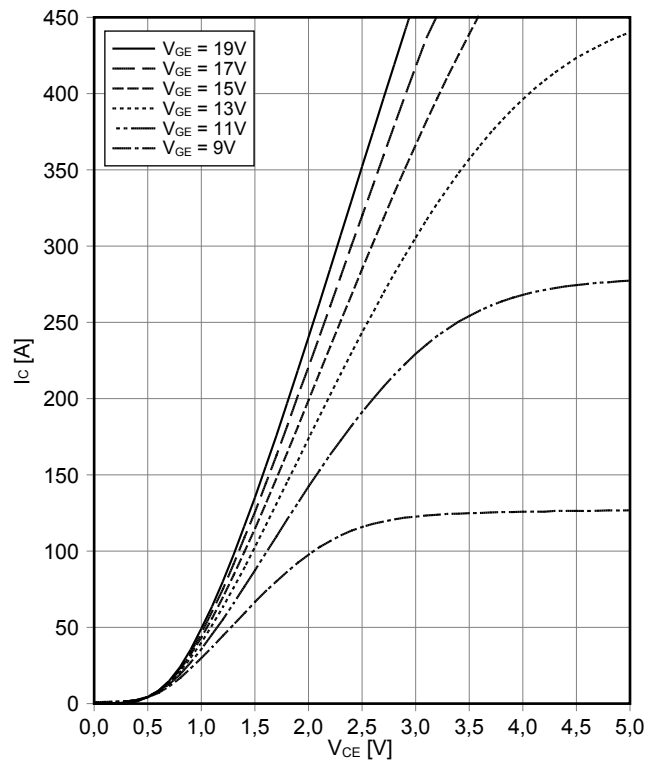
Übertragungscharakteristik IGBT,Wechselrichter (typisch)
transfer characteristic IGBT,Inverter (typical)
$I_C = f(V_{GE})$
$V_{CE} = 20\ V$
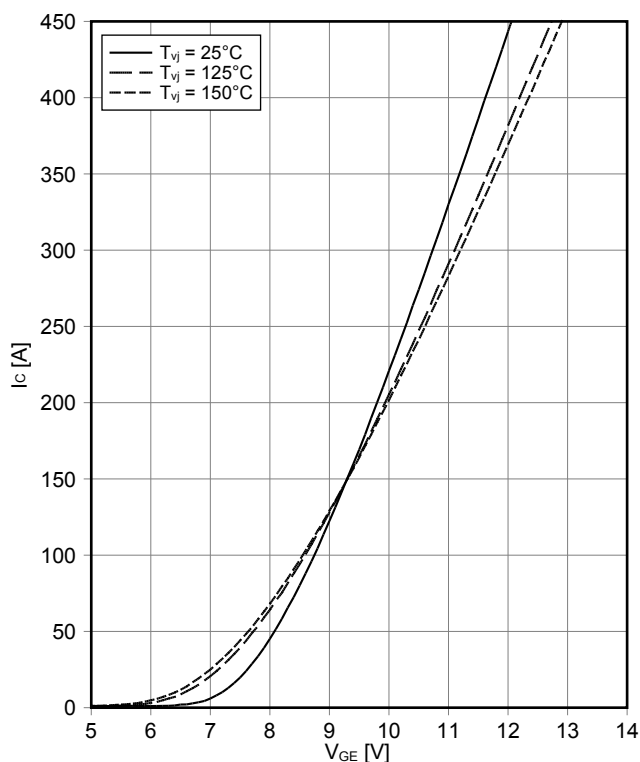
Schaltverluste IGBT,Wechselrichter (typisch)
switching losses IGBT,Inverter (typical)
$E_{on} = f(I_C),\ E_{off} = f(I_C)$
$V_{GE} = \pm15\ V,\ R_{Gon} = 1.6\ \Omega,\ R_{Goff} = 1.6\ \Omega,\ V_{CE} = 600\ V$
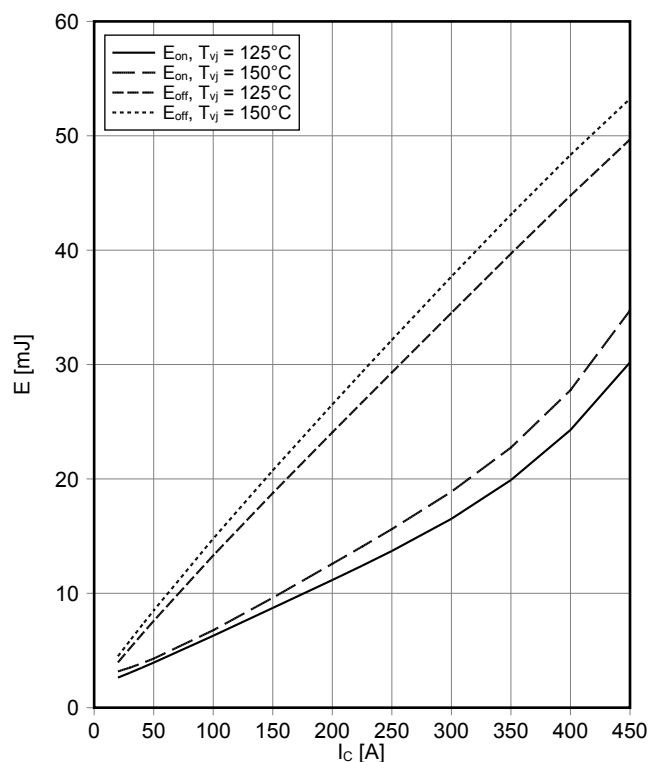
FF225R12ME4P

Infineon

Schaltverluste IGBT,Wechselrichter (typisch)
switching losses IGBT,Inverter (typical)
$E_{on} = f(R_G)$, $E_{off} = f(R_G)$
$V_{GE} = \pm15$ V, $I_C = 225$ A, $V_{CE} = 600$ V

Legend:
- E_{on}, $T_{vj} = 125°C$
- E_{on}, $T_{vj} = 150°C$
- E_{off}, $T_{vj} = 125°C$
- E_{off}, $T_{vj} = 150°C$

Axes: E [mJ] vs R_G [Ω]
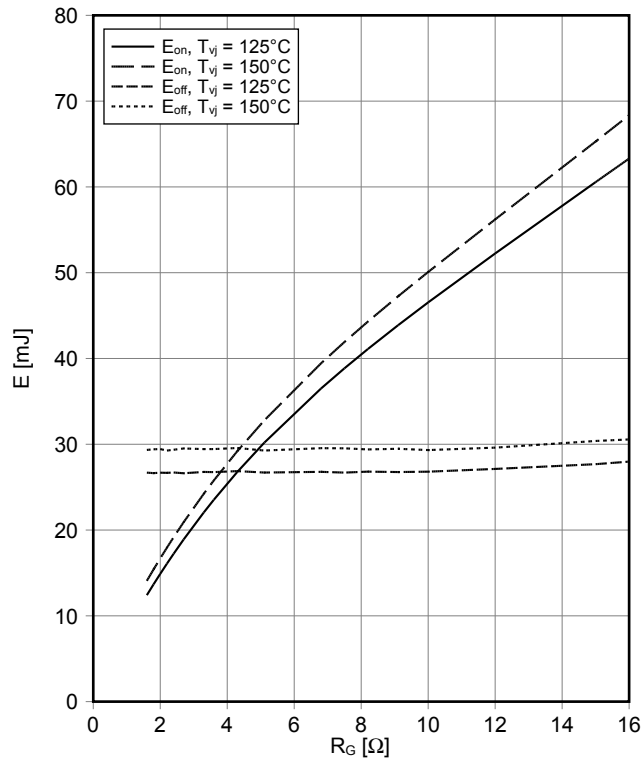
Transienter Wärmewiderstand IGBT,Wechselrichter
transient thermal impedance IGBT,Inverter
$Z_{thJH} = f(t)$

Legend: Z_{thJH} : IGBT

Axes: Z_{thJH} [K/W] vs t [s]

i:	1	2	3	4
r_i[K/W]:	0,0116	0,0653	0,0768	0,0213
τ_i[s]:	0,000543	0,0237	0,122	1,22
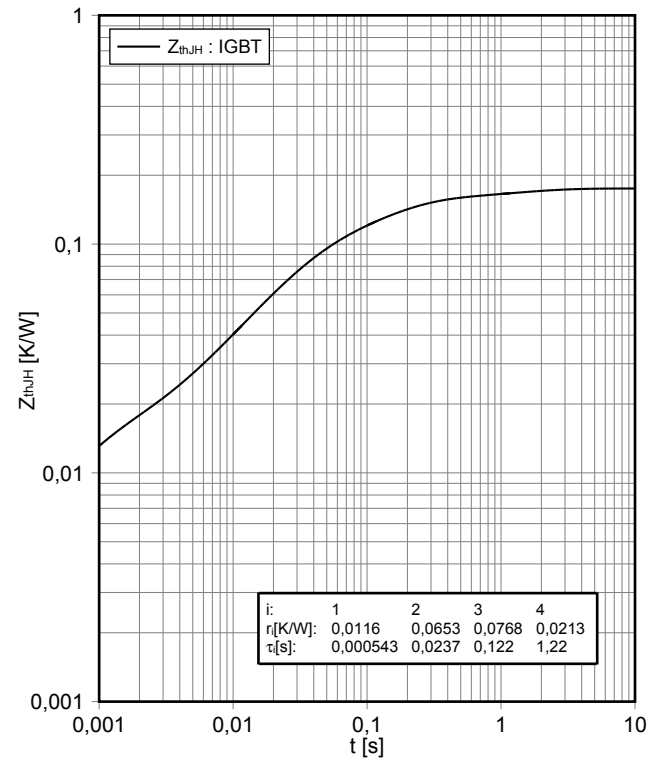
Sicherer Rückwärts-Arbeitsbereich IGBT,Wechselrichter (RBSOA)
reverse bias safe operating area IGBT,Inverter (RBSOA)
$I_C = f(V_{CE})$
$V_{GE} = \pm15$ V, $R_{Goff} = 1.6$ Ω, $T_{vj} = 150°C$

Legend:
- I_C, Modul
- I_C, Chip

Axes: I_C [A] vs V_{CE} [V]
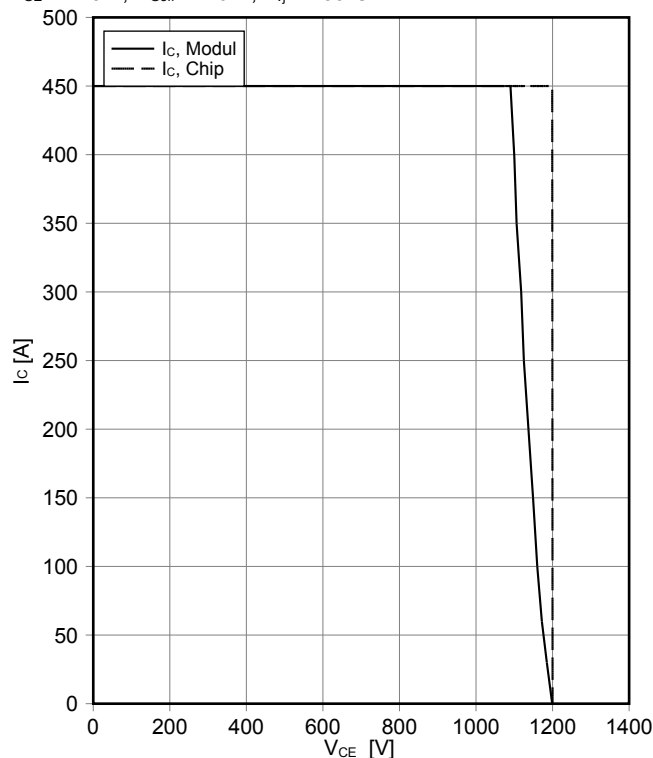
Durchlasskennlinie der Diode, Wechselrichter (typisch)
forward characteristic of Diode, Inverter (typical)
$I_F = f(V_F)$
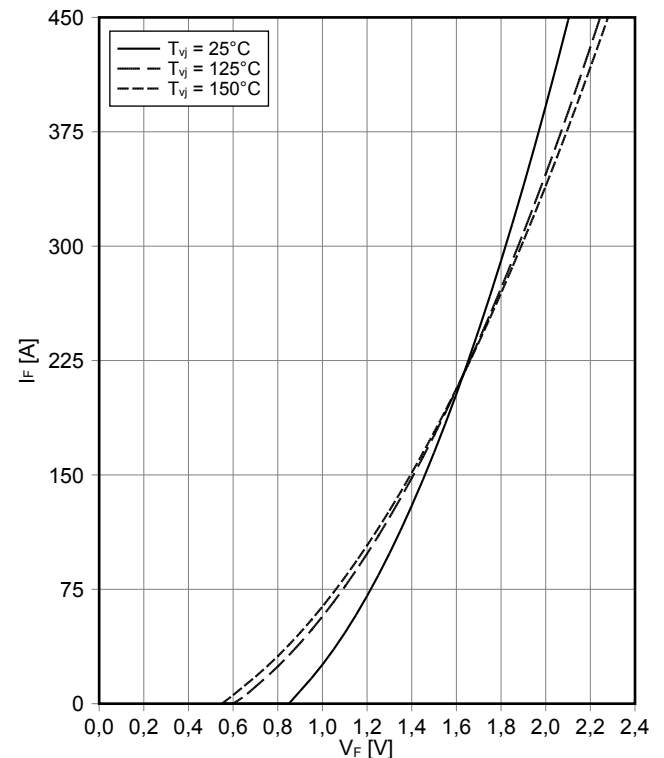
Legend:
- $T_{vj} = 25°C$
- $T_{vj} = 125°C$
- $T_{vj} = 150°C$

Axes: I_F [A] vs V_F [V]

FF225R12ME4P

Infineon

Schaltverluste Diode, Wechselrichter (typisch)
switching losses Diode, Inverter (typical)
$E_{rec} = f(I_F)$
$R_{Gon} = 1.6\ \Omega$, $V_{CE} = 600\ V$
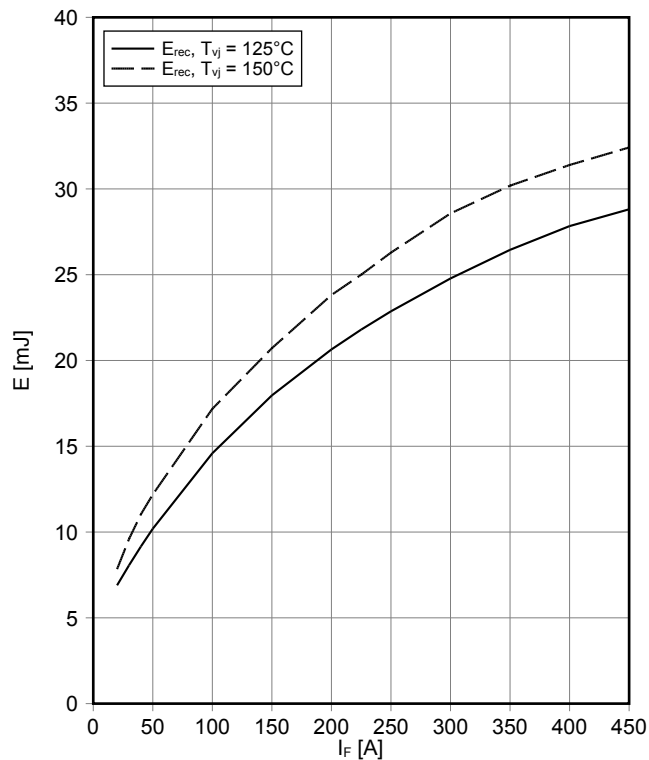
Schaltverluste Diode, Wechselrichter (typisch)
switching losses Diode, Inverter (typical)
$E_{rec} = f(R_G)$
$I_F = 225\ A$, $V_{CE} = 600\ V$
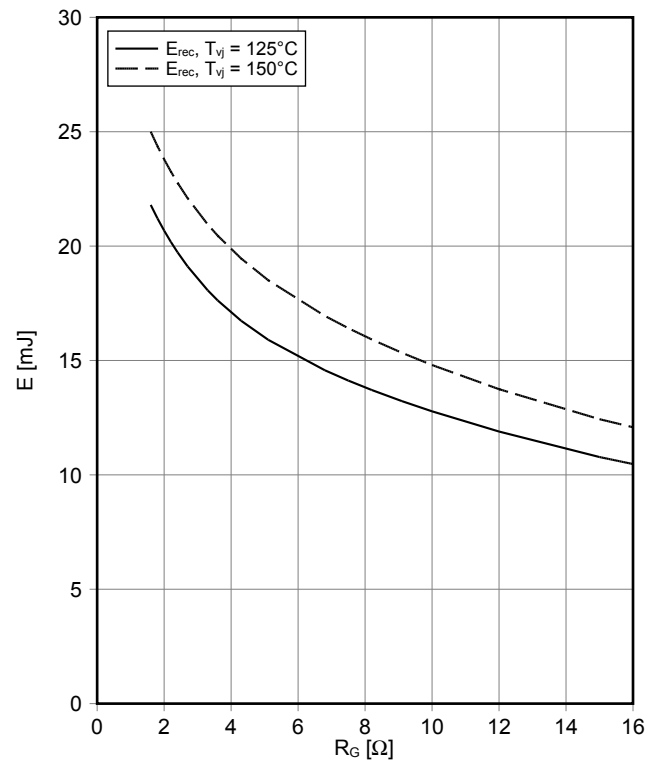
Transienter Wärmewiderstand Diode, Wechselrichter
transient thermal impedance Diode, Inverter
$Z_{thJH} = f(t)$

i:	1	2	3	4
r_i[K/W]:	0,0141	0,0768	0,0841	0,022
τ_i[s]:	0,000542	0,023	0,121	1,19
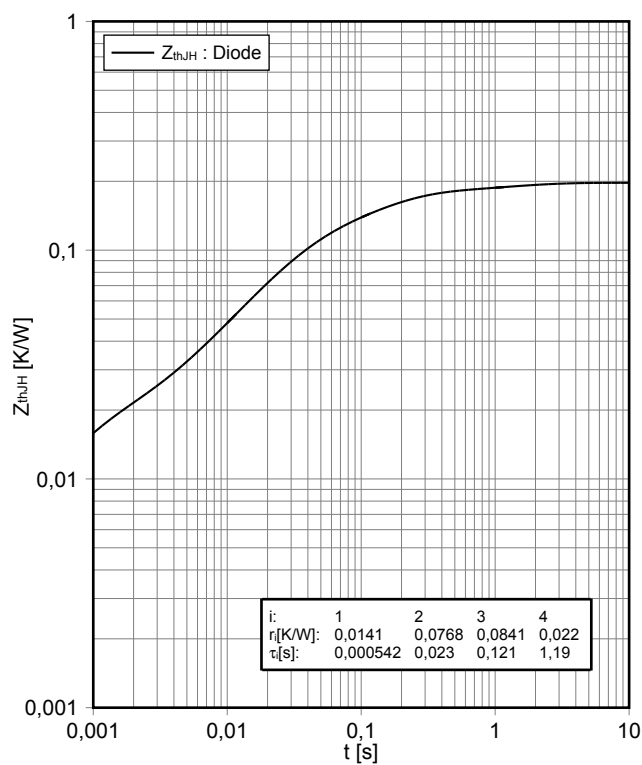
NTC-Widerstand-Temperaturkennlinie (typisch)
NTC-Thermistor-temperature characteristic (typical)
$R = f(T)$
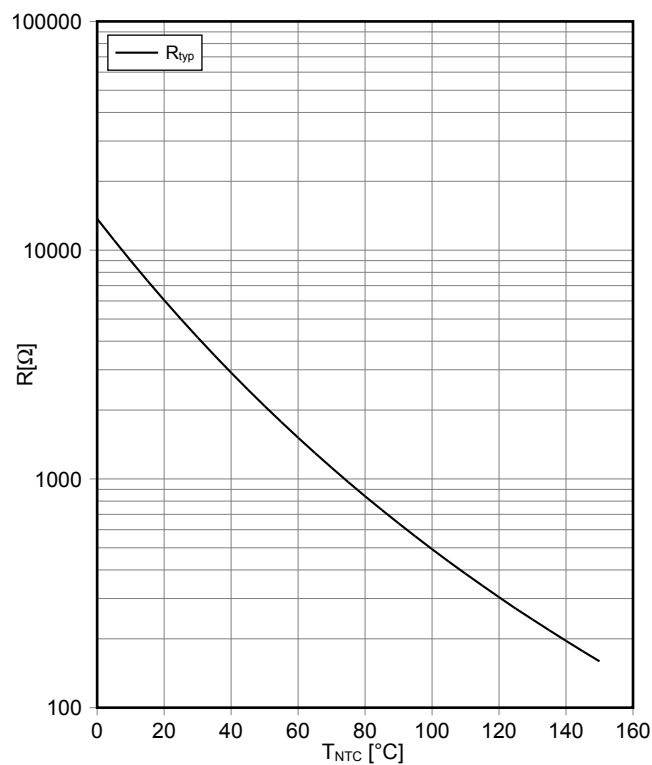
Schaltplan / Circuit diagram
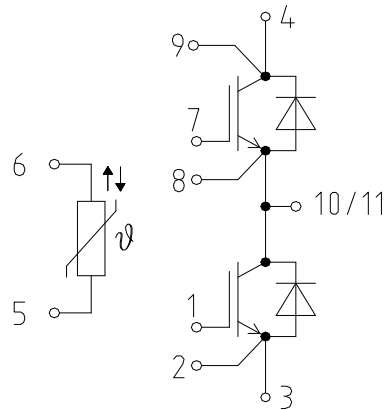
Gehäuseabmessungen / Package outlines

✳ = all dimensions with a tolerance of $\oplus \varnothing 0.5$

dimensions valid in mounted condition

restricted area for Thermal Interface Material

Mouser Electronics

Authorized Distributor

Click to View Pricing, Inventory, Delivery & Lifecycle Information:

[Infineon]():
  [FF225R12ME4PBPSA1]()

2SP0115T2A0-FF225R12ME4 and 2SP0115T2A0C-FF225R12ME4 Data Sheet

Compact, high-performance, plug-and-play dual-channel IGBT driver based on SCALE™-2 technology for individual and parallel-connected modules

Abstract

The SCALE™-2 plug-and-play driver 2SP0115T2A0-FF225R12ME4 / 2SP0115T2A0C-FF225R12ME4 (Coated version using ELPEGUARD SL 1307 FLZ/2 from Lackwerke Peters with a typical thickness of 50μm) is a compact dual-channel intelligent gate driver designed for Infineon's EconoDUAL™ IGBTs FF225R12ME4. The driver features an electrical interface with a built-in DC/DC power supply.

For drivers adapted to other types of high-power and high-voltage IGBT modules, refer to

www.power.com/gate-driver/go/plug-and-play

Features

- ✓ Plug-and-play solution
- ✓ Allows parallel connection of IGBT modules
- ✓ Shortens application development time
- ✓ Extremely reliable; long service life
- ✓ Built-in DC/DC power supply
- ✓ 20-pin flat cable interface
- ✓ Duty cycle 0... 100%
- ✓ Active clamping of V_{ce} at turn-off
- ✓ IGBT short-circuit protection
- ✓ Monitoring of supply voltage
- ✓ Safe isolation to EN 50178
- ✓ UL compliant
- ✓ Suitable for FF225R12ME4

Applications

- ✓ Wind-power converters
- ✓ Industrial drives
- ✓ UPS
- ✓ Power-factor correctors
- ✓ Traction
- ✓ Railroad power supplies
- ✓ Welding
- ✓ SMPS
- ✓ Radiology and laser technology
- ✓ Research
- ✓ and many others

EconoDUAL is a trademark of Infineon Technologies AG, Munich

Data Sheet

Safety Notice!

The data contained in this data sheet is intended exclusively for technically trained staff. Handling all high-voltage equipment involves risk to life. Strict compliance with the respective safety regulations is mandatory!

Any handling of electronic devices is subject to the general specifications for protecting electrostatic-sensitive devices according to international standard IEC 60747-1, Chapter IX or European standard EN 100015 (i.e. the workplace, tools, etc. must comply with these standards). Otherwise, this product may be damaged.

Important Product Documentation

This data sheet contains only product-specific data. For a detailed description, must-read application notes and common data that apply to the whole series, please refer to "Description & Application Manual for 2SP0115T SCALE-2 IGBT Drivers" on www.power.com/gate-driver/go/2SP0115T.

When applying SCALE-2 plug-and-play drivers, please note that these drivers are specifically adapted to a particular type of IGBT module. Therefore, the type designation of SCALE-2 plug-and-play drivers also includes the type designation of the corresponding IGBT module. These drivers are not valid for IGBT modules other than those specified. Incorrect use may result in failure.

Mechanical Dimensions

Dimensions: Refer to "Description & Application Manual for 2SP0115T SCALE-2 IGBT Drivers"
Mounting principle: Soldered onto EconoDUAL™ module FF225R12ME4

Absolute Maximum Ratings

Parameter	Remarks	Min	Max	Unit
Supply voltage V_{CC}	VCC to GND	0	16	V
Logic input and output voltages	To GND	-0.5	VCC+0.5	V
SO_x current	Fault condition, total current		20	mA
Gate peak current I_{out}	Note 1	-8	+15	A
Average supply current I_{CC}	Note 2		290	mA
Output power per gate	Ambient temperature ≤ 70°C (Note 3)		1.2	W
	Ambient temperature ≤ 85°C (Note 3)		1	W
Switching frequency f			36	kHz
Test voltage (50Hz/1min.)	Primary to secondary (Note 16)		3800	$V_{AC(eff)}$
	Secondary to secondary (Note 16)		3800	$V_{AC(eff)}$
DC-link voltage	Note 4		800	V
|dV/dt|	Rate of change of input to output voltage		50	kV/µs
Operating voltage	Primary/secondary, secondary/secondary		1200	V_{peak}

Data Sheet

Parameter	Remarks	Min	Max	Unit
Operating temperature	Note 20	-20	85	°C
Storage temperature	Note 21	-40	50	°C
Surface temperature	Only 2SP0115T2A0C-FF225R12ME4 (Note 22)		125	°C

Recommended Operating Conditions

Parameter	Remarks	Min	Typ	Max	Unit
Supply voltage V_{CC}	To GND	14.5	15	15.5	V
Resistance from TB to GND	Blocking time ≠ 0, ext. value	128		∞	kΩ
SO_x current	Fault condition, 3.3V logic			4	mA

Electrical Characteristics

Power Supply	Remarks	Min	Typ	Max	Unit
Supply current I_{CC}	Without load		33		mA
Efficiency η	Internal DC/DC converter		85		%
Coupling capacitance C_{io}	Primary side to secondary side, total, per channel		23		pF
Power Supply Monitoring	**Remarks**	**Min**	**Typ**	**Max**	**Unit**
Supply threshold V_{CC}	Primary side, clear fault	11.9	12.6	13.3	V
	Primary side, set fault (Note 5)	11.3	12.0	12.7	V
Monitoring hysteresis	Primary side, set/clear fault	0.35			V
Supply threshold V_{isox}-V_{eex}	Secondary side, clear fault	12.1	12.6	13.1	V
	Secondary side, set fault (Note 6)	11.5	12.0	12.5	V
Monitoring hysteresis	Secondary side, set/clear fault	0.35			V
Supply threshold V_{eex}-V_{COMx}	Secondary side, clear fault	5	5.15	5.3	V
	Secondary side, set fault (Note 6)	4.7	4.85	5	V
Monitoring hysteresis	Secondary side, set/clear fault	0.15			V
Logic Inputs and Outputs	**Remarks**	**Min**	**Typ**	**Max**	**Unit**
Input impedance	V(INx) > 3V (Note 7)	3.5	4.1	4.6	kΩ
Turn-on threshold	V(INx) (Note 8)		2.6		V
Turn-off threshold	V(INx) (Note 8)		1.3		V
SOx output voltage	Fault condition, I(SOx) < 8mA			0.7	V

Data Sheet

Short-circuit Protection	Remarks	Min	Typ	Max	Unit
Vce-monitoring threshold	Between auxiliary terminals		10.2		V
Response time	DC-link voltage > 550V (Note 9)		5.4		µs
Delay to IGBT turn-off	After the response time (Note 10)		1.4		µs
Blocking time	After fault (Note 11)		90		ms

Timing Characteristics	Remarks	Min	Typ	Max	Unit
Turn-on delay $t_{d(on)}$	Note 12		75		ns
Turn-off delay $t_{d(off)}$	Note 12		65		ns
Jitter of turn-on delay	Note 18		±2		ns
Jitter of turn-off delay	Note 18		±4		ns
Output rise time $t_{r(out)}$	G_x to E_x (Note 13)		5		ns
Output fall time $t_{f(out)}$	G_x to E_x (Note 13)		10		ns
Dead time between outputs	Half-bridge mode (Note 19)		3		µs
Jitter of dead time	Half-bridge mode		±50		ns
Transmission delay of fault state	Note 14		400		ns

Outputs	Remarks	Min	Typ	Max	Unit
Turn-on gate resistor $R_{g(on)}$	Note 15		1.6		Ω
Turn-off gate resistor $R_{g(off)}$	Note 15		2.5		Ω
Gate voltage at turn-on			15		V
Gate-voltage at turn-off	P=0W		-9.2		V
	P=1.2W		-7.1		V
Gate resistance to COMx			4.7		kΩ

Electrical Isolation	Remarks	Min	Typ	Max	Unit
Test voltage (50Hz/1s)	Primary to secondary side (Note 16)	3800	3850	3900	V_{eff}
	Secondary to secondary side (Note 16)	3800	3850	3900	V_{eff}
Partial discharge extinction volt.	Primary to secondary side (Note 17)	1220			V_{peak}
	Secondary to secondary side (Note 17)	1200			V_{peak}
Creepage distance	Primary to secondary side	12.6			mm
	Secondary to secondary side	6.6			mm
	Primary to NTC	6.5			mm
Clearance distance	Primary to secondary side	12.3			mm
	Secondary to secondary side	6.6			mm
	Primary to NTC	6.5			mm

All data refer to +25°C and V_{CC} = 15V unless otherwise specified

Data Sheet

Footnotes to the Key Data

1) The gate current is limited by the gate resistors located on the driver.
2) If the specified value is exceeded, this indicates a driver overload. It should be noted that the driver is not protected against overload.
3) If the specified value is exceeded, this indicates a driver overload. It should be noted that the driver is not protected against overload. From 70°C to 85°C, the maximum permissible output power can be linearly interpolated from the given data.
4) This limit is due to active clamping. Refer to the "Description & Application Manual for 2SP0115T SCALE-2 IGBT Drivers".
5) Undervoltage monitoring of the primary-side supply voltage (VCC to GND). If the voltage drops below this limit, a fault is transmitted to the corresponding outputs and the IGBTs are switched off.
6) Undervoltage monitoring of the secondary-side supply voltage (Visox to Veex and Veex to COMx which correspond with the approximate turn-on and turn-off gate-emitter voltages). If the corresponding voltage drops below this limit, the IGBT is switched off and a fault is transmitted to the corresponding output.
7) The input impedance can be modified to values <18 kΩ (customer-specific solution).
8) Turn-on and turn-off threshold values can be increased (customer-specific solution).
9) The resulting pulse width of the direct output of the gate drive unit for short-circuit type I (excluding the delay of the gate resistors) is the sum of response time plus delay to IGBT turn-off.
10) The turn-off event of the IGBT is delayed by the specified time after the response time.
11) Factory set value. The blocking time can be reduced with an external resistor. Refer to the "Description & Application Manual for 2SP0115T SCALE-2 IGBT Drivers".
12) Measured from the transition of the turn-on or turn-off command at the driver input to direct output of the gate drive unit (excluding the delay of the gate resistors).
13) Output rise and fall times are measured between 10% and 90% of the nominal output swing with an output load of 10Ω and 40nF. The values are given for the driver side of the gate resistors. The time constant of the output load in conjunction with the present gate resistors leads to an additional delay at the load side of the gate resistors.
14) Transmission delay of the fault state from the secondary side to the primary status outputs.
15) The gate resistors can be leaded or surface mounted. Power Integrations reserves the right to determine which type will be used. Typically, higher quantities will be produced with SMD resistors and small quantities with leaded resistors.
16) HiPot testing (= dielectric testing) must generally be restricted to suitable components. This gate driver is suited for HiPot testing. Nevertheless, it is strongly recommended to limit the testing time to 1s slots as stipulated by EN 50178. Excessive HiPot testing at voltages much higher than $850V_{AC(eff)}$ may lead to insulation degradation. No degradation has been observed over 1min. testing at $3800V_{AC(eff)}$. The transformer of every production sample shipped to customers has undergone 100% testing at the given value or higher (< $5100V_{AC(eff)}$) for 1s.
17) Partial discharge measurement is performed in accordance with IEC 60270 and isolation coordination specified in EN 50178. The partial discharge extinction voltage between primary and either secondary side is coordinated for safe isolation to EN 50178.
18) Jitter measurements are performed with input signals INx switching between 0V and 15V referred to GND, with a corresponding rise time and fall time of 8ns.
19) Note that the dead time may vary from sample to sample. A tolerance of approximately ±20% may be expected. If higher timing precisions are required, Power Integrations recommends using direct mode and generating the dead time externally.
20) A version with extended operating temperature range of –40°C…85°C (2SP0115T2B0) can also be supplied.
21) The storage temperature inside the original package (1) or in case the coating material of coated products may touch external parts (2) must be limited to the given value. Otherwise, it is limited to 90°C.
22) The component surface temperature, which may strongly vary depending on the operating condition, must be limited to the given value for coated driver versions to ensure long-term reliability of the coating material.

Data Sheet

Legal Disclaimer

The statements, technical information and recommendations contained herein are believed to be accurate as of the date hereof. All parameters, numbers, values and other technical data included in the technical information were calculated and determined to our best knowledge in accordance with the relevant technical norms (if any). They may base on assumptions or operational conditions that do not necessarily apply in general. We exclude any representation or warranty, express or implied, in relation to the accuracy or completeness of the statements, technical information and recommendations contained herein. No responsibility is accepted for the accuracy or sufficiency of any of the statements, technical information, recommendations or opinions communicated and any liability for any direct, indirect or consequential loss or damage suffered by any person arising therefrom is expressly disclaimed.

Data Sheet

Ordering Information

Our international terms and conditions of sale apply.

Power Integrations Driver Type #	Related IGBT
2SP0115T2A0-FF225R12ME4 (Temperature range –20°C…85°C)	FF225R12ME4
2SP0115T2A0C-FF225R12ME4 (Temperature range –20°C…85°C, conformal coating)	FF225R12ME4

Product home page: www.power.com/gate-driver/go/2SP0115T

Refer to www.power.com/gate-driver/go/nomenclature for information on driver nomenclature

---

Information about Other Products

For other drivers, evaluation systems product documentation and application support

Please click: www.power.com

We reserve the right to make any technical modifications without prior notice.   Version 2.0 from 2019-04-08

Data Sheet

Power Integrations Sales Offices

WORLD HEADQUARTERS
5245 Hellyer Avenue
San Jose, CA 95138 USA
Tel: +1-408-414-9200
Fax: +1-408-414-9765
Email: usasales@power.com

AMERICAS EAST
7360 McGinnis Ferry Road
Suite 225
Suwannee, GA 30024 USA
Tel: +1-678-957-0724
Fax: +1-678-957-0784
Email: usasales@power.com

AMERICAS CENTRAL
333 Sheridan Road
Winnetka, IL 60093 USA
Tel: +1-847-721-6293
Email: usasales@power.com

AMERICAS WEST
5245 Hellyer Avenue
San Jose, CA 95138 USA
Tel: +1-408-414-8778
Fax: +1-408-414-3760
Email: usasales@power.com

CHINA (Shanghai)
Room 2410, Charity Plaza
No. 88 North Caoxi Road
Shanghai, 200030 China
Tel: +86-21-6354-6323
Fax: +86-21-6354-6325
Email: chinasales@power.com

CHINA (Shenzhen)
17/F, Hivac Building, No 2
Keji South 8th Road, Nanshan District
Shenzhen, 518057 China
Tel: +86-755-8672-8689
Fax: +86-755-8672-8690
Email: chinasales@power.com

GERMANY (AC-DC/LED Sales)
Einsteinring 24
85609 Aschheim, Germany
Tel: +49-89-5527-39100
Fax: +49-89-1228-5374
Email: eurosales@power.com

GERMANY (Gate Driver Sales)
HellwegForum 1
59469 Ense, Germany
Tel: +49-2938-64-39990
Email: gate-drivers.sales@power.com

INDIA (Bangalore)
#1, 14th Main Road
Vasanthangar
Bangalore, 560052 India
Tel 1: +91-80-4113-8020
Tel 2: +91-80-4113-8028
Fax: +91-80-4113-8023
Email: indiasales@power.com

INDIA (Mumbai)
Unit: 106-107, Sagar Tech Plaza-B
Sakinaka, Andheri Kurla Road
Mumbai, Maharashtra 400072 India
Tel 1: +91-22-4003-3700
Tel 2: +91-22-4003-3600
Email: indiasales@power.com

INDIA (New Delhi)
#45, Top Floor
Okhla Industrial Area, Phase - III
New Delhi, 110020 India
Tel 1: +91-11-4055-2351
Tel 2: +91-11-4055-2353
Email: indiasales@power.com

ITALY
Via Milanese 20
20099 Sesto San Giovanni (MI), Italy
Tel: +39-02-4550-8708
Email: eurosales@power.com

JAPAN
Kosei Dai-3 Bldg.
2-12-11, Shin-Yokohama, Kohoku-ku
Yokohama-shi, Kanagawa
Japan 222-0033
Tel: +81-45-471-1021
Fax: +81-45-471-3717
Email: japansales@power.com

KOREA
RM602, 6FL, 22
Teheran-ro 87-gil, Gangnam-gu
Seoul, 06164 Korea
Tel: +82-2-2016-6610
Fax: +82-2-2016-6630
Email: koreasales@power.com

SINGAPORE
51 Newton Road
#19-01/05 Goldhill Plaza
Singapore, 308900
Tel 1: +65-6358-2160
Tel 2: +65-6358-4480
Fax: +65-6358-2015
Email: singaporesales@power.com

TAIWAN
5F, No. 318, Nei Hu Rd., Sec. 1
Nei Hu Dist.
Taipei, 114 Taiwan
Tel: +886-2-2659-4570
Fax: +886-2-2659-4550
Email: taiwansales@power.com

UNITED KINGDOM
Building 5, Suite 21
The Westbrook Centre
Milton Road
Cambridge, CB4 1YG United Kingdom
Tel: +44-7823-557-484
Email: eurosales@power.com

Koolance

www.koolance.com
**Specifications Sheet**

Generated: 2023-10-09

The Koolance PMP-500 offers a high flow rate and very high static head pressure at just 12V. A mounting bracket is included.

- Maximum Flow Rate: 16L/min (4.2 gal/min)
- Maximum Head Pressure: 7.5m (24.6ft)
- Motor: Brushless DC
- Power Consumption (at max): 32W
- Voltage Range: 6 to 12 VDC
- Maximum Temperature: 75°C (167°F)
- Electrical Connector: 4-pin Molex power supply connection + 3-pin (single lead) tach
- Hose Connections: G 1/4 BSPP Threads
- Noise: Less than 50dBA
- Weight: 454g (1lbs)

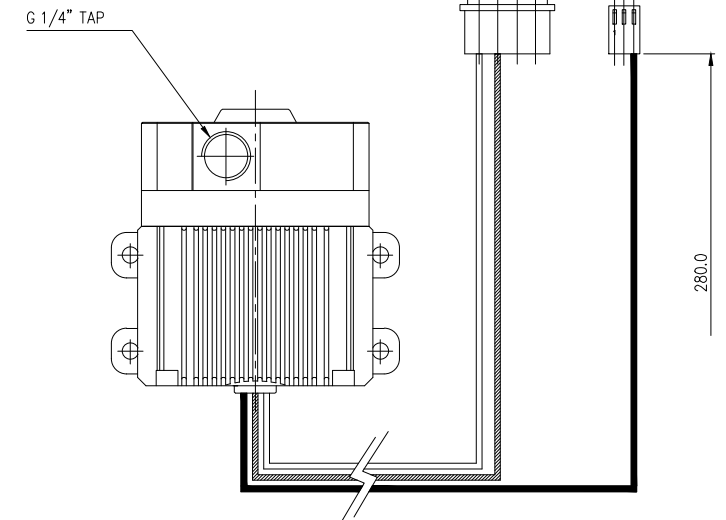| General	
Weight	1.20 lb (0.54 kg)
Fitting Thread	G 1/4 BSPP
Max Pressure Tolerance @ 25°C	1.5kgf/cm2 (21.3psi)
Max Temperature Tolerance	75°C (167°F)
Wetted Materials	PPE, Carbon, Ceramic, EPDM, ABS, POM, Ferrite
Pumps	
Expected Lifetime	30,000 hrs. MTBF
Max Flow Rate	16L/min (4.2GPM)
Max Power	32W
Max Static Head	7.5m (24.6ft)
Native Hose Connection	G 1/4 BSP Threads
Speed Knob	no
Tachometer	yes
Type	Magnetic Centrifugal
Voltage	6-12 VDC

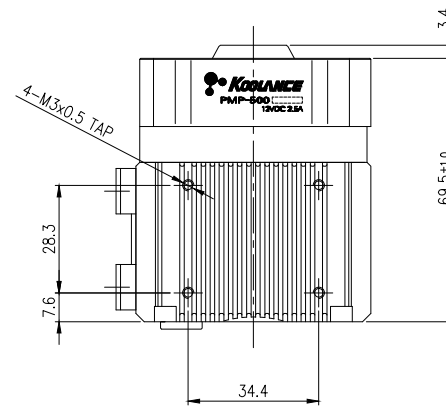PMP-500
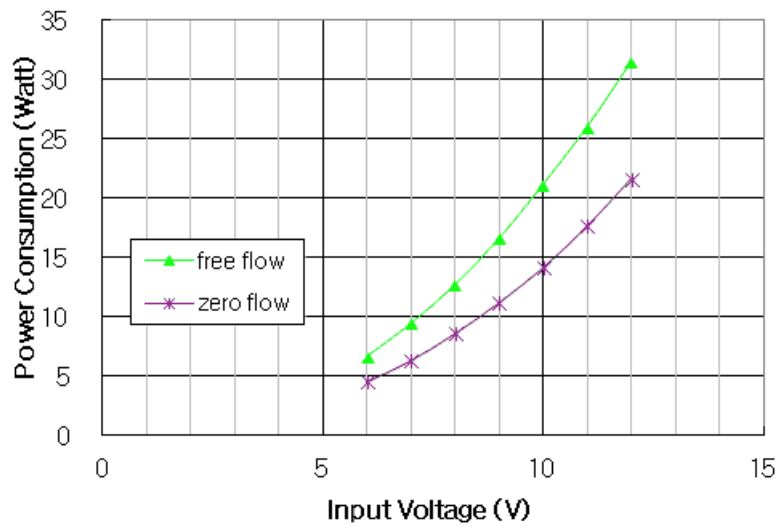
Flow Rate vs. Head Pressure
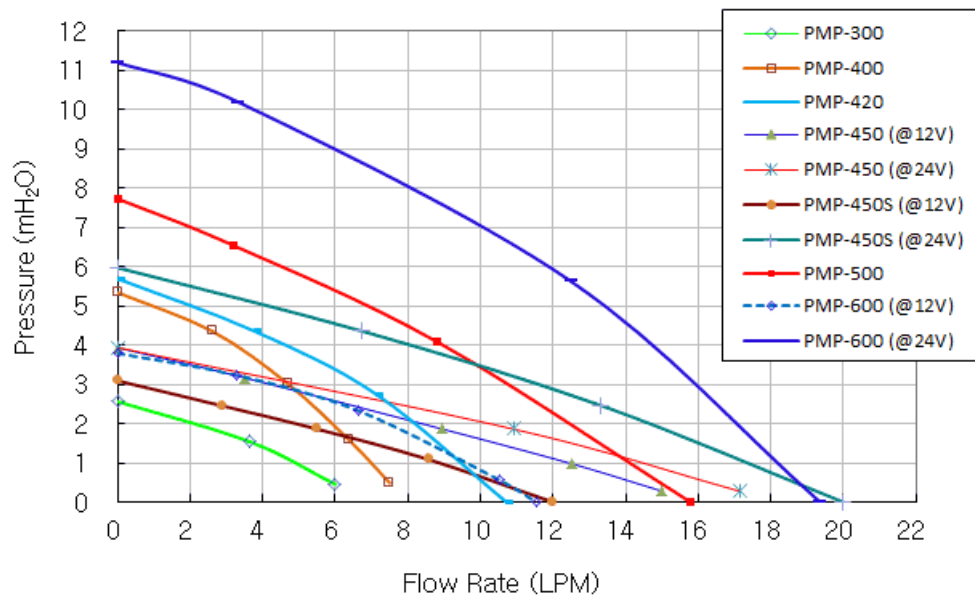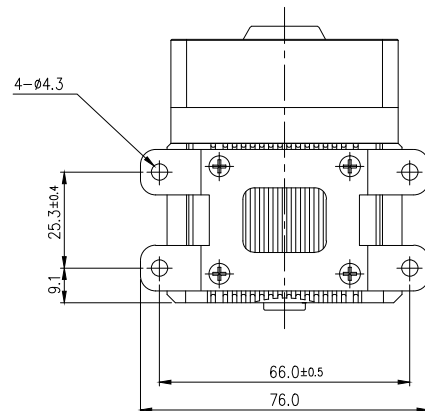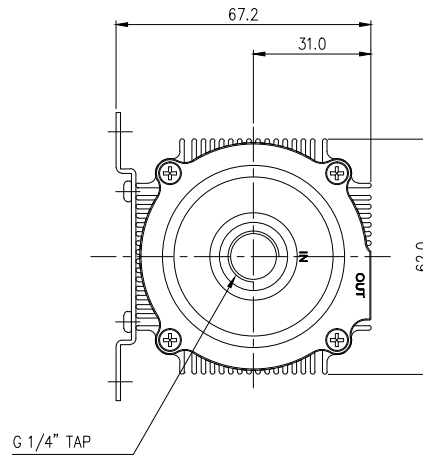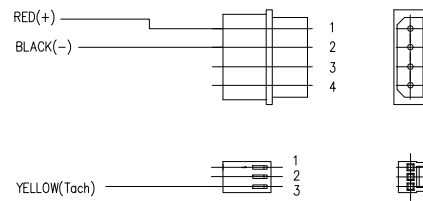
< 4 pin CONNECTOR >
- Housing : ALEX 6060-04 (or Equivalent)
- Terminal : ALEX 62T (or Equivalent)

< 3pin CONNECTOR >
- Housing : Molex 5051-03 (or Equivalent)
- Terminal : Molex 5159 (or Equivalent)

- 12VDC, 2.5A

RED(+)
BLACK(-)
1
2
3
4

YELLOW(Tach)
1
2
3

67.2
31.0
62.0
IN
OUT
G 1/4" TAP

4-⌀4.3
25.3±0.4
9.1
66.0±0.5
76.0

4-M3x0.5 TAP
28.3
7.6
34.4
3.4
69.5±1.0

G 1/4" TAP
280.0

NO.	DESCRIPTION			PART NO.		QTY.		REMARKS

KOOLANCE

				UNIT	MM	ITEM	Pump	
	DRAWN BY	BY	BY	APPRO BY	SCALE	N/S	TITLE	Assy
DATE						3RD ANGLE		
MAR.25.2021	S.J.LEE			J.S.PARK	KK CODE NO.		DRAWING NO.	REV
					PMP-500		-	-

REV	DATE	CONTENTS	REV'D BY	CHKD BY	APPD BY
⚠	MAY.18.2021	CHANGED VDC SPEC.	S.J.LEE		J.S.PARK

REVISION

CIPOS™ Mini IM535

IM535-U6D/IM535-U6DS

Description

The CIPOS™ IM535 product family offers the chance for integrating various power and control components to increase reliability and optimize PCB size and system cost. It is designed to control three-phase motors in variable speed drives. The package concept is specially adapted to power applications, which need good thermal conduction and electrical isolation, but also less EMI and overload protection. To deliver excellent electrical performance, Infineon's leading-edge TRENCHSTOP™ IGBTs and anti-parallel diodes are combined with an optimized SOI gate driver.

Features

Package

- Fully isolated dual in-line molded module
- Very low thermal resistance due to DCB substrate
- Lead-free terminal plating; RoHS compliant

Inverter

- TRENCHSTOP™ IGBTs for inverter
- Rugged SOI gate driver technology with stability against transient and negative voltage
- Allowable negative V_S potential up to -11 V for signal transmission at V_{BS} = 15 V
- Integrated bootstrap functionality
- Over-current shutdown
- Built-in NTC thermistor for temperature monitor
- Under-voltage lockout at all channels
- Low-side emitter pins accessible for phase current monitoring (open emitter)
- Sleep function
- Cross-conduction prevention
- All of 6 switches turn off during protection

Potential applications

- Home appliances, low power motor drives

Please read the Important Notice and Warnings at the end of this document

page 1 of 23

Verison 2.1

2021-04-09
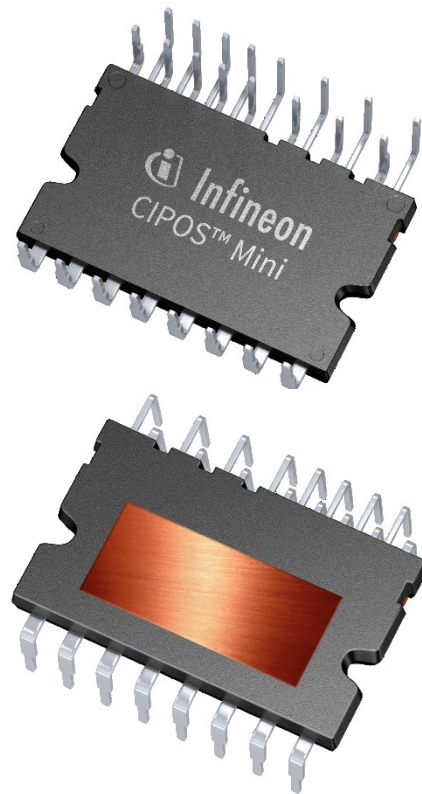
Product validation

Qualified for industrial applications according to the relevant tests of JEDEC47/20/22.

Table 1   **Product Information**

Base Part Number	Package Type	Standard Pack		Remarks
		Form	**MOQ**	
IM535-U6D	DIP 36x21D	14 pcs / Tube	280 pcs	
IM535-U6DS	DIP 36x21D	14 pcs / Tube	280 pcs	Extended stand-off

Table of Contents
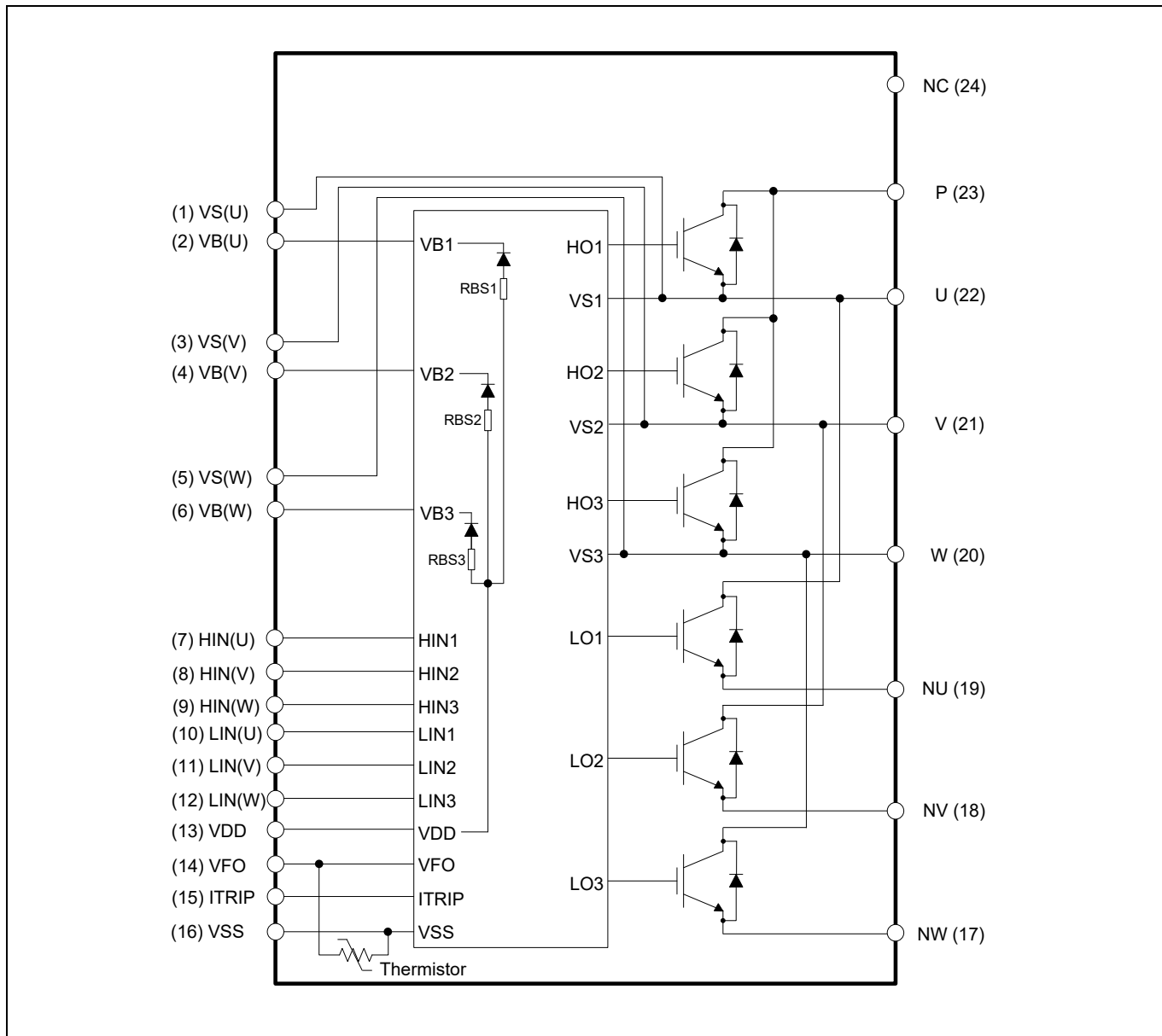
1 Internal Electrical Schematic

Figure 1   Internal electrical schematic

2 Pin Description

2.1 Pin Assignment

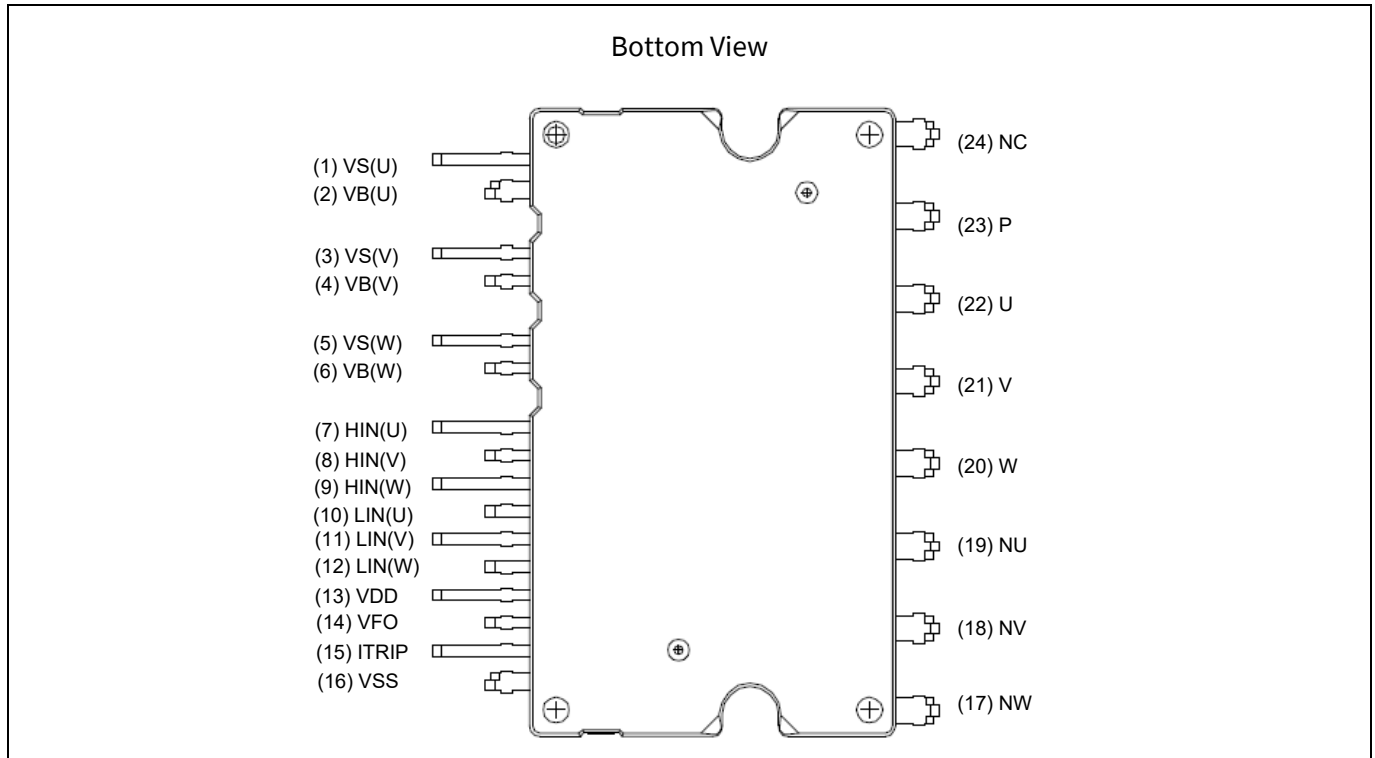**Figure 2 Pin configuration**

Table 2 Pin assignment

Pin Number	Pin name	Pin Description
1	$V_S(U)$	U-phase high-side floating IC supply offset voltage
2	$V_B(U)$	U-phase high-side floating IC supply voltage
3	$V_S(V)$	V-phase high-side floating IC supply offset voltage
4	$V_B(V)$	V-phase high-side floating IC supply voltage
5	$V_S(W)$	W-phase high-side floating IC supply offset voltage
6	$V_B(W)$	W-phase high-side floating IC supply voltage
7	HIN(U)	U-phase high-side gate driver input
8	HIN(V)	V-phase high-side gate driver input
9	HIN(W)	W-phase high-side gate driver input
10	LIN(U)	U-phase low-side gate driver input
11	LIN(V)	V-phase low-side gate driver input
12	LIN(W)	W-phase low-side gate driver input
13	V_{DD}	Low-side control supply
14	V_{FO}	Fault output / temperature monitor
15	ITRIP	Over-current shutdown input
16	V_{SS}	Low-side control negative supply
17	NW	W-phase low-side emitter

Pin Description

Pin Number	Pin name	Pin Description
18	NV	V-phase low-side emitter
19	NU	U-phase low-side emitter
20	W	Motor W-phase output
21	V	Motor V-phase output
22	U	Motor U-phase output
23	P	Positive bus input voltage
24	NC	No connection

2.2 Pin Description

HIN(U, V, W) and LIN(U, V, W) (Low-side and high-side control pins, Pin 7 - 12)

These pins are positive logic and they are responsible for the control of the integrated IGBTs. The Schmitt-trigger input thresholds of them are such to guarantee LSTTL and CMOS compatibility down to 3.3 V controller outputs. A pull-down resistor of about 5 kΩ is internally provided to pre-bias input during supply start-up, and a zener clamp is provided to protect the pin. Negative pulses down to an absolute minimum of -5.5 V are allowed that offers an outstanding robustness. Input Schmitt-trigger and noise filter provide noise rejection to short input pulses.

The noise filter suppresses control pulses shoter than the filter time $t_{FIL,IN}$. The Figure 4 describes how the filter works. An input pulse-width shorter than 1 µs is not recommended.
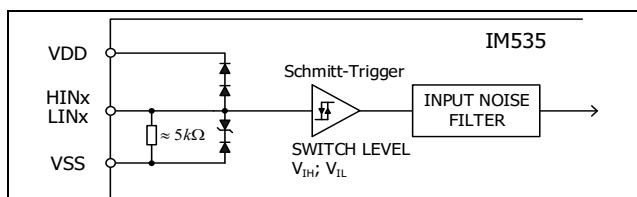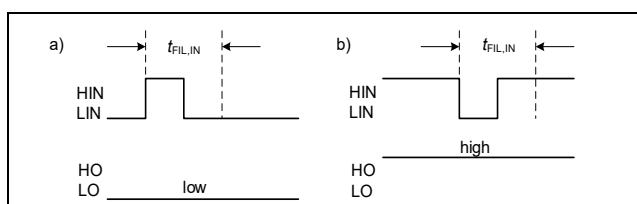

Figure 3   Input pin structure

Figure 4   Input filter timing diagram

The integrated gate driver additionally provides a shoot-through prevention capability that avoids the simultaneous on-states of the same leg (i.e.

HO1 and LO1, HO2 and LO2, HO3 and LO3). When both inputs of the same leg are activated, only formerly activated one is remained activated so that the leg is kept steadily in a safe state.
A minimum deadtime insertion of typically 360 ns is also provided by driver, in order to reduce cross-conduction of the IGBTs.

V_{FO} (Fault-output and NTC, Pin 14)

The V_{FO} pin indicates a module failure in case of under voltage at pin V_{DD} or in case of triggered over-current detection at ITRIP. An external pull-up resistor is required.
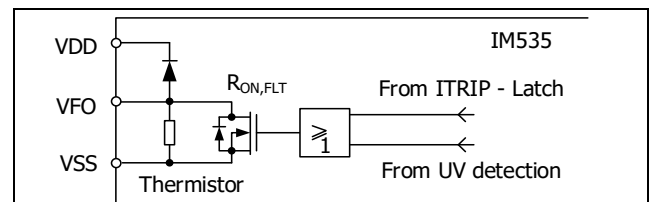

Figure 5   Internal circuit at pin V_{FO}

The sleep function is activated after each trigger of ITRIP or under-voltage lockout. A new edge input signal is mandatory to activate gate drives after falut-clear time as shown in Figure 10.

ITRIP (Over-current detection function, Pin 15)

The IM535 product family provides an over-current detection function by connecting the ITRIP input with the IGBT current feedback. The ITRIP comparator threshold (typ. 0.525 V) is referenced to V_{SS}. An input noise filter ($t_{ITRIPMIN}$ = typ. 300 ns) prevents the driver to detect false over-current events.
Over-current detection generates a shutdown of outputs of the gate driver. Fast track shutdown

Pin Description

function allows low-side outputs to be turned off faster than high side outputs about 200 ns.

The fault-clear time is set to minimum 100 µs.

V_{DD}, V_{SS} (Low-side control supply and reference, Pin 13, 16)

V_{DD} is the control supply and it provides power both to input logic and to output stage. Input logic is referenced to V_{SS} ground.

The under-voltage circuit enables the device to operate at power on when a supply voltage of at least a typical voltage of V_{DDUV+} = 12.4 V is present.

The gate driver shuts down all the outputs, when the V_{DD} supply voltage is below V_{DDUV-} = 11.5 V. This prevents the IGBTs from critically low gate voltage levels during on-state and therefore from excessive power dissipation.

V_B(U, V, W) and V_S(U, V, W) (High-side supplies, Pin 1 - 6)

V_B to V_S is the high-side supply voltage. The high-side circuit can float with respect to V_{SS} following the high-side IGBT emitter voltage.

Due to the low power consumption, the floating driver stage is supplied by integrated bootstrap circuit.

The under-voltage detection operates with a rising supply threshold of typical V_{BSUV+} = 11.5 V and a falling threshold of V_{BSUV-} = 10.7 V.

V_S(U, V, W) provide a high robustness against negative voltage in respect of V_{SS} of -50 V transiently. This ensures very stable designs even under harsh conditions.

NW, NV, NU (Low-side emitter, Pin 17 - 19)

The low-side emitters are available for current measurement of each phase leg. It is recommended to keep the connection to pin V_{SS} as short as possible to avoid unnecessary inductive voltage drops.

W, V, U (High-side emitter and low-side collector, Pin 20 - 22)

These pins are connected to motor U, V, W input pins

P (Positive bus input voltage, Pin 23)

The high-side IGBTs are connected to the bus voltage. It is noted that the bus voltage does not exceed 450 V.

3 Absolute Maximum Ratings

(V_{DD} = 15 V and T_J = 25°C, if not stated otherwise)

3.1 Module Section

Description	Symbol	Condition	Value	Unit
Storage temperature range	T_{STG}		-40 ~ 125	°C
Operating case temperature	T_C	Refer to Figure 7	-40 ~ 125	°C
Operating junction temperature	T_J		-40 ~ 150	°C
Isolation test voltage	V_{ISO}	1 min, RMS, f = 60 Hz	2000	V

3.2 Inverter Section

Description	Symbol	Condition	Value	Unit
Max. blocking voltage	V_{CES}	I_C = 250 µA	600	V
DC link supply voltage of P-N	V_{PN}	Applied between P-N	450	V
DC link supply voltage (surge) of P-N	$V_{PN(surge)}$	Applied between P-N	500	V
Continuous collector current	I_C	T_C = 25°C, T_J < 150°C	±30	A
		T_C = 80°C, T_J < 150°C	±22	
Maximum peak collector current	$I_{C(peak)}$	T_C = 25°C, T_J < 150°C less than 1 ms	±60	A
Power dissipation per IGBT	P_{tot}		83.3	W
Short circuit withstand time[1]	t_{SC}	$V_{DC} \leq$ 400V, T_J = 150°C	5	µs

3.3 Control Section

Description	Symbol	Condition	Value	Unit
High-side offset voltage	V_S		600	V
Repetitive peak reverse voltage of bootstrap diode	V_{RRM}		600	V
Module supply voltage	V_{DD}		-1 ~ 20	V
High-side floating supply voltage (V_B reference to V_S)	V_{BS}		-1 ~ 20	V
Input voltage(LIN, HIN, ITRIP)	V_{IN}		-1 ~ V_{DD}+0.3	V

---

[1] Allowed number of short circuits: < 1000; time between short circuits: > 1 s.

4 Thermal Characteristics

Description	Symbol	Condition	Value			Unit
			Min.	Typ.	Max.	
Single IGBT thermal resistance, junction to case	R_{thJC}	Low-side U-phase (See Figure 7 for T_C measurement point)			1.49	K/W
Single diode thermal resistance, junction to case	$R_{thJC,D}$	Low-side U-phase			2.18	K/W

5 Recommended Operation Conditions

All voltages are absolute voltages referenced to V_{SS} -potential unless otherwise specified.

Description	Symbol	Value			Unit
		Min.	Typ.	Max.	
DC link supply voltage of P-N	V_{PN}	0	300	450	V
Low-side supply voltage	V_{DD}	13	15	17.5	V
High-side floating supply voltage (V_B vs. V_S)	V_{BS}	13	-	17.5	V
Logic input voltages LIN, HIN, ITRIP	V_{IN} V_{ITRIP}	0	-	5	V
Inverter PWM carrier frequency	f_{PWM}	-	-	20	kHz
External deadtime between HIN and LIN	DT	2	-	-	µs
Voltage between V_{SS} – N (including surge)	V_{COMP}	-5	-	5	V
Minimum input pulse width	$PW_{IN(ON)}$ $PW_{IN(OFF)}$	1	-	-	µs
Control supply variation	$\Delta V_{BS,}$ ΔV_{DD}	-1 -1	- -	1 1	V/µs

6 Static Parameters

(V_{DD} = 15 V and T_J = 25°C, if not stated otherwise)

6.1 Inverter Section

Description	Symbol	Condition	Value			Unit
			Min.	Typ.	Max.	
Collector-emitter voltage	$V_{CE(Sat)}$	I_C = 30 A, T_J = 25°C	-	1.8	2.1	V
		I_C = 30 A, T_J = 150°C	-	2.05	-	
Collector-emitter leakage current	I_{CES}	V_{CE} = 600 V	-	-	1	mA
Diode forward voltage	V_F	I_F = 30 A, T_J = 25°C	-	1.95	2.35	V
		I_F = 30 A, T_J = 150°C	-	1.9	-	

6.2 Control Section

Description	Symbol	Condition	Value			Unit
			Min.	Typ.	Max.	
Logic "1" input voltage (LIN, HIN)	V_{IH}		1.7	2.0	2.3	V
Logic "0" input voltage (LIN, HIN)	V_{IL}		0.7	0.9	1.1	V
ITRIP positive going threshold	$V_{IT,TH+}$		475	525	570	mV
ITRIP input hysteresis	$V_{IT,HYS}$		45	70	-	mV
V_{DD} and V_{BS} supply under-voltage positive going threshold	V_{DDUV+}		11.5	12.4	13.1	V
	V_{BSUV+}		10.6	11.5	12.2	
V_{DD} and V_{BS} supply under-voltage negative going threshold	V_{DDUV-}		10.6	11.5	12.3	V
	V_{BSUV-}		9.7	10.7	11.7	
V_{DD} and V_{BS} supply under-voltage lockout hysteresis	V_{DDUVH} V_{BSUVH}		0.5	0.9	-	V
Quiescent V_{Bx} supply current (V_{Bx} only)	I_{QBS}	H_{IN} = 0 V	-	-	300	µA
Quiescent V_{DD} supply current (V_{DD} only)	I_{QDD}	L_{IN} = 0 V, H_{INX} = 5 V	-	-	1.1	mA
Input bias current for LIN, HIN	I_{IN+}	V_{IN} = 5 V	-	1.1	1.7	mA
Input bias current for ITRIP	I_{ITRIP+}	V_{ITRIP} = 5 V	-	68	185	µA
Input bias current for V_{FO}	I_{FO}	V_{FO} = 5 V, V_{ITRIP} = 0 V	-	60	-	µA
V_{FO} output voltage	V_{FO}	I_{FO} = 10 mA, V_{ITRIP} = 1 V	-	0.35	-	V
Bootstrap diode forward voltage	V_{F_BSD}	I_F = 0.3 mA	-	1.0	-	V
Bootstrap diode resistance	R_{BSD}	Between V_{F1} = 4 V and V_{F2} = 5 V	-	37	-	Ω

7 Dynamic Parameters

(V_{DD} = 15 V and T_J = 25°C, if not stated otherwise)

7.1 Inverter Section

Description	Symbol	Condition	Value			Unit
			Min.	Typ.	Max.	
Turn-on propagation delay time	t_{on}	$V_{LIN, HIN}$ = 5 V, I_C = 30 A, V_{DC} = 300 V	-	725	-	ns
Turn-on rise time	t_r		-	85	-	ns
Turn-on switching time	$t_{c(on)}$		-	295	-	ns
Reverse recovery time	t_{rr}		-	320	-	ns
Turn-off propagation delay time	t_{off}	$V_{LIN, HIN}$ = 0 V, I_C = 30 A, V_{DC} = 300 V	-	900	-	ns
Turn-off fall time	t_f		-	25	-	ns
Turn-off switching time	$t_{c(off)}$		-	90	-	ns
Short circuit propagation delay time	t_{SCP}	From $V_{IT,TH+}$ to 10% I_{SC}	-	1550	-	ns
IGBT turn-on energy (includes reverse recovery of diode)	E_{on}	V_{DC} = 300 V, I_C = 30 A T_J = 25°C T_J = 150°C	- -	1430 1820	- -	µJ
IGBT turn-off energy	E_{off}	V_{DC} = 300 V, I_C = 30 A T_J = 25°C T_J = 150°C	- -	495 730	- -	µJ
Diode recovery energy	E_{rec}	V_{DC} = 300 V, I_C = 30 A T_J = 25°C T_J = 150°C	- -	105 245	- -	µJ

7.2 Control Section

Description	Symbol	Condition	Value			Unit
			Min.	Typ.	Max.	
Input filter time ITRIP	t_{ITRIP}	V_{ITRIP} = 1 V	-	530	-	ns
Input filter time at LIN, HIN for turn on and off	$t_{FIL,IN}$	$V_{LIN, HIN}$ = 0 V or 5 V	-	290	-	ns
Fault clear time after ITRIP-fault	t_{FLTCLR}		100	280	-	µs
ITRIP to fault propagation delay	t_{FLT}	$V_{LIN, HIN}$ = 0 or $V_{LIN, HIN}$ = 5 V, V_{ITRIP} = 1 V	-	680	1000	ns
Internal deadtime	DT_{IC}		-	360	-	ns
Matching propagation delay time (on and off) all channels	M_T	External dead time > 500 ns	-	20	-	ns

8   Thermistor

Description	Condition	Symbol	Value			Unit
			Min.	**Typ.**	**Max.**	
Resistance	$T_{NTC} = 25°C$	R_{NTC}	-	85	-	kΩ
B-constant of NTC (negative temperature coefficient) thermistor		B(25/100)	-	4092	-	K

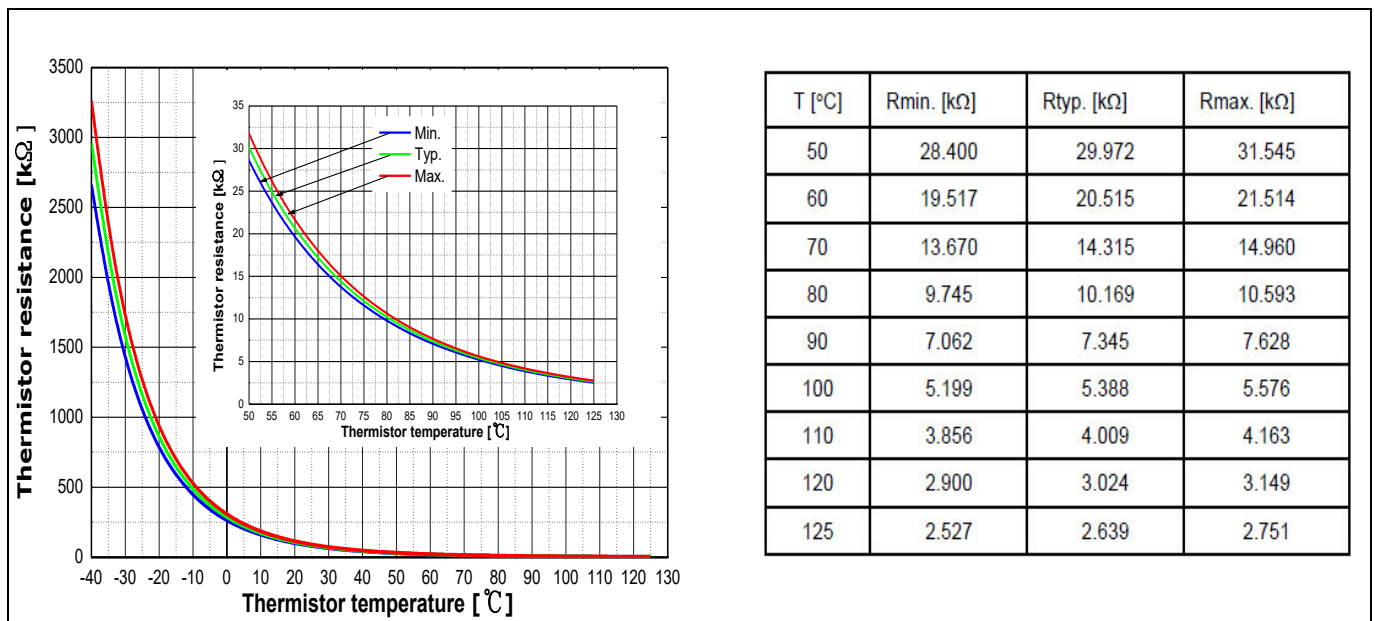| T [°C]	Rmin. [kΩ]	Rtyp. [kΩ]	Rmax. [kΩ]
50	28.400	29.972	31.545
60	19.517	20.515	21.514
70	13.670	14.315	14.960
80	9.745	10.169	10.593
90	7.062	7.345	7.628
100	5.199	5.388	5.576
110	3.856	4.009	4.163
120	2.900	3.024	3.149
125	2.527	2.639	2.751

Figure 6   Thermistor resistance – temperature curve and table
(For more information, please refer to the application note)

9 Mechanical Characteristics and Ratings

Description	Condition	Value			Unit
		Min.	**Typ.**	**Max.**	
Comparative tracking index (CTI)		600	-	-	V
Mounting torque	M3 screw and washer	0.49		0.78	Nm
Backside curvature	Refer to Figure 8	-50	-	100	µm
Weight		-	6.58	-	g

10   Qualification Information

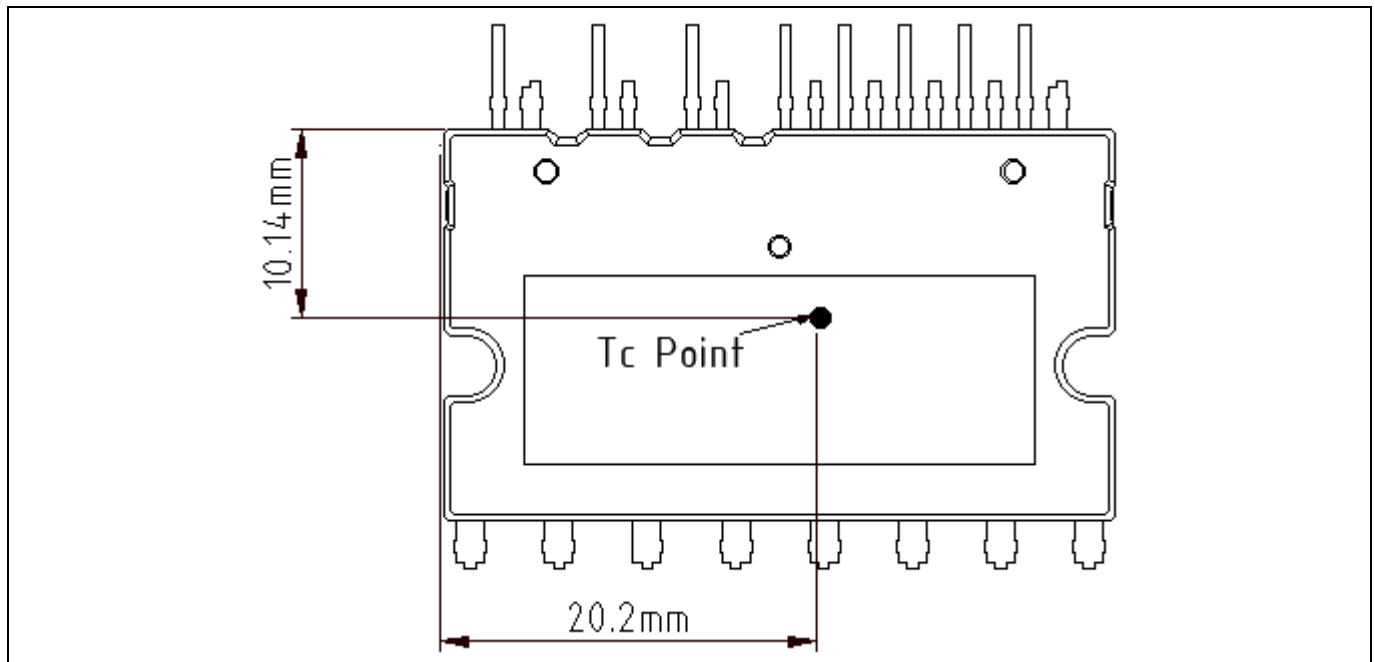|		
UL certification	File number: E314539	
Moisture sensitivity level (SOP23 only)	-	
RoHS compliant	Yes (Lead-free terminal plating)	
ESD	HBM(human body model) class	2
	CDM(charged device model) class	C3

11 Diagrams and Tables

11.1 T$_C$ Measurement Point

Figure 7 T$_C$ measurement point[1]

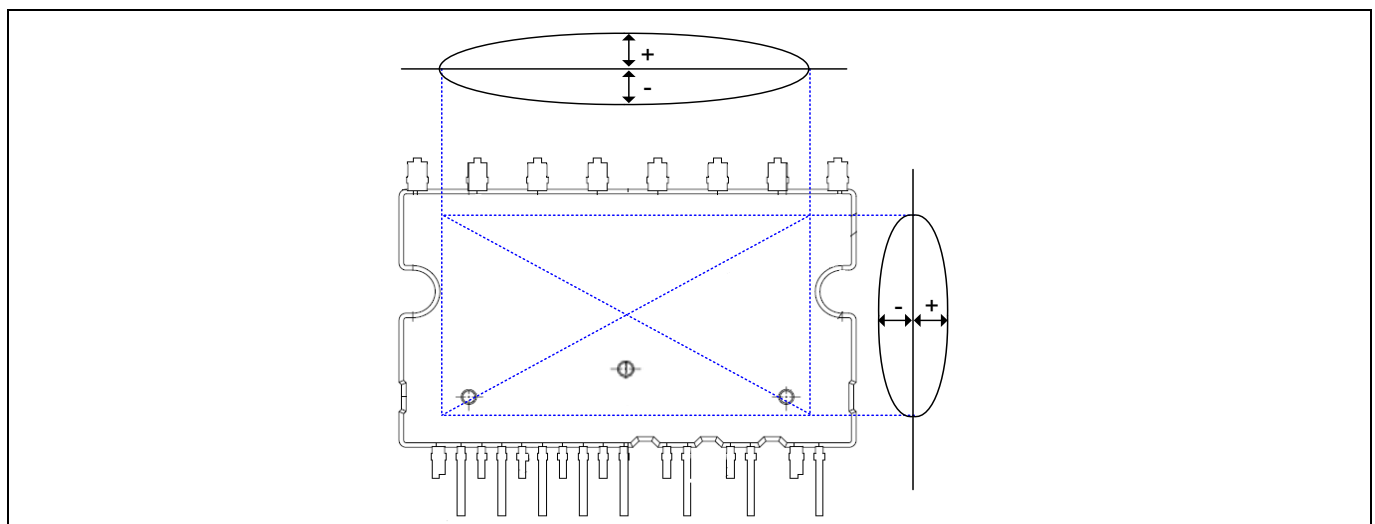## 11.2 Backside Curvature Measurment Point

Figure 8 Backside curvature measurement position

---

[1]Any measurement except for the specified point in Figure 7 is not relevant for the temperature verification and brings wrong or different information.

11.3 Switching Time Definition

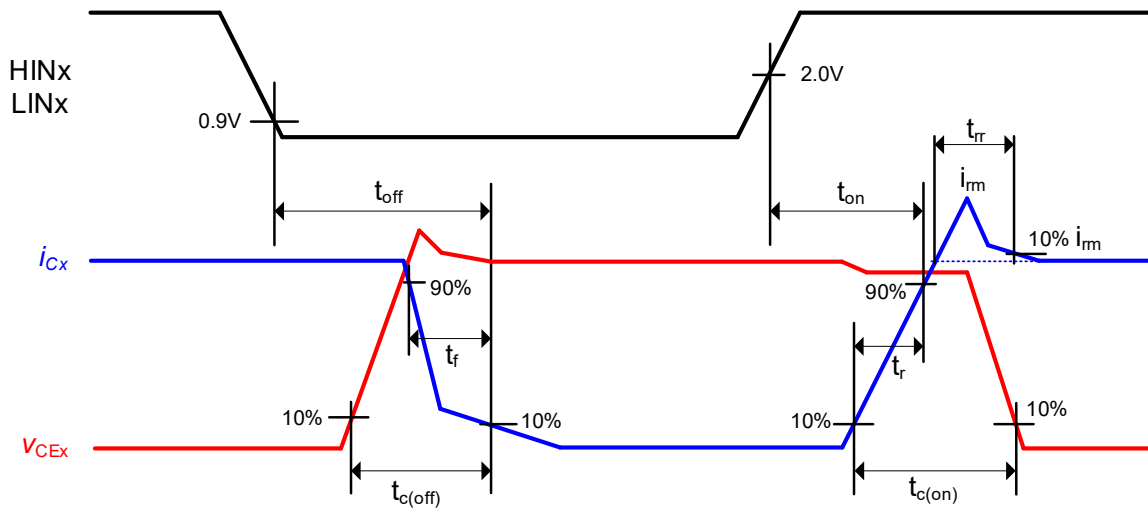**Figure 9   Switching time definition**
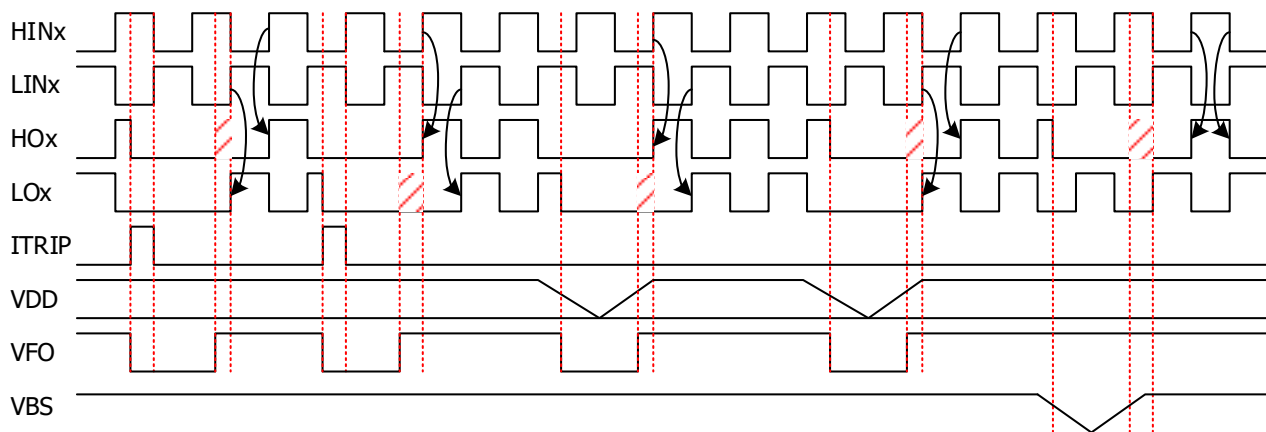
11.4 Sleep function timing diagram

Figure 10   Sleep function timing diagram

12 Application Guide
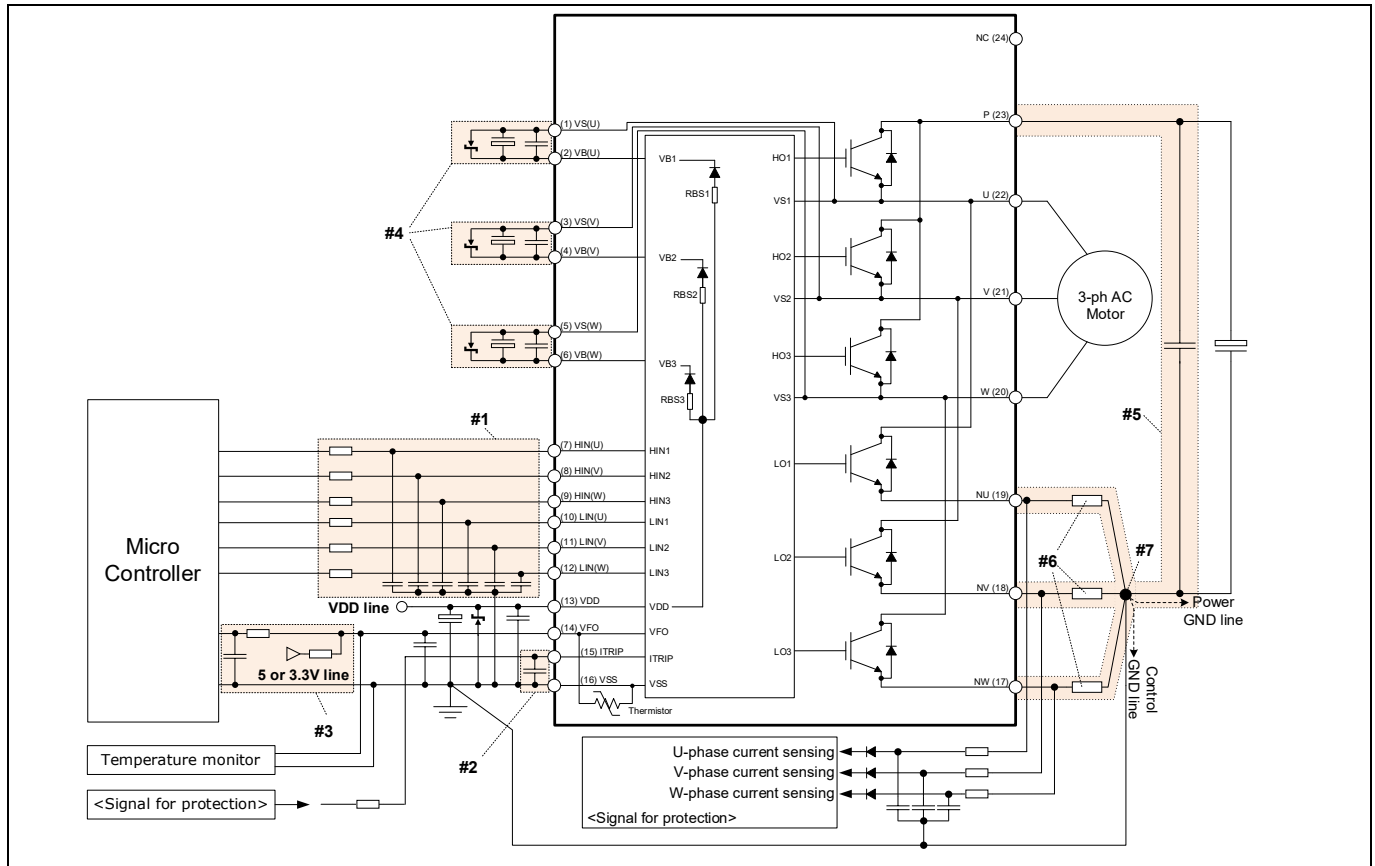
12.1 Typical Application Schematic

Figure 11   Typical application circuit

- #1 Input circuit
  - RC filter can be used to reduce input signal noise. (100 Ω, 1 nF)
  - The capacitors should be located close to the IPM (to V_{SS} terminal especially).
- #2 ITRIP circuit
  - To prevent a mis operation of protection function, RC filter is recommended.
  - The capacitor should be located close to ITRIP and V_{SS} terminals.
- #3 V_{FO} circuit
  - V_{FO} pin is open drain configuration. This terminal should be pulled up to the bias voltage of the 5 V/3.3 V through a proper resistor.
  - It is recommended that RC filter is placed close to the controller.
- #4 V_B-V_S circuit
  - Capacitors for high-side floating supply voltage should be placed close to V_B and V_S terminals.
- #5 Snubber capacitor
  - The wiring among the IPM, snubber capacitor and shunt resistors should be short as possible.
- #6 Shunt resistor
  - SMD type shunt resistors are strongly recommended to minimize its internal stray inductance.
- #7 Ground pattern
  - Pattern overlap of power ground and signal ground should be minimized. The patterns should be connected at one end of shunt resistor only for the same potential.
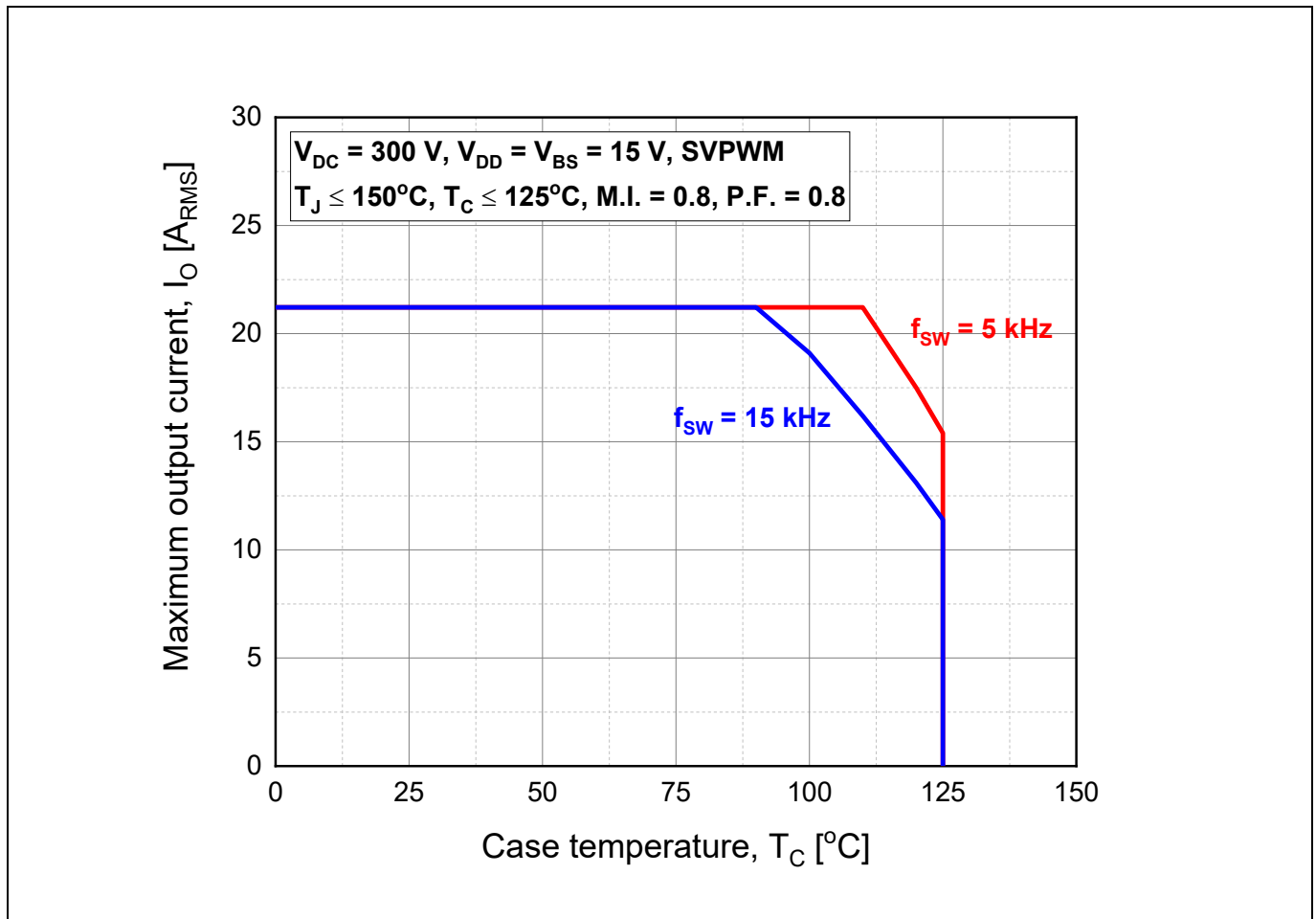
12.2 Performance Chart

$V_{DC} = 300\ V,\ V_{DD} = V_{BS} = 15\ V,\ SVPWM$

$T_J \leq 150^o C,\ T_C \leq 125^o C,\ M.I. = 0.8,\ P.F. = 0.8$

$f_{SW} = 5\ kHz$

$f_{SW} = 15\ kHz$

Maximum output current, I_O [A_{RMS}]

Case temperature, T_C [^{o}C]

Figure 12   Maximum operating current SOA[1]

---

[1]This maximum operating current SOA is just one of example based on typical characteristics for this product. It can be changed by each user's actual operating conditions.
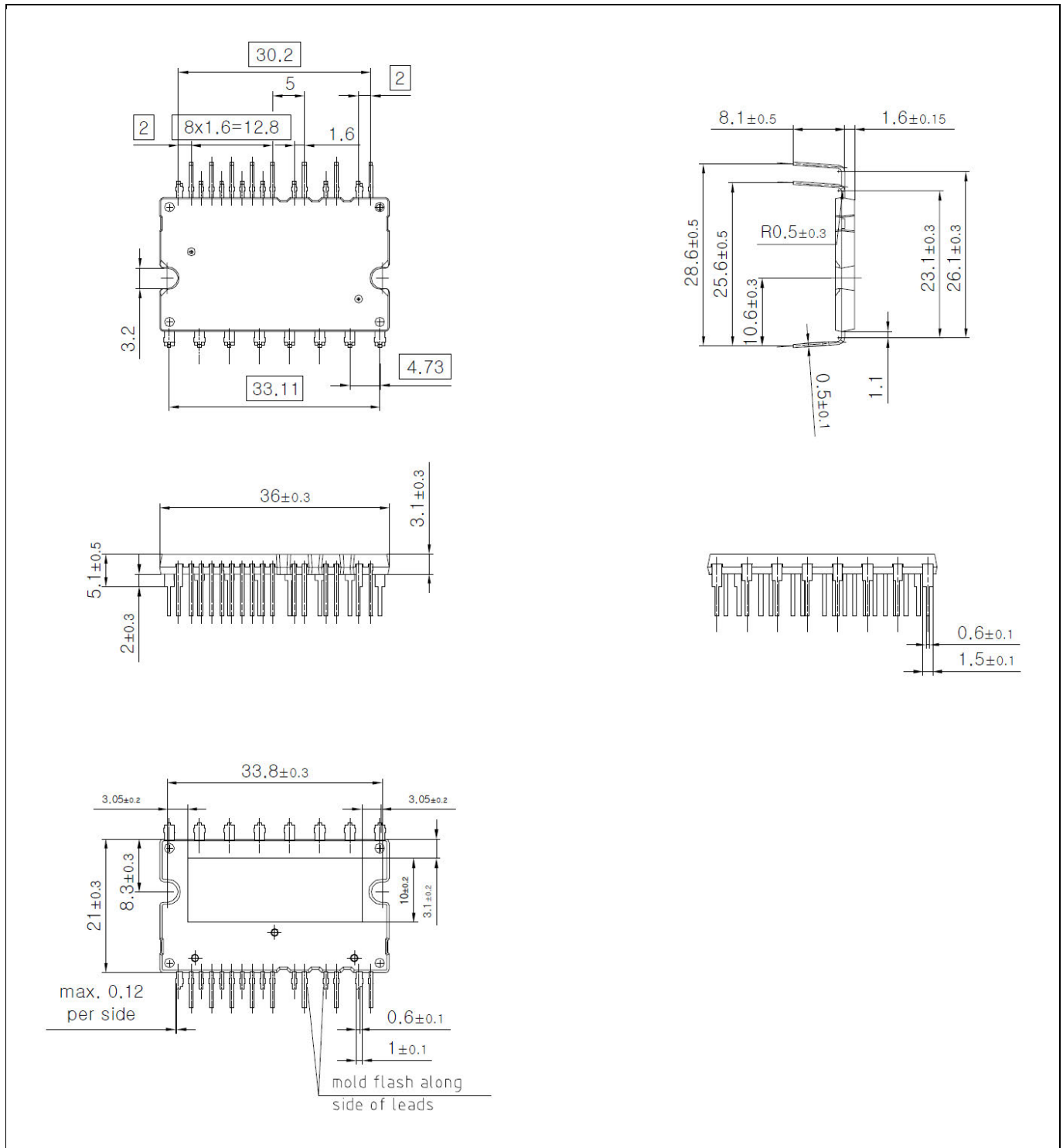
13 Package Outline

Figure 13   IM535-U6D

Package Outline

Figure 14   IM535-U6DS

Revision history

Document version	Date of release	Description of changes
Version 2.0	2020-05-07	Initial release
Version 2.1	2021-04-09	Corrected typo in page 8 Corrected error in Figure 9 Updated Figure 11

Trademarks
All referenced product or service names and trademarks are the property of their respective owners.

EMRAX Mounting Bracket and Output Shaft

CONTENTS

348.30

114.70

208.60

16.85

Ø8.50

281.55

142°

128°

80.00

190.00

295.00

Ø10.50

16.85
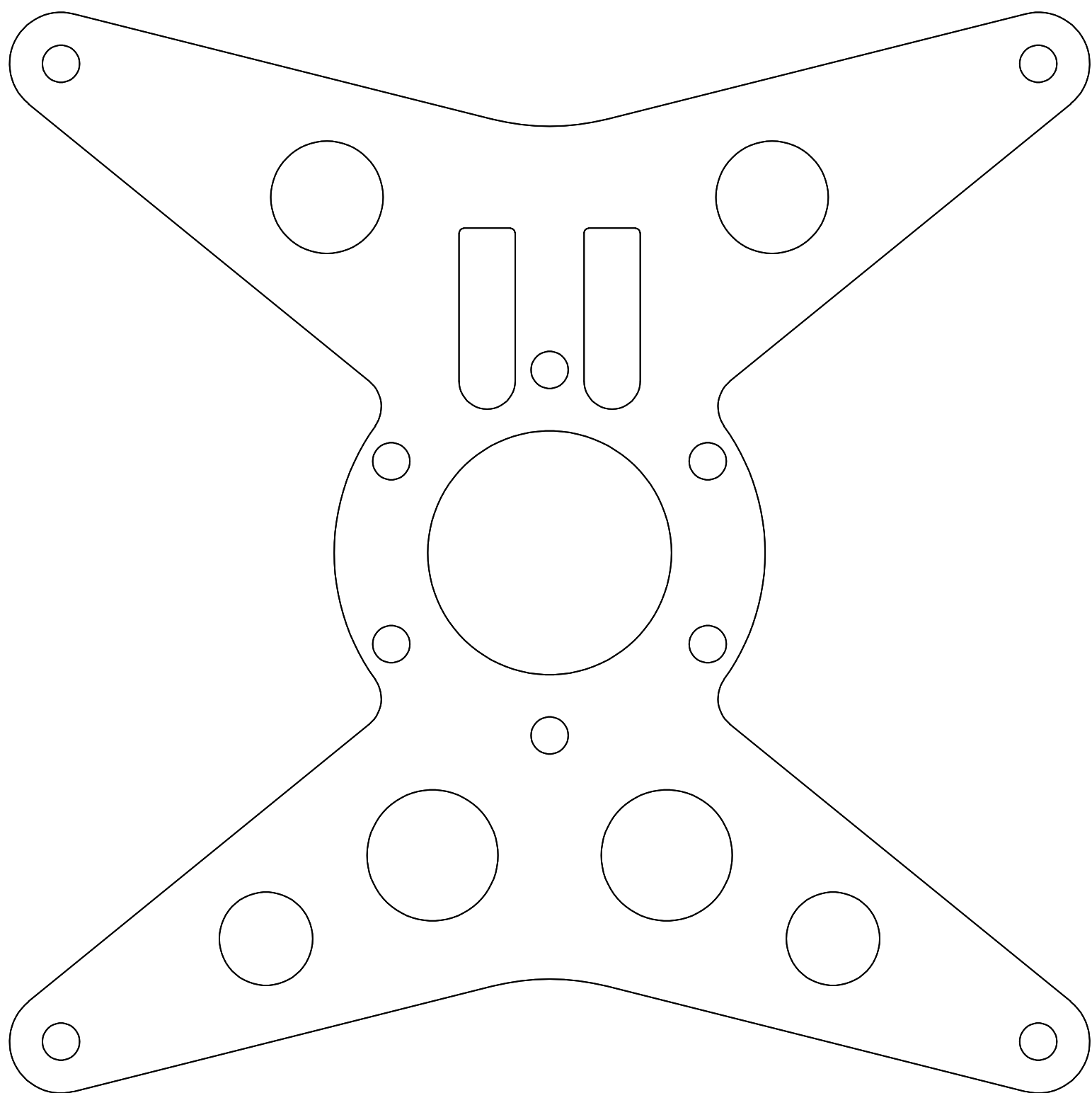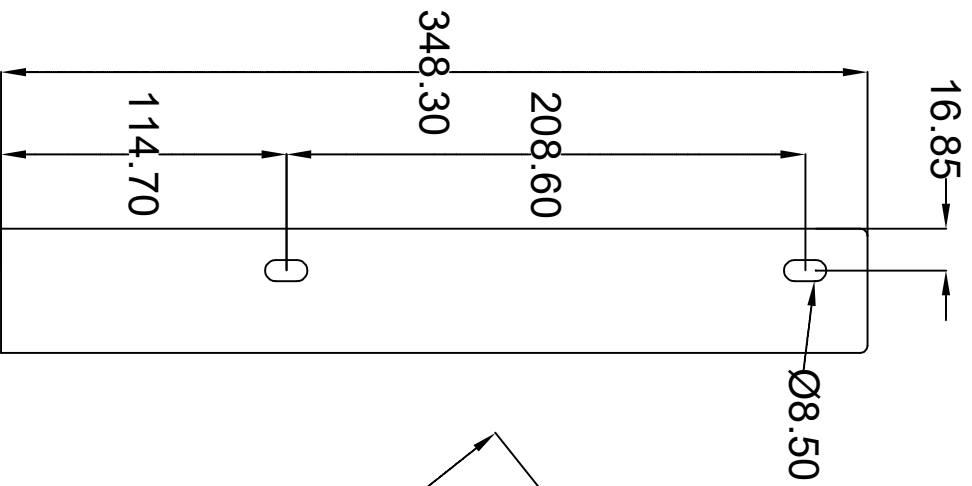
Two of each component required.
To be made from 50 x 6mm flat bar.
Note: Holes are slotted to allow for adjustment.

120.70

208.60

80.00

190.00

50.00

6.00

120.70

208.60

80.00

190.00

50.00

6.00
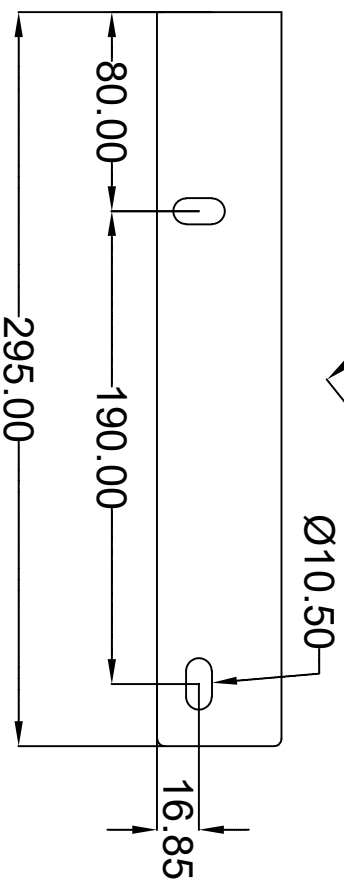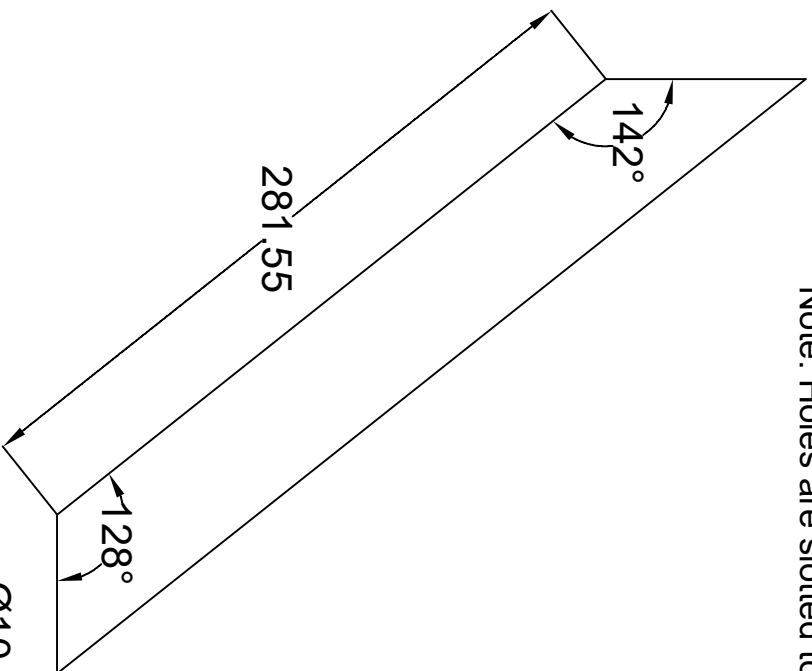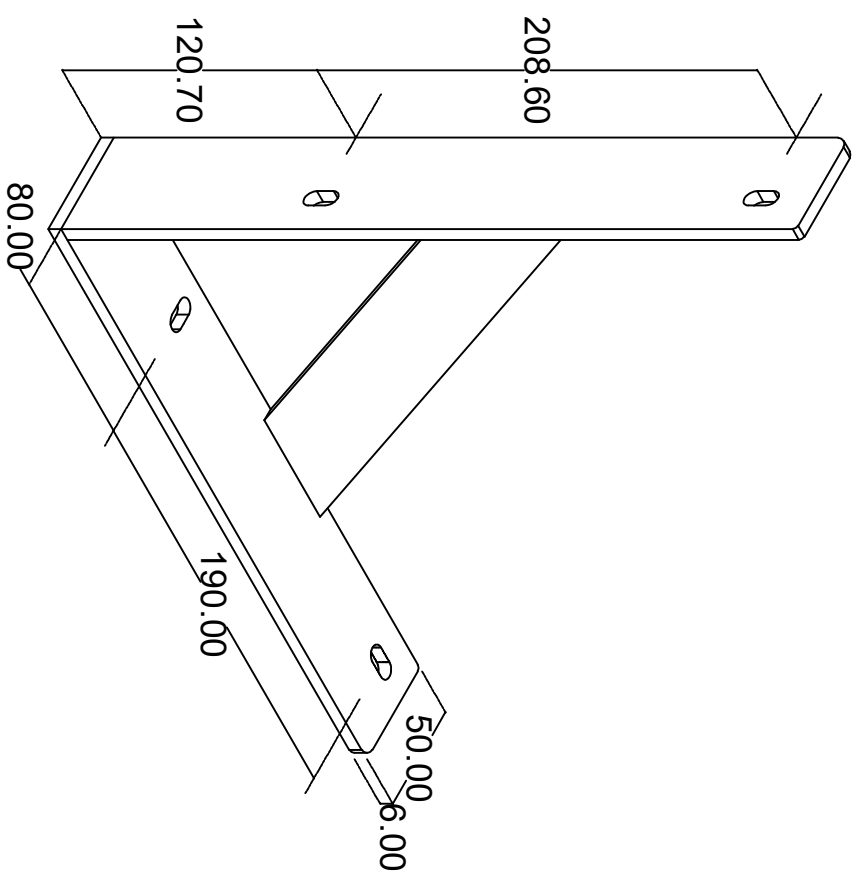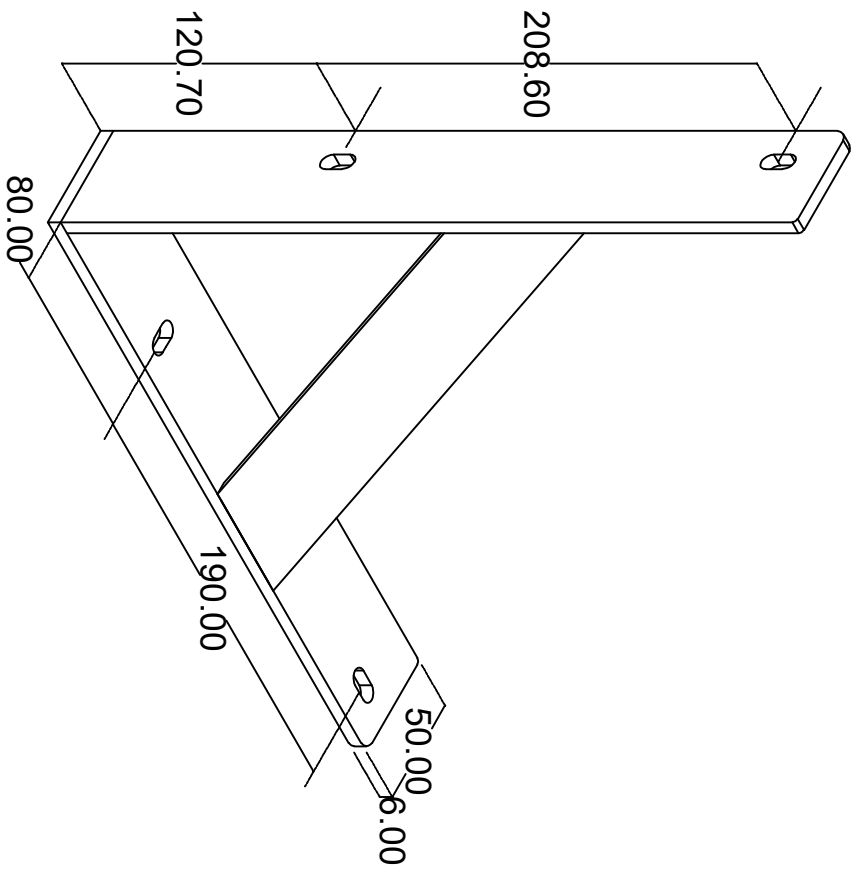
Shaft to suit existing coupling.
Requires 8mm key way.
Existing coupling will be provided to workshop.

Ø94.00

37.50

Ø7.70

8.00

65.00

15.00

28.00
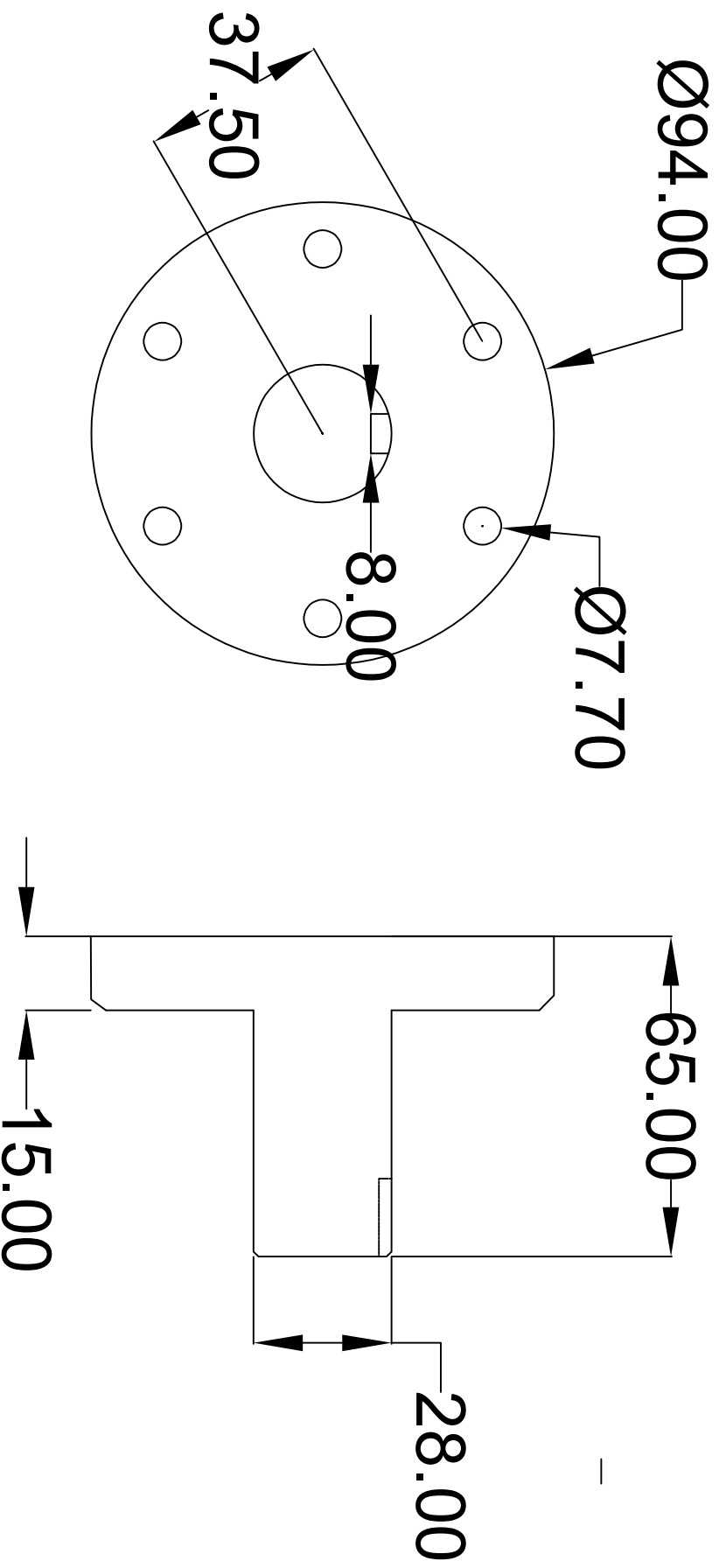
Appendix D

Odrive Programming Script

Odrive Settings for EMRAX 228 HC - CC
This motor is rated to 9.8 rpm/v unloaded, due to additional weight (output shaft and coupling) 9.5rpm/v will be used.
##Supply voltage is a nominal 36V

```
odrv0.axis0.motor.config.current_lim = 5 #Set current limit in amperage
odrv0.axis0.controller.config.vel_limit = 5.7 #Set velocity limit in turn/s [(9.5*36)/60 = 5.7]
odrv0.axis0.motor.config.calibration_current = 4.5
odrv0.axis0.motor.config.pole_pairs = 10
odrv0.axis0.motor.config.torque_constant = 1 #Set to 1 to control by current
odrv0.axis0.motor.config.motor_type = 0 #Set to 0 for high current motor
odrv0.config.enable_brake_resistor = True

odrv0.save_configuration() #Save configuration, reboots after this

odrv0.axis0.controller.config.vel_gain = 0.05
odrv0.axis0.controller.config.vel_integrator_gain = 0
odrv0.axis0.controller.config.control_mode = CONTROL_MODE_VELOCITY_CONTROL
odrv0.axis0.config.sensorless_ramp.vel = 358 #in radians/s (36*(9.5/60)*10(pole pairs)*2pi)
odrv0.axis0.controller.config.vel_limit = 5.7
odrv0.axis0.config.sensorless_ramp.accel = 15 #in radians/s^2
odrv0.axis0.sensorless_estimator.config.pm_flux_linkage = 5.51328895422 / (10 * 9.5)
odrv0.axis0.config.enable_sensorless_mode = True

odrv0.save_configuration() #Save configuration, reboots after this
.0
##Motor calibration to calculate phase resistance and inductance
odrv0.axis0.requested_state = 4

odrv0.axis0.motor.config.phase_inductance
odrv0.axis0.motor.config.phase_resistance

##Run
odrv0.axis0.requested_state = 8

dump_errors(odrv0)
odrv0.config.max_regen_current = 3
odrv0.clear_errors()
```

Appendix D

```
#Install brake resistor
odrv0.config.brake_resistance = 5
odrv0.config.enable_brake_resistor = True
odrv0.config.dc_max_negative_current = -2

odrv0.config.dc_max_negative_current = -0.1
odrv0.axis0.controller.config.vel_integrator_gain = 0.0
odrv0.axis0.config.sensorless_ramp.accel = 15
odrv0.axis0.motor.config.pre_calibrated = True
```

Appendix D

Water cooling circuit calculated flow vs pressure drop MATLAB Script

```matlab
% Author:        Samuel Baker
% Student #:     ████████
% Date:          05-04-2022

close('all'); clear; clc;

% Component data
flow_gpm_1001 = [0.2    0.3    0.4    0.5    0.7    1.0    1.5    2.0];
% Advanced Termal Solutions - Cold Plate [ATS-CP-1001] flow rate values from
datasheet (in gallons per minute)
press_psi_1001 = [0.1    0.175    0.25    0.35    0.6    0.88    1.5    2.2];
% Advanced Termal Solutions - Cold Plate [ATS-CP-1001] pressure drop values from
datasheet (in psi)
thermRes_1001 = [0.013  0.009    0.0075  0.007    0.0063  0.0053  0.005    0.0044 ];
% Advanced Termal Solutions - Cold Plate [ATS-CP-1001] thermal resistance values
from datasheet (in degC/W)

flow_gpm_HE23 = [0.0    0.5    1.0    1.5    2.0    2.5];    % Advanced Termal
Solutions - Heat Exchanger [ATS-HE23] flow rate values from datasheet (in gallons
per minute)
press_psi_HE23 = [0.0    2.0    4.75    10.0    17.0    25.0];  % Advanced Termal
Solutions - Heat Exchanger [ATS-HE23] pressure drop values from datasheet (in psi)
thermRes_HE23 = [0.0    1/85    1/105    1/110    1/115    1/120]; % Advanced Termal
Solutions - Heat Exchanger [ATS-HE23] thermal resistance values from datasheet (in
degC/W)

flow_lpm_EMRAX228 =  [2    3    4    5    6    7    8    9    10];
% EMRAX 228 Motor flow rate values (in litres per minute)
press_bar_EMRAX228 = [0.1    0.15    0.22    0.31    0.44    0.56    0.75    0.94
1.15]; % EMRAX 228 Motor pressure drop values (in bar)

% Additional pump data
flow_lpm_400 = [0.0 2.5 4.7 6.5 7.5];   % Koolance PMP-400 - Water Pump flow rate
values from datasheet (in litres per minute)
press_mH2O_400 = [5.5 4.5 3.0 1.6 0.5]; % Koolance PMP-400 - Water Pump pressure
drop values from datasheet (in mH2O)
flow_lpm_500 = [0.0 3.1 8.8 16.0];      % Koolance PMP-500 - Water Pump flow rate
values from datasheet (in litres per minute)
press_mH2O_500 = [7.5 6.5 4.1 0.0];     % Koolance PMP-500 - Water Pump pressure
drop values from datasheet (in mH2O)

% Conversion Factors
```

```matlab
GPM_to_LPM = 3.78541;  % Coversion ratio. Gallons per minute to litres per minute.
PSI_to_kPa = 6.89476;  % Coversion ratio. Psi to kPa
mH2O_to_kPa = 9.80665; % Coversion ratio. mH2O to kPa

% Convert the data to LPM and kPa
flow_lpm_1001 = flow_gpm_1001 * GPM_to_LPM;    % Advanced Termal Solutions - Cold
Plate [ATS-CP-1001]
press_kpa_1001 = press_psi_1001 * PSI_to_kPa;  % Advanced Termal Solutions - Cold
Plate [ATS-CP-1001]
flow_lpm_HE23 = flow_gpm_HE23 * GPM_to_LPM;    % Advanced Termal Solutions - Heat
Exchanger [ATS-HE23]
press_kpa_HE23 = press_psi_HE23 * PSI_to_kPa;  % Advanced Termal Solutions - Heat
Exchanger [ATS-HE23]
press_kpa_EMRAX228 = press_bar_EMRAX228 * 100; % 1 bar = 100 kPa
press_kpa_400 = press_mH2O_400 * mH2O_to_kPa;  % Koolance PMP-400 - Water Pump
press_kpa_500 = press_mH2O_500 * mH2O_to_kPa;  % Koolance PMP-500 - Water Pump

% Define the common range
common_flow = linspace(0,10,1e5); % Set interpolation range

% Interpolate the data to the common range
press_kpa_1001_interp = interp1(flow_lpm_1001, press_kpa_1001, common_flow,
'linear', 'extrap');
press_kpa_HE23_interp = interp1(flow_lpm_HE23, press_kpa_HE23, common_flow,
'linear', 'extrap');
press_kpa_EMRAX228_interp = interp1(flow_lpm_EMRAX228, press_kpa_EMRAX228,
common_flow, 'linear', 'extrap');
press_kpa_400_interp = interp1(flow_lpm_400, press_kpa_400, common_flow, 'linear',
'extrap');
press_kpa_500_interp = interp1(flow_lpm_500, press_kpa_500, common_flow, 'linear',
'extrap');
thermal_resistance1001_interp = interp1(flow_lpm_1001, thermRes_1001, common_flow,
'linear', 'extrap');
thermal_resistanceHE23_interp = interp1(flow_lpm_HE23, thermRes_HE23, common_flow,
'linear', 'extrap');

% Plot each interpolated curve on individual figures
figure;
plot(common_flow, press_kpa_1001_interp);
xlabel('Flow (LPM)');
ylabel('Pressure (kPa)');
title('Interpolated Curve for 1001');
grid on;

figure;
plot(common_flow, press_kpa_HE23_interp);
xlabel('Flow (LPM)');
ylabel('Pressure (kPa)');
title('Interpolated Curve for HE23');
grid on;
```

Appendix E

```matlab
figure;
plot(common_flow, press_kpa_EMRAX228_interp);
xlabel('Flow (LPM)');
ylabel('Pressure (kPa)');
title('Interpolated Curve for EMRAX228');
grid on;

% Sum the interpolated data
total_press_kpa = press_kpa_1001_interp + press_kpa_HE23_interp + ...
press_kpa_EMRAX228_interp;

% Plot the combined curve for previous pumps
figure;
plot(common_flow, total_press_kpa, 'LineWidth', 2);
hold on;

% Plot the interpolated curves for 400 and 500 pumps for one pump
plot(common_flow, press_kpa_400_interp, '--r', 'LineWidth', 2);
plot(common_flow, press_kpa_500_interp, '--g', 'LineWidth', 2);

% Plot the interpolated curves for 400 and 500 pumps for two pumps in series
plot(common_flow, 2*press_kpa_400_interp, '-r', 'LineWidth', 2);
plot(common_flow, 2*press_kpa_500_interp, '-g', 'LineWidth', 2);

% Add labels and legend
xlabel('Flow (LPM)', 'FontSize', 14);
ylabel('Pressure (kPa)', 'FontSize', 14);
ylim([0 350]);
title('Motor Controller - Water Cooling Circuit Calculated Flow v Pressure', ...
'FontSize', 18, 'FontWeight', 'bold');
legend('Combined ATS-CP-1001, ATS-HE23 and EMRAX 228 pressure drop', 'Single PMP-400 Pump', 'Single PMP-500 Pump', 'Dual PMP-400 Pumps', 'Dual PMP-500 Pumps', ...
'Location', 'Best', 'FontSize', 14);
grid on;
hold off;


% Tolerance for finding intersections
tolerance = 1.5e-3;

% Find Intersection Points and Print them
for i = 1:length(common_flow)
    % Intersection with 400 Pump (1x)
    if abs(press_kpa_400_interp(i) - total_press_kpa(i)) <= tolerance
        fprintf('Intersection with 400 Pump (1x) at Flow: %.2f LPM (%.2f GPM), Pressure: %.2f kPa (%.2f PSI)\n', common_flow(i), common_flow(i)/GPM_to_LPM, press_kpa_400_interp(i), press_kpa_400_interp(i)/PSI_to_kPa);
        % Find the thermal resistance for the determined flow rate
        determined_thermal_resistance = interp1(common_flow, thermal_resistance1001_interp, common_flow(i), 'linear');
        % Output the thermal resistance for the determined flow rate
```

Appendix E

```matlab
        fprintf('The cooling plate thermal resistance for a flow rate of %.2f LPM
is: %.4f degC/W\n\n', common_flow(i), determined_thermal_resistance);
    end
    % Intersection with 500 Pump (1x)
    if abs(press_kpa_500_interp(i) - total_press_kpa(i)) <= tolerance
        fprintf('Intersection with 500 Pump (1x) at Flow: %.2f LPM (%.2f GPM),
Pressure: %.2f kPa (%.2f PSI)\n', common_flow(i), common_flow(i)/GPM_to_LPM,
press_kpa_500_interp(i), press_kpa_500_interp(i)/PSI_to_kPa);
        % Find the thermal resistance for the determined flow rate
        determined_thermal_resistance = interp1(common_flow,
thermal_resistance1001_interp, common_flow(i), 'linear');
        % Output the thermal resistance for the determined flow rate
        fprintf('The cooling plate thermal resistance for a flow rate of %.2f LPM
is: %.4f degC/W\n\n', common_flow(i), determined_thermal_resistance);
    end
    % Intersection with 400 Pump (2x)
    if abs(2*press_kpa_400_interp(i) - total_press_kpa(i)) <= tolerance
        fprintf('Intersection with 400 Pump (2x) at Flow: %.2f LPM (%.2f GPM),
Pressure: %.2f kPa (%.2f PSI)\n', common_flow(i), common_flow(i)/GPM_to_LPM,
2*press_kpa_400_interp(i), 2*press_kpa_400_interp(i)/PSI_to_kPa);
        % Find the thermal resistance for the determined flow rate
        determined_thermal_resistance = interp1(common_flow,
thermal_resistance1001_interp, common_flow(i), 'linear');
        % Output the thermal resistance for the determined flow rate
        fprintf('The cooling plate thermal resistance for a flow rate of %.2f LPM
is: %.4f degC/W\n\n', common_flow(i), determined_thermal_resistance);
    end
    % Intersection with 500 Pump (2x)
    if abs(2*press_kpa_500_interp(i) - total_press_kpa(i)) <= tolerance
        fprintf('Intersection with 500 Pump (2x) at Flow: %.2f LPM (%.2f GPM),
Pressure: %.2f kPa (%.2f PSI)\n', common_flow(i), common_flow(i)/GPM_to_LPM,
2*press_kpa_500_interp(i), 2*press_kpa_500_interp(i)/PSI_to_kPa);
        % Find the thermal resistance for the determined flow rate
        determined_thermal_resistance = interp1(common_flow,
thermal_resistance1001_interp, common_flow(i), 'linear');
        % Output the thermal resistance for the determined flow rate
        fprintf('The cooling plate thermal resistance for a flow rate of %.2f LPM
is: %.4f degC/W\n', common_flow(i), determined_thermal_resistance);

        % Find the thermal resistance of heat exchanger for the determined flow
rate
        determined_thermal_resistance = interp1(common_flow,
thermal_resistanceHE23_interp, common_flow(i), 'linear');
        % Output the thermal resistance of heat exchanger for the determined flow
rate
        fprintf('The heat exchanger thermal resistance for a flow rate of %.2f LPM
is: %.4f degC/W\n\n', common_flow(i), determined_thermal_resistance);
    end
end
```

Appendix E

Water cooling circuit steady state temperatures MATLAB Script

```matlab
% Author:       Samuel Baker
% Student #:    ████████
% Date:         16-04-2022

close('all'); clear; clc;

temp_ambient = 50; %degC - Ambient temperature of a hot summer day

IGBT_tot = 239.85; %115A total losses for the IGBT, in Watts
Diode_tot = 111.19; %115A total losses for the Diode, in Watts

transistor_PWR_loss = IGBT_tot + Diode_tot; %Total transistor power losses
combined, in Watts

cont_mtr_PWR = 55e3; % The continuous motor power is 55kW
service_eta = 0.92; % Motor efficiency is assumed to be no less than 92% at
continuous power
liquidCooling = 2/3; % As advised by EMRAX, 2/3 of cooling performed through the
liquid
EMRAX_PWR_loss = liquidCooling * (cont_mtr_PWR/service_eta - cont_mtr_PWR);
%Calculated power loss at continuous current, in Watts

junction_max = 150; %degC - Maximum permissible junction temperature


%% Thermal Resistances

RI_thJH = 0.175; % (K/W) IGBT thermal resistance, junction to heatsink (cooling
plate) [from datasheet]
RD_thJH = 0.197; % (K/W) Diode thermal resistance, junction to heatsink (cooling
plate) [from datasheet]

R_thCP = 0.005; % (K/W) Cooling plate thermal resistance, cooling plate to water

R_thHE = 0.0090; % (K/W) Heat exchanger thermal resistance, water to ambient

T_water = temp_ambient + (transistor_PWR_loss)*R_thHE; % Cooling water temperature
T_CP = T_water + transistor_PWR_loss*R_thCP;          % Cooling plate temperature
T_junctionI = T_CP + IGBT_tot*RI_thJH;      % IGBT Junction temperature
T_junctionD = T_CP + Diode_tot*RD_thJH;     % Diode junction temperature
```

```matlab
T_water_EMRAX = temp_ambient + (EMRAX_PWR_loss + transistor_PWR_loss)*R_thHE; %
Cooling water temperature
T_CP_EMRAX = T_water_EMRAX + transistor_PWR_loss*R_thCP;          % Cooling plate
temperature
T_junctionI_EMRAX = T_CP_EMRAX + IGBT_tot*RI_thJH;      % IGBT Junction temperature
T_junctionD_EMRAX = T_CP_EMRAX + Diode_tot*RD_thJH;     % Diode junction
temperature


%% Steady State Results

disp('<strong>IGBT Power Loss ONLY</strong>'); fprintf('\n')

if T_junctionI < junction_max && T_junctionD < junction_max %Checking to confirm
maximum junction temperature is not exceeded by either the diode or IGBT
    fprintf('System is SAFE! The maximum junction temperature of %0.2f degC will
NOT be exceeded.\n\n',junction_max)
else
    fprintf('!!WARNING!!\nSystem FAILURE! The maximum junction temperature of
%0.2f degC will be exceeded.\n\n',junction_max)
end

fprintf('IGBT junction temperature  =   %0.2f degC\n',T_junctionI)
fprintf('Diode junction temperature =   %0.2f degC\n',T_junctionD)
fprintf('Cooling plate temperature  =   %0.2f degC\n',T_CP)
fprintf('Coolant water temperature  =   %0.2f degC\n',T_water)
fprintf('Ambient temperature        =   %0.2f degC\n\n',temp_ambient)


fprintf('\n***************************************************\n\n')


disp('<strong>IGBT and EMRAX Power Losses</strong>'); fprintf('\n')

if T_junctionI < junction_max && T_junctionD < junction_max %Checking to confirm
maximum junction temperature is not exceeded by either the diode or IGBT
    fprintf('System is SAFE! The maximum junction temperature of %0.2f degC will
NOT be exceeded.\n\n',junction_max)
else
    fprintf('!!WARNING!!\nSystem FAILURE! The maximum junction temperature of
%0.2f degC will be exceeded.\n\n',junction_max)
end

fprintf('IGBT junction temperature  =   %0.2f degC\n',T_junctionI_EMRAX)
fprintf('Diode junction temperature =   %0.2f degC\n',T_junctionD_EMRAX)
fprintf('Cooling plate temperature  =   %0.2f degC\n',T_CP_EMRAX)
fprintf('Coolant water temperature  =   %0.2f degC\n',T_water_EMRAX)
fprintf('Ambient temperature        =   %0.2f degC\n',temp_ambient)
```

Appendix F

ST Microelectronics deadtime setting MATLAB Script

```matlab
% Author:        Samuel Baker
% Student #:     ████████
% Date:          19-05-2022

close('all'); clear; clc;
format ShortEng

%% Timer Dead-time Setting for STM32F4

APB2_timer_freq = 84e6; % APB2 timer clock frequency. TIM1 uses wthis clock.
Currently set at 84 MHz
Prescaler = 0;
Deadtime = 2e-6; % Desired deadtime

Multiplier = round(Deadtime*(APB2_timer_freq / (Prescaler + 1)));

% Calculates the closest "Dead Time" controller setting for the desired dead time
if Multiplier <= 127
    T = Multiplier;
elseif Multiplier >= 128 && Multiplier <= 254
    T = round((Multiplier-128)/2)+128;
elseif Multiplier >= 256 && Multiplier <= 504
    T = round((Multiplier-256)/8)+192;
elseif Multiplier >= 512 && Multiplier <= 1008
    T = round((Multiplier-512)/16)+224;
else
   error('Desired dead time is unachievable with current clock frequency and
prescaler')
end

% Identify an expected dead time from a known "Dead Time" value
deadtime_entered = 200;
% T = deadtime_entered;

% Determines what actual dead time will be experienced from the "Dead Time"
setting calculated
if T <= 127
    actual_dead_time = T;
elseif T >= 128 && T <= 191
    actual_dead_time = ((T-128)*2)+128;
elseif T >= 192 && T <= 223
    actual_dead_time = ((T-192)*8)+256;
elseif T >= 224
    actual_dead_time = ((T-224)*16)+512;
```

```matlab
end
actual_dead_time = actual_dead_time/(APB2_timer_freq / (Prescaler + 1));

% Prints findings to the command window
fprintf('Settings used: APB2 timer clock frequency of %.2f MHz with a prescaler of
%d.\n\n', APB2_timer_freq/1e6, Prescaler)
fprintf('The desired dead time used for these calculations was
%.2f%cs.\n',Deadtime*1e6, char(181))
fprintf('A dead time of %.2f%cs will be achieved using a "Dead Time" value of
%d.\n', actual_dead_time*1e6, char(181), T)
```

Appendix G

Centre biasing, bi-polar signal, op-amp resistor selection

```matlab
% Author:         Samuel Baker
% Student #:      ████████
% Date:           24-04-2022

close('all'); clear; clc;

format shortEng

VDD = 3.3; %ADC Input Voltage
Imax = 50; %Current max in Amps
Rs = 3e-3; %Current sense shunt resistor in ohms

Gmax = VDD/(2*Imax*Rs); % Maximum allowable gain before ADC saturation is achieved
Gain = 10.5;            % Gain selected (usually slightly below the calculated
Gmax)
R1 = 2.1e3;             % All other calculations are based of the preselected
value of R1

R2 = (Gain - 0.5)*R1;
Rb_exact = (1-(0.5/Gain))*R1; % Calculation of ideal Rb value
Rb = 2e3;                     % Slight discrepancy of Rb is permitted, therefore
select Rb is entered here
Ra = 2*Gain*round(Rb,2);


%% Print results to command window

fprintf('G_max = %0.2f\n',Gmax)
fprintf('Gain selected = %0.2f\n\n',Gain)
fprintf('R1 = %0.2f\n',R1)
fprintf('R2 = %0.2f\n\n',R2)
fprintf('Calculated Rb = %0.5f\n',Rb_exact)
fprintf('Rb selected = %0.5f\n\n',Rb)
fprintf('Ra = %0.2f\n',Ra)
```

Electronic Schematic

Title: IM535 Motor Driver + Auxiliary Circuits

Samuel Baker
Sheet: /
File: STM32F401RE_IM535.kicad_sch
Size: A3   Date:
KiCad E.D.A. eeschema 7.0.2
Rev: 0
Id: 1/1